Antiviral and antimicrobial inflammasome formation in intestinal epithelial cells

Florian Nikolaus Gohr

ORCID ID:

0000-0001-7167-8431

from Würselen, Germany

Submitted in total fulfilment of the requirements of the joint degree of

Doctor of Philosophy (PhD)

of

The Medical Faculty

The Rheinische Friedrich-Wilhelms-Universität Bonn

and

The Department of Microbiology and Immunology

The University of Melbourne

Bonn/Melbourne, 2024

Performed and approved by The Medical Faculty of the Rheinische Friedrich-Wilhelms-Universität Bonn and The University of Melbourne

1. Supervisor: Florian Ingo Schmidt
2. Supervisor: Jason Mackenzie
3. Supervisor: Sarah Londrigan

Month and year of the original thesis submission:	09/2023
Month and year of the oral examination:	07/2024

Institute in Bonn: From the Institute of Innate Immunity

Director: Prof. Dr. Dagmar Wachten

Table of Contents

Abbreviations

(+)ssRNA	positive single-stranded RNA
ACE2	angiotensin converting enzyme 2
AIM2	absent in melanoma 2
ALR	AIM2-like recptor
ASC	Apoptosis-associated speck-like protein containing a CARD
ATP	adenosine triphosphate
BFP	blue fluorescent protein
BHK	baby hamster kidney
BSA	bovine serum albumin
C1C	caspase-1CARD
C4C	caspase-4CARD
CARD	caspase activation and recruitment domain
CDL	CARD domain linker
cDNA	complementary DANN
CLR	C-type lectin receptor
COP	CARD only protein
COVID-19	coronavirus disease 19
CPE	cytopathic effect
cryo-EM	cryo-electron microscopy
CTO	celltracker orange
DAMP	danger associated molecular pattern
DFD	death-fold domain
DHX	DEAH-box helicase
DLP	double-layered particle
DMEM	Dulbecco's Modified Eagle Medium
DMSO	dimethyl sulfoxide
DNA	deoxyribonucleic acid
dNTP	deoxynucleoside triphosphyte
DPP	dipeptidylpeptidases
dsDNA	double-stranded DNA
dsRNA	double-stranded RNA
E. coli	*Escherischia coli*
e.g.	*exempli gratia* (for example)
EDTA	ethylenediaminetetraacetic acid
EEC	enteroendocrine cell
EGF	epidermal growth factor
EGFP	enhanced green fluorescent protein
ELISA	enzyme-linked immunosorbent assay

EMCV	encephalomyocarditis virus
ER	endoplasmic reticulum
FACS	fluorescence-activated cell sorting
FBS	fetal bovine serum
Fc	constant fragment
FIIND	function-to-find
FLICA	fluorochrome inhibitor of caspases
FSC	forward scatter
GBP	guanylate binding protein
gMFI	geometric mean of fluorescence intensity
GSK	glycogen synthase kinase
GST	glutathione-S-transferase
HEK	hamster embryonic kidney
HEPES	4-(2-hydroxyethyl)-1-piperazineethanesulfonic acid
HIE	human intestinal enteroid
HMW	high molecular weight
HPRT	hypoxanthine phophoribosyltransferase
HR	heptad repeat
HTRF	homogenous time-resolved fluorescence
i.e.	*id est* (that is)
IDL	interdomain linker
IEC	intestinal epithelial cell
IFN	interferon
IL	interleukin
INCA	inhibitory CARD
IPTG	isopropyl-β-D-thiogalactopyranoside
IRES	internal ribosome entry site
IRF	interferon regulatory factor
ISG	interferon stimulated gene
ISGF	interferon-stimulated gene factor
LB	lysogeny broth
LDH	lactate dehydrogenase
LFn	lethal factor N-terminus
LLPS	liquid-liquid phase separation
LMW	low molecular weight
LRR	leucine-rich repeat
LTA	lipoteichoic acid
M-CSF	macrophage colony stimulating factor
MAP	mitogen-activated protein
MAVS	mitochondrial antiviral signalling protein
MEM	Minimum Essential Medium

MERS-CoV	Middle East respiratory syndrome coronavirus
MIE	mouse intestinal enteroid
MOI	multiplicity of infection
MΦ	macrophage
NAIP	NLR family apoptosis inhibitory protein
NBD	nucleotide-binding domain
NFκB	nuclear factor κB
nig	nigericin
NLR	NBD and LRR containing receptor
NLRC	NLR family CARD containing
NLRP	NLR family PYD containing
NSP	non-structural protein
NTA	nitriloacetic acid
OD	optical density
ODM	organoid differentiation medium
OGM	organoid growth medium
PAMP	pathogen associated molecular pattern
PBS	phosphate buffered saline
PCC	Pearson's correlation coefficient
pCMV	cytomegalovirus promoter
pEF1α	elongation factor 1α promoter
PEI MAX	polyethylenimine “Max”
PI	propidium iodide
PMA	Phorbol-12-myristat-13-acetat
pMT	metallothionein promoter
poly(dA:dT)	poly(deoxyadenylic-deoxythymidylic) acid
poly(I:C)	poly(inosinic-cytidylic) acid
PRR	pattern recognition receptor
PTM	posttranslational modification
pUbC	ubiquitin C promoter
PYD	pyrin domain
RBD	receptor binding domain
RCF	relative centrifugal force
RFP	red fluorescent protein
RIG	retinoic acid-inducible gene
RLR	RIG-I-like receptor
RNA	ribonucleic acid
RT-qPCR	reverse transcription quantitative polymerase chain reaction
RV	rotavirus
S. flexneri	*Shigella flexneri*
S. Thyphimurium	*Salmonella enterica* serovar Typhimurium

SARS-CoV	severe acute respiratory syndrome coronavirus 2
scFv	single-chain variable fragment
SEC	size exclusion chromatography
SEM	standard error of the mean
SPI	*Salmonella* pathogenicity island
SPR	surface plasmon resonance
SSC	side scatter
STAT	signal transducer and activator of transcription
T3SS	type III secretion system
TB	Terrific Broth
TLR	toll-like receptor
TNF	tumor necrosis factor
TSB	tryptic soy broth
UPA	UNC5, PIDD, Ankyrin
UT	untreated
VCAM-1	vascular cell adhesion molecule 1
VH	variable domain of the heavy chain
VHH	variable domain of the heavy chain of a heavy chain only antibody
VL	variable domain of the light chain
VSV	vesicular stomatitis virus
WT	wild type
ZU5	ZO1, UNC5

List of Tables

List of Figures

Abstract

Inflammasomes coordinate inflammation by inducing rapid cytokine secretion and protect against invading pathogens by initiating death of infected cells. We developed and characterised a novel fluorescent reporter that visualises inflammasome formation and reports on the recruitment of the effector protein caspase-1 without impairing downstream signalling. Using this reporter, I could demonstrate how caspase-1 is recruited to the inflammasome via the formation of filaments. I additionally show how the CARD-only protein CARD17 inhibits caspase-1 recruitment, and thus cytokine secretion, by terminating caspase-1 filaments. Next, I investigated inflammasome responses in human and mouse intestinal enteroids as models for functional tissues. I found that triggers of the NAIP/NLRC4 inflammasome, including bacteria, activate inflammasomes in mouse enteroids, resulting in cell death and expulsion. However, cells in human enteroids were not able to assemble inflammasomes due to a lack of sensor expression. This implies there may be some differences that exist between the inflammatory response between the mouse and human enteric system, or that some caution and further investigation is required for *in vitro* analyses with human intestinal enteroids.

In response to the emerging coronavirus pandemic, we used our expertise in nanobodies to contribute to the efforts against the disease with new nanobody based research tools and potential therapeutics. We generated nanobodies against the SARS-CoV-2 spike protein and selected four potently neutralizing nanobodies. Combination of two or three nanobodies into multimeric fusions enhanced their activity. I developed a cell fusion assay, where I discovered that some nanobodies neutralize the virus via a novel mechanism, as they prematurely activate the spike protein and convert it to its inactive post-fusion conformation.

In summary, I have developed and applied novel research tools to investigate: i) the induction of the inflammasome response in different cellular systems upon different stimuli, and ii) the mechanism of action of SARS-CoV-2 specific neutralizing nanobodies.

Declaration

(i) This thesis comprises only my original work towards the Doctor of Philosophy except where indicated in the preface;

(ii) due acknowledgement has been made in the text to all other material used; and

(iii) this thesis is fewer than the maximum word limit of 100,000 words in length, exclusive of tables, figures, maps, references, and appendices.

Florian Gohr

Preface

(I) Contribution of others:

Florian Schmidt and Jason Mackenzie acted as primary supervisors, and Sarah Londrigan acted as a secondary supervisor throughout this PhD.

i) Cell line generation

T55, T60 T72, T74, HFT61, and HFT63 were generated by Florian Schmidt.
T693, T684, and HFT18 were generated by Sabine Normann.
T590, T591, T592, T635, and HFT87 were generated by Monika Endl.
H92 was generated by Lisa Schiffelers.
iMAC1 was generated by Yonas Tesfamariam.
T76S was generated by Maria Christensen.
H8, HFT85, and K14 were generated by Karl-Elmar Lange.
Lab internal nomenclature for cell lines was used. Refer to Table A.1 (appendix).

ii) Experimental contributions:

Chapter 3
Experiments for Figure 3.2A-C were carried out by Maria Christensen.
Experiments for Figure 3.2D-E were carried out by Lea Jenster.
Experiments for Figure 3.2F were carried out by Yonas Tesfamariam.
Experiments for two replicates of Figure 3.4A-D were carried out by Dorothee Lapp; experimental design and data analysis were performed by me.
Experiments for Figure 3.4H was carried out by Florian Schmidt.
Experiments for Figure 3.6B were carried out by Florian Schmidt; data analysis was performed by me.

In the experiments for Figure 3.6C-E, the cell culture was carried out by Florian Schmidt, and the cells were recorded by Yonas Tesfamariam under my instruction; data analysis was performed by me.

Experiments for two replicates of Figure 3.6F-G were carried out by Dorothee Lapp; experimental design and data analysis were performed by me.

In the experiments for Figure 3.6A-B, E-F, cells were seeded by Monika Endl, stimulated by Yonas Tesfamariam, and recorded by me; the experiments were coordinated and the analysis was performed by me.

Experiments for Figure 3.7C-D were carried out by Yonas Tesfamariam.

Chapter 4

Human intestinal tissue samples for enteroid generation were obtained in collaboration with Sven Wehner and Alexandra Seinsche.

Experiments for Figure 4.3C-D were carried out together with the student Hanna Torianyk who I supervised during her rotation.

Laboratory space for experiments for Figure 4.4 and 4.9A was provided by Zeinab Abdullah.

Experiments for Figure 4.8 were carried in collaboration with Susanne Schmidt and her team; RNA samples were prepared by me, and RNA sequencing was performed and the count matrix was provided by Susanne Schmidt and her team; further data analysis was performed by me.

SARS-CoV-2 infections were performed in collaboration with Beate Kümmerer (data not shown).

Chapter 5

Visualisations and normalizations for Figure 5.1, 5.3, and 5.5 were performed by Paul-Albert König; all experiments and all other data analyses were performed by me.

(II) The thesis was proof-read for grammar and typos by Belinda Adem and Gabriel Gohr; both are not knowledgeable in the academic discipline of the thesis.

(III) Publication status:
All results presented in chapter 5 are published in Science (2021), volume 371, issue 6530, eabe6230.
All other data presented in this thesis is unpublished and not yet submitted for publication.

(IV) Acknowledgement of funding sources
The project has been funded by the German DAAD through the Bonn-Melbourne Research Training Group IRTG2168.
In addition, the project was partly supported by the Emmy Noether Programme 322568668 and the Klaus Tschira Boost fund (KT07).

Acknowledgements

The PhD journey is largely about personal development, learning how to be a scientist, and contributing to the research. The aim of this thesis is to present the work that I have conducted towards these goals during my own endeavour. However, a large part of such a journey is about the environment and the people in it. I consider myself extremely lucky to have worked in a collaborative and stimulating environment with people who supported me on a professional and personal level. While this was most true for my closest colleagues, it also extended beyond the institute, making it impossible to acknowledge everyone, who helped me along the way.

I am grateful to Florian for giving me the opportunity to do my PhD in the Schmidt lab. Thank you for your guidance throughout this journey and for always providing me with the supervision I needed at any specific time. While you motivated and inspired me with all your ideas, you also encouraged me to find my own way and grow as a scientist. I particularly enjoyed when our meetings went beyond discussing experiments and towards speculating about ideas and concepts. I also want to thank you for your generosity during all the lab trips and celebrations and for fostering a friendly and fun environment.

Next, I want to thank Jason for supervising me from across the globe. Your insights were always much appreciated and I always knew that I could count on your support whenever I needed it. I am especially grateful for the opportunity to spend time in your lab and for all the scientific discussions we had. Your ideas and suggestions were always highly valued. I also thank you for our time in the bouldering gym. The community tournament we went to was a highlight for me; I should have participated as you said.

I would like to thank Sarah for co-supervising me and for providing me with insights, cell lines, and viruses. Many thanks to Thomas for being my advisory committee chair and for supporting me throughout my PhD, especially with

administrative issues. Finally, I thank Seth for supplementing my advisory committee and for giving valuable comments and feedback.

My friends from the office ‘007’ and fellow PhD students Lea*, Lisa*, and Yonas* were an integral part of my PhD journey. Thank you all for contributing to a fantastic work environment, for the mutual support, and for all the fun we had outside the lab. I appreciate that you joined me for a somewhat crazy hike; we should repeat that. Thank you, Lea, for all your help, from teaching me flow cytometry to your invaluable support during the writing of this thesis. Thank you also for all the discussions and laughs about science (a shame that our theory about “krasse specks” didn’t hold up) as well as off-topics. To Lisa, I am glad we could start this journey together and help each other out in the beginning. Hartelijk bedankt for driving me to and from my parents countless times and for introducing me into your orchestras. Our concerts and the mountain bike weekend were personal highlights for me. Yonas, I thank you for all the discussions we had about science, politics, and bicycles. I also thank you for encouraging me to do more sports and for going cycling and running with me.

*These co-workers contributed equally.

I would like to thank Jen for always providing expertise on interferons and viruses. Thank you also for all our lengthy conversations and for supporting me whenever I was frustrated by my project. I further thank the new generation of PhD students Doro, Stefan, and José. The monthly dinners and regular coffee times contribute a lot to the lab environment. I thank Sabine, Jan, Steffen, and Moni for their support in the lab and for keeping the lab running.

I am grateful for the opportunity to work with Lisa, Gonzalo, Hanna, Leonie, and Katia as lab rotation students. Supervising you was one of my favourite things about my work.

To my lab mates in Melbourne, Alice, Carol, Julio, Katelyn, and Milou, thank you for welcoming me into your lab and making my time in Australia unforgettable. Thank you for all the fun and laughs and for joining me for bouldering. I am very fond of the memories from our trip after the virology conference; and I am sorry for bringing all the leeches into the car. I am very glad went camping on my last weekend; sugarloaf peak was one my my all-time favourite hikes. Also, thank you for ‘Our Adventure Book’. I will always keep it safe.

I thank all members of the IRTG2168 for all the support and the fun times during meetings and retreats. It was great to know someone from almost every immunology lab in Bonn. I would like to especially thank Andrea for organising the shipment to Australia and Rebecca, Leonie, and Manja for our hiking adventures in Australia.

List of publications

Jenster LM, Lange KE, Normann S, vom Hemdt A, Wuerth JD, Schiffelers LDJ, Tesfamariam YM, **Gohr FN**, Klein L, Kaltheuner IH, Ebner S, Lapp DJ, Mayer J, Moecking J, Ploegh HL, Latz E, Meissner F, Geyer M, Kümmerer BM, Schmidt FI. *P38 kinases mediate NLRP1 inflammasome activation after ribotoxic stress response and virus infection*. Journal of Experimental Medicine 220(1). 2023

Steiner A, Reygaerts T, Pontillo A, Ceccherini I, Moecking J, Moghaddas F, Davidson S, Caroli F, Grossi A, Morato Castro FF, Kalil J, **Gohr FN**, Schmidt FI, Bartok E, Zillinger T, Hartmann G, Geyer M, Gattorno M, Oliveira Mendonça L, Masters SL. *Recessive NLRC4-Autoinflammatory Disease Reveals an Ulcerative Colitis Locus.* Journal of Clinical Immunology 42(10). 2022

Koenig PA, Das H, Liu H, Kümmerer BM, **Gohr FN**, Jenster L, Schiffelers LDJ, Tesfamariam YM, Uchima M, Wuerth JD, Gatterdam K, Ruetalo N, H Christensen MH, Fandrey CI, Normann S, Tödtmann JMP, Pritzl S, Hanke L, Boos J, Yuan M, Zhu X, Schmid-Burgk JL, Kato H, Schindler M, Wilson IA, Geyer M, Ludwig KU, Hällberg BM, Wu NC, Schmidt FI. *Structure-guided multivalent nanobodies block SARS-CoV-2 infection and suppress mutational escape.* Science 371(6530):eabe6230. 2021

Ma JK, **Gohr FN**, Teh AY, Dessain S, Szeto TH and Sack M. *Plant production of monoclonal antibodies for rabies*. In Rupprecht CE, Fooks AR, Abela-Ridder B (Ed.): Laboratory techniques in rabies (Fifth edition. Volume 2), p. 160-178, WHO. 2019

Hanke R, Bailly N, Demling P, **Gohr FN**, Opdensteinen P, Osthege MJ, Joppich M, Sudarsan S, Schwaneberg U, Wiechert W and Blank LM. *Development of a Modular Biosensor System for Rapid Pathogen Detection.* In Rinken T (Ed.): A Prospective Way for Rapid Analysis, p. 89-110, IntechOpen. 2017

Chapter 1: Introduction

1.1 The innate immune system

While the adaptive immune response can fight pathogens with high specificity and effectiveness, it is slow to develop. The innate immune system, on the other hand, can detect pathogens rapidly to mount an early response and activate the adaptive immune system. Pattern recognition receptors (PRRs) are employed to detect pathogen-associated molecular patterns (PAMPS) or damage-associated molecular patterns (DAMPS). PRRs are divided into five families based on their domain architecture, namely Toll-like receptors (TLRs), C-type lectin receptors (CLRs), retinoic acid-inducible gene (RIG)-I-like receptors (RLRs), nucleotide-binding domain (NBD) and leucine-rich repeat (LRR) containing receptors (NLRs), and absent in melanoma 2 (AIM2)-like receptors (ALRs). TLRs are transmembrane receptors that survey the cell surface and endosomal compartments for various components of common pathogens. TLR signalling can lead to a wide range of different outcomes, depending on the type of the TLR and the cell. These outcomes include the expression of cytokines via nuclear factor (NF)-κB signalling or the induction of interferons (IFNs). CLRs exist as either membrane-bound or soluble proteins, whereby the former function as PRRs that bind carbohydrates on various microbes. CLR signalling can either promote the expression of pro-inflammatory cytokines or modulate TLR signalling. RLRs are cytosolic sensors for RNA and thus play a crucial role in the detection of viruses. Upon activation, RLRs signal via the adaptor protein mitochondrial antiviral signalling protein (MAVS), leading to the NF-κB-mediated induction of pro-inflammatory cytokines or IFN induction (Takeuchi and Akira, 2010; Brubaker *et al.*, 2015; Faenza and Blalock, 2022). NLRs and ALRs are also cytosolic sensors and will be discussed in greater detail in the next section (1.1.1).

An important aspect of innate immunity is the induction of inflammation, which is characterised by redness, swelling, pain, and increased temperature in the affected tissue, as defined by the Roman scholar Celsus. These hallmarks are a result of cytokine-induced dilation and increased leakage of local blood vessels.

This mediates the migration of immune cells into the tissue and the influx of other molecules from the blood. The main cell population that is present during early inflammation are tissue-resident macrophages. Neutrophil granulocytes are rapidly recruited in large numbers together with monocytes, which differentiate into inflammatory macrophages (Murphy, Kenneth and Weaver, Casey, 2017). While inflammation is a prerequisite for a successful immune response, it can lead to pathogenesis if not regulated appropriately. Chronic inflammation presents in a range of diseases, including degenerative, metabolic, and autoimmune diseases as well as cancer (Furman *et al.*, 2019).

IFNs are important in antiviral immunity. They are typically induced by phosphorylation of the transcription factors interferon regulatory factor (IRF) 3 or 7, which then translocate into the nucleus to induce the expression of type I IFNs. The production and secretion of type I IFN then results in subsequent signalling via binding to cognate interferon receptors, which recruits and promotes the association of IRF9 with signal transducer and activator of transcription (STAT) 1 and 2, resulting in a complex called IFN-stimulated gene factor (ISGF) 3. ISGF3 serves as a transcription factor and induces the expression of various IFN-stimulated genes (ISGs), which facilitate antiviral defence in multiple ways (Stanifer *et al.*, 2019; Dalskov *et al.*, 2023).

1.1.1 Inflammasomes

Inflammasomes are multimeric complexes representing a central signalling hub of innate immunity. They integrate cytosolic information on cell damage or infection, coordinate immune responses through the secretion of pro-inflammatory cytokines, and initiate death of infected cells by pyroptosis.

Inflammasomes are initiated by two families of PRRs, namely by NLRs and ALRs (Meunier and Broz, 2017). NLRs typically contain an N-terminal effector domain, a central conserved NACHT domain, and an LRR domain. NACHT is an NTPase domain and its name represents some NACHT-containing proteins: **NA**IP, **C**IITA, **H**ET-E, and **T**EP-1. Inflammasome sensors feature either a pyrin domain (PYD) or a caspase recruitment and activation domain (CARD) as their N-terminal effector domain (Figure 1.1A). Both are part of the death-fold domain (DFD) superfamily and mediate homotypic domain interactions between proteins. Once activated, these receptors assemble large pro-inflammatory multi-protein complexes called inflammasomes (Martinon *et al.*, 2002; Broz and Dixit, 2016; Hayward *et al.*, 2018). The canonical inflammasome pathway commences with the oligomerization of the receptor into a wheel-like structure, which enables the N-terminal effector domains to recruit apoptosis-associated speck-like protein containing a CARD (ASC). ASC monomers polymerize into filamentous structures that cluster into one single microscopic complex per cell, which is termed an ASC speck. The ASC complex then recruits caspase-1 with its respective CARDs and thereby mediates self-cleavage and activation of caspase-1. Finally, caspase-1 processes the pro-inflammatory cytokines interleukin (IL)-1β or IL-18 and promotes a highly pro-inflammatory type of programmed cell death termed pyroptosis by cleaving the pore-forming protein gasdermin D (GSDMD). Next to the death of infected cells, this leads to the

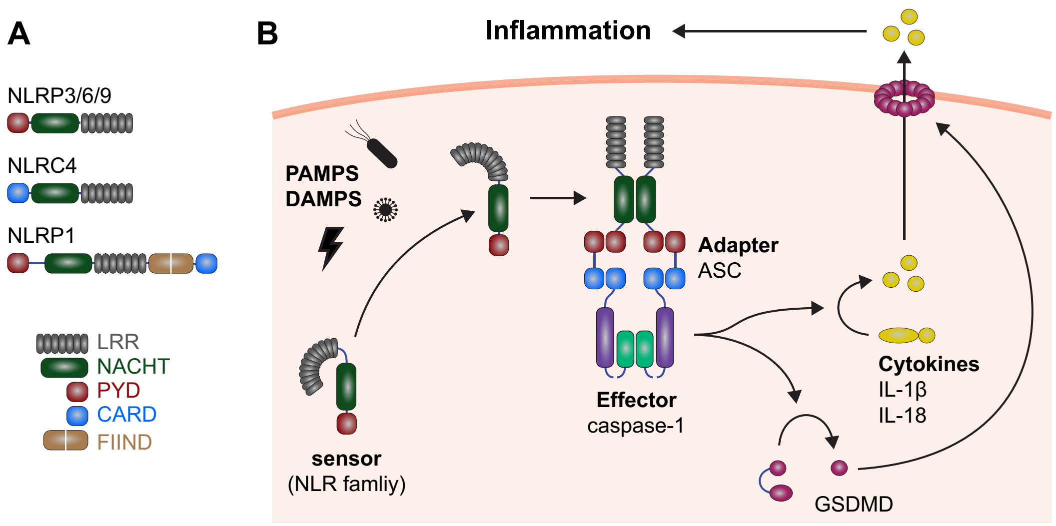

Figure 1.1: Inflammasome signalling. (**A**) Domain architecture of representative human NLRs. (**B**) Inflammasome sensors get activated by PAMPS or DAMPs and recruits the effector protein caspase-1 via the adaptor molecule ASC. Caspase-1 cleaves the cytokines IL-1β or IL-18 and GSDMD, which forms pores in the plasma membrane and causes pyroptosis. Cytokines are released through GSDMD pores or cell rupture and induce inflammation.

activation of further immune responses and the establishment of inflammation through cytokines and DAMPs (Figure 1.1B).

In general, inflammasomes describe macromolecular protein complexes that recruit and activate pro-inflammatory caspases. ASC-containing inflammasomes form spherical macroscopic structures. When stained, they appear as prominent specks. The observation of such specks therefore serves as a direct readout for inflammasome formation (Stutz *et al.*, 2013).

NLR family PYD containing 3 (NLRP3) is the most intensely investigated inflammasome. For activation, it typically requires two steps. The first step is called priming and induces the expression of NLRP3. This can be achieved by TLR4 stimulation with lipopolysaccharide (LPS), which leads to subsequent NF-κB signalling and transcription of NLRP3 and pro-IL-1β. The second step is the activation of NLRP3, which can be triggered by diverse cellular events such as ionic flux or the production of reactive oxygen species among others (Bauernfeind *et al.*, 2009; Muñoz-Planillo *et al.*, 2013; Kelley *et al.*, 2019). For example, NLRP3 can be activated by nigericin, which acts as a ionophore and mediates K^+ efflux (Perregaux and Gabel, 1994; Mariathasan *et al.*, 2006).

AIM2 is an inflammasome sensor from the ALR family. It senses cytosolic double-stranded DNA (dsDNA), which can be a sign for infection or mitochondrial damage. When bound to DNA, AIM2 oligomerizes and recruits ASC through homotypic PYD interaction, leading to inflammasome signalling (Hornung *et al.*, 2009)

1.1.2 Structural aspects of inflammasome assembly

In resting cells, inflammasome sensors exist in an autoinhibited state in which the PYD or CARD is prevented from recruiting ASC. For instance, NLRC4 (technically an adapter) is kept in a monomeric state (Hu *et al.*, 2013), whereas inactive NLRP3 was described to form cage-like decamers (Hochheiser, Pilsl, *et al.*, 2022). Upon activation, the inflammasome sensors change their conformation and oligomerize into assemblies, which are described as ‘disc-like‘ in those cases where structural information is available. The main function of this assembly is to bring the individual PYDs or CARDs into close enough proximity to serve as a seed for the nucleation of ASC filaments, which display a three-start helical symmetry with right-handed rotation (Lu *et al.*, 2015). Three-start helical symmetry means that the filament consists of three helical strands that are arranged in a three-fold rotational symmetry around the axis. The PYDs of AIM2, NLRP3, and NLRP6 can also form filaments on their own, and their structures have been solved (Lu *et al.*, 2014; Shen *et al.*, 2019; Hochheiser, Behrmann, *et al.*, 2022). For NLRP3^{PYD} filaments, the transition into ASC^{PYD} filaments has recently been investigated in further detail by Hochheiser *et al.* (2022), who describe a possible nucleation mechanism: sensor oligomerization causes locally high PYD concentrations that lead to the formation of short filaments, which are then extended by ASC^{PYD}. Some NLRs, for instance NLR family CARD containing 4 (NLRC4), recruit ASC via homotypic CARD interactions. In that case, it is assumed that one layer of ASC is recruited via CARD:CARD interaction, which then forms a PYD nucleus for the formation of ASC^{PYD} filaments. Multiple ASC filaments within a cell are further cross-linked through ASC^{CARD}:ASC^{CARD} interaction, leading to the macromolecular complex that is observed as a speck (Figure 1.2). This CARD:CARD interaction can be blocked by nanobodies against ASC^{CARD}, leading to the stabilisation of visible ASC filaments in living cells (Schmidt *et al.*, 2016; Dick *et al.*, 2016).

Ultimately, the polymerized ASC serves as a recruiting platform for the inflammasome effector molecule caspase-1. Caspase-1 belongs to the family of cysteine-aspartate proteases and consists of an N-terminal CARD, a large and a small catalytic domain (Van Opdenbosch and Lamkanfi, 2019). The CARD and the large catalytic domain are connected by the CARD domain linker (CDL) and the catalytic domains are joined by the interdomain linker (IDL) (Schmidt, 2023). Two caspase-1 monomers (p46) can form a dimer ($(p46)_2$), which exerts basal enzymatic activity, leading to self-cleavage within the IDL (Elliott *et al.*, 2009; Boucher *et al.*, 2018). This cleaved dimer ($(p33/p10)_2$) is the mature form of

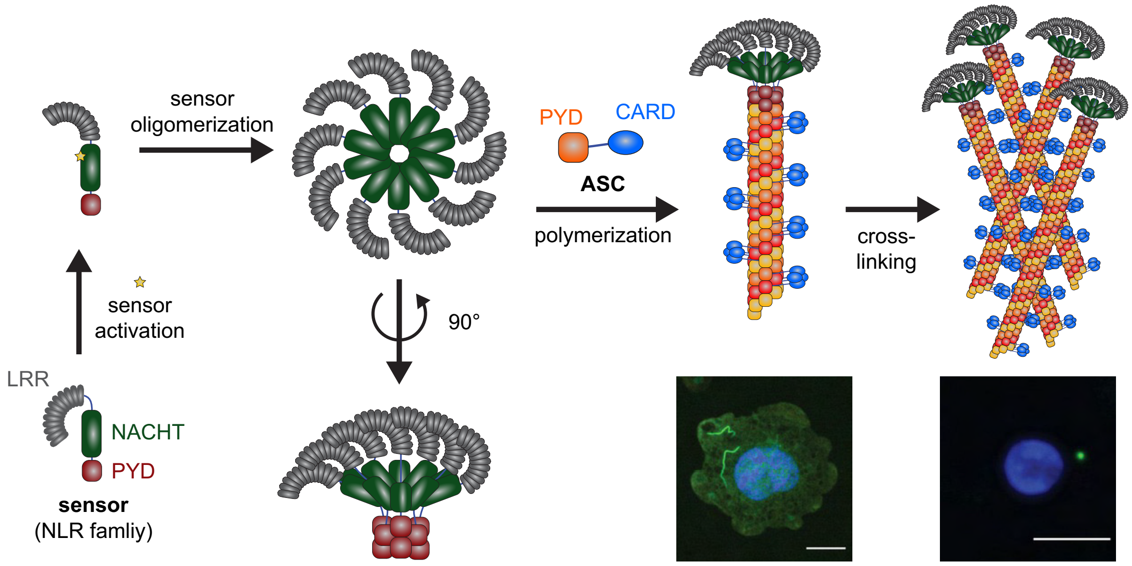

Figure 1.2: Inflammasome assembly. Upon activation, inflammasome sensors form a complex, in which their PYDs cluster together. This nucleates the polymerization of ASC into filaments. Multiple filaments generate a macromolecular complex by cross-linking via homotypic CARD interaction. ASC filaments can be stabilised using nanobodies against ASC^{CARD} (left microscopy image). Otherwise, the inflammasome is visible as speck (right microscopy image). Microscopy images are taken from Schmidt *et al*. (2016). Scale bars: 10 µm.

caspase-1 and has maximal activity. During further processing, the CDL is cleaved resulting in the $(p20/p10)_2$ form that lacks the CARD and is thus released from the inflammasome. This free tetrameric complex rapidly loses its activity (Boucher *et al.*, 2018; Ross *et al.*, 2022) (Figure 1.3A).

Taken together, dimerization is the minimal requirement for caspase-1 to be activated. While it is undisputed that this is achieved through CARD-mediated recruitment to the inflammasome, the exact mode of recruitment is less clear. The model of proximity-induced dimerization (Figure 1.3B, model A) postulates that caspase-1 clustering within the inflammasome leads to elevated local concentrations, dimerization, and self-processing (Ross *et al.*, 2022). Model B, on the other hand, proposes that caspase-1 is recruited to ASC by assembling filaments that are formed by its CARD. Caspase-1^{CARD} (C1C) forms filaments *in vitro*, which can be nucleated by ASC^{CARD} or CARD18 (Karasawa *et al.*, 2015; Lu *et al.*, 2016). It remains to be determined whether these C1C filaments also occur in inflammasomes in living cells. ASC^{CARD} would be brought into close proximity

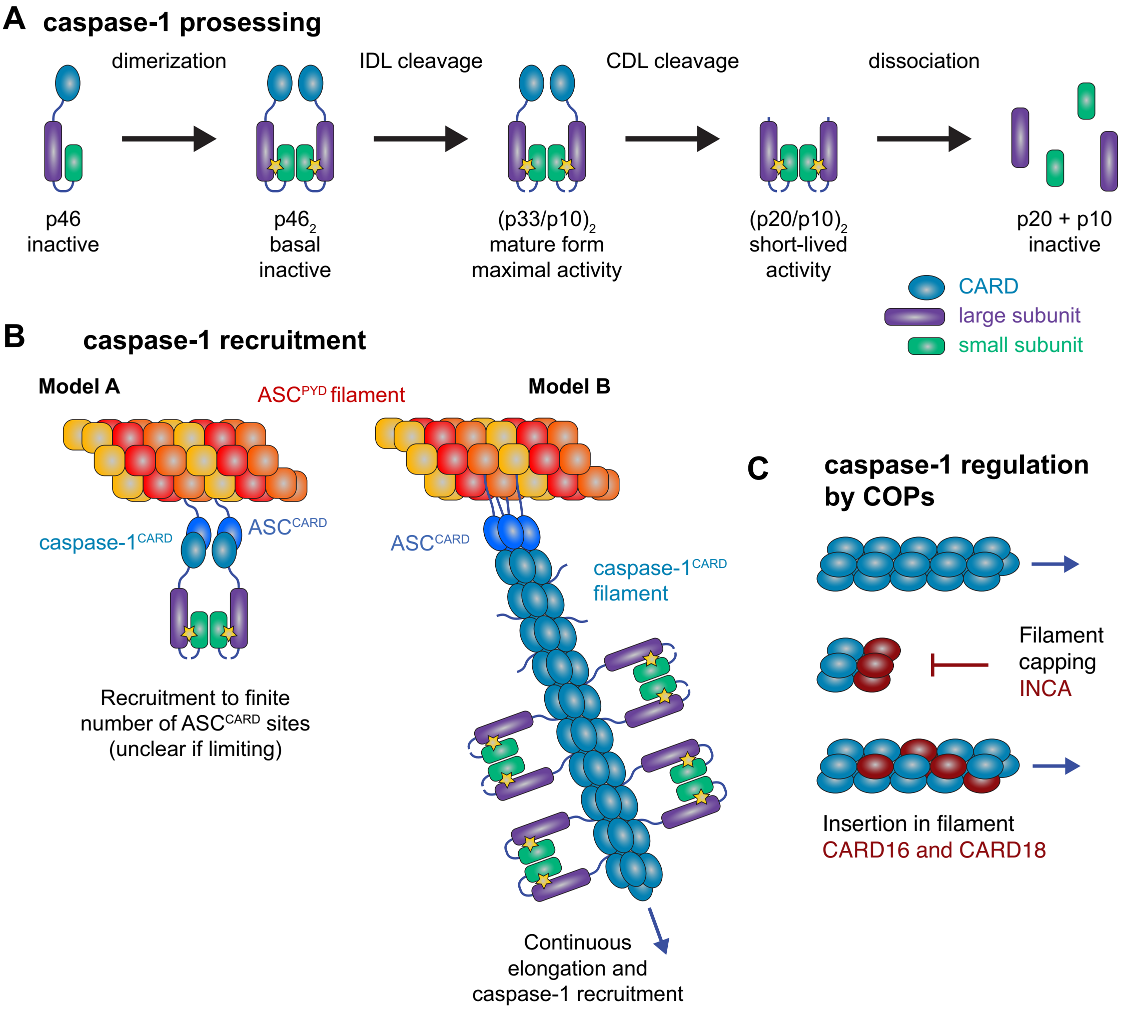

Figure 1.3: Regulation of caspase-1 activity. (**A**) Caspase-1 is activated and inactivated by step-wise processing. Dimerization leads to basal enzymatic activity, which allows cleavage of the IDL, resulting in the maximally active $(p33/p10)_2$ form. Subsequent CDL cleavage leads to release of the $(p33/p10)_2$ complex from the inflammasome. In this state, caspase-1 rapidly dissociates and loses its activity. (**B**) Caspase-1 is activated by oligomerizing on the inflammasome. For activation dimerization of the p46 form is required. This can be achieved in two ways. According to model A, caspase-1 dimerizes on existing ASC polymers via CARD interaction. Caspase-1 would thus be dependent on the availability of ASC^{CARD} sites. Model B predicts that ASC^{CARD} nucleates C1C filaments, thereby bringing many p46 subunits into close proximity for activation. In this mode, infinite recruitment is possible due to the growing filament. (**C**) C1C filaments can potentially be regulated by COPs. C1C filaments can be terminated by CARD17, because its interfaces are incompatible with filament formation. CARD16 and CARD18 can intercalate with C1C filaments, but do not terminate it. Based on Schmidt (2023).

on ASC filaments, enabling them to form a nucleus for the polymerization of C1C-filaments (Lu and Wu, 2015; Lu *et al.*, 2016; Broz and Dixit, 2016; Hochheiser, Behrmann, *et al.*, 2022). One difference is that in model A the recruitment sites for caspase-1 are finite, even though it is unclear whether they are limiting. Model B implies that growing filaments create infinite recruitment sites.

C1C filaments have been generated *in vitro* and a structure has been determined by cryo-electron microscopy. The filaments are characterised by a one-start helical symmetry with left-handed rotation. The end proximal to the filament nucleation is called a-end and the growing, distal end is termed b-end. One C1C monomer within the filament interacts with six adjacent monomers via three types of interaction interfaces (type I, II, III) (Lu *et al.*, 2016).

1.1.3 Regulation of caspase-1 assemblies by CARD-only proteins

CARD-mediated assemblies provide a target for potential disruption by additional factors. CARD-only proteins (COPs) CARD16 (also known as pseudo-ICE), CARD17 (also known as INCA), and CARD18 (also known as ICEBERG) are located in close proximity to the cluster of inflammatory caspases (caspase-1, 4, and 5) in the genome and they probably are a result of duplication events. They have a sequence homology with C1C of 92 %, 81 %, and 53 %, respectively (Stehlik and Dorfleutner, 2007; Devi *et al.*, 2020). All three COPs have been reported to interact with C1C and inhibit inflammation (Humke *et al.*, 2000; Druilhe *et al.*, 2001; Lee *et al.*, 2001; Lamkanfi *et al.*, 2004; Göblös *et al.*, 2016; Devi *et al.*, 2020; Devi *et al.*, 2023).

CARD17 cannot oligomerize, because the type I and II interfaces, which are needed for filament formation, are defective. Thus, CARD17 can disrupt C1C filaments by a capping mechanism (Lu *et al.*, 2016). If C1C filaments play a role in inflammasome signalling, which is so far speculative, this mechanism would explain the inhibitory action of CARD17. In this regard, the other COPs are somewhat more complicated. Even though there are multiple reports that describe CARD16 and CARD18 as negative regulators, both proteins can form filaments on their own and induce C1C polymerization resulting in filaments in which C1C is intercalated by CARD16 or CARD18. CARD16 has also been shown to augment IL-1β release (Karasawa *et al.*, 2015; Lu *et al.*, 2016).

1.1.4 CARD-containing inflammasome sensors

As mentioned earlier, some inflammasome sensors do not signal via a PYD, but instead via a CARD. This suggests the possibility to recruit caspase-1 directly via homotypic CARD interaction. NLRC4 has been shown to directly interact with and activate caspase-1 (Poyet *et al.*, 2001). However, ASC seems to be necessary for efficient IL-1β processing (Mariathasan *et al.*, 2004; Broz, Newton, *et al.*, 2010). In the absence of ASC, caspase-1 processing is impaired, stabilising the p46 form with basal activity. In this state, caspase-1 is able to initiate cell death by cleaving GSDMD, but cytokine processing is significantly impaired (Broz, von Moltke, *et al.*, 2010; He *et al.*, 2015; Boucher *et al.*, 2018).

NLRP1 is another inflammasome sensor that signals through its CARD. Human NLRP1 has a somewhat more complex architecture compared to other NLRPs: in addition to the PYD, NACHT, and LRR domain, it harbours a function-to-find domain (FIIND) and a CARD at its C-terminus (Figure 1.1A). The FIIND consists of a ZU5 (ZO1, UNC5) and a UPA (UNC5, PIDD, Ankyrin) subdomain and undergoes proteolytic cleavage between these subdomains (D'Osualdo *et al.*, 2011; Finger *et al.*, 2012; Bauernfried and Hornung, 2022). In contrast to other sensors, the N-terminal PYD is not involved in signalling. Instead, activation of NLRP1 involves the release of the C-terminal UPA-CARD fragment, which engages ASC for inflammasome assembly. In steady-state, the UPA-CARD fragment remains bound to the N-terminal part of NLRP1. Released UPA-CARD fragments are sequestered by the dipeptidylpeptidases DPP8 or DPP9. NLRP1 can be activated by inhibition of DPP8/9 using the small molecule talabostat (also known as Val-boro-Pro), which causes the dissociation of the NLRP1–DPP8/9 complex and thus the release of the active UPA-CARD fragment (Hollingsworth, Sharif, *et al.*, 2021; Huang *et al.*, 2021; Jenster, 2024). This is can also be achieved by proteasomal degradation of the NLRP1 N-terminus, which can be triggered by viral or microbial proteases as well as ribotoxic stress (Okondo *et al.*, 2018; Sandstrom *et al.*, 2019; Robinson *et al.*, 2020; Robinson *et al.*, 2022; Jenster *et al.*, 2023). A closely related protein is CARD8, which consists of a FIIND and a CARD, resembling the C-terminal portion of NLRP1. Like NLRP1, CARD8 can be activated by talabostat (Johnson *et al.*, 2018; Taabazuing *et al.*, 2020). Despite their similarities, NLRP1 and CARD8 have different ways of signalling: while NLRP1 exclusively recruits ASC but not caspase-1, CARD8 is unable to interact with ASC and instead can only directly recruit caspase-1. Interestingly, caspase-1 auto-processing was reported to be critical for CARD8-mediated pyroptosis (Ball *et al.*, 2020; Hollingsworth, Liron, *et al.*, 2021; Gong *et al.*, 2021).

Another form of ASC-independent inflammasome has been termed non-canonical inflammasome. The non-canonical inflammasome does not activate caspase-1, but instead employs alternative inflammatory caspases. In humans, these are caspase-4 and caspase-5, in mice caspase-11 (Shi *et al.*, 2014; Downs *et al.*, 2020; Dorfleutner and Stehlik, 2023). These caspases can directly bind intracellular LPS without the involvement of ASC or an upstream sensor (Kayagaki *et al.*, 2011; Casson *et al.*, 2015; Kayagaki *et al.*, 2015). Non-canonical inflammasomes can induce pores and pyroptosis by cleaving GSDMD, but require a secondary NLRP3 inflammasome in order to process IL-1β or IL-18 (Rühl and Broz, 2015; Schmid-Burgk *et al.*, 2015). For caspase-11, it has been shown that dimerization and IDL cleavage are necessary for its function (Ross *et al.*, 2018). More recently, it has been demonstrated that guanylate-binding protein (GBP) 1 can bind to LPS and, in concert with GBP2-4, serves as a recruitment and activation platform that exposes LPS to caspase-4 (Santos *et al.*, 2020; Wandel *et al.*, 2020).

The terminology of inflammasomes is not well defined. For this thesis, I will therefore use the following definitions: the term inflammasome describes any macromolecular protein complex that recruits and activates pro-inflammatory caspases. Canonical inflammasomes are recruitment platforms of higher order, *i.e.* multiple filaments assemble into a single structure. According to current knowledge, this can only be achieved via ASC assemblies. Canonical inflammasomes fully activate caspase-1, leading to pyroptosis and cytokine release. Non-canonical inflammasomes refer to less complex assemblies that activate pro-inflammatory caspases without employing ASC. Non-canonical inflammasomes are typically associated with caspase-4, -5, or -11, but I also consider ASC-independent inflammasomes that recruit caspase-1 as non-canonical inflammasomes. Non-canonical inflammasomes usually induce pyroptosis but not cytokine maturation.

1.1.5 Intestinal inflammasomes

In mice, intestinal inflammasomes are involved in the control of viral and bacterial pathogens, as well as homeostasis of the gut microbiome. As the intestinal inflammasome sensors are shared between mice and humans, this suggests that they are medically relevant in humans. Excessive activation of intestinal inflammasomes can lead to severe autoinflammatory diseases such as inflammatory bowel disease (Zmora *et al.*, 2017). The intestine contains a whole biotope of microorganisms. While the intestinal epithelium is important for taking up nutrients, it also serves as a crucial barrier for potential pathogens. The intestinal epithelial cells (IECs) are the first to contact invading pathogens and an appropriate response is paramount to restrict infection and stimulate other branches of the immune system. Mechanisms of action include increased expulsion of infected cells, release of pro-inflammatory cytokines (Sellin *et al.*, 2014; Rauch *et al.*, 2017), and increased mucus secretion (Wlodarska *et al.*, 2014). Inflammasomes and NLRs have been implicated in all of these effects, including NLRC4 as well as NLRP6 and NLRP9.

1.1.5.1 NLRC4

The NLRC4 inflammasome is the most studied intestinal inflammasome. NLRC4 does not function as a receptor itself but cooperates with receptors of the NLR family of apoptosis inhibitory proteins (NAIPs). While humans have only one *NAIP* gene, mice possess seven *Naip* genes. In C57BL/6 mice, which were used in the present study, only *Naip1*, *2*, *5*, *6* are functional. NAIPs can bind various bacterial ligands, such as flagellin and components of bacterial type III secretion systems (T3SS), and a single activated NAIP nucleates the oligomerization of NLRC4, which recruits ASC or caspase-1 for downstream inflammasome signalling (Vance, 2015).

Human NAIP and mouse NAIP1 can bind bacterial T3SS needle proteins (*e.g. Salmonella* PrgI or *Shigella* MxiH), whereas NAIP2 binds T3SS rod proteins (*e.g. Burkholderia* BsaK), and NAIP5/6 binds flagellin (Zhao *et al.*, 2011; Yang *et al.*, 2013; Rayamajhi, Zak, *et al.*, 2013; Rauch *et al.*, 2016). *Salmonella* has two pathogenicity islands (SPI), both of which harbour a T3SS. The SPI-1 T3SS is needed for invasion of IECs and the SPI-2 T3SS plays a role in the later stages of infection, including intracellular survival and replication (Bao *et al.*, 2020). Mouse macrophages were able to activate NLRC4 inflammasomes in response to the SPI-1 T3SS rod protein PrgJ, but not the SPI-2 T3SS rod protein SsaI (Miao *et al.*, 2010). In human macrophages, SPI-2 even subverts SPI-1-induced inflammasome responses (Bierschenk *et al.*, 2019). In contrast, a recent study found that the SP2 T3SS needle protein SsaG activates NAIP/NLRC4 in human macrophages (Naseer, Egan, *et al.*, 2022). While NLRC4 and NLRP3 play redundant roles in the defence against *Salmonella* in mouse myeloid cells, NLRC4 seems to have a more prominent role in IECs (Crowley *et al.*, 2016).

As described earlier, the canonical consequences of inflammasome activation are pyroptotic cell death and pro-inflammatory cytokine release. In the context of NAIP/NLRC4, further effects have been reported in mouse IECs. Inflammasome signalling in these cells leads to expulsion of infected cells and release of eicosanoids. Cell expulsion is coordinated in a cell autonomous manner and relies on myosin-dependent focal contractions. By this mechanism, NAIP/NLRC4 preserves epithelial integrity and protects mice from *Salmonella* infection (Sellin *et al.*, 2014; Rauch *et al.*, 2017; Hausmann *et al.*, 2020; Fattinger *et al.*, 2021; Samperio Ventayol *et al.*, 2021). The NAIP/NLRC4 response in humans remains less well investigated.

1.1.5.2 NLRP6

NLRP6 is predominantly expressed in the intestine and has been assigned a range of ligands and roles. (Ghimire *et al.*, 2020; Li *et al.*, 2022). Mouse NLRP6 has been found to confer susceptibility to bacterial infection by impeding NF-κB signalling and immune cell recruitment or by inflammasome-dependent IL-18 release. This effect was dependent on ASC and inflammatory caspases. Lipoteichoic acid (LTA) and LPS have been proposed as bacterial ligands for NLRP6 (Anand *et al.*, 2012; Ghimire *et al.*, 2018; Hara *et al.*, 2018; Leng *et al.*, 2020). In addition, the microbiota-associated metabolites taurine, histamine, and spermine have been reported to modulate the NLRP6 inflammasome (Levy *et al.*, 2015). In the context of viral infection, NLRP6 has been reported to play a protective role. One proposed mechanism is that NLRP6 cooperates with the RNA helicase DEAH-box helicase 15 (DHX15) to bind viral RNA. NLRP6 then engages MAVS to induce IFN signalling, thereby protecting mice against murine norovirus and encephalomyocarditis virus (EMCV) virus in an inflammasome-independent manner (Wang *et al.*, 2015). Even though NLRP6 has been implicated in viral infections, at the commencement of this study NLRP6 had not been shown to form ASC specks, and the involvement of NLRP6-mediated inflammasomes in viral infection remains to be confirmed. It is also unclear how NLRP6 can induce two potential signalling pathways, *i.e.* either the inflammasome or IFN axis, as insights were merely drawn from knockout animals and cytokine levels.

NLRP6 has also been associated with various human diseases. These include Hirschsprung’s disease, pulpitis and periodontitis, rheumatoid arthritis, and cancer (Lin and Luo, 2017; Wang *et al.*, 2018; Lu *et al.*, 2019; Tomuschat *et al.*, 2019; X. Wang *et al.*, 2020; Tian *et al.*, 2021; Yu *et al.*, 2021).

Another proposed function of NLRP6 is its role in colonic mucus secretion. Mucus is produced by specialised epithelial goblet cells and forms a protective barrier on the intestinal mucosa. It was reported that mucus secretion is controlled by NLRP6 in a subset of goblet cells termed sentinel goblet cells (Wlodarska *et al.*, 2014; Birchenough *et al.*, 2016). However, a later study found that baseline colonic mucus function is independent of NLRP6 (Volk *et al.*, 2019). It was also shown that ASC- and NLRP6-dependent IL-18 production changes the gut microbiota in mice through antimicrobial peptides. These findings have, however, been challenged (Elinav *et al.*, 2011; Levy *et al.*, 2015; Mamantopoulos *et al.*, 2017; Lemire *et al.*, 2017; Gálvez *et al.*, 2017; Elinav *et al.*, 2018; Mamantopoulos *et al.*, 2018).

1.1.5.3 NLRP9

NLRP9 is a poorly investigated member of the NLR family. While there is only a single human NLRP9, rodents express three isoforms termed NLRP9a, NLRP9b, and NLRP9c. NLRP9 has been proposed to have functions in embryonic development, mainly due to its expression in reproductive tissues (Mullins and Chen, 2021). Reproductive defects were only observed in mice that carry mutations in all three isoforms (Kanzaki *et al.*, 2020).

Only one study is published that examines the role of NLRP9 in immunity (Zhu *et al.*, 2017), where mouse NLRP9b was shown to restrict rotavirus infection *in vivo*. Zhu *et al.* proposed that short RNA species are detected via the RNA helicase DHX9, leading to inflammasome-dependent IL-18 and GSDMD maturation. While an interaction between RNA, DXH9 and NLRP9 has been shown in cell lysates, it is not clear whether this is the mode of action in the context of rotavirus infection, or whether RNA is sufficient to activate NLRP9. Assemblies of signalling platforms have not yet been described, and molecular reconstitution has not been achieved.

1.2 Viruses

1.2.1 Rotavirus

Rotavirus (RV) belongs the family of *Sedoreoviridae*. It has a double-stranded RNA (dsRNA) genome, which consists of 11 fragments. The virion is non-enveloped and has a diameter of ~80 nm. It has a triple capsid, which is composed of the viral proteins VP2 (inner capsid), VP6 (intermediate capsid), VP7, and VP4 (cleaved into VP5 and VP8) (outer capsid). Based on VP6, rotaviruses are divided into ten species (A-J), from which RV A is most relevant as a human pathogen (Crawford *et al.*, 2017).

RV infection leads to mild to severe diarrhea with vomiting and fever. It is a major cause of death in children under five years (Troeger *et al.*, 2018; Omatola and Olaniran, 2022). The burden for RV is especially high in developing countries (Tate *et al.*, 2016).

RV binds sialoglycans and histo-blood group antigens via VP8 in the outer capsid (Lopez and Arias, 2006). Infectivity is increased by tryptic cleavage of VP4 into VP5 and VP8 (Li *et al.*, 2017; Herrmann *et al.*, 2021). After attachment, different RV strains enter the cell by different endocytic mechanisms (Gutiérrez *et al.*, 2010). The low Ca^{2+} level in the endosome triggers the loss of the outer capsid and the release of the double-layered particle (DLP) into the cytosol (Papa *et al.*, 2021). The dsRNA segments are transcribed within the DLP and positive-stranded RNAs ((+)ssRNA) are released into the cytosol through channels within the capsid (Patton and Spencer, 2000). The (+)ssRNA is then translated and the viroplasm, a protein-RNA condensate that serves as a viral factory, is formed by liquid-liquid phase separation (LLPS), which is driven by the non-structural protein (NSP) 2 and NSP5 (Eichwald *et al.*, 2004; Geiger *et al.*, 2021). In addition, the viroplasm contains VP1, VP2, VP3, VP6, and (+)ssRNA of all genome segments (Cheung *et al.*, 2010). (+)ssRNA is encapsulated into subviral particles, which mediate dsRNA synthesis. Addition of VP6 finally yields new DLPs (Long and McDonald, 2017). It was previously thought that the outer capsid proteins VP4 and VP7 are acquired by budding of immature particles into the endoplasmic reticulum (ER), but this view has been challenged by a recent study that proposed a new model: NSP4 and the outer capsid proteins are initially associated with the ER, but are eventually released from the ER into cytoplasmic vesicles that further traffic to the viroplams. Immature particles then interact with NSP4 and bud through the associated membranes to acquire the outer membrane proteins, resulting in transiently enveloped particles (Crawford *et al.*, 2019). The envelope is finally lost via an unknown mechanism, and the outer capsid proteins are rearranged on the particle.

1.2.2 Encephalomyocarditis virus

The encephalomyocarditis virus (EMCV) is a cardiovirus and belongs to the family of *Picornaviridae*, which also includes poliovirus. It has a (+)ssRNA genome of ~7.8 kb. The virion is non-enveloped and has a diameter of 30 nm. The icosahedral capsid is composed of VP1-4 with VP4 located on the interior of the particle (Carocci and Bakkali-Kassimi, 2012).

EMCV is prevalent worldwide and infects a wide range of mammals, including primates (Helwig and Schmidt, 1945; Gainer, 1967; Dea *et al.*, 1991; Reddacliff *et al.*, 1997; Maurice *et al.*, 2005; Billinis, 2009; An *et al.*, 2009; Ge *et al.*, 2010; Canelli *et al.*, 2010; Czechowicz *et al.*, 2011). While the pathology varies between hosts and virus strains, EMCV induces a range of symptoms, including myocarditis, and can be fatal in pigs and non-human primates (Carocci and Bakkali-Kassimi, 2012). Even though the potential of EMCV as a zoonotic disease is not fully elucidated, human populations have been found to be seroprevalent and human cases of EMCV-induced illness have been described (Tesh, 1978; Juncker-Voss *et al.*, 2004; Oberste *et al.*, 2009; Czechowicz *et al.*, 2011). However, infection with EMCV seems to show low morbidity in humans.

Viral infection starts with attachment to the host cell. Host proteins described as attachment proteins are mouse vascular cell adhesion molecule 1 (VCAM-1) and sialylated glycophorin A (Burness and Pardoe, 1983; Huber, 1994; Jin *et al.*, 1994). A recent CRISPR-Cas9 screen has identified the cell surface protein ADAM9 as an additional crucial factor for EMCV infection (Bazzone *et al.*, 2019). The entry mechanism for EMCV is poorly understood. Acidification of intracellular compartments is not necessary (Madshus *et al.*, 1984). For poliovirus, a model has been proposed in which VP1 inserts into the membrane and forms a channel, which facilitates RNA release (Hogle, 2002). The genome is then translated into a polyprotein by host ribosomes from its internal ribosome entry site (IRES).

Processing of the polyprotein is mostly achieved by the viral 3C protease (Carocci and Bakkali-Kassimi, 2012). Picornavirus replication takes place at replication complexes that are made from rearranged ER and Golgi membranes (Schlegel *et al.*, 1996). A viral RNA-dependent RNA polymerase, in association with other viral proteins, synthesizes the negative-stranded RNA, resulting in the double-stranded replication form (Gamarnik and Andino, 1998). Positive single-stranded RNA genomes are finally encapsulated and new virions are released through cell lysis. EMCV rapidly lyses the host cell while inhibiting apoptosis (Romanova *et al.*, 2009; Carocci *et al.*, 2011).

1.2.3 SARS-CoV-2

At the end of the year 2019, a new coronavirus disease (COVID-19) emerged, which is caused by the severe acute respiratory syndrome coronavirus (SARS-CoV)-2. SARS-CoV-2 belongs to the family of *Coronaviridae* within to the order of *Nidovirales* and has a positive-stranded RNA genome. Viruses of this family are enveloped and spherical with a diameter of 120-160 nm. The particles present a prominent spike protein at their surface, which leads to an appearance reminiscent of the solar corona, hence the name. Coronaviruses possess the largest genome among all identified RNA viruses with 26.4-31.7 kb (ICTV, 2011).

Most coronaviruses cause only mild disease in humans. More recently however, highly pathogenic coronaviruses emerged, that can cause life-threatening respiratory disease: SARS-CoV-1, Middle East respiratory syndrome coronavirus (MERS-CoV), and SARS-CoV-2 (V'kovski *et al.*, 2021). While SARS-CoV-1 and MERS-CoV already caused public health emergencies, SARS-CoV-2 caused a pandemic of unprecedented proportions. In August 2023 over 750 million cases have been confirmed leading to almost 7 million deaths (WHO, 2023).

1.2.3.1 The spike protein

The spike protein (also called S protein) is presented as trimers on the surface of coronaviruses and is responsible for binding the SARS-CoV-2 cellular receptor angiotensin converting enzyme 2 (ACE2). As a class I viral fusion protein, it also mediates membrane fusion and thus cell entry. Spike is the target for most neutralizing antibodies. The structure of spike in different conformations has been solved by many groups (Wrapp, Wang, *et al.*, 2020; Yan *et al.*, 2020; Xia *et al.*, 2020; Walls *et al.*, 2020; Shang, Ye, *et al.*, 2020; Lan *et al.*, 2020; Q. Wang *et al.*, 2020; Cai *et al.*, 2020; Turoňová *et al.*, 2020; Yao *et al.*, 2020; C. Liu *et al.*, 2020; Bangaru *et al.*, 2020; Ke *et al.*, 2020; Gobeil *et al.*, 2021; Zhang *et al.*, 2021). The spike protein is proteolytically cleaved into two subunits, that are denoted S1 and S2. S1 constitutes the outer part of the trimeric spike and consists of four domains: the N-terminal domain, the receptor binding domain (RBD), and two C-terminal domains. The central S2 subunit contains the fusion peptide, two heptad repeats, the transmembrane domain, and the cytoplasmic tail (Figure 1.4A). Importantly, the RBD, which is located at the top of the spike trimer, can exist in two states: the up-configuration, which is accessible for ACE2 binding, and the down-configuration, which is inaccessible (Jackson *et al.*, 2022).

1.2.3.2 Cell entry

The obligate receptor for SARS-CoV-2 is ACE2, which binds the spike RBD in its up state (Zhou *et al.*, 2020; Xiao *et al.*, 2021). For membrane fusion, two cleavage events are necessary in the spike protein. The S1 and S2 subunits are separated by a multibasic furin cleavage site. Uniquely for SARS-CoV-2, this site is already processed during virus maturation in the virus producing cell, but the two subunits stay associated (Hoffmann, Kleine-Weber and Pöhlmann, 2020). The second site, S2’, is located within the S2 subunit and is cleaved by proteases of the target cell. This happens either at the cell surface by transmembrane serine protease 2 (TMPRSS2) or in endolysosomes by cathepsin L (Hoffmann, Kleine-Weber, Schroeder, *et al.*, 2020; Blaess *et al.*, 2020). If TMPRSS2 is present, SARS-CoV-2 enters the cell directly via fusion at the cell surface. Otherwise, it can also be endocytosed to be processed by cathepsins (Bayati *et al.*, 2021). Binding to ACE2 locks the spike protein in a state in which all RBDs are in the up conformation. This is assumed to cause conformational changes that expose the S2’ site for proteolytic processing, which likely leads to destabilisation of S1. Because the peptide bond between S1 and S2 is already hydrolysed, this induces

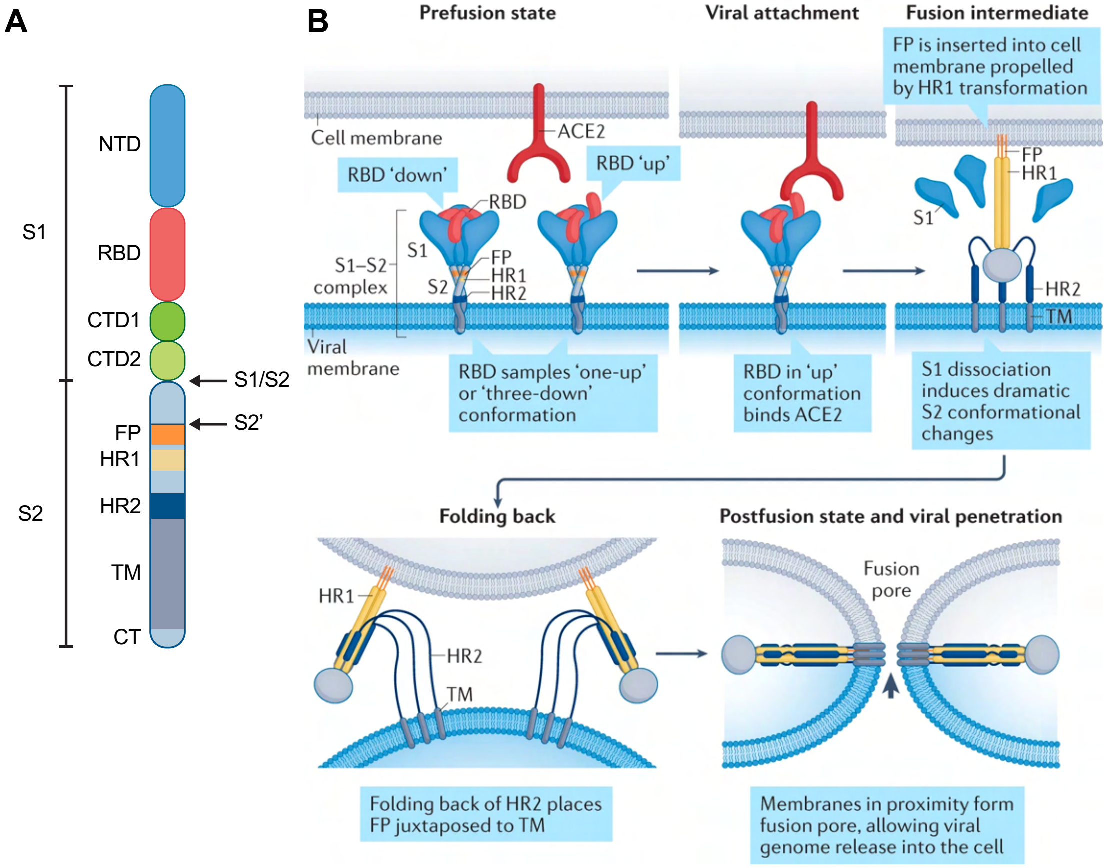

Figure 1.4: Spike structure and membrane fusion. (**A**) Domain architecture of the SARS-CoV 2 spike protein. Cleavage sites are marked by arrows. NTD: N-terminal domain, RBD: receptor binding domain, CTD: C-terminal domain, FP: fusion peptide, HR: heptad repeat, TM: transmembrane domain, CT: cytoplasmic tail. (**B**) Model for spike induced membrane fusion. ACE2 binding to the RBD in the 'up' conformation enables the cleavage of the S2' site. This leads to the dissociation of S1 and the refolding events that propel the FP towards the target membrane. The HRs then fold back into the postfusion conformation that brings the two membranes into close proximity, facilitating the formation of the fusion pore. Taken from Jackson *et al.*, 2022.

the complete dissociation of S1. This leaves S2 in an energetically unfavourable metastable conformation. The ensuing membrane fusion is then coupled to the irreversible transition into the post-fusion conformation. Conformational changes during this transition propel the fusion peptide towards the target membrane where it inserts. Formation of the energetically favourable 6-helix bundle by heptad repeat 1 (HR1) and HR2 then drives large conformational rearrangements that force the viral and the cellular membranes into close proximity, facilitating fusion (Walls *et al.*, 2017; Fan *et al.*, 2020; Jackson *et al.*, 2022) (Figure 1.4B).

1.2.3.3 Coronavirus replication

Once the viral genome reaches the cytosol, two polypeptides are translated and then proteolytically cleaved into 16 NSPs. Most of these proteins are involved in the formation of the viral replication and transcription complex as well as in RNA synthesis. Coronaviruses possess a unique RNA proofreading capacity with a 3’-5’ exonuclease activity. Negative-sense genome copies are then generated, from which new positive-sense genomes are synthesized. Those are either used for further translation or packaged into virions. A unique discontinuous transcription process is employed to generate subgenomic RNAs, from which the accessory and structural proteins, including spike, are translated. While most coronaviruses bud at the ER and Golgi compartments, it is believed that betacoronaviruses such as SARS-CoV-2 egress via lysosomal trafficking (V’kovski *et al.*, 2021).

1.3 Nanobodies

Antibodies are an integral part of our adaptive immune system. They harbour two variable binding sites, that can bind to antigens presented on pathogens, infected cells, or toxins. While binding alone can neutralize many pathogens, antibodies also possess a constant fragment (Fc), which recruits further capacities of the immune system. Antibodies consist of two heavy chains and two light chains, that are connected by disulfide bridges. Each antibody binding site is made up from one variable domain of the heavy chain (V_H) and one variable domain of the light chain (V_L). Camelids have evolved antibodies that consist of only two heavy chains and are thus termed heavy chain-only antibodies. Their antigen binding sites consist of single V_H domains (Muyldermans, 2013). The V_H of a heavy chain only antibody (VHH) can bind antigens autonomously and is termed nanobody when expressed as a soluble protein. Heavy chain-only antibodies have first been found in dromedaries (*Camelus dromedarius*) (Hamers-Casterman *et al.*, 1993). Nanobodies can be generated by immunising dromedaries, cloning their antibody repertoire, and identifying binders by phage display (Arbabi Ghahroudi *et al.*, 1997). Later llamas (*Lama glama*) and alpacas (*Vicugna pacos*) were identified as more convenient sources for VHHs (van der Linden *et al.*, 2000; Harmsen *et al.*, 2000; Rothbauer *et al.*, 2006; Maass *et al.*, 2007). Antibodies that lack light chains are also found in cartilaginous fishes, including sharks, but are the result of convergent evolution (Greenberg *et al.*, 1995; Zielonka *et al.*, 2015).

Nanobodies possess multiple traits that make them an attractive alternative for conventional antibodies. Being only approximately 15 kDa they are only one tenth of the size of conventional antibodies and half the size of scFvs (single-chain variable fragment), the smallest possible derivatives of conventional antibodies. Nanobodies also show desirable physical properties, as they are highly soluble and thermostable (Anderson *et al.*, 2008). Nanobodies do not rely on chain pairing or disulfide bonds and can be expressed to high levels in microorganisms and mammalian cells (Frenken *et al.*, 1998; Frenken *et al.*, 2000; Arbabi-Ghahroudi *et al.*, 2005; Ismaili *et al.*, 2007). Because of their properties, many of them can be properly folded and retain their antigen-binding capacity when expressed in the reducing environment of the cytosol (Ingram *et al.*, 2018). This makes them useful research tools, as they can perturb interactions between endogenous proteins. Because nanobodies are easily fused to other proteins, they can be equipped with various functions. Prominent examples are fluorescent fusions to monitor protein localization or E3 ubiquitin ligase adapters to target proteins for degradation (Caussinus *et al.*, 2011).

1.4 Aims and structure of the thesis

Inflammasomes are characterised by large protein assemblies that mediate cell death and inflammation. Yet, they are often studied by examining the downstream effects without scrutinising the signalling platform itself. Accordingly, we lack detailed information of caspase-1 recruitment and its effect on caspase activation. Information on single cell level is also often lost. The aim of chapter 3 was to evaluate a novel reporter for inflammasome assembly and caspase-1 recruitment. After verifying the functionality of the reporter, it was used to investigate whether caspase-1 forms filaments on inflammasomes and how this can be exploited by COPs to regulate inflammasome signalling (Figure 1.3).

Another area in inflammasome biology is its role in functional tissues. Different functions of tissue-specific inflammasomes have been described, which accommodate for pyroptosis or confer protection or vulnerability against invading pathogens. These effects, however, are difficult to investigate, because tissue cannot be kept alive *in vitro* for extended experiments. Most insights in tissue-specific inflammasomes thus stem from knockout studies in mice, while the knowledge of human biology is even more scarce. The advent of organoid cultures vastly increased the range of techniques that can be performed with tissue models, including genetic manipulation and infection. Research with mouse intestinal enteroids already yielded significant mechanistic insights into inflammasome-mediated responses to enteric bacteria. Therefore, the aim of chapter 4 was to generate mouse and human intestinal enteroids, introduce the new inflammasome reporter, and investigate intestinal inflammasomes in response to infection with enteric bacteria and viruses.

The COVID-19 pandemic caused unprecedented challenges for society and the health system. The Schmidt lab contributed to the search for biologics for the treatment and diagnosis of the disease by generating potently neutralizing nanobodies. The aim of chapter 5 was to determine the neutralising mechanism of these nanobodies. As a model for spike-catalysed cell fusion, a critical step in virus infection of host cells, a cell-based fusion assay was established. The results are also published in Science (2021), volume 371, issue 6530, eabe6230.

Chapter 2: Material and Methods

2.1 Material

2.1.1 Antibodies

Rabbit antibody against ASC (AL177) was purchased from Adipogen (AG-25B-0006-C100). Mouse antibody against haemagglutinin (HA) tag (16B12) was purchased from Biolegend (901503). Mouse antibody against double-stranded RNA (dsRNA, J2) was purchased from Scicons (J2-1820). Mouse antibody against RV viral protein 6 (VP6, 2B4) was purchased from Covalab (00012745). Alexa Fluor 647 (AF647) conjugated, polyclonal goat antibodies against mouse and rabbit IgG were purchased from Invitrogen (A32733, A32728).

2.1.2 Reagents

VX-765 (Selleckchem), Z-VAD FMK (MedChemExpress), LPS (tlrl-peklps, InvivoGen), flagellin (tlrl-bsfla, InvivoGen), PAM3SCK4 (tlrl-pms, InvivoGen), nigericin (Cayman Chemical Company), CRID3 (Tocris), talabostat (MedChemExpress), anisomycin (Sigma-Aldrich), lipoteichoic acid (LTA), poly(dA:dT, Invivogen), LMW poly(I:C) (Invivogen), LMW poly(I:C) (Invivogen), MxiH (self-made), protective antigen (PA, self-made), IFN-α2A (Pbl assay science), IFN-β (StemCell), IFN-γ (Immunotools), IFN-λ1 (Biologend), DAPT (Sigma-Aldrich), Y-27632 (Tocris), epidermal growth factor (EGF, Peprotech), noggin (Peprotech), R-spondin (Peprotech), CHIR-99021 (Selleckchem), Hoechst 3342 (Thermo Fisher Scientific), Acti-stain^{TM} 555 or 670 phalloidin (Tebubio), CellTox^{TM} Green (Promega), propidium iodide (PI, Biozol), CellTracker^{TM} Orange CMRA (CTO, Invitrogen), protease inhibitor cocktail (Sigma-Aldrich), polybrene (Merck), M-CSF (Immunotools), doxycycline (Cayman Chemical Company)

2.1.3 Cell lines

All cell lines used in this thesis are listed in the Table A.1 (appendix).

2.1.4 Viruses

RV SA11 was received from Thomas Zillinger (University of Bonn). EMCV was received from Alexander Falkenhagen (Bundesinstitut für Risikobewertung, Berlin, Germany). A norovirus (GII) positive stool sample was received from Anna Maria Eis-Hübinger (University Hospital Bonn).

2.1.5 Bacteria

Salmonella enterica serovar Typhimurium expressing mCherry (stably integrated into the genome) was received from Zeinab Abdullah (University of Bonn). *Shigella flexneri* expressing DsRed (Günther *et al.*, 2020) was received from Hamid Kashkar (University of Cologne).

2.2 Cell culture methods

2.2.1 Cell line maintenance

Adherent cells HEK 293, BHK-21, MA104, HeLa, and iMacs were cultured in Dulbecco's Modified Eagle Medium (DMEM) supplemented with 10 % fetal bovine serum (FBS). THP-1 monocytes were cultured in Roswell Park Memorial Institute (RPMI) medium with 10 % FBS. For differentiation, the cells were treated with 50 ng/mL phorbol 12-myristate 13-acetate (PMA) overnight. The medium was then exchanged and the cells rested for another day. Primary human monocytes and macrophages were cultivated in RPMI supplemented 10 % FBS, 1x GlutaMAX^{TM}, 1 mM sodium pyruvate, and 100 U/mL penicillin-streptomycin. All cells were kept at 37 °C and 5 % CO_2. N/TERT keratinocytes were cultured in Keratinocyte serum-free medium (Thermo Fisher Scientific) supplemented with 0.5x bovine pituitary extract, 0.2 µg/mL EGF, 0.4 mM $CaCl_2$, and 100 U/mL penicillin-streptomycin. The culture of enteroids is described separately. For antibiotics, see Table A.1.

2.2.2 Generation of HEK 293 Flp-In T-Rex cell lines

Flp-In™ T-REx™ 293 cells (Thermo Fisher Scientific Cat# R78007, RRID:CVCL_U427) were generated using the Flp-In system (Thermo Fisher

Scientific) according to the manufacturer’s recommendations. In brief, Flp-In™ T-REx™ 293 were transfected in a 24-well plate with a Flp-In™ compatible expression vector (pEXPR TO FRT derived from pcDNA5/FRT/TO) together with pOG44 encoding the Flp-recombinase. On the next day, the cells were expended to a 10 cm dish and, after the cells attached, 4 µg/mL blasticidin S were added. 24 hours later the medium was replaced and the cells were selected with 4 µg/mL blasticidin S and 50 µg/mL hygromycin B.

2.2.3 Generation of cell lines using lentiviral transduction

Cell lines expressing various transgenes were generated using customised lentiviral vectors based on either pInducer20 (Meerbrey *et al.*, 2011) for doxycycline-inducible expression or on pRRL (Dull *et al.*, 1998) for constitutive expression with different promoters. Culture media for cell lines were supplemented with appropriate antibiotics for selection: 50 µg/mL hygromycin B, 1 µg/mL puromycin (0.75 µg/mL for THP-1 cells), or 500 µg/mL G418.

Lentiviruses were generated by transfecting HEK 293T cells with the lentiviral vector together with the packaging plasmid psPAX2 and the VSV G expression vector pMD2.G. As transfection reagent, polyethylenimine “Max” (PEI MAX, Polysciences) was used. For a well of a 6-well plate, 10 µL PEI MAX were mixed with 150 µL Opti-MEM™ and incubated at room temperature for 5 minutes. The plasmids (lentiviral vector: 1.5 µg, psPAX2: 0.65 µg, pMD2.G: 0.35 µg) were likewise diluted in 150 µL Opti-MEM™. Both mixtures were then combined, carefully mixed, and incubated at room temperature for another 20 minutes. The cells were then covered in fresh DMEM with 2 % FBS and the DNA-PEI MAX complexes were added dropwise to the cells. The medium was exchanged after 6 hours and the cells were incubated at 37 °C and 5 % CO_2 for 48 hours. The supernatants were then harvested, filtered through a 0.45 µm filter, aliquoted, and either used instantly or stored at -80 °C. Optionally, the lentivirus was concentrated by mixing the supernatant with 1/3 of its volume of Lenti-X™ Concentrator (Takara Bio), incubating at 4 °C for at least 30 minutes, and sedimenting at 1500 g and 4 °C for 45 minutes. The supernatant was then removed completely and the virus pellet was resuspended in the desired volume of the medium appropriate for the cell type to be transduced.

Cells were transduced by incubating the parental cell line (1 subconfluent well of a 24-well plate or 10^5 THP-1 cells) with lentivirus and 10 µg/mL polybrene for 6 hours. Starting on the next day, the cells were selected using appropriate antibiotics until all mock-transduced cells died. If monoclonal cell lines with single insertions were desired (here only the case for HEK 293 cells), the cells were transduced with a 10x serial dilution of the lentivirus. After selection, clones were recovered from colonies arising from the lowest possible lentivirus concentrations.

2.2.4 Transfection of adherent cells

Cells were typically transfected using Lipofectamine^{TM} 2000 (Thermo Fisher Scientific). Per well to be transfected, 1.75 µL Lipofectamine^{TM} 2000 was mixed with 50 µL Opti-MEM^{TM} and incubated at room temperature for 5 minutes. The agent to be transfected (typically plasmid DNA or a stimulus) was likewise diluted in 50 µL Opti-MEM^{TM}. Both mixtures were then combined, carefully mixed, and incubated at room temperature for another 20 minutes. The complexes were then dropwise added to the cells in a 24-well plate. The medium was typically exchanged after 6 hours.

2.2.5 Generation of enteroids

In preparation of enteroid generation, Matrigel was thawed on ice, 500 mL PBS were precooled, and a 24-well plate was prewarmed at 37 °C. Human tissue was obtained from adult patients in collaboration with Sven Wehner (University Hospital Bonn, Germany). All steps were carried out on ice. For mouse enteroids, a C57BL/6 mouse was sacrificed and the small intestine between the stomach and the cecum was recovered. The intestine was then cut open longitudinally and the feces were washed out with cold PBS. Regardless of the species, the intestinal tissue was rid of fat and blood vessels as much as possible and washed again with cold PBS. The remaining tissue was then cut into small pieces (approximately 2 mm) and collected in a small beaker with a small volume of PBS (approximately 2 mL). Using scissors, the pieces were then cut further into as small pieces as possible, before another 10 ml cold PBS were added. The next steps were carried out using a 25 mL pipette that had been coated in basal organoid medium (DMEM/F12, 1x GlutaMAX^{TM}, 10 mM HEPES, 100 U/mL penicillin-streptomycin) with 1 % bovine serum albumin (BSA). The tissue pieces were then transferred to a 50 mL tube, the beaker rinsed with another 10 mL cold PBS, which was then added to the 50 mL tube. After the tissue pieces sedimented by gravity (20-30 s), the supernatant was discarded. The tissue was then washed multiple times as follows: 1) 20 mL cold PBS were added, 2) the pieces were pipetted up and down 3-4 times using the precoated 25 mL pipette, 3) the pieces were sedimented by gravity for 20-30 s, 4) the supernatant was discarded. This procedure was repeated until the supernatant stayed clear. For mouse enteroids typically 15 washes were performed, whereas human tissue needed less washes (5-10). After washing, 20 mL cold PBS with 2 mM EDTA were added to the tissue, which was then incubated at 4 °C for 30 minutes while rolling. The tissue was again sedimented by gravity for 20-30 s and the supernatant was discarded. Then, four fractions of crypts were isolated as follows: 1) 15 mL cold PBS were added, 2) the pieces were forcefully pipetted up and down 3-4 times using a precoated 10 mL pipette, 3) the pieces were sedimented by gravity for 20-30 s, 4) the supernatant was collected and passed through a 70 µm cell strainer. The fractions were then centrifuged at 300 g and 4 °C for 5 minutes. All following steps were performed under sterile conditions. The supernatant was discarded and the pellet was resuspended in 1 mL basal organoid medium. A small amount (approx. 10 µL) was inspected for the presence of crypts and fractions with a high ratio of crypts versus other cells or debris were selected. Those were typically fractions 3-4. The cells were sedimented at 200 g and 4 °C for 5 minutes. The supernatant was aspirated and the cells were resuspended in an appropriate volume of Matrigel with culture medium at a 1:1 ratio and kept on ice. The volume depended on the number of crypts. The culture medium for mouse enteroids was ERN organoid differentiation medium (ODM) (basal organoid medium, 1x B27 supplement, 1x N2 supplement, 1 mM *N*-acetyl-L-cysteine, 50 ng/mL recombinant mouse epidermal growth factor (EGF), 100 ng/mL recombinant human R-spondin, 100 ng/mL recombinant mouse noggin) and the culture medium for human enteroids was IntestiCult^{TM} Organoid Growth Medium (OGM, StemCell). The cell suspension was then pipetted as 50 µL domes into the middle of prewarmed 24-wells and solidified at 37 °C for 15 minutes. Finally, 500 µL of appropriate growth medium supplemented with 10 µM Y-27632 was added. For mouse enteroids the medium was replaced every 3-4 days and for human enteroids every 2-3 days. The enteroids were passaged when fully grown (typically after 7 days).

2.2.6 Enteroid passaging

In preparation of enteroid passaging, Matrigel was thawed on ice, PBS with 0.5 mM EDTA was precooled on ice, and a 24-well plate was prewarmed at 37 °C. After removal of the culture medium, the Matrigel was solubilized by adding 750 µL cold PBS with 0.5 mM EDTA and forcefully pipetting up and down 10-15 times. The enteroids were transferred to a 15 mL tube and the well was rinsed with another 750 µL PBS/EDTA, which was then added to the 15 mL tube. Enteroids from up to six wells were collected in one tube. The enteroids were then incubated at room temperature on a roller for 10 minutes and centrifuged at 200 g and 4 °C for 5 minutes (mouse enteroids can also be sedimented at 100 g). The supernatant was then aspirated and the cells were thoroughly resuspended in 5 mL basal organoid medium. The cells were then sedimented as before and the supernatant was aspirated. The cells were finally resuspended in an appropriate volume of Matrigel with culture medium at a 1:1 ratio and kept on ice. The volume depended on the number of new wells to be seeded: for each well 25 µl of each, medium and Matrigel, were used. Mouse enteroids were typically split 1:2 and human enteroids 1:5. The culture medium for mouse enteroids was ERN ODM and the culture medium for human enteroids was IntestiCult^{TM} OGM (StemCell). The cell suspension was then pipetted as 50 µL domes into the middle of prewarmed 24-wells and solidified at 37 °C for 15 minutes. Finally, 500 µL of appropriate growth medium was added. For mouse enteroids the medium was replaced every 3-4 days and for human enteroids every 2-3 days. The enteroids were passaged when fully grown (typically after 7 days).

2.2.7 Generation of inside-out enteroids

Apical-out enteroids were generated as established previously (Co *et al.*, 2019). Seven days old enteroids from one 24-well were gently resuspended in 750 µL ice-cold PBS (without Ca^{2+}) with 5 mM EDTA and collected in a 15 mL tube. The well was rinsed with another 750 µL PBS/EDTA, which was then added to the 15 mL tube. The enteroids were then incubated for one hour at 4°C on a rotator and centrifuged at 200 g for 3 minutes. Then they were washed with 5 mL basal organoid medium and sedimented again. Finally, the enteroids were resuspended in 500 µL ERN ODM and seeded into a 24-well ultra-low adhesion plate. Alternatively, standard culture plates were treated with anti-adherence rinsing solution (Stemcell). After 72 hours, the enteroids were used for experiments.

2.2.8 Generation of enteroid monolayers

Monolayers from human enteroids were seeded into 96-well plates. These were first coated with Matrigel by incubating the wells with 100 µL per well of a 1:50 dilution of Matrigel in PBS at 37 °C for at least 1 hour. For each 96-well to be coated, a 24-well of mature enteroids was used. After removal of the culture medium, the Matrigel was solubilized by adding 750 µL cold PBS with 0.5 mM EDTA and forcefully pipetting up and down 10-15 times. The enteroids were transferred to a 15 mL tube and the well was rinsed with another 750 µL PBS/EDTA, which was then added to the 15 mL tube. Enteroids from up to six wells were collected in one tube. The enteroids were then incubated at room temperature on a roller for 10 minutes and centrifuged at 200 g and 4 °C for 5 minutes. The supernatant was then aspirated and the cells were thoroughly resuspended in 5 mL cold basal organoid medium. The cells were then sedimented as before and the supernatant was aspirated. The cells were then thoroughly resuspended in 500 µL 0.05 % Trypsin-EDTA and incubated at 37 °C for 10 minutes. The enteroids were mechanically disrupted into single cells or small cell clusters as necessary by forcefully pipetting them up and down (typically 50 times) using a 200 µL pipette. Sufficient disruption was confirmed using a microscope. After addition of 1 mL basal organoid medium, the cells were sedimented at 300 g and 4 °C for 5 minutes. The supernatant was removed and the cells were resuspended in IntestiCult^{TM} OGM supplemented with 10 µM Y-27632 (100 µL per well to be seeded). From the 96-well plate, excess Matrigel solution was removed and 100 µL cell suspension was carefully added. The cells were incubated at 37 °C and 5 % CO_2. The medium was exchanged every 2-3 days (without Y-27632). The cells were used for experiments after reaching confluency, which was typically after 2-3 days. Monolayers remain viable for at least 2-3 weeks, provided that the medium is changed regularly.

2.2.9 Cryopreservation of enteroids

For freezing, mature enteroids were harvested by solubilizing the Matrigel in 750 µL cold PBS. The enteroids were transferred to a 15 mL tube and the well was rinsed with another 750 µL PBS, which was then added to the 15 mL tube. Enteroids from up to six wells were collected in one tube. The enteroids were then centrifuged at 200 g and 4 °C for 5 minutes (mouse enteroids can also be sedimented at 100 g). The supernatant was then aspirated and the cells were resuspended in 5 mL basal organoid medium. The cells were sedimented as before and the supernatant was aspirated. The enteroids were then resuspended in cryopreservation medium (80 % basal organoid medium, 10 % FBS, 10 % DMSO). Mouse enteroids were resuspended in 500 µL medium for each original well and human enteroids in 1 mL. The cells were then transferred to cryotubes (1 mL per tube) and frozen at -80 °C in a freezing container. After 1 day, the cells were transferred to -150 °C for permanent storage.

Before thawing enteroids, Matrigel was thawed on ice. Mouse enteroids were thawed in a 37 °C water bath and directly combined with 9 mL basal organoid medium with 10 % FBS. The cells were centrifuged at 200 g and 4 °C for 5 minutes and washed in 5 mL basal organoid medium. This washing step was repeated once and the medium was aspirated leaving approximately 50 µL medium on the pellet. Then 50 µL Matrigel was added and the cells were resuspended. The cell suspension was then pipetted as 50 µL domes into the middle of prewarmed 24-wells and solidified at 37 °C for 15 minutes. Finally, 500 µL of warm ERN OGM supplemented with 10 µM Y-27632 was added.

The protocol for cryopreserving human enteroids was adapted from the IntestiCult^{TM} supplementary protocols (StemCell). The enteroids were thawed in a 37 °C water bath, directly mixed with 1 mL wash solution (basal organoid medium with 1 % BSA), and transferred to a 15 mL tube with 2 mL wash solution. The cryotube was then rinsed two more times with wash solution, which was then added to the 15 mL tube. The enteroids were centrifuged at 200 g and 4 °C for 5 minutes and the supernatant was aspirated. The enteroids were then resuspended in 200 µL of Matrigel with IntestiCult^{TM} OGM at a 1:1 ratio and kept on ice. The cell suspension was then pipetted as 50 µL domes into the middle of prewarmed 24-wells and solidified at 37 °C for 15 minutes. Finally, 500 µL of IntestiCult^{TM} OGM was added.

2.2.10 Enteroid suspension culture

To expand human enteroid cultures, mainly for the purpose of up-scaling monolayer experiments, the enteroids were cultured in suspension. The protocol was adapted from the IntestiCult^{TM} ODM protocols (StemCell). In preparation, Matrigel was thawed on ice and a well of a 6-well plate was filled with 3 mL IntestiCult^{TM} OGM and prewarmed at 37 °C. For each 6-well, 4-6 24-wells with mature enteroids were harvested: after removal of the culture medium, the Matrigel was solubilized by adding 750 µL cold PBS with 0.5 mM EDTA and forcefully pipetting up and down 10-15 times. The enteroids were transferred to a 15 mL tube and the well was rinsed with another 750 µL PBS/EDTA, which was then added to the 15 mL tube. The enteroids were then incubated at room temperature on a roller for 10 minutes and centrifuged at 200 g and 4 °C for 5 minutes. The supernatant was then aspirated and the cells were thoroughly resuspended in 5 mL basal organoid medium. The cells were then sedimented as before and the supernatant was aspirated. The cells were finally resuspended in 500 µL Matrigel and kept on ice. The suspension was slowly pipetted into the centre of the 6-well with the prewarmed medium and incubated at 37 °C and 5 % CO_2. A half-medium change was performed every 2-3 days: the plate was tilted and 1.5 mL medium was removed without removing any enteroids. The same volume of fresh IntestiCult^{TM} OGM was then added. The amount of enteroids from one well of a 6-well plate was considered equal to 18 wells of a 24-well plate with enteroid domes. Suspension enteroid cultures were harvested by transferring them to a 15 mL tube and sedimenting them at 200 g and 4 °C for 5 minutes. The cells were then resuspended in 5 mL cold PBS with 0.5 mM EDTA and from then treated as if harvested from domes.

2.2.11 Lentiviral transduction of enteroids

Lentiviruses for enteroid transduction were produced as described in 2.2.3. For one transduction, the lentivirus from one 15 cm dish of HEK 293T cells was concentrated into 250 µL organoid transduction medium (IntestiCult^{TM} OGM with 8 µg/mL polybrene and 10 µM Y-27632). The lentivirus was preferentially used immediately or, alternatively, stored at -80 °C.

The protocol for enteroid transduction was adapted from a published protocol (Koo *et al.*, 2013). For each transduction, including mock transduction, one well of a 24-well plate of enteroids was cultivated in a dome for 3 days after passaging. In order to enrich stem cells, mouse enteroids were treated with 10 µM CHIR-99021 and 10 mM nicotinamide for the entire duration. After removal of the culture medium, the Matrigel was solubilized by adding 750 µL cold PBS with 0.5 mM EDTA and forcefully pipetting up and down 10-15 times. The enteroids were transferred to a 15 mL tube and the well was rinsed with another 750 µL PBS/EDTA, which was then added to the 15 mL tube. Enteroids from up to six wells were collected in one tube. The enteroids were then incubated at room temperature on a roller for 10 minutes and centrifuged at 200 g and 4 °C for 5 minutes. The supernatant was then aspirated and the cells were resuspended in 5 mL cold basal organoid medium. The cells were then sedimented as before and the supernatant was aspirated. The cells were then thoroughly resuspended in 500 µL 0.05 % Trypsin-EDTA and incubated at 37 °C for 10 minutes. The enteroids were mechanically disrupted into single cells or small cell clusters as necessary by forcefully pipetting them up and down (typically 50 times) using a 200 µL pipette. Sufficient disruption was confirmed using a microscope. After addition of 1 mL basal organoid medium, the cells were sedimented at 300 g and 4 °C for 5 minutes. For each transduction, including mock transduction, 250 µL organoid transduction medium was added to the cell pellet. The cells were then resuspended and distributed into a 48-well plate with 250 µL per well. Then, 250 µL of lentivirus or, for the mock transduction, organoid transduction medium was added to each well. The plate was sealed with Parafilm® and centrifuged at 600 g and 32 °C for 60 minutes. The Parafilm® was then removed and the cells incubated at 37 °C for 6 hours. Then, the cells were collected in 1.5 mL tubes and centrifuged at 500 g and 4 °C for 5 minutes. The supernatant was aspirated and the cells were resuspended in 100 µL Matrigel. The cell suspension was then pipetted as 50 µL domes into the middle of prewarmed 24-wells and solidified at 37 °C for 15 minutes. Finally, 500 µL of appropriate growth medium supplemented with 10 µM Y-27632 was added. After 2-3 days, the medium was replaced with standard culture medium. When the enteroids had recovered the selection with antibiotics was started (typically after 3 days). The following concentrations were used: puromycin: 2 µg/mL, G418: 200 µg/mL, hygromycin B: 25 µg/mL.

2.2.12 Bacterial infection of mouse enteroids

Mouse enteroids were infected with either *Salmonella enterica* serovar Typhimurium (*S.* Typhimurium) or *Shigella flexneri* (*S. flexneri*) strains expressing mCherry (Günther *et al.*, 2020). 3 days before infection, the bacteria were streaked out onto Congo red agar plates (tryptic soy broth (TSB) with 0.1 g/L Congo red) and incubated overnight. Single colonies were picked to inoculate a preculture in 5 mL lysogeny broth (LB). In the case of *S. flexneri* white colonies were avoided, because the inability to absorb Congo red indicates the loss of the virulence plasmid. To avoid loss of the plasmid during the preculture, it was grown at 30 °C. Otherwise, all cultivation steps were performed at 37 °C while shaking.

On the day of infection, 100 µL of the preculture were transferred to 5 mL fresh LB medium and incubated at 37 °C for 3 hours while shaking. To generate the inocula, the bacteria were diluted in infection medium (DMEM/F12 with 10 mM HEPES and 1x GlutaMAX^{TM}).

To prepare the enteroids for infection, the medium was aspirated and the Matrigel was solubilized in 500 µL cold PBS. The suspension was transferred to a 1.5 mL tube, the well was rinsed with another 500 µL PBS and everything was combined in the 1.5 mL tube. The enteroids were sedimented at 100 g and 4 °C for 5 minutes. The supernatant was then removed and the pellet was resuspended in 500 µL bacterial or mock inoculum. The enteroids were then incubated at 37 °C for 15-30 minutes and thereafter centrifuged at 100 g and 4 °C for 5 minutes. The inoculum was aspirated and the enteroids resuspended in a 1:1 mix of Matrigel and infection medium and pipetted into a prewarmed 24-well plate to form a dome. For imaging, the dome was placed onto a cover slip within the well-plate. The Matrigel was solidified at 37 °C for 15 minutes and 500 µL warm infection medium was added. The enteroids were then incubated as indicated.

2.2.13 Virus infection of enteroids

Enteroids can be infected as 2-dimensional monolayers or as 3-dimensional structures. Human enteroids were mostly infected as monolayers, which were differentiated in IntestiCult^{TM} ODM (StemCell) for 3 days. For infection, the inoculum was added on top of the cell layer and incubated at 37 °C and 5 % CO_2 for an appropriate time interval, usually 1 hour. The inoculum was then aspirated and the cells kept in IntestiCult^{TM} ODM for the duration of the experiment.

For infection of 3-dimensional enteroids, the Matrigel was solubilized by adding 750 µL cold PBS with 0.5 mM EDTA and forcefully pipetting up and down 10-15 times. The enteroids were transferred to a 15 mL tube and the well was rinsed with another 750 µL PBS/EDTA, which was then added to the 15 mL tube. Enteroids from up to six wells were collected in one tube. The enteroids were then incubated at room temperature on a roller for 10 minutes and centrifuged at

200 g and 4 °C for 5 minutes. The supernatant was then aspirated and the cells were thoroughly resuspended in 5 mL basal organoid medium. The cells were then sedimented as before, resuspended in 200 µL virus (virus dilution in ODM with 0.2 % BSA) or mock inoculum and incubated at 37 °C and 5 % CO_2 for one hour. 1 mL of basal organoid medium was then added and the cells were sedimented as described before. The supernatant was aspirated leaving approximately 25 µL medium on top of the cell pellet. Then 25 µL Matrigel was added and the cells were resuspended. The cell suspension was then pipetted as 50 µL domes into the centre of wells in a prewarmed 24-well plate and solidified at 37 °C for 15 minutes. For imaging, the domes were placed onto cover slips within the well plate. Finally, 500 µL of warm ODM was added and the infected enteroids were kept at 37 °C and 5 % CO_2 for the duration of the experiment.

2.2.14 Rotavirus preparation

RV strain SA11 was obtained from Alexander Falkenhagen (Bundesinsstitut für Risikobewertung, Berlin, Germany). Preparation of RV was performed based on a published protocol (Arnold *et al.*, 2009). MA104 cells were seeded into 12 T175 flasks with complete medium (Minimum Essential Medium (MEM), 1x GlutaMAX^{TM}, 10 % FBS, 100 U/mL Penicillin-Streptomycin) and grown to confluency. The cells were infected with a multiplicity of infection (MOI) of 0.05, assuming $1.5{\cdot}10^7$ cells per flask: the virus stock was diluted in 5 mL infection medium (Modified Eagle Medium (MEM), 1x GlutaMAX^{TM}, 100 U/ml Penicillin-Streptomycin). For activation, 10 µg/mL trypsin (from bovine pancreas, TPCK treated) was added and incubated at 37 °C for 1 hour. The virus was then diluted with 115 mL infection medium. The MA104 cells were washed three times with 10 mL infection medium and 10 mL inoculum was added to each flask. The cells were then incubated at 37 °C for 1 hour, while being rocked every 15 minutes. The inoculum was then removed, the cells were washed with 10 mL infection medium, and 25 mL infection medium with 0.5 µg/mL trypsin were added per flask. The virus was harvested when the monolayer of cells was completely detached (typically after 3-5 days). The cells were 3 times frozen at -80 °C and thawed at room temperature. The content was then transferred to 50 mL tubes, the cell debris was spun down at 300 g and 4 °C for 10 minutes, and the supernatant was transferred to fresh tubes.

The virus was then purified through a sucrose cushion. For that purpose, virus-containing supernatant was transferred to SW32 tubes (35 mL per tube) and underlaid with 35 %(w/v) sucrose in TNC buffer (20 mM Tris, 100 mM NaCl, 1 mM $CaCl_2$, pH 8.0). Using a SW32Ti rotor, virions were sedimented at 29,000 rpm (average relative centrifugal force (RCF): 103,282 g) and 4 °C for 1.5 hours. The supernatants were aspirated, and all pellets were resuspended in 1 mL TNC buffer and pooled into a 50 mL tube. The virus was further homogenised by two times sonicating for 10 seconds and, if necessary, resuspending with a 25-G needle. The virus was finally aliquoted, and stored at -80 °C.

2.2.15 EMCV preparation

EMCV was obtained from Thomas Zillinger (University of Bonn, Germany). Preparation of EMCV was performed loosely based on a published protocol (Burrill *et al.*, 2013). BHK-21 cells were seeded into 10 T175 flasks with complete medium (MEM, 1x GlutaMAX^{TM}, 10 % FBS, 100 U/mL Penicillin-Streptomycin) and grown to confluency. The cells were infected with an MOI of 0.05, assuming $1.5 \cdot 10^7$ cells per flask: the virus stock was diluted in 120 mL infection medium (MEM, 1x GlutaMAX^{TM}, 100 U/ml Penicillin-Streptomycin). The BHK-21 cells were washed with 10 mL infection medium and 10 mL inoculum was added to each flask. The cells were then incubated at 37 °C for 1 hour, while being rocked every 15 minutes. The inoculum was then removed, and 25 mL medium (MEM, 1x GlutaMAX^{TM}, 5 % FBS, 100 U/ml Penicillin-Streptomycin) were added per flask. The virus was harvested when approximately 70 % of the cells were detached (typically after 24 hours). The cells were 3 times frozen at -80 °C and thawed at room temperature. The content was then transferred to 50 mL tubes, the cell debris was spun down at 2500 g and room temperature for 10 minutes, and the supernatant was transferred to fresh tubes.

The virus was then purified through a sucrose cushion. For that purpose, virus-containing supernatant was transferred to SW32 tubes (35 mL per tube) and underlaid with 30 %(w/v) sucrose in TNC buffer (20 mM Tris, 100 mM NaCl, 1 mM $CaCl_2$, pH 8.0). Using a SW32Ti rotor, virions were sedimented at 28,000 rpm (average RCF: 96,281 g) at 20 °C for 4 hours. The supernatants were aspirated, and all pellets were resuspended in 1 mL TNC buffer. The virus was then pooled, aliquoted, and stored at -80 °C

2.2.16 Generation of stool filtrates

Human norovirus-positive or -negative stool filtrates were generated as described in (Zou *et al.*, 2019). Stool was weighed into a 15 mL tube and PBS was added to obtain a 10 %(w/v) suspension. Solids were broken up by pipetting as necessary. The stool suspension was vortexed two times for 30 seconds with a 5 minute break in between. Next, the suspension was sonicated three times for 1 minute, rested on ice for 1 minute in between. Debris was removed by centrifugation at 1500 g for 10 minutes. The supernatant was transferred to a fresh 15 mL tube and centrifuged again. Finally, the supernatant was serially passed through a 0.45 µm and a 0.22 µm filter, aliquoted, and stored at -80 °C.

2.3 Analytical methods

2.3.1 Cytokine measurement

IL-1β and TNF-α were measured using the homogeneous time-resolved fluorescence (HTRF) human IL-1β or TNF-α kit (Cisbio) according to the manufacturer's recommendations. A two-fold dilution series of the standards was prepared in OptiMEM or DMEM (according to the medium of the samples), including a medium only sample. The standard concentrations ranged from 101.56 – 6500 pg/mL. First, 3 µL antibody mix were transferred to a white (opaque) 384-well plate. Then, 12 µL of sample or standard were added. Each sample or standard was measured in technical duplicates. The plate was then sealed, shortly spun down, and incubated overnight at 4 °C in the dark. The seal was removed and the plate was measured using a SpectraMax i3 plate reader with an excitation wavelength of 340 nm and emission wavelengths of 616 and 665 nm. Cytokine concentrations were calculated based on the standard curve by the SoftMax Pro 6.3 software (Molecular Devices).

2.3.2 Flow cytometry

For flow cytometry experiments, cells were typically cultured and treated in 24-well plates. When measuring inflammasome assembly, inflammasome competent cells, such as macrophages, were treated with VX-765 to prevent loss of cells by pyroptosis. Adherent cells were harvested by trypsinization and resuspension. Enteroids were harvested by solubilizing the Matrigel as described in 2.2.6. Enteroid fragments were then thoroughly resuspended in 500 µL 0.05 % Trypsin-EDTA and incubated at 37 °C for 10 minutes. The enteroids were mechanically disrupted into single cells by forcefully pipetting them up and down (typically 50 times) using a 200 µL pipette. Sufficient disruption was confirmed using a microscope. Harvested cells were fixed in 4 % formaldehyde for 20 minutes. The cells were then either directly analysed by flow cytometry or subjected to staining.

For intracellular staining, cells were permeabilized in Permeabilization Buffer (Biolegend) and stained either with primary and fluorescently labelled secondary antibodies or with labelled nanobodies as indicated, diluted in Permeabilization Buffer. After each staining step, the cells were washed with Permeabilization Buffer. Finally, the cells were resuspended in FACS buffer (PBS, 2 % FBS, 5 mM EDTA, 0.02% NaN_3).

HA-tag was stained with the mouse antibody 16B12 (1:1000). dsRNA was stained with J2 (1:100). RV VP6 was stained with self-made VHH 2KD1-AF647 (1:500) or with the mouse antibody 2B4 (1:100). AF647 conjugated secondary antibodies were diluted 1:500.

Cells were analysed using a FACSCanto II (BD Biosciences) or LSR Fortessa (BD Biosciences), recording area, width, and height of the forward scatter (FSC), side scatter (SSC), and the applicable fluorophores. The flow cytometers were provided by the Flow Cytometry Core Facility (Medical Faculty, University of Bonn, Germany). The resulting data was analysed using the FlowJo software. Single cells were identified based on the FSC and SSC signals. Specking cells were identified by plotting the height of the ASC or reporter signal over its width. The population with increased height and decreased width was considered as specking cells, *i.e.* cells with assembled inflammasomes.

2.3.3 Microscopy

For microscopy experiments, cells were seeded on 12 mm cover slips within 24-well plates or in tissue culture-treated CellCarrier-96 Ultra Microplates (Perkin Elmer). For enteroids, the Matrigel dome was placed onto the cover slip. For 96-well plates the dome was reduced to a volume of 10 µL. Cells were fixed in 4 % formaldehyde, permeabilized in permeabilization buffer (PBS, 0.3 % Triton X-100, 1 % BSA) for 10 minutes and blocked in blocking buffer (PBS, 3 % BSA). The cells were then stained either with primary and fluorescently labelled secondary antibodies, or with labelled nanobodies as indicated. All staining reagents were diluted in blocking buffer. DNA was stained with Hoechst 3342 (1:5000, Thermo Fisher Scientific) and, if indicated, actin was stained with Acti-stain^{TM} 555 or 670 phalloidin (1:100, Tebubio). Those dyes were applied together with fluorescently labelled antibodies. After each staining step, the cells were washed three times with PBS. After staining, the cells were stored in PBS and cover slips mounted to object slides using Fluoromount G. Images were recorded either with a Zeiss Observer.Z1 wide field microscope using a PlanApochromat 20x0.8 objective or a Leica SP8 confocal microscope using an HC PL APO CS2 63x1.20 water (96-well plates) or a 63x1.4 oil (cover slips) objective. The microscopes were provided by the Microscopy Core Facility (Medical Faculty, University of Bonn, Germany). For live-cell microscopy, the sample was kept at 37 °C with 5 % CO_2. The Images were processed using ImageJ software or further analysed using Imaris (Oxford Instruments) as described below.

ASC was stained with AL177 (1:200). dsRNA was stained with J2 (1:200). AF647 conjugated secondary antibodies were diluted 1:1000. RV VP6 was stained with self-made VHH 2KD1-AF647 (1:200)

2.3.4 Specking quantification from images

Images were loaded into Imaris (Oxford Instruments) as Z-stacks. Using the channel for endogenous ASC, 'spots' were defined with an estimated diameter of 2 µm. The 'quality' parameter was adjusted manually to define a threshold that excluded background signal. For all spots, the sum intensity was exported for all channels. The intensity for fluorescent reporters in each spot was normalized by the ASC intensity. Data compilation and further calculations were done using R software. The fraction of ASC specks that contain a reporter was determined by the frequency of ASC specks, in which the reporter sum intensity exceeded a background threshold.

2.3.5 VHH-induced SARS-CoV-2 spike fusion assay

Cells fusion assays are described in Koenig *et al*. (2021). HEK 293 SARS-CoV-2 spike Δ18 EGFP (enhanced green fluorescent protein) and HEK 293 SARS-CoV-2 spike Δ18 tag-RFP-t cells were seeded in tissue culture-treated CellCarrier-96 Ultra Microplates (Perkin Elmer) at a density of 10^5 cells of each cell line per well in phenol red-free full medium containing 1 µg/mL doxycycline. 24 hours after seeding, the cells were treated with the indicated concentrations of nanobodies and cultivated at 37°C, 5% CO_2. Every 20 min, images were recorded in four fields of view per well for 14 hours using a Zeiss Observer Z1 wide-field microscope with 20X PlanApochromat objective (NA = 0.8). EGFP and tagRFP-t colocalization was quantified using ImageJ plugin EzColocalization (Stauffer *et al.*, 2018). Pearson correlation coefficients (PCC) between both channels were determined for each time point, including all pixels (no thresholding).

2.3.6 SARS-CoV-2 spike-ACE2 fusion assay

Cells fusion assays are described in Koenig *et al*. (2021). HEK 293 SARS-CoV-2 spike Δ18 EGFP and HEK 293T ACE2-tagRFP-t labelled with CellTracker^{TM} Orange CMRA (CTO, 1:5000) were seeded in tissue culture-treated CellCarrier-96 Ultra Microplates (Perkin Elmer) at a density of 10^5 cells of each cell line per well in phenol red-free full medium. 24 hours after seeding, cells were treated with 1 µg/mL doxycycline and 1 µM of the indicated nanobodies, and cultivated at 37°C, 5% CO2. Every 20 min, images were recorded in four fields of view per well for 14 hours using a Zeiss Observer Z1 wide-field microscope with 20X PlanApochromat objective (NA = 0.8). EGFP and tagRFP-t colocalization was quantified using the ImageJ plugin EzColocalization (Stauffer *et al.*, 2018). Pearson correlation coefficients (PCC) between both channels were determined for each time point, including all pixels (no thresholding). To normalize fusion, PCC values at 1 hour were subtracted from PCC values of each time point. Average values of four fields of view were corrected by average values of uninduced cells from the same time point. Fusion at t = 12 in samples with doxycycline and no nanobodies hours was defined as 100% fusion.

2.3.7 RT-qPCR

Gene expression in enteroids was measured using reverse transcription quantitative polymerase chain reaction (RT-qPCR). Differentiated enteroids from three different donors were treated with 10 % stool filtrate (1:10), macrophage supernatant (1:10), human IFN-α (500 U/mL), IFN-β (500 U/mL), IFN-γ (500 U/mL), IFN-λ (500 U/mL), LPS (200 ng/mL), flagellin (1 µg/mL), or PAM3SCK4 (1µg/mL) overnight. After solubilizing the Matrigel in cold PBS and washing the enteroids in PBS, the RNA was extracted using the RNeasy Micro Kit (Qiagen) according to the manufacturer's recommendations and stored at -80 °C. To generate cDNA, 300 ng RNA of each sample were mixed with oligo(dT) primers and incubated at 65 °C for 5 minutes and on ice for one minute. Then, 0.5 µM dNTPs, 50 µM DTT (final concentration) and 0.1 µL SuperScript^{TM} III reverse transcriptase (Thermo Fisher Scientific) were added with the appropriate buffer to a final volume of 20 µL. The reaction was incubated at 50 °C for 1 hour

Table 2.1: qPCR primers

gene	orientation	sequence	reference
HPRT	forward	TCAGGCAGTATAATCCAAAGATGGT	(Chu *et al.*, 2021)
HPRT	reverse	AGTCTGGCTTATATCCAACACTTCG	
NLRC4	forward	GGAAAGTGCAAGGCTCTGAC	~
NLRC4	reverse	TGTCTGCTTCCTGATTGTGC	
NLRP6	forward	CTGTTCTGAGCTACTGCGTGAG	~
NLRP6	reverse	AGGCTCTTCTTCTTCTTCTCCTG	
NLRP9	forward	CTAGCCTCTCCCAGTCTGACAT	~
NLRP9	reverse	GCGATGTCTTCACAAACTTCAC	
PYCARD	forward	CTGACGGATGAGCAGTACCA	~
PYCARD	reverse	CAAGTCCTTGCAGGTCCAGT	
CASP1	forward	GGGGTACAGCGTAGATGTGAA	~
CASP1	reverse	CTTCCCGAATACCATGAGACA	
CASP8	forward	AGAAGAGGGTCATCCTGGGAGA	~
CASP8	reverse	TCAGGACTTCCTTCAAGGCTG	
IL1B	forward	CCACAGACCTTCCAGGAGAA	~
IL1B	reverse	GTGATCGTACAGGTGCATCG	
IL18	forward	CACCCCGGACCATATTTATT	~
IL18	reverse	TCATGTCCTGGGACACTTCTC	
GSDMD	forward	GTGTGTCAACCTGTCTATCAAGG	~
GSDMD	reverse	CATGGCATCGTAGAAGTGGAAG	
GBP1	forward	CGAGGGTCTGGGAGATGTAG	(Ali *et al.*, 2020)
GBP1	reverse	TAGCCTGCTGGTTGATGGTT	

and at 85 °C for 10 minutes. For the qPCR, the samples were diluted 1:5 in water. In a total volume of 10 µL, 2 µL cDNA were mixed with forward and reverse primer (0.4 µM), and 5 µL SYBR dye (Thermo Fisher Scientific). The target genes and primers are listed in Table 2.1. The qPCR was done using the QuantStudio^{TM} 6 Flex Real-Time PCR System (Thermo Fisher Scientific). Expression relative to the housekeeping gene *HPRT* was determined using the ΔCT method. All calculation were done in the R software.

2.3.8 RNA sequencing

Enteroids from three different gut segments (duodenum, jejunum, ileum) were grown in IntestiCult^{TM} OGM (StemCell) or differentiated in IntestiCult^{TM} ODM (StemCell) supplemented with 5 µM DAPT for three days. For each sample, two wells of a 24-well plate were harvested by solubilizing the Matrigel as described in 2.2.6. The enteroids were finally lysed in 700 µL trizol and handed over to

Susanne Schmidt (University of Bonn), who performed bulk 3’ RNA sequencing. The counts were normalised by DESeq2’s median of ratios (Anders and Huber, 2010): The counts were divided by sample-specific size factors determined by median ratio of gene counts relative to geometric mean per gene. The resulting count matrix was further analysed using the R software.

2.4 Protein chemical methods

2.4.1 Nanobody expression and purification

DNA encoding the nanobody VHH 2KD1 (Garaicoechea *et al.*, 2008) was ordered (Integrated DNA Technologies) and cloned into a pHEN6-based expression vector for bacterial, periplasmic expression with a C-terminal LPETG-His$_6$ tag via Gibson assembly (New England Biolabs). *Escherischia coli* (*E. coli*) WK6 was transformed with expression vectors. An overnight culture in LB was used to inoculate Terrific Broth (TB), and expression was induced at an optical density at 600 nm (OD$_{600}$) of 0.6 with 1 mM isopropyl-β-D-thiogalactoside (IPTG). Expression took place at 30 °C for 16 hours. The bacteria were spun down, resuspended in TES buffer (200 mM Tris pH 8.0, 0.65 mM EDTA, 500 mM sucrose), and incubated at 4 °C for at least one hour. Periplasmic extracts were generated by osmotic shock in 0.25x TES buffer. The debris was removed by two centrifugation steps.

The nanobody was first purified via the His$_6$ tag by Ni-NTA (nitriloacetic acid) affinity purification. Ni-NTA slurry was transferred into a gravity flow column and equilibrated with one column volume of wash buffer (50 mM Tris pH 7.5, 150 mM NaCl, 10 mM imidazole). The periplasmic extract was applied to the column two times, and the resin was washed three times with wash buffer. The nanobody was eluted in three fractions using elution buffer (50 mM Tris pH 7.5, 150 mM NaCl, 500 mM imidazole).

The protein was further purified by size exclusion chromatography (SEC) on a HiLoad 16/600 Superdex 75 pg column. The column was first equilibrated with SEC buffer (20 mM HEPES pH 7.4, 150 mM NaCl, 10 % glycerol, filtered). The elution fractions from the Ni-NTA chromatography were then applied to the column and fractionated. Fractions containing the protein were pooled, concentrated using an Amicon spin-concentrator with 10 kDa cutoff (Millipore), and frozen in liquid nitrogen.

2.4.2 Sortase labelling of nanobodies

Fluorescently labelled nanobodies were produced using sortase A labelling (Guimaraes *et al.*, 2013). 0.67 µg VHH-LPETG-His_6 were incubated with 166.5 µM GGG-Alexa Flour 647 (AF647) and 20 µM His-tagged sortase A 7m in 1 mL HEPES buffer (20 mM HEPES pH 7.4, 150 mM NaCl) at 4 °C overnight. Sortase and unreacted nucleophile was removed by incubating the mixture two times with 100 µL equilibrated Ni-NTA beads at 4 °C for 15 minutes. The labelled nanobody was purified by SEC on an S75 column. Fractions containing labelled nanobody were pooled and concentrated.

2.4.3 SDS-PAGE

Sodium dodecyl sulphate polyacrylamide gel electrophoreses (SDS-PAGE) was used to analyse proteins. Samples were denatured in SDS-PAGE sample buffer (50 mM Tris pH 6.8, 100 mM dithiothreitol (DTT), 0.01 % Bromphenol Blue, 10 % glycerol, 2 % SDS) and heated to 95 °C for 10 min. The samples were then loaded onto a 15 % polyacrylamide gel in running buffer (25 mM Tris, 192 mM glycine, 0.1 % SDS), and a voltage of 150 V was applied for approximately 40 minutes. Precision Protein Dual Color Standards (Biorad) were used as molecular weight standards. After the gel was washed in desalted water, proteins were stained with colloidal Coomassie (0.12 %(w/v) Coomassie Brilliant Blue G-250, 10 %(w/v) orthophosphoric acid, 10 %(w/v) $(NH_4)SO_4$, 20 %(v/v) methanol), and the gel was destained in desalted water.

Chapter 3: A novel reporter for inflammasome activation and caspase-1 recruitment

3.1 Introduction

Inflammation is a critical step in the response against invading pathogens, as it establishes the immune system for an effective defence. However, excessive inflammation can lead to severe disease symptoms or cause autoinflammatory diseases such as gout (So and Martinon, 2017), rheumatoid arthritis (Spel and Martinon, 2020), cryopyrin-associated periodic syndrome (Booshehri and Hoffman, 2019), Familial Mediterranean fever (Lancieri *et al.*, 2023), and Alzeimer’s disease (Heneka *et al.*, 2015; Venegas and Heneka, 2019). Understanding the biology of inflammation, including its activation, regulation, and consequences is therefore important regarding a plethora of different diseases, including both infectious and sterile ones.

On a cellular level, inflammation is coordinated by inflammasome signalling. Inflammasomes are activated by cytosolic sensors that integrate signs of infection (PAMPs) and cell damage (DAMPs). Once activated, the sensors oligomerize and recruit the adapter molecule ASC via homologous domain interactions. ASC then forms filaments and higher order structures, yielding a single macromolecular complex per cell, which is termed the inflammasome. This serves as a recruitment platform for caspase-1, which is then autoproteolytically activated to cleave GSDMD and the pro-inflammatory cytokines IL-1β or IL-18. GSDMD proceeds to form pores in the plasma membrane to facilitate cytokine release and pyroptotic cell death (Martinon *et al.*, 2002; Broz and Dixit, 2016; Hayward *et al.*, 2018).

Most current methods detect inflammasome formation indirectly by measuring its functional consequences. Pyroptosis can be measured via the uptake of DNA dyes such as propidium iodide, the release of lactate dehydrogenase (LDH), or by characterising cell morphology (Rayamajhi, Zhang, *et al.*, 2013). Release of IL-1β/ IL-18 can be measured by enzyme-linked immunosorbent assay (ELISA) or HTRF (Schneider *et al.*, 2013). The proteolysis of caspase-1, GSDMD, and cytokines is commonly examined by western blotting using specific antibodies (Jakobs *et al.*, 2013). The assembly of ASC complexes can also be seen by western blotting after cross-linking ASC or by blue native PAGE (Kofoed and Vance, 2013). Most of these methods are bulk measurements and single cell resolution is lost using these approaches. To detect inflammasome forming cells on a single cell level, ASC can be stained with specific antibodies to visualise ASC specks in fixed and permeabilized cells. Additionally, investigation of live cells is made possible using fluorescent fusions of ASC (Stutz *et al.*, 2013). Because overexpression of ASC leads to spontaneous speck formation, this approach requires careful promoter choice and selection of clones with low background. A mouse line that ectopically expresses a fluorescent ASC fusion is available, but functional inflammasome signalling was only observed when the reporter was expressed in addition to endogenous ASC (Tzeng *et al.*, 2016). Another mouse line expresses ASC-mCherry from the endogenous *Pycard* locus (*Pycard* encodes ASC), but I encountered functional problems with enteroids derived from this mouse line (shown in section 4.2.2). Furthermore, this approach is not suitable to study human inflammasomes.

In order to further our understanding of inflammasome biology, especially with regard to specialised cell types for which cell lines are not available, we need tools to investigate inflammation in the context of primary tissues. At the same time, we need strategies to monitor signalosome formation in real time, ideally at endogenous levels of the involved components. Finally, we need to clarify the genuine mechanism of caspase-1 recruitment and activation.

Because we currently lack the tools necessary to address these issues, we developed a new, non-invasive inflammasome reporter with low background that is compatible with microscopy, flow cytometry, and cell sorting. Moreover, it directly reports on the recruitment of caspase-1, which allowed us to investigate the mode of caspase-1 recruitment and enables the visualisation of ASC-independent caspase-1 recruitment.

3.2 Results

3.2.1 Caspase-1^{CARD} is efficiently recruited to ASC specks and exhibits negligible background

As currently available techniques do not allow the straightforward visualisation and monitoring of inflammasome responses, we aimed to develop a novel reporter that fulfils the following criteria: 1) it should not require staining; 2) it should identify inflammasome activation in living or fixed cells; 3) it should be suitable for primary cells and tissues; 4) it should have single cell resolution; 5) it should be measurable by microscopy and flow cytometry; 6) it should have low background; 7) and it should report on the recruitment of caspase-1.

Canonical inflammasomes are characterised by the polymerization of ASC into a single macromolecular complex. Therefore, fluorescent fusions of ASC (*e.g.* ASC-EGFP) are the most commonly used intracellular reporters (Stutz *et al.*, 2013). Though this is a helpful tool, it has inherent shortcomings, including the necessity to alter the concentration of ASC, prominent background, and the inability to visualise caspase-1 recruitment. All downstream effects of inflammasomes depend on the recruitment of caspase-1 via its CARD. We thus investigated whether the CARD of caspase-1 could be used to recapitulate caspase-1 recruitment. For our new inflammasome reporter we therefore utilised a genetic fusion of EGFP (or another fluorescent protein) to caspase-1^{CARD} (C1C). We expected C1C-EGFP to be recruited to the inflammasome complex similarly to ASC-EGFP, albeit one step further downstream (Figure 3.1A).

We generated THP-1 cells that express C1C-EGFP under the control of the weak constitutive Ubiquitin C promoter (pUbC, THP-1$^{C1C\text{-}EGFP}$) or a doxycycline-inducible promoter (THP-1$^{C1C\text{-}EGFP(i)}$). To verify that C1C-EGFP identifies true ASC specks, we treated those cells with LPS and nigericin to activate the NLRP3 inflammasome, stained endogenous ASC with specific antibodies, and analysed the distribution of both proteins in the cell by microscopy. Upon treatment, C1C-EGFP efficiently redistributed into specks that colocalized with endogenous ASC, thus confirming that the reporter visualises *bona fide* inflammasomes (Figure 3.1B). Although quantification is possible via imaging, we opted for a faster and more scalable way of quantification and therefore sought to measure inflammasome formation by flow cytometry. A time-of-flight-based method for inflammasome detection has been pioneered before (Sester *et al.*, 2015), which relies on the relocalization of ASC during inflammasome formation. Compared to the diffuse ASC distribution in resting cells, the specks in activated cells are much smaller and of higher intensity. In flow cytometry, this change translates into a decreased fluorescent pulse width along with an increased signal height. Since microscopy revealed a redistribution of C1C-EGFP equivalent to that of ASC, we expected this assay to work equally well with C1C-EGFP instead of ASC. Indeed, when we measured LPS and nigericin-treated cells in flow cytometry and plotted the GFP height over the GFP width, we observed a separate population of specking cells (Figure 3.1C).

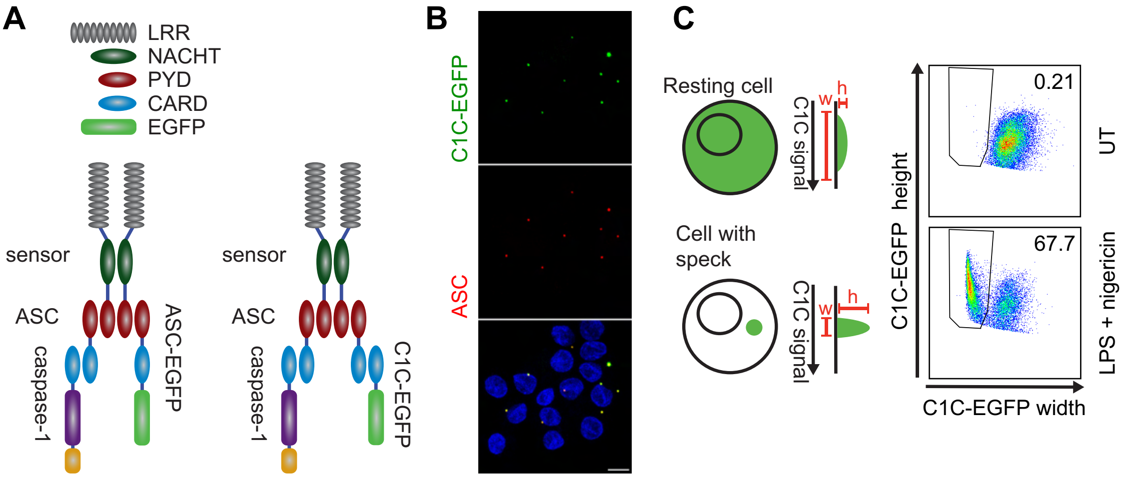

Figure 3.1: C1C-EGFP allows detection of inflammasome assembly. (**A**) Schematic representation of the inflammasome reporters ASC-EGFP and C1C-EGFP. ASC-EGFP binds via PYD interactions to the sensor (or ASC) and C1C-EGFP via CARD interactions to ASC (or caspase-1). (**B**) PMA differentiated THP-1$^{\text{C1C-EGFP(i)}}$ cells were treated with 200 ng/mL LPS for 3 h and 10 µM nigericin for 1 h in the presence of 40 µM VX-765 for 15 minutes before and during nigericin treatment. Endogenous ASC was stained and the cells were recorded by confocal microscopy. Scale bar: 10 µm. (**C**) THP-1$^{\text{C1C-EGFP}}$ cells were differentiated with PMA and treated with LPS and nigericin as in B. UT: untreated. Specking cells were identified by flow cytometry using the altered width and height signal of C1C-EGFP as illustrated.

In contrast to ASC, C1C-EGFP does not bind to most inflammasome sensors and is typically only recruited to existing ASC specks. We therefore expected that its recruitment, and thus the readout, is independent of the upstream sensor. To test this, we stimulated THP-1 cells that inducibly express C1C-EGFP (THP-1$^{\text{C1C-EGFP(i)}}$) for activation of different inflammasome sensors. NLRP3 was activated by priming with LPS stimulation with nigericin (Figure 3.2A). To activate NAIP/NLRC4, we delivered MxiH (*Shigella* needle protein) into the cytosol using the anthrax toxin delivery system: MxiH was fused to the anthrax lethal factor N-terminus (LFn) and administered together with the anthrax protective antigen (PA) (Figure 3.2B). AIM2 was activated by transfecting poly(dA:dT) (Figure 3.2C). For NLRP1, we generated C1C-EGFP-expressing N/TERT-1 keratinocytes (N/TERT-1$^{\text{C1C-EGFP}}$), which endogenously express NLRP1, and treated them with talabostat (also known as Val-boroPro) (Figure 3.2D). Specking cells were quantified by flow cytometry. C1C-EGFP allowed detection of a distinct population of cells with assembled inflammasomes after stimulation of all sensors. As expected, no C1C-EGFP specks were detected after NLRP3 activation in the absence of ASC, but recruitment of C1C-EGFP to ASC specks was observed in the absence of endogenous caspase-1 (Figure 3.2E). To make the reporter available for research in mice, we also generated mouse caspase-1$^{\text{CARD}}$ (mC1C)-EGFP. We introduced this reporter into iMacs, an immortalized mouse macrophage cells line (iMac$^{\text{mC1C-EGFP}}$), and stimulated NLRP3, NAIP1/NLRC4, and AIM2 (Figure 3.2F). All treatments resulted in a robust specking response, confirming the functionality of the reporter system in mouse models.

To study inflammasome responses in the context of virus infections, it is desirable to generate C1C-EGFP reporter viruses that themselves encode and express C1C-EGFP in infected cells. This allows quantification of infection and inflammasome assembly by flow cytometry in the same experiment. As a proof of concept, we infected mouse iMacs with vaccinia virus (VACV) that encoded C1C-EGFP under the control of the early promoter (Tesfamariam *et al.*, manuscript in preparation). Because VACV is a dsDNA virus, we hypothesized that it is detected by AIM2, a known inflammasome sensor for DNA. To induce

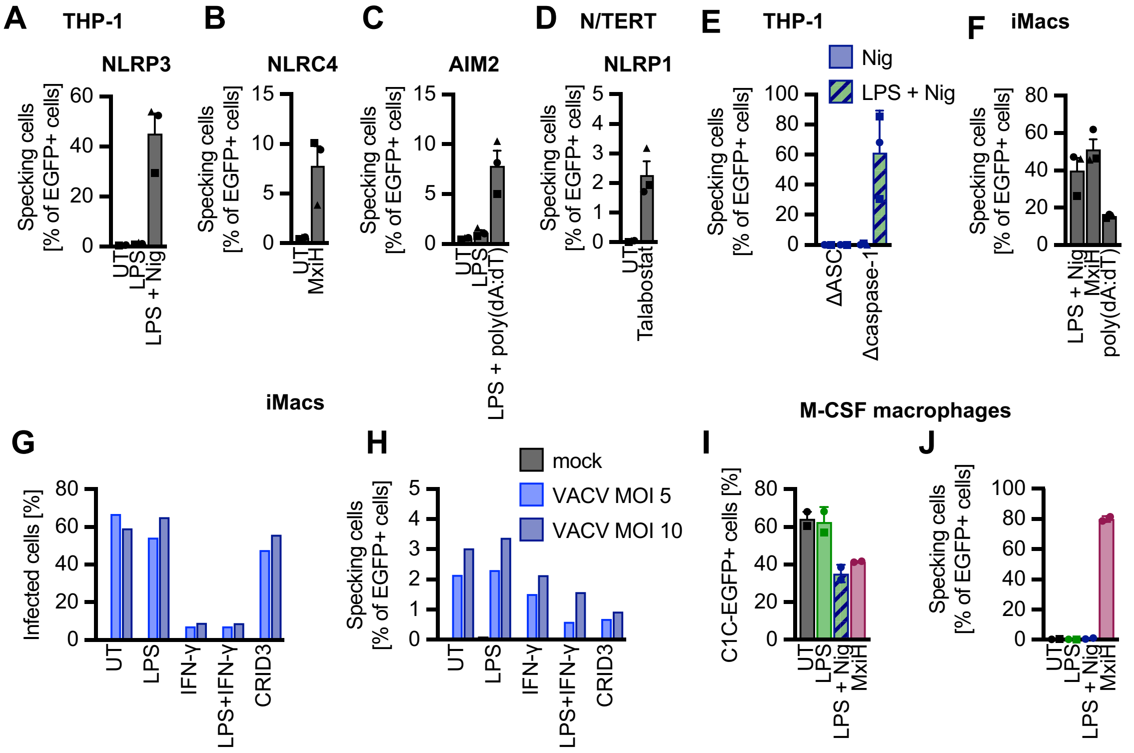

Figure 3.2: C1C-EGFP works for different sensors and cell types. (**A**-**D**) PMA differentiated THP-1$^{\text{C1C-EGFP(i)}}$ cells (A-C) or N/TERT-1$^{\text{C1C-EGFP}}$ keratinocytes (D) were treated as indicated in the presence of 40 µM (A-C) or 100 µM (D) VX-765. The fraction of specking cells was measured by flow cytometry. NLRP3 (A) was activated with 200 ng/mL LPS for 3 h and 10 µM nigericin for 1 h, NLRC4 (B) with 0.1 µg/mL LFn-MxiH and 1 µg/mL PA for 1 h, AIM2 (C) by 3 h LPS pre-treatment, transfection of poly(dA:dT) using Lipofectamine$^{\text{TM}}$ 2000, and another incubation of 4 h, and NLRP1 (D) with 30 µM talabostat for 20 h. (**E**) THP-1$^{\text{C1C-EGFP,}\Delta\text{ASC}}$ or THP-1$^{\text{C1C-EGFP,}\Delta\text{caspase-1}}$ cells were differentiated with PMA and treated with LPS and nigericin as indicated and described in A. (**F**) iMacs$^{\text{mC1C-EGFP}}$ were pre-treated with LPS and then treated as indicated and described before. (**G**-**H**) iMacs were left untreated or pre-treated with 200 ng/mL LPS for 3 h and/or 500 U/mL IFN-γ for 20 h, as indicated. Cells were infected with VACV WR E mC1C-EGFP at MOI 5 or 10 for 20 h in the presence of 100 µM VX-765 and/or 2.5 µM CRID3 15 minutes before, during and after infection as indicated. Cells were analysed by flow cytometry; infection was quantified by C1C-EGFP expression and specking cells were identified as before. (**I**-**J**) Primary human monocytes isolated from buffy coats were differentiated into macrophages with 1 µg/mL M-CSF for 3 days, seeded into 24-well plates (150,000 cells per well), and transduced with 3x concentrated lentivirus containing packaging Vpx-Vpr and encoding pUbC:C1C-EGFP. After 2 days, the cells were treated as indicated in the presence of 40 µM XV-765. Data represents mean values from 3 independent experiments ± SEM.

AIM2 expression in iMacs, we pre-treated them with IFN-γ. Approximately 60 % of the cells were infected (Figure 3.2G) and this number was drastically reduced in IFN-γ treated cells. A small fraction of infected iMacs (~3 %) readily formed specks when infected with VACV (Figure 3.2H). This response could not be enhanced by LPS pre-treatment but was slightly reduced by IFN-γ, which might be connected to the reduced infection after IFN-γ exposure. However, the NLRP3 inhibitor CRID3 (also known as MCC950) inhibited the response, suggesting an involvement of NLRP3. The reporter virus approach is particularly helpful in cells that cannot be genetically manipulated, including many primary cells. However, primary macrophages, which are of particular interest in inflammasome research, can be kept in culture long enough to be genetically manipulated for reporter expression. To demonstrate this, we differentiated primary human monocytes into macrophages using M-CSF. C1C-EGFP was then introduced into the cells by lentiviral transduction and the cells were subsequently treated with either LPS (and nigericin) or MxiH. After transduction, 60 % of the cells expressed C1C-EGFP (Figure 3.2I). This number was reduced to 40 % after the cells were treated with nigericin or MxiH, despite the use of the caspase-1 inhibitor VX-765. We observed that a high frequency of cells assembled an inflammasome in response to MxiH, showing that M-CSF macrophages are capable of forming NAIP/NLRC4 inflammasomes (Figure 3.2J). The cells did not respond to the well-characterised NLRP3 trigger nigericin, even after LPS pre-treatment. This result is very surprising and requires further investigation.

Taken together these results demonstrate that the new C1C-EGFP reporter works robustly to detect inflammasomes by microscopy and flow cytometry. It could be effectively used to detect inflammasome assembly after stimulation of different sensors and in different cell types, including primary cells. In addition, it can be encoded within recombinant viruses to assess the ability of these viruses to activate an inflammasome response.

3.2.2 Caspase-1^{CARD} does not form oligomers by overexpression

When using ASC-EGFP in the past, we noticed that it is prone to produce specks even without specific inflammasome activation. As a result, the choice of the promoter is vital to keep ASC expression low enough to obtain an acceptable background. After extensive use of our C1C based reporters, we never encountered issues with background. While both reporters allow robust inflammasome detection with the right promoter, we aimed to evaluate the different behaviours between the two reporters. We proposed that the proteins exhibit an inherently different propensity to oligomerize in the absence of inflammasome stimuli. To test this hypothesis in a relevant, ASC-expressing cell line, THP-1 monocytes were transduced with lentivirus encoding ASC-EGFP or C1C-EGFP under the control of different constitutive promoters with varying strength. The weakest promoter was the metallothionein promoter (pMT), followed by the ubiquitin C promoter (pUbC). The cytomegalovirus promoter (pCMV) and the elongation factor 1α promoter (pEF1α) drive strong transgene transcription and expression. Transduced cells were differentiated with PMA and rested for two days in the presence of the caspase-1 inhibitor VX-765 in order to not loose specking cells due to pyroptosis. All cells were then harvested and the reporter expression and the fraction of specking cells were measured and evaluated.

ASC-EGFP was highly expressed under the control of pCMV; an expression level much higher compared to all other promoters (Figure 3.3A). Accordingly, a high background of ASC specks was only observed in cells expressing ASC-EGFP under the control of pCMV (Figure 3.3B). The background in all other samples was negligible. C1C-EGFP, on the other hand, exhibited weaker expression with all promoters. The difference was most prominent with pCMV, as C1C-EGFP did not reach the high expression levels that were observed for ASC-EGFP (Figure 3.3A). The difference in expression offers a possible explanation for the tendency of ASC-EGFP to cause background but makes an objective comparison of the proteins capacity to spontaneously form specks much harder.

To assess the spontaneous oligomerization in relation to the expression of the EGFP fusion, we binned cells with similar levels of reporter expression (GFP-A) and analysed the fraction of cells with specks in each bin (Figure 3.3C). The bins are labelled with their respective upper limit. Figure 3.3D shows the count of cells in each bin on the left ordinate (green) and the respective specking frequency on

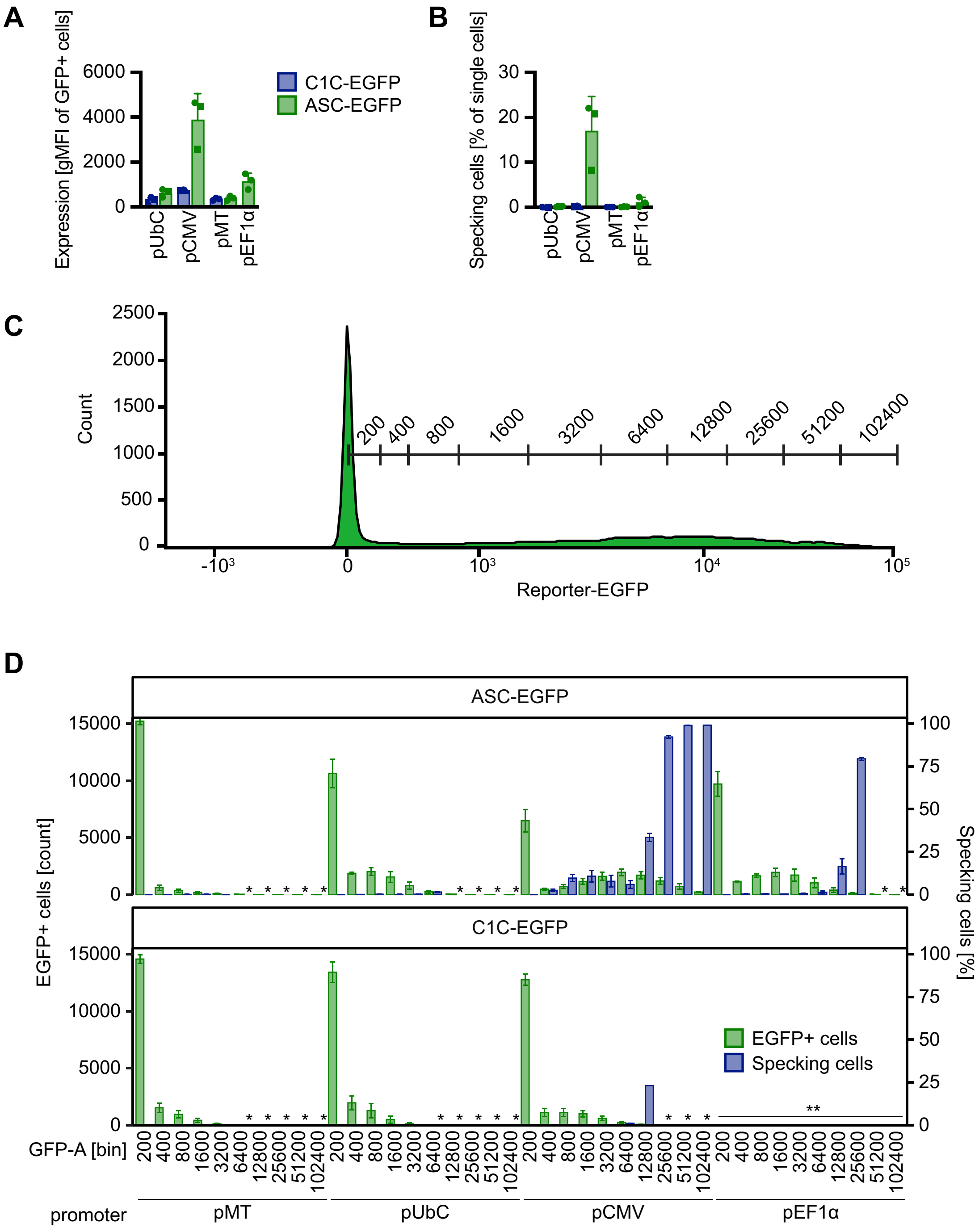

Figure 3.3: C1C-EGFP does not cause relevant background. WT THP-1 cells were transduced with lentivirus encoding ASC-EGFP or C1C-EGFP under the control of different constitutive promoters for 6 h and directly differentiated with PMA overnight without selection. Cells were cultivated for 24 h in the presence of 100 µM VX-765 and expression of ASC-EGFP or C1C-EGFP and the fraction of specking cells was measured by flow cytometry. (**A**) Geometric mean of ASC-EGFP or C1C-EGFP fluorescence intensity (gMFI) of EGFP-positive cells. (**B**) Overall fraction of specking cells. (**C**) Binning strategy of expression levels based on fluorescence intensity. The number indicates the upper limit of the respective bin. (**D**) Expression of ASC-EGFP or C1C-EGFP and the respective fraction of specking cells for each expression bin. *: The fraction of specking cells was excluded because the bin contained less than 100 events. **: Experiment not conducted. Data represents mean values from 3 independent experiments ± SEM.

the right ordinate (blue). To obtain robust results, the specking cells were only considered in bins with at least 100 cells. The green bars represent a histogram for the distribution of reporter expression for each promoter. While in most samples the expression was restricted to lower levels (*i.e.* <6400 GFP-area), pCMV and to a lesser extent pEF1α caused a considerable amount of cells to reach ASC-EGFP expression levels over 6400. At around this expression threshold, a low frequency of specks could be observed with both reporters. Almost all cells with an expression level of higher than 12800 formed specks. However, such high expression levels could only be reached for ASC-EGFP. On the other hand, the only fraction with a considerable amount of C1C-EGFP specks (~20 %) was found in the pCMV sample, but was negligible due to the small number of cells in that bin. Surprisingly, ASC-EGFP expressed under the control of pCMV caused a relevant frequency (~15 %) of specks also in lower bins (400-6400).

The occurrence of non-specific specks largely depended on the reporter expression. For most samples, it appeared there was a threshold at approximately 6400 where specking occurred. While this observation held true for both reporters, C1C-EGFP was only expressed at levels above this background in a few outlying cells. Thus, it appeared that the main reason for the low background of C1C-EGFP is due to its inability to be expressed at high levels in THP-1 cells. The capacity of ASC-EGFP to induce non-specific specks is dependent on the promoter choice, but this can be managed. Although the lower bins (400-6400) were populated by three different promoters, only pCMV caused ASC-EGFP specks to occur in these bins. The fact that those specks did not appear with other promoters at the same expression levels precludes those expression levels to be sufficient for causing specks. More likely, they are somehow connected to the prevalence of other cells in the same sample that speck due to extreme overexpression.

In summary, ASC-EGFP and C1C-EGFP have a similar inherent propensity to polymerize upon reaching a certain threshold concentration. This concentration is only reached for ASC-EGFP when expressed from some promoters, particularly pCMV. In contrast, C1C-EGFP almost never exceeded this threshold even via transcription from strong promoters, but sufficient expression was observed via the use of all promoters assessed. This makes the use of C1C-EGFP much less sensitive to promoter choices compared to ASC-EGFP.

3.2.3 C1C-EGFP does not interfere with inflammasome signalling

C1C-EGFP is recruited to inflammasomes using the same interactions as caspase-1 itself, which raises the question of whether it competes with caspase-1 for recruitment and thereby hampers its recruitment and activation. To assess this, we compared WT THP-1 macrophages with THP-1$^{\text{C1C-EGFP}}$ and THP-1$^{\text{C1C-EGFP(i)}}$. We observed that the fraction of C1C-EGFP positive cells after induction was comparable to the constitutive expression under all conditions evaluated (Figure 3.4A). We next determined LPS-mediated activation of TLR4 by measuring tumor necrosis factor α (TNF-α) secretion, and observed that cytokine secretion, and thus LPS priming, was not impaired in any cell line (Figure 3.4B). All cells expressing C1C-EGFP, whether induced or constitutive, showed assembled specks after treatment with nigericin and MxiH (Figure 3.4C). The inflammasome response to nigericin was stronger after LPS priming as described. The amount of released IL-1β into the medium was comparable between all cell lines and, most importantly, not reduced by the expression of C1C-EGFP (Figure 3.4D). Furthermore, the frequencies of specking cells and the

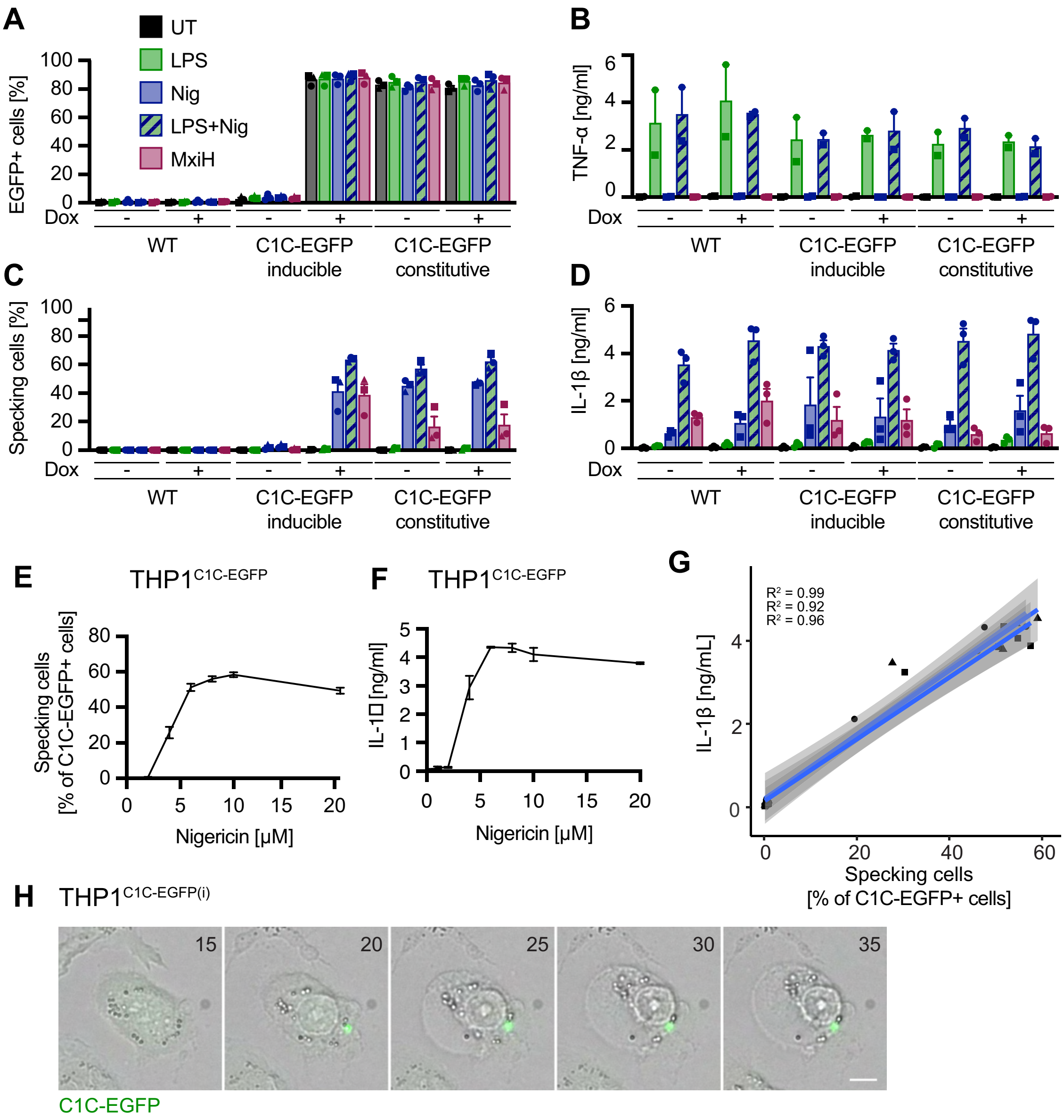

Figure 3.4: C1C-EGFP does not interfere with inflammasome signalling. (**A-D**) PMA differentiated WT THP-1, THP-1$^{C1C\text{-}EGFP}$, or THP-1$^{C1C\text{-}EGFP(i)}$ were treated with 200 ng/mL LPS for 3 h and 10 µM nigericin or with 0.1 µg/mL LFn-MxiH and 1 µg/mL PA and for 1 h. Cells for flow cytometry (A,B) were stimulated in the presence of 40 µM VX-765. The fraction of C1C-EGFP positive cells (A) and specking cells (B) was quantified by flow cytometry. TNF-α secretion after LPS treatment (C) and IL-1β release after nigericin treatment (D) were measured by HTRF after LPS treatment. (**E**-**G**) PMA differentiated THP-1$^{C1C\text{-}EGFP}$ were treated with 200 ng/mL LPS for 3 h and indicated concentrations of nigericin for 1 h. Cells for flow cytometry (E) were stimulated in presence of 40 µM VX-765. The fraction of specking cells was quantified by flow cytometry (E) and secreted IL-1β quantified by HTRF (F). The linear correlation for 3 independent experiments with confidence band 0.95 is plotted in (G). (**H**) PMA differentiated THP-1$^{C1C\text{-}EGFP(i)}$ cells were treated with 200 ng/mL LPS for 3 h and 10 µM nigericin. Live cells were recorded using widefield microscopy. The number indicates the time point in minutes. Scale bar: 50 µm. Data represents mean values from 3 independent experiments ± SEM (2 for C).

respective IL-1β release correlated in response to the same treatments. A difference was observed when the cells were treated with nigericin without LPS-priming. While specking showed a robust inflammasome response, IL-1β release was reduced, probably due to limited pro-IL-1β expression in the absence of LPS stimulation. This highlights an advantage of assessing inflammasomes on the basis of assembly, as it does not depend on the upregulation of pro-IL-1β.

To assess the correlation between specking frequency and IL-1β release, we treated THP-$1^{\text{C1C-EGFP}}$ cells with LPS and different concentrations of nigericin to obtain responses of varying intensity (Figure 3.4E-G). A robust inflammasome activation was observed with 4 µM nigericin and plateaued at around 10 µM (our standard working concentration). A linear regression between the fraction of specking cells and IL-1β resulted in a good correlation with R^2 of well over 90 % (Figure 3.4G). This result indicates that the amount of cytokine secreted is primarily dependent on the number of responding cells rather than the strength of individual responses.

Ultimately, the formation of inflammasomes leads to pyroptosis, which is associated with swelling of the affected cells due to the influx of water through GSDMD pores. Using live-cell imaging, we also show that specking cells undergo pyroptosis in the presence of C1C-EGFP (Figure 3.4H). This also highlights the possibility to use the reporter in living cells to investigate the dynamics of inflammasome signalling.

In summary, we show that the detection of ASC specks via C1C-EGFP is a robust method to detect inflammasome signalling that does not interfere with the pathway and is consistent with well-established methods like cytokine measurement.

3.2.4 C1C-EGFP represents the recruitment of caspase-1, which forms filaments in living cells

In contrast to ASC-based reporters, C1C-EGFP not only indicates the formation of ASC specks, but also serves as a model for caspase-1 recruitment. C1C can assemble into helical filaments *in vitro* using three asymmetric interfaces for CARD:CARD interaction (Lu *et al.*, 2016). In such filaments, each C1C subunit interacts with six neighbouring subunits in three types of interfaces (type I, II, III, Figure 3.5A). The end of the filament proximal to the nucleation seed is termed a-end, while the distal elongating end is termed b-end. Each subunit is recruited via its a-side and recruits further subunits via its b-side. However, it is currently unclear whether these filaments also occur within intracellular ASC specks, as they have thus far only been studied using recombinant protein. Recent reviews either assume that caspase-1 dimerizes through CARD dimers or proximity; or extrapolate from *in vitro* data that caspase-1 indeed polymerizes through CARD filaments (Figure 3.5, model A and B). C1C-EGFP provides an experimental setup to assess this question in intact cells.

To investigate the involvement of potential C1C assemblies in living cells, we generated mutants of C1C-EGFP that are defective in different interaction interfaces. As the Ia interface is necessary for the interaction with ASC$^{\mathrm{CARD}}$, we expected the Ia defective mutant (R10E K11E) not to be recruited to ASC specks. For mutants that are defective in their type b interfaces (Ib: D27R E28R, IIb: Y82E) we expected that they are still recruited to ASC specks, because those interfaces are not involved in the interaction with ASC$^{\mathrm{CARD}}$, but they cannot recruit further C1C subunits in a potential growing filament (Lu *et al.*, 2016). In the possible case that caspase-1 forms filaments on ASC specks, which is so far speculative, we would expect the type b mutants to terminate (cap) those filaments and thus limit caspase-1 recruitment and processing (Figure 3.5B, model B, right).

We treated THP-1 macrophages expressing the different mutants of C1C-EGFP with LPS and nigericin, immune-stained endogenous ASC and imaged the cells

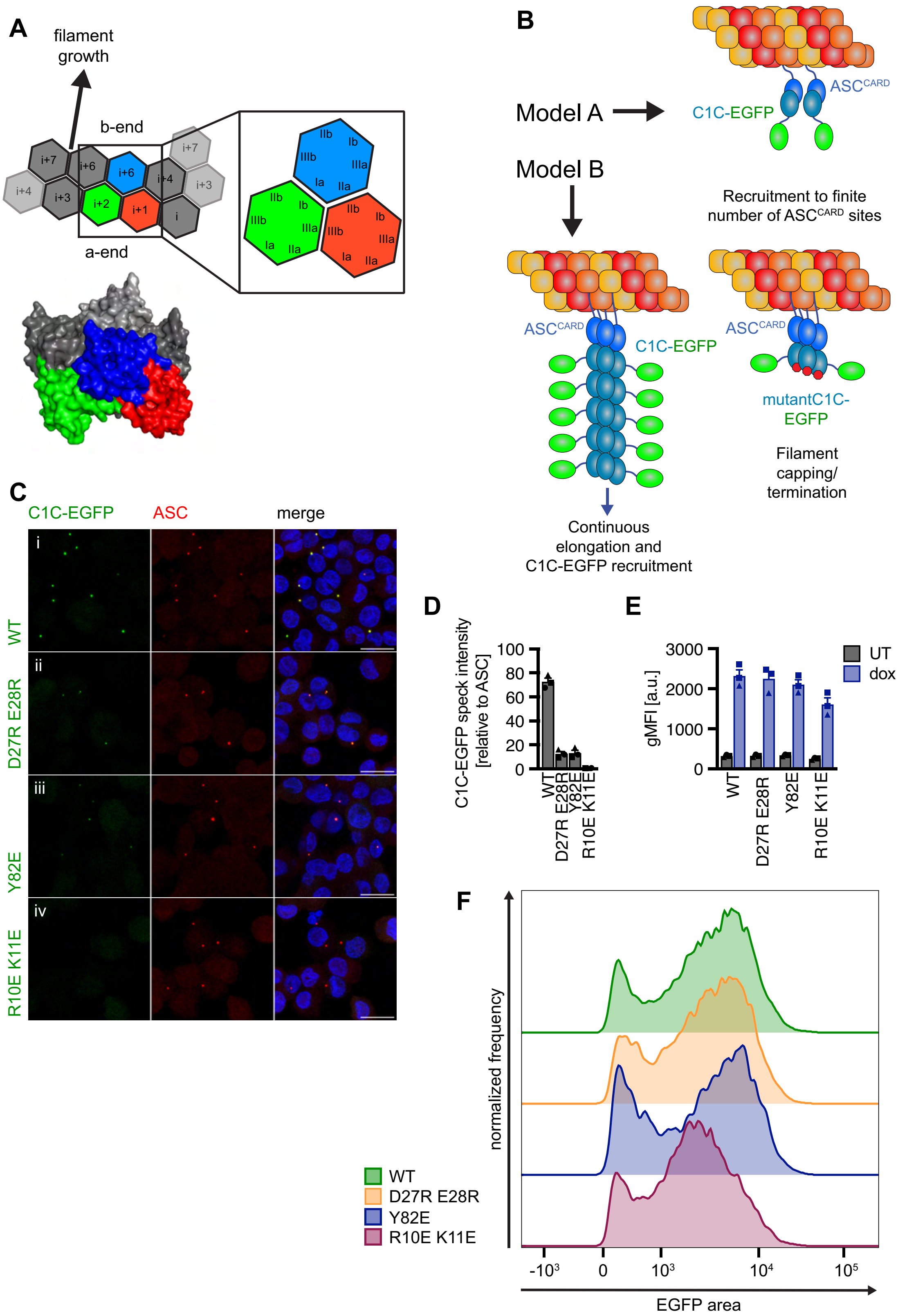
A
filament growth
b-end
a-end
i+7
i+6
i+6
i+4
i+4
i+3
i+3
i+2
i+1
i
i+7
IIb
Ib
IIIb
IIIa
Ia
IIa
B
Model A
Model B
ASC^CARD
C1C-EGFP
Recruitment to finite number of ASC^CARD sites
ASC^CARD
C1C-EGFP
ASC^CARD
mutantC1C-EGFP
Filament capping/ termination
Continuous elongation and C1C-EGFP recruitment
C
C1C-EGFP
ASC
merge
i
ii
iii
iv
WT
D27R E28R
Y82E
R10E K11E
D
C1C-EGFP speck intensity [relative to ASC]
100
80
60
40
20
0
WT
D27R E28R
Y82E
R10E K11E
E
gMFI [a.u.]
3000
2000
1000
0
UT
dox
WT
D27R E28R
Y82E
R10E K11E
F
normalized frequency
EGFP area
-10³
0
10³
10⁴
10⁵
WT
D27R E28R
Y82E
R10E K11E

Figure 3.5: Caspase-1 is recruited to inflammasomes as filaments. (**A**) Schematic representation of interaction interfaces within a C1C filament. Generated after Lu *et al.* (2016). Structure: PDB 5FNA. (**B**) Illustration of the models for caspase-1 recruitment. Capping mutations (red octagons) are predicted to terminate filaments in model B. (**C**) PMA differentiated THP-1$^{C1C-EGFP(i)}$ or comparable cell lines inducibly expressing the indicated C1C-EGFP mutants were induced with doxycycline and the next day treated with 200 ng/mL LPS for 3 h and 10 µM nigericin for 1 h in the presence of 40 µM VX-765 15 minutes before and during stimulation. Endogenous ASC was stained and Z-stacks of cells were recorded by confocal microscopy. Scale bars: 20 µm. (**D**) ASC specks were detected by Imaris based on the staining of endogenous ASC. For WT, D27R E28R, Y82E, and R10E K11E a total of 255, 362, 287, and 293 specks were analysed, respectively. The sum intensity of C1C-EGFP was measured in each speck and normalized to the respective ASC intensity. (**E**-**F**) The expression of C1C-EGFP was induced in the cell lines used in (C), and the expression was measured by flow cytometry. Data represents mean values from 3 independent experiments ± SEM.

using confocal microscopy (Figure 3.5C). While ASC specks were readily observed in all cell lines, prominent C1C specks were only found with WT C1C (Figure 3.5C i). For the Ia mutant (R10E K11E) no C1C-EGFP recruitment was visible (Figure 3.5C iv). The Ib (D27R E28R) and IIb (Y82E) mutants still resulted in C1C-EGFP specks, although they were much smaller and of weaker intensity (Figure 3.5C ii, iii), indicating lower recruitment levels. We used Imaris software to quantify the results as follows: we identified ASC specks based on the staining and defined ‘spots’ (volumes of interest) around each speck. Then, we measured the total intensity of C1C-EGFP in each ‘spot’ and normalized it to the respective ASC intensity to quantify the amount of C1C that was recruited in relation to ASC (Figure 3.5D). WT C1C-EGFP led to a prominent signal within the specks, representing full recruitment. As apparent from the images, this signal was completely abolished in the Ia mutant. The speck intensity of the capping mutants, which are mutated in the b interfaces, were drastically reduced compared to the WT and were thus recruited to a much lesser extent (Figure 3.5D). These differences cannot be attributed to differences in expression (Figure 3.5E,F) and must therefore result from different recruitment behaviours.

As mutations in the type b interfaces are expected to only impair filament formation, but not interaction with ASC, we conclude that the strong WT C1C-

EGFP signal arises from filaments with many C1C-EGP molecules per ASC^{CARD}. The C1C-EGFP signal from capping mutants is diminished as a result of filament termination. These data strongly support model B (Figure 3.5B), in which caspase-1 is recruited to inflammasomes in the form of growing filaments.

3.2.5 C1C filaments are a target for regulation by CARD17

The CARD only protein (COP) CARD17 (also known as INCA) is a naturally occurring variant of C1C, which is unable to form filaments and thus resembles the capping mutants of C1C (D27R E28R, Y82E). Assuming that filaments play a role in inflammasome signalling, CARD17 would have the capacity to terminate those filaments and thereby suppress caspase-1 recruitment and activation (Figure 3.6A).

We generated THP-1 cell lines that express C1C-mCherry from an inducible promoter either alone (THP-1$^{C1C\text{-}mCherry(i)}$) or in combination with constitutive expression of CARD17-EGFP (THP-1$^{C1C\text{-}mCherry(i)+CARD17\text{-}EGFP}$) or CARD17 R55E-EGFP (THP-1$^{C1C\text{-}mCherry(i)+CARD17\ R55E\text{-}EGFP}$), a mutant of the type Ia interface that is recruitment deficient (Lu *et al.*, 2016). We then treated these cells with LPS and nigericin and quantified the fraction of specking cells by flow cytometry (Figure 3.6B). We could not detect any C1C-mCherry specks in the presence of WT CARD17, whereas the mutant CARD17 did not affect C1C-mCherrry speck formation. However, when we recorded the cells by microscopy, we found that C1C-mCherry was still recruited to ASC specks in the presence of CARD17 (Figure 3.6C). These specks, however, were much smaller, which probably limits their detection by flow cytometry. Therefore, we used the microscopy-based approach outlined above to quantify C1C-mCherry intensity at the ASC speck. We found that almost all ASC specks were also positive for C1C-mCherry, *i.e.* above a threshold of 1000. This was only very slightly reduced in the presence of CARD17 (Figure 3.6D). However, the intensity of C1C-mCherry per ASC and thus the number of recruited molecules was drastically reduced in the presence of CARD17, probably as a result of CARD17-mediated filament termination

(Figure 3.6E). A small amount of CARD17-EGFP was also recruited to the specks.

We then asked whether CARD17 can inhibit cytokine release via this mechanism and measured IL-1β in the supernatants of the cells (Figure 3.6F,G). Along with reduced C1C-mCherry recruitment to ASC specks, IL-1β release was reduced to

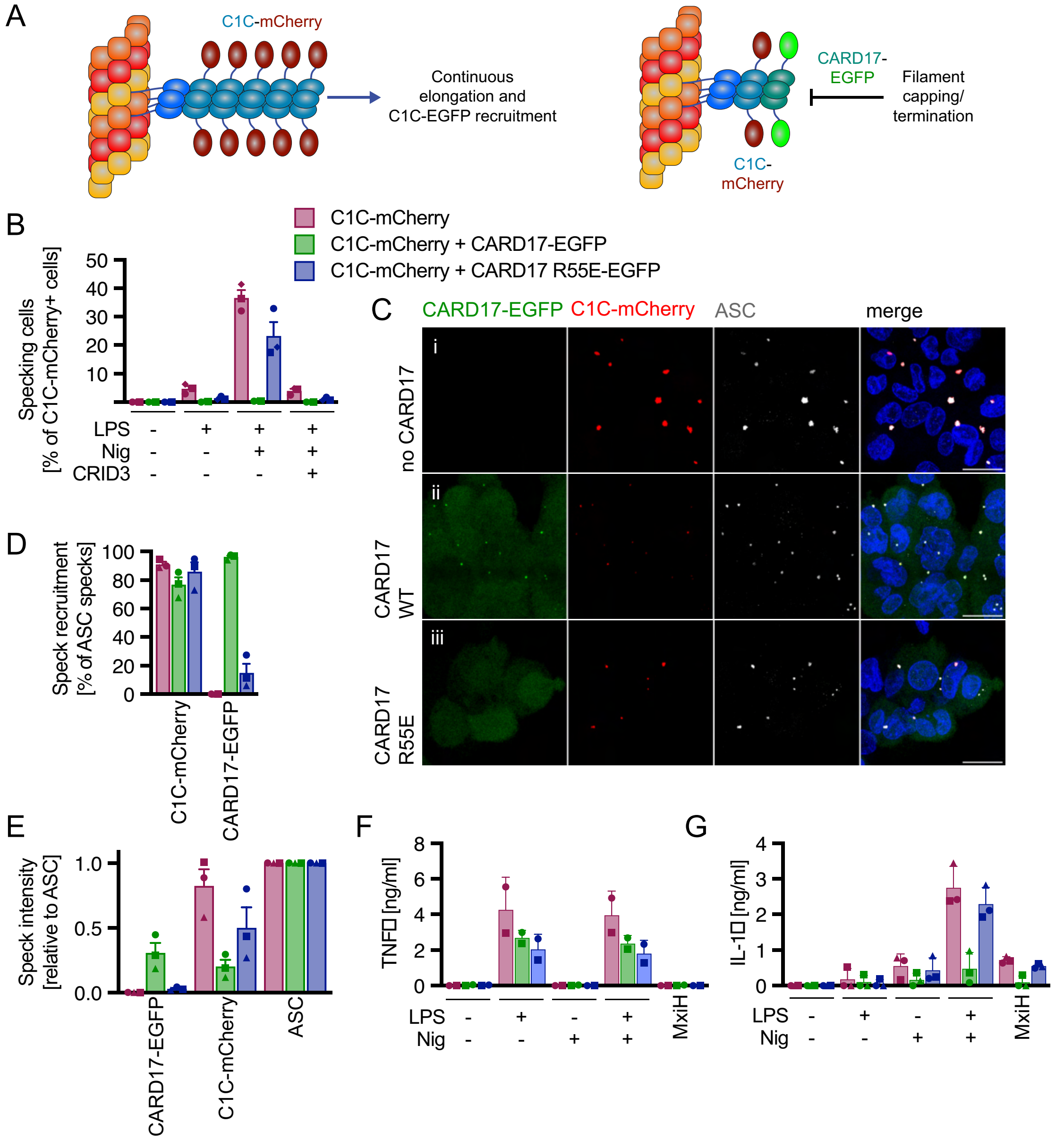

Figure 3.6: CARD17 inhibits caspase-1 by terminating filaments. (**A**) Illustration of the model for CARD17-mediated termination of C1C filaments. (**B**) PMA differentiated THP-1$^{C1C\text{-}mCherry}$, THP-1$^{C1C\text{-}mCherry+CARD17\text{-}EGFP}$, or THP-1$^{C1C\text{-}mCherry+CARD17\ R55E\text{-}EGFP}$ cells were treated with 200 ng/mL LPS for 3 h and 10 µM nigericin for 1 h in the presence of 40 µM VX-765 and where indicated 2.5 µM CRID3. The fraction of specking cells was measured by flow cytometry. (**C**) Cells were treated with LPS and nigericin as in (B), endogenous ASC was stained, and Z-stacks were recorded by confocal microscopy. Representative maximum intensity projections are shown. Scale bars: 20 µm (**D**-**E**) ASC specks from C were identified by Imaris based on the staining of endogenous ASC. For THP-1$^{C1C\text{-}mCherry}$, THP-1$^{C1C\text{-}mCherry+CARD17\text{-}EGFP}$, and THP-1$^{C1C\text{-}mCherry+CARD17\ R55E\text{-}EGFP}$ a total of 1282, 1713, and 944, specks were analysed, respectively. The fraction of ASC specks that were positive for C1C-mCherry or CARD17-EGFP (sum intensity $\geq$ 1000) was calculated (D). The sum intensity of C1C-mCherry and CARD17-EGFP was measured in each speck and normalized to the respective ASC intensity (E). (**F-G**) Cells were treated with LPS for 3 h and TNF-α in the supernatant was measured by HTRF (F). The cells were then treated with 10 µM nigericin or with 0.1 µg/mL LFn-MxiH and 1 µg/mL PA for 1 h. IL-1β released into the supernatant was measured by HTRF (G). Data represents mean values from 3 independent experiments ± SEM (2 for G).

a similar extent, revealing a mechanism for modulating inflammasome signalling downstream of ASC polymerization.

In summary, we describe a mechanism for inflammasome inhibition by CARD17: effective caspase-1 recruitment and activation relies on the formation and growth of caspase-1 filaments. CARD17 terminates those filaments and thus limits caspase-1 recruitment, activation, and IL-1β release. These findings also demonstrate that fluorescently labelled caspase-1^{CARD} is a powerful tool to investigate the molecular mechanisms of inflammasome signalling, as it not only indicates the formation of inflammasomes but also the recruitment of caspase-1.

3.2.6 C1C-EGFP can indicate ASC-independent caspase-1 recruitment

In some instances, caspase-1 can be recruited and activated in the absence of ASC. One example is NLRC4, which has its own CARD and can thus bind caspase-1 directly without the adapter ASC. Another CARD containing protein is CARD8, which closely resembles the active fragment of NLRP1 (UPA-CARD). Both proteins can be activated by the chemical talabostat. Consequently, responses to talabostat cannot be attributed to one or the other if both are expressed. However, CARD8 recruits caspase-1 directly and cannot bind ASC (Schmidt lab, unpublished data). NLRP1, on the other hand, was reported not to interact with caspase-1 directly (Ball *et al.*, 2020; Hollingsworth, Liron, *et al.*, 2021; Gong *et al.*, 2021). We have previously shown that our new reporter allows us to visualise ASC-independent caspase-1 recruitment in the form of C1C-EGFP filaments. Thus, to study the interaction of NLRP1 and CARD8 with C1C in the absence of ASC, we generated HEK 293 cells expressing either of these sensors together with C1C-EGFP (HEK$^{\text{NLRP1-SH(i)+C1C-EGFP}}$, HEK$^{\text{CARD8-SH(i)+C1C-EGFP}}$), treated them with talabostat and analysed them by confocal microscopy (Figure 3.7A,B) and flow cytometry (Figure 3.7C-D). Filaments can be quantified by flow cytometry in the same way as specks, even though the populations are not as well separated. As expected, CARD8 formed filaments together with C1C-EGFP (Figure 3.7A-D). To our surprise and in contrast to the previous reports, we found that also NLRP1 can also induce caspase-1 filament formation, albeit to a lesser extent than CARD8 (Figure 3.7A-D).

N/TERT-1 keratinocytes naturally express NLRP1, but not CARD8 (Bauernfried *et al.*, 2021), and form inflammasomes to different triggers, including talabostat and anisomycin (Jenster *et al.*, 2023). Anisomycin inhibits peptide bond formation during protein synthesis, causing ribosome stalling. This induces the ribotoxic stress response, which leads to the activation of the mitogen-activated protein (MAP) kinase cascade and ultimately NLRP1 (Vind *et al.*, 2020; Robinson *et al.*, 2022; Jenster *et al.*, 2023). When we recorded NTERT-1$^{\text{C1C-EGFP}}$ keratinocytes by microscopy, we observed that even though most NLRP1-induced specks contained ASC, they regularly gave rise to specks with varying degrees of protruding C1C filaments (Figure 3.7E). Moreover, those were regularly found in the nucleus. The filamentous nature of C1C raises the question whether the filamentous specks in keratinocytes might be an artifact of the reporter. Therefore, we treated HEK 293T cells expressing NLRP1 and ASC-EGFP (HEK$^{\text{NLRP1-HA+ASC-EGFP}}$) with talabostat and examined the resulting specks by confocal microscopy. We found that ASC-EGFP likewise forms specks with

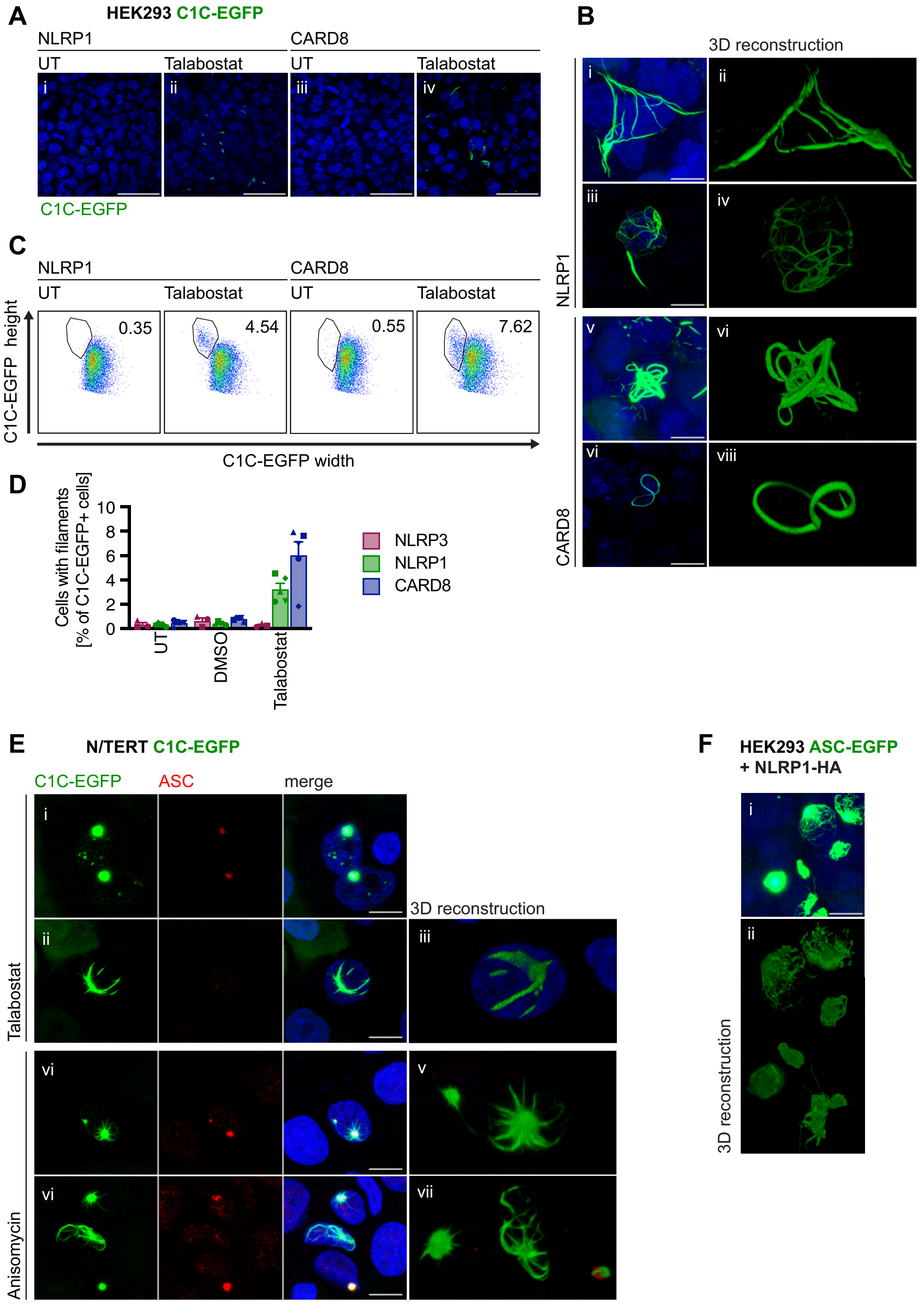
A
HEK293 C1C-EGFP
NLRP1
CARD8
UT
Talabostat
UT
Talabostat
i
ii
iii
iv
C1C-EGFP
B
3D reconstruction
i
ii
iii
iv
NLRP1
v
vi
vi
viii
CARD8
C
NLRP1
CARD8
UT
Talabostat
UT
Talabostat
0.35
4.54
0.55
7.62
C1C-EGFP height
C1C-EGFP width
D
Cells with filaments [% of C1C-EGFP+ cells]
10
8
6
4
2
0
UT
DMSO
Talabostat
NLRP3
NLRP1
CARD8
E
N/TERT C1C-EGFP
C1C-EGFP
ASC
merge
i
ii
3D reconstruction
iii
Talabostat
vi
v
vi
vii
Anisomycin
F
HEK293 ASC-EGFP + NLRP1-HA
i
ii
3D reconstruction

Figure 3.7: C1C-EGFP can detect ASC-independent inflammasomes. (**A**,**B**) $HEK^{NLRP1\text{-}SH(i)+C1C\text{-}EGFP}$ or $HEK^{CARD8\text{-}SH(i)+C1C\text{-}EGFP}$ cells were treated with 30 µM talabostat for 20 h. Z-stacks of cells were recorded by confocal microscopy and representative maximum intensity projections are shown (A,B). The fraction of cells forming C1C-EGFP filaments was quantified by flow cytometry using a similar gating strategy as for specks (C,D). The error bars represent the SEM of 5 independent experiments. (**E**) $NTERT\text{-}1^{C1C\text{-}EGFP}$ keratinocytes were treated with 30 µM talabostat for 20 h or with 15 µM anisomycin for 6 h in the presence of 100 µM or 40 µM VX-765, respectively. Z-stacks were recorded by confocal microscopy. (**F**) $HEK^{NLRP1\text{-}HA+ASC\text{-}EGFP}$ cells were treated with 30 µM talabostat for 20 h in the presence of 100 µM VX-765. Z-stacks were recorded by confocal microscopy. All images are maximum intensity projections. All 3-dimensional reconstructions (B ii, iv, vi, viii, E iii, v, vii, F ii) were generated with Leica Application Suite X. Scale bars: A: 50 µm, B, E, F: 10 µm

protruding filaments in the context of NLRP1 (Figure 3.7F). It is therefore tempting to speculate that this rather unconventional inflammasome morphology might somehow be connected to NLRP1, although this requires further study at endogenous protein levels.

These observations combined illustrate that C1C-EGFP also allows visualisation of C1C-EGFP filaments directly recruited by CARD-containing NLRs, which will be helpful for further research on proteins like CARD8 that do not employ ASC.

3.3 Discussion

In this chapter, I presented a novel reporter for inflammasome activation. It employs a fluorescent fusion of C1C, which is recruited to assembled inflammasomes. Inflammasomes can thus be localized and quantified using microscopy or flow cytometry without the need for staining. Because specking assays provide a cell-based readout, data can be obtained on a single cell level. Furthermore, the reporter can be used for live-cell imaging to capture the dynamics of inflammasome assembly. Compared to the commonly used ASC-EGFP, C1C-EGFP proved to be less prone to generate background. The reporter is functional in human and mouse cells, including primary cells. Even though C1C-EGFP acts on the level of caspase-1 recruitment and activation, it does not impair downstream signalling. I also demonstrated how the reporter can be used to study the structural details of caspase-1 recruitment and ASC-independent inflammasomes.

3.3.1 Reporting on canonical inflammasomes

The hallmark of canonical inflammasomes is the polymerization of ASC, which in turn recruits caspase-1. C1C-EGFP does not only reveal the mere assembly of an inflammasome, but also reports on the recruitment of caspase-1. Because C1C-EGFP acts downstream of the ASC polymerization, it does not directly interact with sensor molecules in canonical inflammasomes. Therefore, it is not expected to affect the behaviour of the sensor and the initiation of inflammasome assembly. *Vice versa*, the function of C1C-EGFP is independent of the upstream sensor. That C1C-EGFP is recruited to inflammasomes using the same domain interactions as caspase-1 itself raises the question whether it interferes in any way with the function of caspase-1 and its downstream signalling. However, cytokine release was not altered in cells in which C1C-EGFP was expressed constitutively or via an inducible promoter. Cytokine release is a validated and recognised approach to investigate inflammasome signalling, but this readout is dependent on the expression of pro-IL-1β in the target cell. This becomes apparent when observing THP-1 cells that were not TLR4 primed. In this case, we found that only minimal IL-1β was released despite robust inflammasome assembly. Apart from this, the frequency of C1C-EGFP specks correlated well with the release of IL-1β. This demonstrates that specking assays serve as a readout that is equally robust as a well-established method for inflammasome detection. A drawback of bulk readouts like IL-1β release is that they do not indicate how many cells respond to a stimulus. In that case, it is not clear whether differences in IL-1β release result from a different fraction of responding cells or a difference in the strength of the response per cell. Using a range of nigericin concentrations, we observed a close correlation between IL-1β release and the frequency of specking cells, indicating that the amount of IL-1β is mostly dictated by the number of responding cells. This hints at inflammasome signalling as a binary, *i.e.* all-or-nothing, response, which may of course change when additional regulatory elements are at play, as will be discussed later. The outcome of inflammasome signalling also depends on the expression of cytokines and GSDMD, and it may therefore be dependent on the context, for instance the cell type or preceding priming. This consideration is particularly important when studying pathogen-induced inflammasomes, because they may interfere with caspase-1 activity or with cytokine release or signalling, as is the case for poxviruses (Veyer *et al.*, 2017). To enable the detection of inflammasome formation, it is therefore beneficial to detect it as upstream as possible, and it is advisable to include the assembly of inflammasome in investigations of this pathway, *e.g.* by using C1C-EGFP.

The ability to visualise inflammasomes in real-time has several advantages. Firstly, it allows live-cell imaging to capture the dynamics of the processes revolving around inflammasome formation. This is particularly interesting when investigating inflammasomes in functional tissues, as we will explore in the next chapter. Live reporters also offer a way of monitoring the cells during the experiment. This is especially convenient when working with stimuli for which the kinetics are unknown. Moreover, assessing inflammasomes without fixing the cells opens up possibilities for downstream applications. For instance, living cells can be sorted by fluorescence-activated cell sorting (FACS) for subsequent sequencing or for further culture.

3.3.2 Self-assembly of inflammasome reporters

It has been reported that inflammasome components exist in a ‘supersaturated’, nucleation-limited state, which drives rapid polymerization once a nucleation seed is provided, *e.g.* by sensor oligomerization (Rodriguez Gama *et al.*, 2023). This poses the risk of spontaneous polymerization, which increases with increasing protein concentration. When ASC-EGFP is introduced into cells, it adds to the pool of endogenously expressed ASC, increasing the total ASC concentration and the risk of spontaneous assembly. In fact, colleagues and I have experienced specking background with ASC-EGFP previously. This necessitates careful promoter choice and attention to the background. When generating cell lines, selection of clones with low specking background is advised.

This is, however, not possible when transducing primary cells that are not suitable for clonal selection. We simulated this scenario by transducing ASC-EGFP into THP-1 cells for overexpression. Binning of the expression levels revealed that spontaneous specks occurred only when a certain threshold expression was reached. However, this happened only with the strong promoters pCMV and pEF1α, indicating that ASC-EGFP can be used in many scenarios.

A curious observation was the occurrence of specks also in lower expression bins, when ASC-EGFP was expressed under the control of pCMV. Because the equivalent bins in other samples did not show specks, the expression level itself can be precluded as the causative reason. Instead, I concluded that those specks are connected to the prevalence of cells that formed specks due to high ASC-EGFP expression in the same sample. It is conceivable that some cells undergo pyroptosis despite VX-765 treatment and release mediators that activate *bona fide* inflammasomes in bystander cells. It is also possible that specks were released and bound to the outside of other cells. As flow cytometry does not resolve the speck location, a non-specking cell with a bound ASC-EGFP assembly (from a different cell) would be detected as a specking cell itself. Potential differences in promoter kinetics might also explain the occurrence of specking cells with pCMV: If the promoter drives faster gene expression, the protein concentration might have been above a critical threshold for longer, increasing the chance of spontaneous polymerization.

For C1C-EGFP, expression was overall lower, and the specking background was negligible. Only a few outlying cells with very high expression indicated that C1C-EGFP can self-assemble, and that the required threshold concentration is similar to that of ASC-EGFP. Although C1C-EGFP barely reached those high expression levels, the expression with weaker promoters was more comparable between both reporters. This makes the use of C1C-EGFP much less sensitive for promoter choices and better suitable for generating cell lines or transducing primary cells. As demonstrated, C1C-EGFP can also be carried into target cells using recombinant viruses. In this case, the choice of possible promoters is dictated by the virus, and thus, C1C might have an essential advantage over ASC-EGFP in recombinant viruses. Furthermore, when C1C-EGFP is overexpressed in less defined cells in which the expression level of ASC is unknown or by recombinant viruses, it is less likely to induce artifacts compared to ASC-EGFP. In addition, C1C-EGFP artifacts are typically filamentous and can thus be differentiated from real inflammasomes.

It remains to be elucidated why C1C-EGFP cannot be highly overexpressed in THP-1 cells. This is in contrast to HEK cells: in the process of generating lentivirus, HEK cells are transfected with a lentiviral plasmid encoding the transgene. This leads to very strong C1C-EGFP expression and the formation of abundant filamentous C1C-EGFP assemblies, suggesting that the expression is not generally limited. Perhaps, cells that express endogenous caspase-1 employ a mechanism to prevent accumulation of excess caspase-1 to minimize aberrant caspase-1 activity. For example, this could be achieved by regulation on the mRNA level or by post-translational degradation. If caspase-1 is targeted by such a mechanism via its CARD, C1C-EGFP would also be affected. Another interesting difference between THP-1 and HEK cells is that C1C-EGFP overexpressed in HEK cells can assemble into filaments. In contrast, the few assemblies I observed in THP-1 cells were spherical specks. ASC filaments are coated in CARDs, which cause cross-linking via homotypic CARD interactions and condensation into the characteristic speck-like inflammasome. Caspase-1 or C1C-EGFP lack a second DFD and thus the ability to form condensed specks. It is unclear how C1C-EGFP overexpression can cause specks specifically in THP-1 cells, but I suggest that it is connected to the presence of ASC. Rodriguez Gama *et al.* (2023) systematically tested which DFDs can seed assemblies of other DFDs in an ortholog expression system. They reported that C1C can seed ASC assemblies. It is thus conceivable that the occurrence of specks instead of filaments could be explained by endogenous ASC, which is seeded into specks by existing C1C-EGFP filaments.

3.3.3 Caspase-1 filaments and their implications for inflammasomes

As mentioned earlier, C1C-EGFP is a model for the recruitment of caspase-1. This allowed me to address the open question regarding the exact mode of caspase-1 recruitment. As described in 1.1.2 (Figure 3.5B), there are two competing models of how caspase-1 is recruited to the inflammasome. Model A describes the direct recruitment of caspase-1 to ASC^{CARD} on existing ASC filaments. Because the recruitment sites are already clustered, this would increase the local concentration of caspase-1 and drive its dimerization, which is the minimal requirement for activation. In model B, recruitment occurs along growing caspase-1 filaments, which emanate from ASC filaments. Ultimately, filaments are another way to increase local caspase-1 concentration, leading to dimerization of its catalytic domain. It has been shown that complexes of ASC and caspase-1 filaments can form *in vitro* (Lu *et al.*, 2014), and the structure of C1C filaments has been solved (Lu *et al.*, 2016). However, all these assemblies have only been observed *in vitro* using purified proteins. They have thus far not been demonstrated to form with endogenous proteins in living cells.

Based on the structure of C1C filaments, we incorporated mutations into C1C-EGFP that render it unable to form these filaments, while retaining its capability to be recruited to ASC. These capping mutants were recruited to the ASC specks to a substantially reduced extent, implying that the majority of C1C recruitment depends on filament formation. To my knowledge, this is the first data that directly support caspase-1 filament formation on true inflammasomes in living cells. It has to be noted, however, that this experiment deviates from the unperturbed situation in several ways: 1) In order to stain and image the cells, we used a caspase-1 inhibitor, which prevents CDL cleavage trapping endogenous caspase-1 on the speck. The C1C-EGFP reporter should not be affected by this, because it lacks enzymatic activity as well as a cleavage site. 2) EGFP has a tendency to dimerize, which might stabilise C1C filaments. However, we see specks of similar size if the reporter contains mCherry, BFP, or emiRFP instead of EGFP and the same is true if the labelling tags Halo and SNAPf are used. My mutant experiments suggest that the speck size is determined by the ability of the

CARD to oligomerize. It thus is rather unlikely that all these tags induce C1C filament formation in a similar manner. It cannot be ruled out that the tags contribute to length, stability and life time of the filaments. The fusion partner is also likely to have steric effects that might alter the architecture of the inflammasome assembly. 3) My experiments rely on endogenously expressed NLRP3 and ASC, whereas C1C-EGFP is expressed ectopically. The current model describes inflammasomes as lattice of PYD and CARD filaments. The length and number of each type of filament likely depends on the abundance of the respective protein domains within the cell. In that regard, the introduction of C1C-EGFP changes the stoichiometry in favour of C1C, which probably supports greater CARD filament length. Overall, C1C-EGFP is a robust tool to detect speck formation and its ability to polymerize caspase-1. It also provides strong indications for the existence of caspase-1 filaments in inflammasome assemblies. It does, however, not provide information on further details about the architecture of an endogenous speck, such as lengths, ratios and lifetime of filaments. In order to formally prove model B, further experiments would have to be performed with endogenous full-length caspase-1. In that case, the mutations to disrupt the interaction interfaces would have to be introduced using genome editing of the caspase-1 locus. Since my results could be predicted based on model B, the respective *in vitro* experiments, and the structure of C1C filaments, they strongly support model B. I will thus use it as a basis for future considerations.

The most important implication of caspase-1 filaments is the possibility of infinite recruitment. Active caspase-1 eventually inactivates itself through CDL cleavage and subsequent dissociation as described by Boucher *et al.* (2018). The authors deduce a model for an inherent caspase-1 limitation and propose that the amount of caspase-1 activation depends on the number of available recruitment sites, *i.e.* the size of the inflammasome, which in turn depends on cellular factors such as the amount of ASC expression. According to their model, caspase-1 will be inactivated shortly after CDL cleavage, leaving behind the CARD portion, which blocks the recruitment site and prevents further caspase-1 recruitment and activation. In the case of continuous caspase-1 filament formation, however, every recruited molecule will generate a new recruitment site. Caspase-1 activation would be only limited by the supply of caspase-1 but not the size of the ASC assembly. Indeed, it was reported that caspase-1 is over-stoichiometric in NLRP3 inflammasomes in THP-1 cells (Lu *et al.*, 2014). Eventually, all available caspase-1 molecules could be activated, again indicating that inflammasomes are an all-or-nothing response. This also provides an explanation why C1C-EGFP does not interfere with cytokine release, independently from whether the recruitment sites on ASC are limited. A practical advantage of the independency of C1C-EGFP from the size of the inflammasome becomes apparent in cells that express only low amounts of ASC. Small specks are hard to resolve with flow cytometry. Lea Jenster (Schmidt lab, Bonn, personal communication) found that the low amount of ASC in T cells resulted in poor resolution of specking cells after staining of endogenous ASC. C1C-EGFP drastically improved speck detection by flow cytometry, probably because its recruitment is not restricted by the small ASC assembly. This would also be relevant in neutrophils, as they express considerably less ASC and form smaller inflammasomes compared to macrophages (Boucher *et al.*, 2018).

3.3.4 The role of COPs

So far, all my data point towards a binary nature of inflammasome signalling, as the inflammasome activation inevitably leads to full polymerization of all participating proteins. This very polymerization can, however, be a target for regulation itself. Lu *et al*. (2016) proposed the following mechanism for regulation of inflammasomes: CARD17, because it lacks functional type b interfaces, can terminate caspase-1 filaments through a capping mechanism. This mode of action was recapitulated and extended within cells during my experiments: the expression of CARD17 reduced the amount of recruited C1C-mCherry to a similar extent as the C1C capping mutations. Importantly, the reduction of the recruitment also translated into a reduction of IL-1β release, implying that also endogenous caspase-1 is affected by this mechanism. CARD17, thus, provides a context in which the caspase-1 recruitment sites become limited and the inactivation by dissociation becomes more critical (Figure 3.8).

While the inhibitory function of CARD17 seems unequivocal, the roles of CARD16 and CARD18 are less clear. Both COPs have been reported to inhibit inflammasome signalling (Devi *et al.*, 2023). However, CARD16 and CARD18 possess functional interaction interfaces and can thus be inserted into C1C filaments without disturbing them. In this regard, they behave similarly to C1C-EGFP, which we demonstrated to not impair caspase-1 activity. It would be interesting to recapitulate these experiments by overexpressing all COPs in THP-1 cells and measuring their ability to reduce IL-1β release. A confirmation of their inhibitory effect would raise the question of their inhibitory mechanism, because, as demonstrated by C1C-EGFP, co-mixing and thus diluting caspase-1 filaments is not sufficient to reduce cytokine maturation, at least at the achieved expression levels. A starting point would be to generate cell lines that express CARD16-EGFP or CARD18-EGFP together with C1C-mCherry. This way their localization and recruitment behaviour could be compared. It is also possible that COPs have additional effects in living cells, such as the recruitment of further factors or posttranslational modifications (PTMs), or that they employ unknown functions by interacting with other CARDs. Of note, CARD16 has about 100 amino acids in addition to its CARD, which might fulfil additional functions.

3.3.5 ASC-independent inflammasomes

Some proteins can recruit caspase-1 independent of ASC, including CARD8 and NLRC4. A cellular reporter for ASC-independent inflammasomes has not been reported before. C1C-EGFP can visualise such assemblies and revealed that CARD8 recruits caspase-1 in a filamentous manner, as was demonstrated in HEK cells. This makes C1C-EGFP a useful tool to assess CARD8. A similar phenomenon can be expected in the case of NAIP/NLRC4 activation in the absence of ASC, although this has yet to be demonstrated. Since CARD8 cannot recruit ASC, C1C filaments are the only way to visualise its activation. As discussed earlier, there is a possibility that caspase-1 can nucleate ASC polymerization in reconstituted systems. It would thus be interesting to see how CARD8 behaves in the presence of ASC and caspase-1, as would be the case for example in T cells (Linder and Hornung, 2022). If C1C filaments can nucleate ASC and thereby induce the formation of complex inflammasomes, CARD8 might also be able to indirectly induce canonical inflammasomes by polymerizing caspase-1. This could be tested by reconstituting CARD8, ASC and C1C-EGFP in HEK cells or by knocking out NLRP1 in THP-1 cells. A more physiological model would be harder to achieve, because CARD8 and ASC-expressing cells often harbour NLRP1, precluding specific activation of CARD8.

NLRP1, even though it signals via its CARD, has been reported to not be capable of recruiting caspase-1 directly (Ball *et al.*, 2020; Hollingsworth, Liron, *et al.*, 2021; Gong *et al.*, 2021). In contrast, when we activated reconstituted NLRP1 in a C1C-EGFP-expressing HEK cells, it was able to nucleate C1C-EGFP filaments akin to CARD8, albeit to a lower extent (Figure 3.7A-D). It is possible that the cellular context plays a role, such as concentration of the individual proteins, PTMs, or other cellular factors.

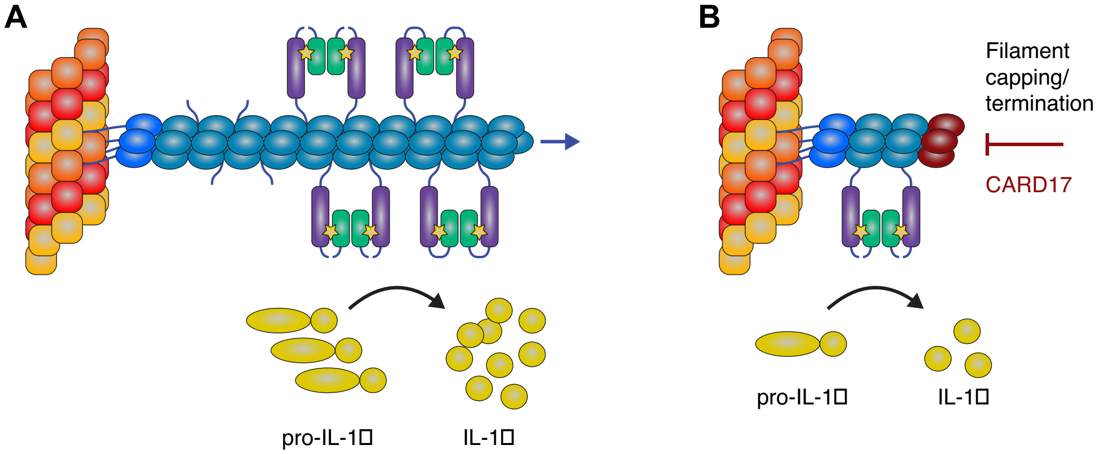

Figure 3.8: Inflammasome regulation by CARD17. (**A**) Caspase-1 forms filaments on existing ASC assemblies. These allow constant recruitment and processing of caspase-1, which leads to the maturation of IL-1β. Caspase-1 CDL cleavage leads to its release from the speck and subsequent inactivation by dissociation. This is mitigated by the constant activation of new caspase-1. (**B**) CARD17 terminates the filaments and stops the continuous supply of caspase-1. Inactivation by dissociation, thus, effectively limits IL-1β maturation.

3.3.6 Differential caspase-1 activity – a matter of complexity?

The intricacies of how inflammasomes are assembled are relevant because they seem to control the degree to which caspase-1 is processed and which substrates it can cleave. This became apparent when it was shown that activation of NLRC4, which can recruit caspase-1 in an ASC-dependent or -independent manner, has different outcomes depending on the involvement of ASC, such that when caspase-1 is activated in the absence of ASC, it induces pyroptosis but does not cleave pro-IL-1β (Mariathasan *et al.*, 2004; Broz, von Moltke, *et al.*, 2010; Dick *et al.*, 2016). Similarly, CARD8, which recruits caspase-1 directly without ASC, is also able to induce pyroptosis but not efficient processing of caspase-1 or IL-1β (Okondo *et al.*, 2017). The data indicate that the differential ability to cleave substrates as well as the degree of caspase-1 processing depends on the polymerization of ASC. Uncleaved, dimerized $(p46)_2$ caspase-1 can be auto-proteolytically cleaved in its IDL to give rise to the fully active $(p33/p10)_2$ form, which ultimately terminates itself by CDL cleavage and subsequent dissociation (Boucher *et al.*, 2018). It is tempting to speculate that the differential cleavage of GSDMD versus IL-1β is mediated by the degree of caspase-1 processing. However, it has been shown that IDL cleavage is necessary for both, GSDMD and IL-1β cleavage (Broz, von Moltke, *et al.*, 2010; Ball *et al.*, 2020). Recently, an exosite was found, which enables the binding of caspases to the GSDMD C-terminus and is only accessible after IDL cleavage (K. Wang *et al.*, 2020; Z. Liu *et al.*, 2020). The additional binding site might offer an explanation why GSDMD can be more readily cleaved compared to cytokines, as it may help to overcome unfavourable conditions. Indeed, GSDMD can still be cleaved by caspase-1 when the cleavage tetrapeptide is substituted with an unfavourable tetrapeptide (K. Wang *et al.*, 2020; Schmidt, 2023). In the absence of ASC, the exosite might likewise enable GSDMD processing despite a minimal amount of fully active caspase-1, while IL-1β is not processed efficiently; it is unknown whether cytokines can similarly bind an exosite on caspases. This suggests a possible model of how ASC can dictate differential outcomes of inflammasome signalling: without ASC, caspase-1 exists mainly in its stable but enzymatically limited $(p46)_2$ form and only small amounts of the fully active

$(p33/p10)_2$ form are generated. In this state, enough GSDMD can be cleaved to mediate pyroptosis, but cytokines are not processed efficiently. ASC greatly increases IDL cleavage and thus enables full caspase-1 activity, including cytokine maturation and self-termination. Boucher *et al.* (2018) compared NLRC4-mediated caspase-1 processing between WT, $ASC^{-/-}$, and $ASC^{+/-}$ macrophages and found that caspase-1 processing was gradual and dependent on the amount of ASC. The authors surmise that the number of caspase-1 binding sites, and thus the size of the inflammasome, is the factor determining the extent of caspase-1 processing, but do not further speculate about a mechanism.

The existence of caspase-1 filaments implies unlimited recruitment sites for caspase-1, precluding a meaningful role for the number of binding sites. In that regard, continuous caspase-1 filaments would in fact render the size or, in the case of NLRC4 or CARD8, the very existence of an ASC assembly irrelevant, assuming the absence of regulators like CARD17. This raises the question how ASC affects caspase-1 to modulate its processing. The existence of flexible interdomain linkers makes an allosteric effect through the direct binding of ASC to caspase-1 unlikely. An observable distinction between the different inflammasome assemblies lies in their complexity: linear caspase-1 filaments generated *e.g.* by CARD8 versus tightly connected and intertwined filaments in a canonical inflammasome. Because caspase-1 dimers display basal activity, it is assumed that this basal activity mediates caspase-1 processing, full activation, and eventually termination. ASC-independent inflammasomes, however, showcase that dimerization is not sufficient to efficiently induce this processing. Extrapolating the observations of caspase-1 filament formation from CARD8 to NLRC4, not even caspase-1 polymerization into filaments is sufficient for efficient auto-processing. It is conceivable that caspase-1 on the outside of a filament is limited regarding its access to neighbouring caspases as enzymatic substrates. Thus, caspase-1 cleavage might only be possible *in trans* from caspases of a different filament. In such a scenario, different caspase-1 filaments might have to engage each other in a distinct conformation, *i.e.* proximity and angle, to allow auto-processing. Such favourable caspase-1 encounters would be rare in

1-dimensional filaments as generated by CARD8 or, presumably, NLRC4 in the absence of ASC. ASC filaments, on the other hand, can nucleate numerous caspase-1 filaments, and condensation forces them into close proximity. The inside of such an inflammasome can be assumed to be highly complex and likely causes multifaceted caspase-1 intersections. Thus, caspase-1 encounters favourable for self-cleavage are much more likely to occur with relevant frequency in a more complex canonical inflammasome.

ASC is most often described as an adapter that facilitates rapid and efficient recruitment of caspase-1. Yet, studies with NLRC4 show that ASC is dispensable for effective induction of pyroptosis, raising the question why most inflammasome sensors employ PYDs and ASC. Herein, I propose a new function for ASC as a generator of complexity, which facilitates full caspase-1 processing and cytokine maturation. The 3-dimensional environment provided by condensed ASC might also limit the diffusion of substrates. This might either impair the access of caspase-1 to its substrates or trap substrates in the inflammasome.

In any case, the morphology of the inflammasome makes a difference in the downstream signalling. In that light, the atypical specks that we observed after NLRP1 stimulation might gain significance. Those specks displayed a hybrid morphology between filaments and canonical specks (Figure 3.76E). The protruding filaments could be seen with ASC-EGFP as well as C1C-EGFP. Interestingly, I have seen such inflammasome morphologies exclusively in the context of NLRP1. Although this phenomenon remains to be established as a real feature, it might be helpful to test the complexity theory, because it would predict differential caspase-1 activity within the same inflammasome. For example, pro-IL-1β can be stained to monitor where exactly it is recruited, as has been done to demonstrate its recruitment to the ASC speck (Broz, Newton, *et al.*, 2010). It is conceivable that it would only be recruited to the condensed parts of NLRP1 filaments, but not the filamentous ones.

3.3.7 Future directions

C1C-EGFP can visualise ASC-dependent or -independent inflammasomes and can be used as a model for caspase-1 recruitment. Because caspase-1 recruitment does not always lead to its cleavage and full activation, it would be beneficial to develop a reporter that does not only visualise caspase-1 recruitment but also its cleavage. Full-length caspase-1 fused to EGFP would be a tool to visualise detachment of caspase-1 from the inflammasome. This approach could be combined with mutants that lack enzymatic activity or are uncleavable in their IDL, CDL, or both. Those tools would help to monitor the stability of inflammasome-bound caspase-1 and compare it between different types of inflammasomes or cell types. Live-cell imaging would be useful to assess the kinetics of caspase-1 recruitment to and its departure from the inflammasome. A more sophisticated approach could report on both, the departed and retained caspase-1, simultaneously. For such a cleavage reporter, I propose the following domain layout: C1C-EGFP-CDL-mCherry. The reporter would initially cause assemblies, that are positive for both colours, and, when CDL cleavage happens, the mCherry signal would leave the inflammasome. The amount of single- versus double-positive specks could be quantified by flow cytometry. Such a reporter would also answer the question whether the CDL alone is sufficient to render the reporter a caspase-1 substrate, or whether additional context of the caspase-1 protein is required as found for GSDMD. For technical reasons, mCherry might have to be exchanged for a different fluorescent protein, *e.g.* BFP (blue fluorescent protein) or emiRFP (far-red fluorescent protein). Using confocal microscopy and the approach demonstrated in 3.2.4, the ratio of both fluorophore intensities within a speck could be measured as a proxy for the fraction of cleaved versus uncleaved reporters in the absence or presence of caspase-1 inhibitors. The high resolution might also enable to localize the sites of caspase-1 processing within the inflammasome, which would be especially interesting in inflammasomes of unconventional morphology. A complementary approach to assess and localize caspase-1 activity would be labelling by fluorescent suicide substrates, such as fluorochrome inhibitor of caspases (FLICA). To delineate the differences between the substrates, a new probe could perhaps be engineered that mimics GSDMD by employing the GSDMD C-terminus, allowing it to engage the caspase-1 exosite.

As discussed earlier, COPs remain poorly understood. While we evaluated the inhibitory role of CARD17 and its mechanism (Figure 3.6), CARD16 and CARD18 remain enigmatic. At this point it is unclear how they could regulate caspase-1 activity when co-mixing with caspase-1 filaments is insufficient to curtail IL-1β release. Fluorescent fusions of CARD16 and CARD18 in combination with a C1C reporter, akin to the experiments with CARD17, would answer first questions: 1) Are these COPs recruited to inflammasomes? 2) To what extent? 3) Do they affect caspase-1 recruitment? 4) Do they affect IL-1β release? In combination with the cleavage reporters proposed before, it could also be examined whether COPs affect caspase-1 cleavage. What makes CARD16 and CARD18 particularly interesting is that they can potentially activate caspase-1 instead of inhibiting it (Karasawa *et al.*, 2015; Lu *et al.*, 2016). COP reporters would help to identify scenarios, in which they oligomerize and nucleate caspase-1. In order to identify additional factors that direct the function of COPs, additional tools might be needed. It is also important to verify the findings from overexpressed proteins by investigating endogenous proteins, *e.g.* by using knockouts.

We currently lack knowledge about proteins that might interact with inflammasomes but are not part of the complex. A possible strategy to identify such proteins is proximity labelling, for example by using C1C-APEX2 (Kalocsay, 2019). APEX2 oxidizes biotin-tyramide to generate short-lived radicals, which label nearby proteins. Biotinylated proteins can then be pulled down and identified, for example by mass spectrometry. An ortholog approach could be employed to identify potential interaction partners of COPs.

3.3.8 Conclusion

As demonstrated in this chapter, C1C-EGFP has great functionality as a new tool to study inflammasome biology. It visualises inflammasomes in real-time and enables readouts by microscopy and flow cytometry. Some advantages over

ASC-EGFP are the broader applicability due to its lower background and the possibility to study caspase-1 recruitment even in the absence of ASC. This has already led to new insights in inflammasome assembly and regulation, *i.e.* the formation of caspase-1 filaments and their regulation by CARD17. Our work also forms a basis for the development of more advanced reporters, which may help us to understand the more puzzling aspects of inflammasome biology in the future.

Chapter 4: Inflammasome activation in intestinal epithelial cells

4.1 Introduction

Inflammasomes are cytosolic signalling hubs that induce pyroptotic cell death and the release of pro-inflammatory cytokines. They are composed of sensors for cytosolic PAMPS or DAMPS, the adaptor protein ASC, and caspase-1. Activated caspase-1 cleaves pro-inflammatory cytokines and GSDMD, which is responsible for the induction of pyroptosis (Martinon *et al.*, 2002; Broz and Dixit, 2016; Hayward *et al.*, 2018).

To date, inflammasomes have mostly been studied in single cells, and inflammasome signalling in the context of complex tissues is poorly understood. Pyroptosis is characterized by swelling of the affected cell and eventually its rupture. A feature of this fulminant type of cell death is the release of cellular components into the extracellular space where they serve as a danger signal for surrounding cells. Cells with structural roles have to maintain tissue integrity while executing pyroptosis. This is especially relevant for epithelia, which form a natural barrier for invading pathogens. Numerous mouse studies have established a role for inflammasomes in intestinal epithelial cells (IECs). NAIP/NLRC4 in mouse IECs is important in the defence against *Salmonella* (Crowley *et al.*, 2016). The epithelial integrity is preserved by the expulsion of affected cells into the gut lumen (Sellin *et al.*, 2014; Rauch *et al.*, 2017), which is achieved by myosin-dependent focal contractions within the epithelium (Samperio Ventayol *et al.*, 2021).

While intestinal NAIP/NLRC4 inflammasomes are well established in mice, the inflammasome sensors NLRP6 and NLRP9 remain more obscure, but have also been reported to play a role in IECs. In mice, NLRP6 confers inflammasome-dependent susceptibility to bacteria but protection from viruses, such as EMCV and murine norovirus, although the antiviral effect was inflammasome-independent (Anand *et al.*, 2012; Wang *et al.*, 2015; Ghimire *et al.*, 2018; Hara *et al.*, 2018). NLRP9b is able to protect mice against RV (Zhu *et al.*, 2017).

Moreover, it was reported that the NLRP6-inflammasome changes the gut microbiota in mice through IL-18 and antimicrobial peptides (Elinav *et al.*, 2011; Levy *et al.*, 2015). Even though the involvement of inflammasome components has been shown, the assembled inflammasomes have not yet been visualised for most intestinal inflammasomes. The molecular mechanisms that lead to their activation and downstream signalling are not well understood. Inflammasomes in human intestinal epithelia have barely been studied at all.

Due to the clear functional role of inflammasomes in the mouse intestine and the likely interplay of pyroptotic cells with other cell types, intestinal epithelia make an interesting case to study inflammasomes in functional tissue. They also benefit from the advances in cell culture techniques in recent years. Human intestine has been difficult to study because of a lack of suitable model systems. Some IEC cell lines are available, but they do not recapitulate the complexity of the intestinal epithelium. Explants from human intestine are only sporadically available, cannot be kept alive for extended periods of time, and cannot be easily genetically modified. Intestinal epithelium can be cultured in form of 3-dimensional structures termed organoids. Organoids combine striking advantages of *in vivo* and *in vitro* systems, as they closely resemble the gut tissue, contain the four main cell types found in IECs and, at the same time, allow for continued culture and genetic modification (Sato *et al.*, 2011; Koo *et al.*, 2011; Schwank and Clevers, 2016). Organoids derived from small intestinal tissue are commonly referred to as enteroids.

We first reconstituted the intestine-specific inflammasomes in HEK 293T cells to study their minimal requirements for activation. We next established cultures of mouse and human enteroids and transduced them to express the new inflammasome reporter C1C-EGFP, which was discussed in the previous chapter. Those reporter enteroids were then used to study inflammasome responses to infection with bacteria and viruses.

4.2 Results

4.2.1 Reconstituted NLRP6 and NLRP9 inflammasomes in HEK 293 cells

As an exemplary tissue to study inflammasomes, we chose the intestine, because intestinal inflammasomes are poorly understood and because organoid models for the intestine are well-established. The intestine is reported to harbour two of the more enigmatic inflammasomes NLRP6 and NLRP9, which play a role in the defence against viruses and bacteria (Anand *et al.*, 2012; Wang *et al.*, 2015; Zhu *et al.*, 2017; Hara *et al.*, 2018).

We first investigated those inflammasomes in a minimalistic cell culture model. All known canonical inflammasome sensors recruit ASC and form a speck even in the absence of specific activation, when overexpressed together with ASC in epithelial HEK 293 cells. To determine whether human NLRP6 and NLRP9 can assemble inflammasomes, we transfected a HEK 293T cell line expressing the inflammasome reporter ASC-EGFP ($\mathrm{HEK}^{\mathrm{ASC\text{-}EGFP}}$) with increasing amounts of expression vectors for NLRP6, NLRP9, or NLRP1 as a positive control. The principle of the ASC-EGFP reporter is described in chapter 3. At steady state, ASC-EGFP is distributed throughout the cytosol. Upon inflammasome activation, all molecules are recruited to a single protein complex, leading to a concentration of the signal into one single speck per cell. This can be easily observed by microscopy or quantified by flow cytometry, comparing the height and the width of the fluorescent signal (see 3.2.1, p. 47, Figure 3.1C). While NLRP1 and NLRP6 induced robust and dose-dependent inflammasome assembly, NLRP9 only formed a miniscule amount of specks, even after transfection with the highest amount of DNA (Figure 4.1A,B). NLRP6 proved to be very prone to form ASC specks after overexpression. Its response far exceeded that of NLRP1 and was comparable to the response of NLRP1 in combination with its activator talabostat.

To assess the ability of NLRP6 and NLRP9 to respond to triggers that have been postulated in the literature, we generated reporter cell lines that constitutively express ASC-EGFP and express NLRP6 ($\mathrm{HEK}^{\mathrm{NLRP6\text{-}HA(i)+ASC\text{-}EGFP}}$) or NLRP9 ($\mathrm{HEK}^{\mathrm{NLRP9\text{-}HA(i)+ASC\text{-}EGFP}}$) from an inducible promoter. We first generated cell lines that express the inflammasome sensor under the control of a doxycycline-inducible promoter using the Flp-In^{TM} T-REx^{TM} system (ThermoFisher). After confirmation of protein expression, we lentivirally modified the cells to express ASC-EGFP under a weak ubiquitin promoter and examined single cell clones with regard to their expression of ASC-EGFP and NLRP6/9, as well as speck formation with and without doxycycline (Figure 4.1C-H). As expected, all clones constitutively expressed ASC-EGFP and expressed NLRP6/9 upon induction. ASC specks in the absence of activators (background) were only seen in the NLRP6 reporter cell line, confirming the finding that NLRP6 is prone to form specks upon overexpression (Figure 4.1A,B). Clone #f of the NLRP6 cell line and clone #g of the NLRP9 cell line were selected for further experiments based on their comparable expression of ASC-EGFP and low speck background. Next, we stimulated these cells with potential chemically defined activators that have been proposed in literature and screened for specking responses (Figure 4.1I). For potential NLRP6 activation, we transfected high molecular weight (HMW) poly(I:C) or two concentrations of lipoteichoic acid (LTA), or treated the cells with taurine (Wang *et al.*, 2015; Levy *et al.*, 2015; Hara *et al.*, 2018). For NLRP9 activation, we transfected the cells with low molecular weight (LMW) poly(I:C). As further controls, we treated the cells with talabostat (NLRP1 activator), or LPS and nigericin. All cells were incubated overnight. We observed some specks in HEK$^{NLRP6\text{-}HA(i)+ASC\text{-}EGFP}$ cells after treatment with lipofectamine (LF) and nigericin, but the response was not increased when any of the proposed activators was transfected. HEK$^{NLRP9\text{-}HA(i)+ASC\text{-}EGFP}$ cells displayed only very low levels of background specks. It was reported that RV activates NLRP9 (Zhu *et al.*, 2017) and EMCV activates NLRP6 (Wang *et al.*, 2015). We infected both reporter cells with either of the RNA viruses and measured the amount of resulting ASC specks (Figure 4.1J). In the case of EMCV infection, we observed minimal speck formation. However, the frequency of specking cells was similar between infected and uninfected cells, demonstrating that this is an unspecific effect. RV infection did not induce a significant inflammasome response above the level observed in mock-infected cells (Figure 4.1J).

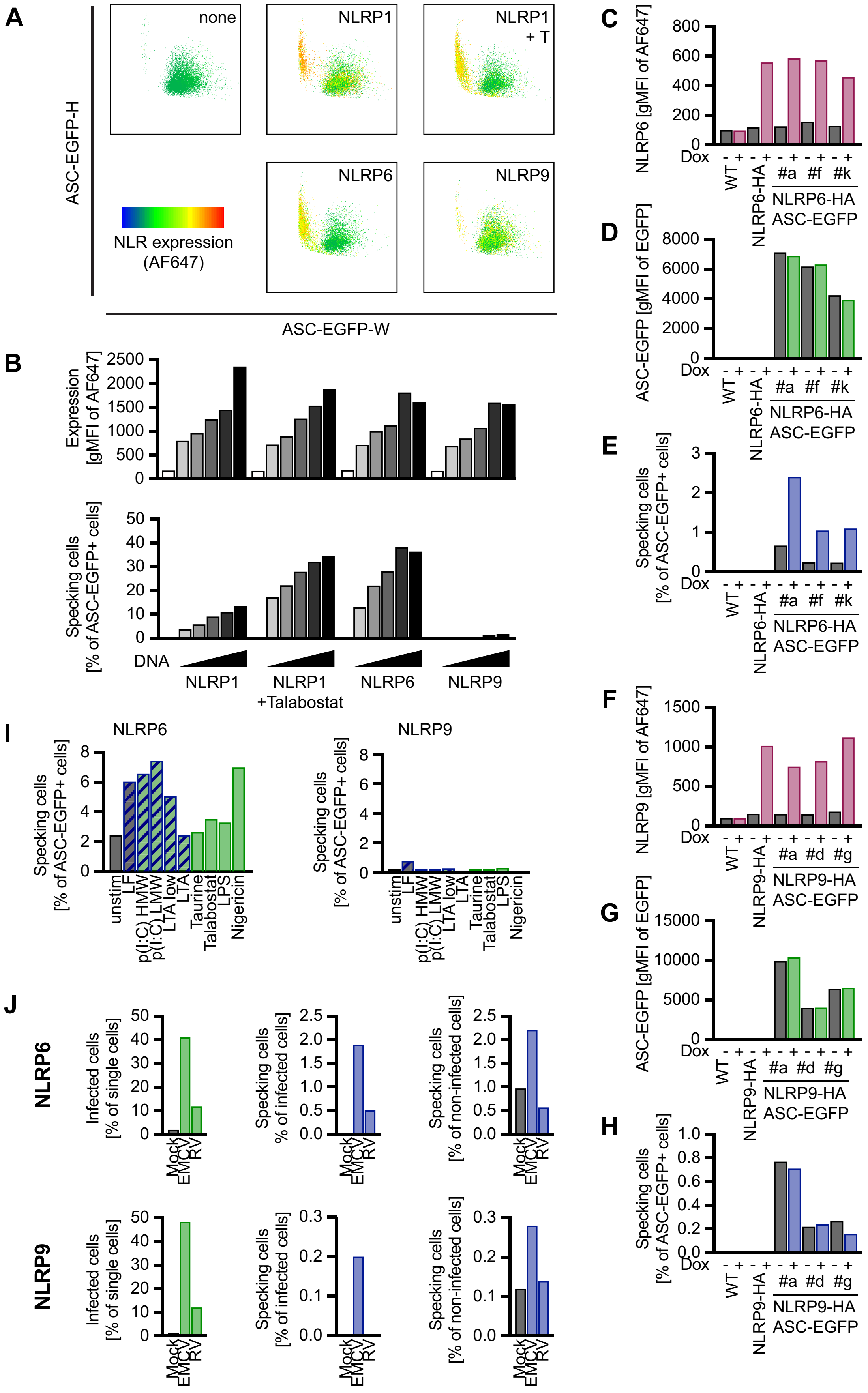
A
ASC-EGFP-H
none
NLRP1
NLRP1
+ T
NLRP6
NLRP9
NLR expression
(AF647)
ASC-EGFP-W
B
Expression
[gMFI of AF647]
2500
2000
1500
1000
500
0
Specking cells
[% of ASC-EGFP+ cells]
50
40
30
20
10
0
DNA
NLRP1
NLRP1
+Talabostat
NLRP6
NLRP9
C
NLRP6 [gMFI of AF647]
800
600
400
200
0
Dox
WT
NLRP6-HA
#a
#f
#k
NLRP6-HA
ASC-EGFP
D
ASC-EGFP [gMFI of EGFP]
8000
6000
4000
2000
0
E
Specking cells
[% of ASC-EGFP+ cells]
3
2
1
0
F
NLRP9 [gMFI of AF647]
1500
1000
500
0
NLRP9-HA
#a
#d
#g
NLRP9-HA
ASC-EGFP
G
ASC-EGFP [gMFI of EGFP]
15000
10000
5000
0
H
Specking cells
[% of ASC-EGFP+ cells]
1.0
0.8
0.6
0.4
0.2
0.0
I
NLRP6
NLRP9
Specking cells
[% of ASC-EGFP+ cells]
8
6
4
2
0
unstim
LF
p(I:C) HMW
p(I:C) LMW
LTA low
LTA
Taurine
Talabostat
LPS
Nigericin
J
NLRP6
NLRP9
Infected cells
[% of single cells]
50
40
30
20
10
0
Specking cells
% of infected cells]
2.5
2.0
1.5
1.0
0.5
0.0
Specking cells
[% of non-infected cells]
Specking cells
[% of infected cells]
0.3
0.2
0.1
0.0
Mock
EMCV
RV

Figure 4.1: NLRP1 and NLRP9 inflammasomes cannot be reconstituted in HEK cells. (**A**-**B**) HEK$^{ASC\text{-}EGFP}$ cells were transfected with increasing concentrations of plasmid for the expression of NLRP1-HA, NLRP6-HA, and NLRP9-HA (0, 50, 100, 200, 400, 800 ng/mL). NLRP1-HA transfected cells were additionally treated with 30 µM talabostat for 20 h. 2 days after transfection, the cells were harvested. The NLR proteins were stained using their HA tag and an AF647 labelled secondary antibody. NLR expression (gMFI of AF647) and the fraction of specking cells was measured by flow cytometry. (**C**-**H**) HEK 293 WT, HEK$^{NLRP6\text{-}HA(i)}$ (C-E), and HEK$^{NLRP9\text{-}HA(i)}$ cells (F-H), as well as three clones of HEK$^{NLRP6\text{-}HA(i)+ASC\text{-}EGFP}$ (C-E) and HEK$^{NLRP9\text{-}HA(i)+ASC\text{-}EGFP}$ (F-H) were treated with doxycycline where indicated and the HA tag was stained. The expression of the NLR-HA (gMFI of AF647, C,F) and ASC-EGFP (gMFI of EGFP, D,G), as well as the fraction of specking cells (E,H) was measured by flow cytometry. (**I**) HEK$^{NLRP6\text{-}HA(i)+ASC\text{-}EGFP}$ or HEK$^{NLRP9\text{-}HA(i)+ASC\text{-}EGFP}$ cells were transfected with 2 µg/mL HMW or LMW poly(I:C), 60 µg/mL LTA or Lipofectamine^{TM} 2000 alone. Alternatively, the cells were treated with 64 µM taurine, 30 µM talabastat, 200 ng/mL LPS, or 10 µM nigericin. After 20 h, the fraction of specking cells was measured by flow cytometry. (**J**) HEK$^{NLRP6\text{-}HA(i)+ASC\text{-}EGFP}$ or HEK$^{NLRP9\text{-}HA(i)+ASC\text{-}EGFP}$ cells were infected with RV SA11 (MOI=175) or EMCV (MOI=215). RV was first activated in 5 µg/mL trypsin at 37 °C for 30 minutes. Trypsin was neutralized by adding one volume of trypsin neutralizer (Thermo Fisher Scientific). The cells were infected with an excess of either virus and incubated for 20 h. Specking cells were quantified by flow cytometry. For all panels, one representative experiment is shown.

Together, these results show that NLRP6 can in principle assemble inflammasomes upon overexpression, but that it does not do so in response to the postulated triggers. We also showed that NLRP9 does not assemble inflammasomes beyond background. It is possible that additional factors are missing in HEK 293 cells that are required for NLRP6 and NLRP9 to respond to their described activators, or that the described activators are not sufficient. Subsequent experiments will thus focus on physiologically more relevant cells *i.e.* IECs in the form of enteroids.

4.2.2 Inflammasome responses in mouse enteroids

According to literature, NLRP6 and NLRP9 form inflammasomes in intestinal epithelial cells (Wang *et al.*, 2015; Zhu *et al.*, 2017; Shen *et al.*, 2019). Thus, we aimed to study these inflammasomes in intestinal enteroids. We generated mouse intestinal enteroids (MIEs) from a C57BL/6 mouse. In brief, we extracted the small intestine (between the stomach and the cecum), washed it, and cut it into small pieces. Crypts, which contain the niches for stem cells, were extracted by treatment with EDTA and mechanical force, and embedded into Matrigel. MIEs were cultivated in medium supplemented with EGF, noggin, and R-spondin. Because MIEs are self-sufficient in maintaining a stem cell niche, they do not require supplementary enhancement of Wnt signalling. Enteroids, thus, readily differentiate into budding structures.

Since activators for intestinal inflammasomes are poorly established, we first addressed fundamental questions of inflammasome formation in MIEs using the NAIP/NLRC4 inflammasome, which has been studied in more detail (Sellin *et al.*, 2014; Rauch *et al.*, 2017). We first confirmed that the NAIP/NLRC4 triggers BsaK, PrgI, and MxiH can induce pyroptosis in MIEs when delivered with the anthrax toxin delivery system. All three components led to complete disintegration of the enteroids and rounding up of the cells (data not shown). The *Shigella flexneri* STI1 T3SS needle protein MxiH, which binds NAIP1, was the most potent activator, and we decided to use this trigger in future experiments. While inflammasome-dependent cell death and cytokine release was previously shown in IECs, ASC speck formation had, to my knowledge, not yet been shown. Thus, we generated enteroids from an ASC-mCherry reporter mouse (Latz lab, MIE$^{\text{ASC-mCherry}}$), treated them with MxiH and recorded them over a time course of 2.5 hours by widefield microscopy (Figure 4.2A). Cell death was assessed by morphology and the cell viability dye CellTox$^{\text{TM}}$ Green (Promega), which reports on the loss of plasma membrane integrity. Within one hour, most cells died and the whole enteroid eventually disintegrated. However, we could not observe any ASC-mCherry relocalization. It is possible that ASC specks were masked by scattered light from different focal planes of the 3-dimensional enteroid. Therefore, we fixed MxiH-treated MIE$^{\text{ASC-mCherry}}$ in order to visualise them by confocal microscopy (Figure 4.2B). In untreated enteroids, ASC-mCherry was mostly diffuse and formed sporadic aggregates. When treated with MxiH, ASC-mCherry formed excessive filaments, which strongly differ from the typically observed ASC specks. To investigate whether this is a true phenotype in IECs or an artifact of the ASC-mCherry reporter, we next treated MIEs with MxiH, stained

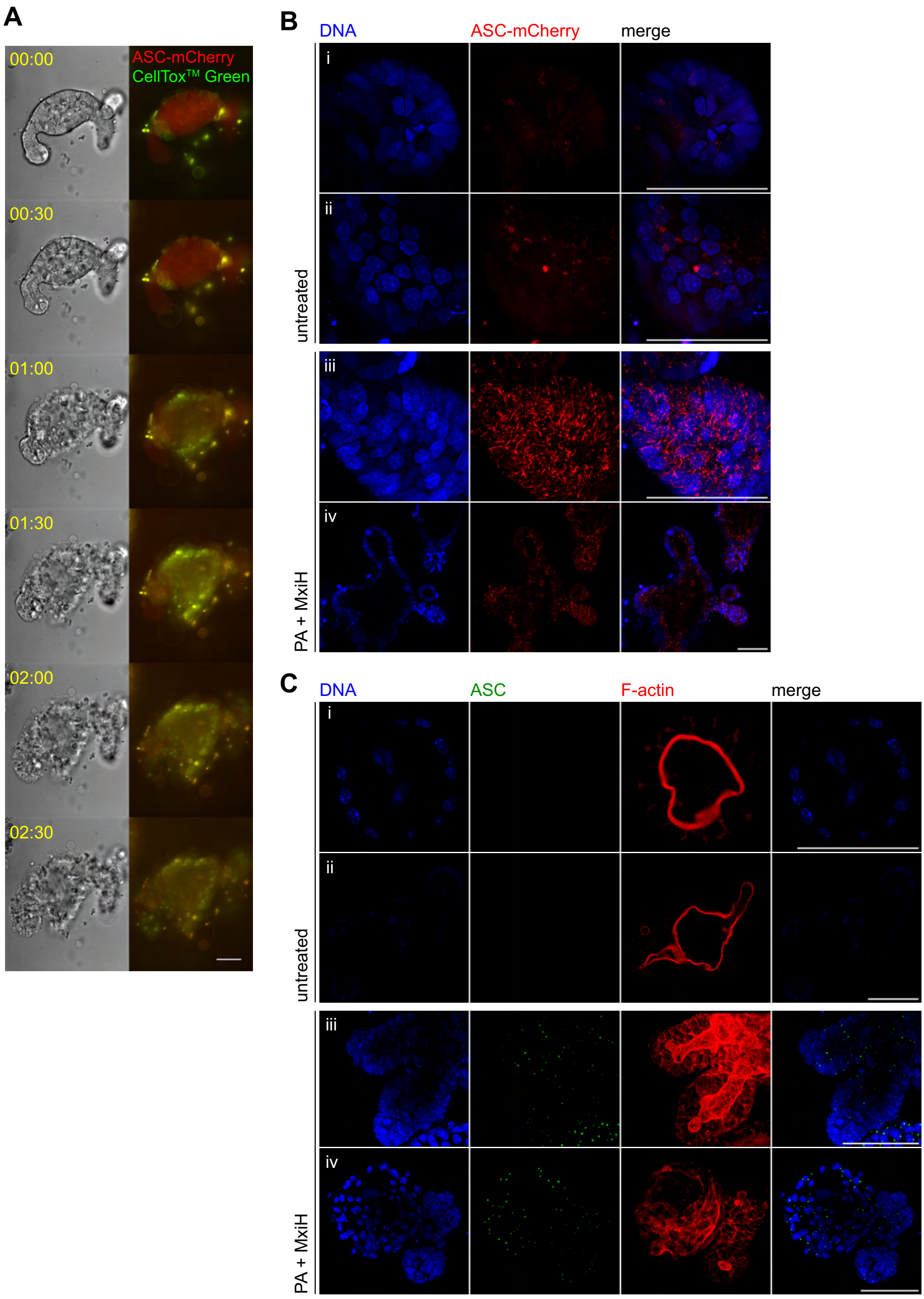
A
00:00
ASC-mCherry
CellTox^{TM} Green
00:30
01:00
01:30
02:00
02:30
B
DNA
ASC-mCherry
merge
i
ii
untreated
iii
iv
PA + MxiH
C
DNA
ASC
F-actin
merge
i
ii
untreated
iii
iv
PA + MxiH

Figure 4.2: Mouse IECs assemble canonical inflammasomes. (**A**) WT MIEs were treated with 1 µg/mL MxiH and 16 µg/mL PA in DMEM without phenol red. CellTox^{TM} Green (1:1000, Promega) was added as a viability dye. Live cells were recorded using widefield microscopy. The time is indicated in hh:mm. (**B**) MIE$^{ASC\text{-}mCherry}$ were treated with MxiH and PA as in A in the presence of 50 µM Z-VAD-FMK. The cells were fixed after 1.5 h and recorded by confocal microscopy. (**C**) WT MIEs were treated with MxiH, PA, and Z-VAD as before. Endogenous ASC was stained, and F-actin was visualised with ActiStain Phalloidin 555 (TebuBio). The cells were recorded by confocal microscopy. Scale bars: 50 µm.

endogenous ASC, and recorded them by confocal microscopy (Figure 4.2C). This revealed that IECs do in fact form typical ASC foci upon inflammasome activation similar to those observed in other cell types. The ASC-mCherry filaments are therefore an artifact linked to the reporter mouse.

In order to investigate the dynamics of inflammasome activation by live-cell imaging, we introduced the newly developed mC1C-EGFP inflammasome reporter into MIEs using lentiviral transduction (MIE$^{mC1C\text{-}EGF}$). The reporter is described in detail in chapter 3. Of note, LGR5^{+} stem cells must be genetically modified to maintain the modification in ongoing enteroid cultures. These cells have to be artificially enriched for lentiviral transduction in MIEs because the enteroids are typically maintained in a differentiated state with few stem cells. In order to achieve sufficient enrichment, we had to boost Wnt signalling using the GSK-3 inhibitor CHIR99021 as described (Koo *et al.*, 2013). To test the ability of the newly generated enteroids to assemble inflammasomes, we treated them with the NAIP/NLRC4 agonist MxiH and recorded the cells using confocal microscopy for the duration of the experiment (Figure 4.3A). ASC foci were already formed within the first 10 minutes after addition of MxiH. After one hour of treatment, the enteroids showed extensive cell death, as seen by propidium iodide (PI) uptake and loss of morphological integrity. Interestingly, we could observe the expulsion of specking cells into the enteroid lumen (Figure 4.3A, arrows; note that excessive cell expulsion causes organoids to burst open, and expelled cells are pushed to the outside at late timepoints), a process that was previously described and linked to epithelial inflammasomes (Rauch *et al.*, 2017;

Samperio Ventayol *et al.*, 2021). To confirm that the C1C-EGFP specks correlate with ASC specks, we treated MIE$^{mC1C-EGF}$ with MxiH in the presence of a caspase inhibitor, stained endogenous ASC, and visualised the enteroids by confocal microscopy (Figure 4.3B). The signal of C1C-EGFP specks colocalized with that of endogenous ASC as can be seen by the yellow hue in the merge channel.

Next, we tested if inflammasome assembly in enteroids can also be quantified by flow cytometry as described in chapter 3. To avoid pyroptotic cell death, we treated the enteroids with the pan-caspase inhibitor Z-VAD FMK. After stimulation with MxiH or LPS and nigericin, we trypsinized the enteroids to dissociate them into single cells and measured the fluorescence by flow cytometry (Figure 4.3C). Cells with an assembled inflammasome could easily be identified using our standard gating strategy as described before. MxiH induced a robust inflammasome response while LPS and nigericin did not. This demonstrates that the NAIP1/NLRC4 but not the NLRP3 inflammasome is active in MIEs.

Enteroids expose their basolateral side towards the outside while the apical site points inwards, enclosing a functional lumen. Cell expulsion into the lumen is therefore rather difficult to observe. The apical side, which is buried within the enteroids, is not accessible, hampering infection of intact 3-dimensional enteroids. We therefore generated apical-out enteroids (Co *et al.*, 2019), in which cells are expected to be expelled to the outside. The successful inversion can be confirmed by actin staining, which indicates the apical side of the cells (Figure 4.3D). After MxiH treatment, specking cells are indeed expelled outside, followed be dissociation of the enteroids.

These results prove the utility of C1C-EGFP as an inflammasome reporter in a complex 3-dimensional cell culture system and encourage its use in other organoid models and tissues. We confirmed published findings on mouse intestinal NLRC4 inflammasomes and showed the assembly of macromolecular caspase-1 recruitment platforms in IECs.

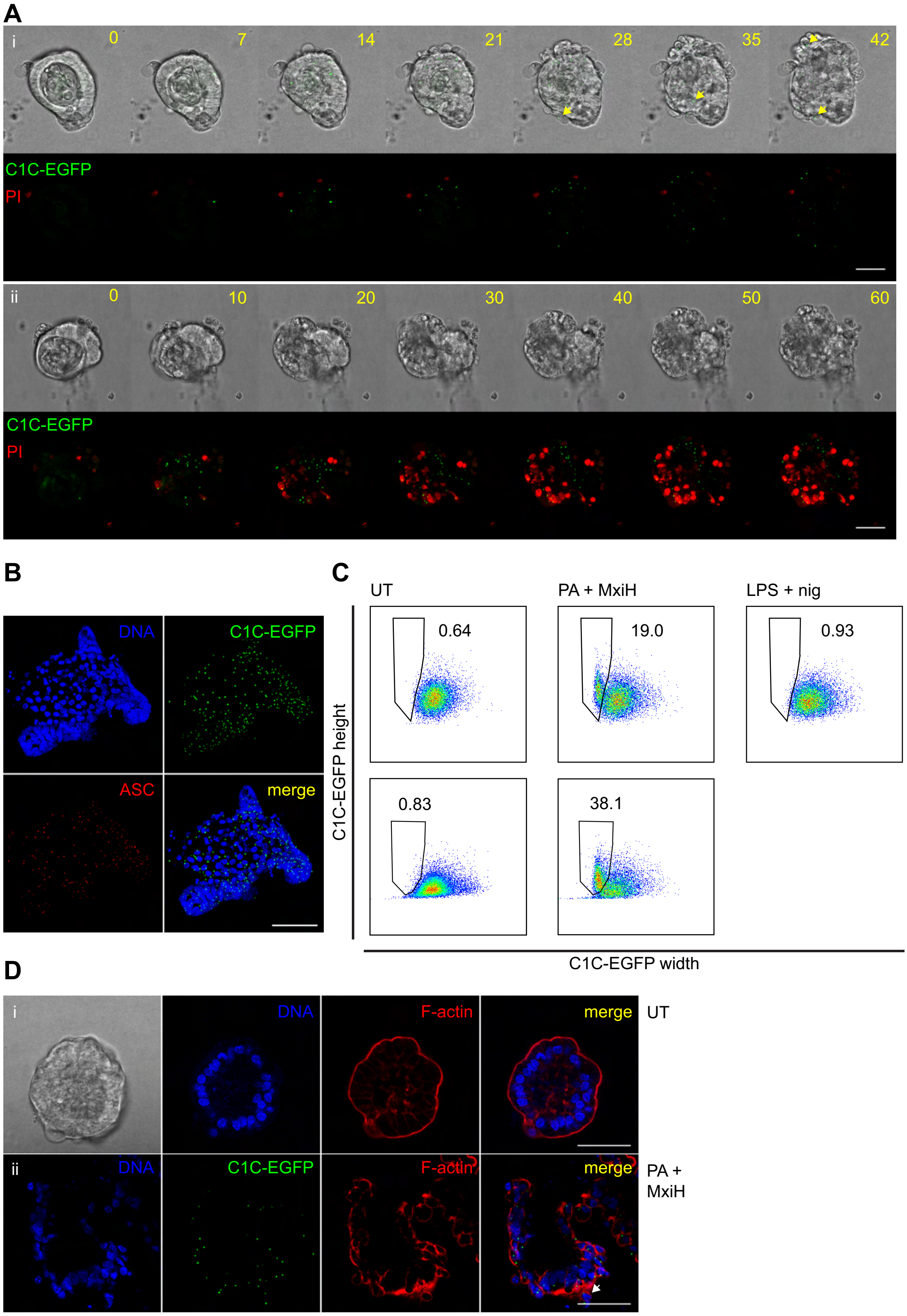
A
i
0
7
14
21
28
35
42
C1C-EGFP
PI
ii
0
10
20
30
40
50
60
C1C-EGFP
PI
B
DNA
C1C-EGFP
ASC
merge
C
UT
PA + MxiH
LPS + nig
0.64
19.0
0.93
0.83
38.1
C1C-EGFP height
C1C-EGFP width
D
i
DNA
F-actin
merge
UT
ii
DNA
C1C-EGFP
F-actin
merge
PA + MxiH

Figure 4.3: C1C-EGFP visualises inflammasomes in organoids. (**A**) MIE$^{mC1C\text{-}EGF}$ were treated with 1 µg/mL MxiH and 16 µg/mL PA in DMEM without phenol red. PI was used as a viability dye. Either a single focal plane (i, upper panel) or a Z-stack (ii, lower panel, maximum intensity projection) of living cells was recorded. The number indicates the time point in minutes. (**B**-**C**) MIE$^{mC1C\text{-}EGF}$ were treated with MxiH and PA as in A in the presence of 50 µM Z-VAD-FMK. Endogenous ASC was stained, and the cells were recorded by confocal microscopy (B). A representative maximum intensity projection of a Z-stack is shown. Enteroids were dissociated and the fraction of specking cells was measured by flow cytometry (C). (**D**) Inside-out MIE$^{mC1C\text{-}EGF}$ were treated with MxiH and PA as in A. F-actin was stained with ActiStain Phalloidin 555 (TebuBio), and the cells were recorded by confocal microscopy. Arrows indicate expelled cells. Scale bars: 50 µm.

4.2.2.1 Antibacterial inflammasomes

It has previously been reported, that mouse IECs form NAIP/NLRC4-dependent inflammasomes in response to infection with enteric bacteria (Sellin *et al.*, 2014; Rauch *et al.*, 2017). However, the assembly of a *bona fide* inflammasome has so far not been shown. To test whether specks are formed in response to bacterial infection, we infected MIE$^{mC1C\text{-}EGF}$ with *Samonella enterica* serovar Typhimurium or *Shigella flexneri* and examined speck formation by confocal microscopy (Figure 4.4).

We observed inflammasome assembly in both *Salmonella*- and *Shigella*-infected enteroids, although the response was much more prominent in the *Salmonella*-infected cells (Figure 4.4A). Moreover, it was evident that most specking cells were found within the lumen of the enteroids (inside), presumably due to expulsion of infected cells, a process that has been linked to inflammasome signalling in IECs (Rauch *et al.*, 2017; Samperio Ventayol *et al.*, 2021). In some cases, cells were caught in the process of being expelled (Figure 4.4B). Interestingly, specking cells were also commonly observed at the basal side of the enteroids (outside). This was always accompanied by alterations of the enteroid morphology as revealed by the actin staining (Figure 4.4A,C, arrows). In some instances, there were gaps between cells that appear as actin tunnels, which might possibly represent compromised membrane integrity and a means of breaching the epithelium by bacteria. A time course experiment of *Salmonella*

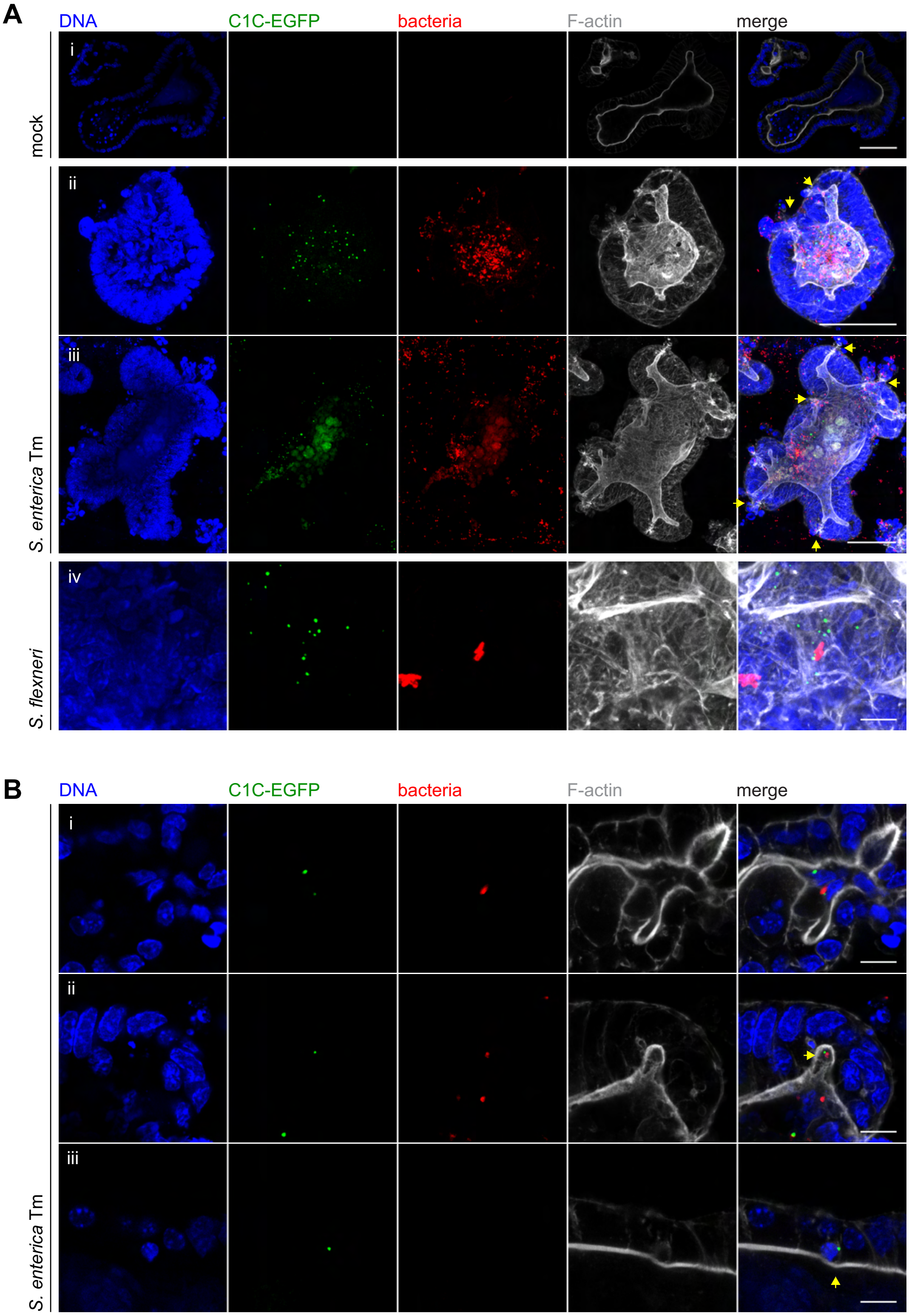
A
DNA
C1C-EGFP
bacteria
F-actin
merge
i
mock
ii
iii
S. enterica Tm
iv
S. flexneri
B
DNA
C1C-EGFP
bacteria
F-actin
merge
i
ii
iii
S. enterica Tm

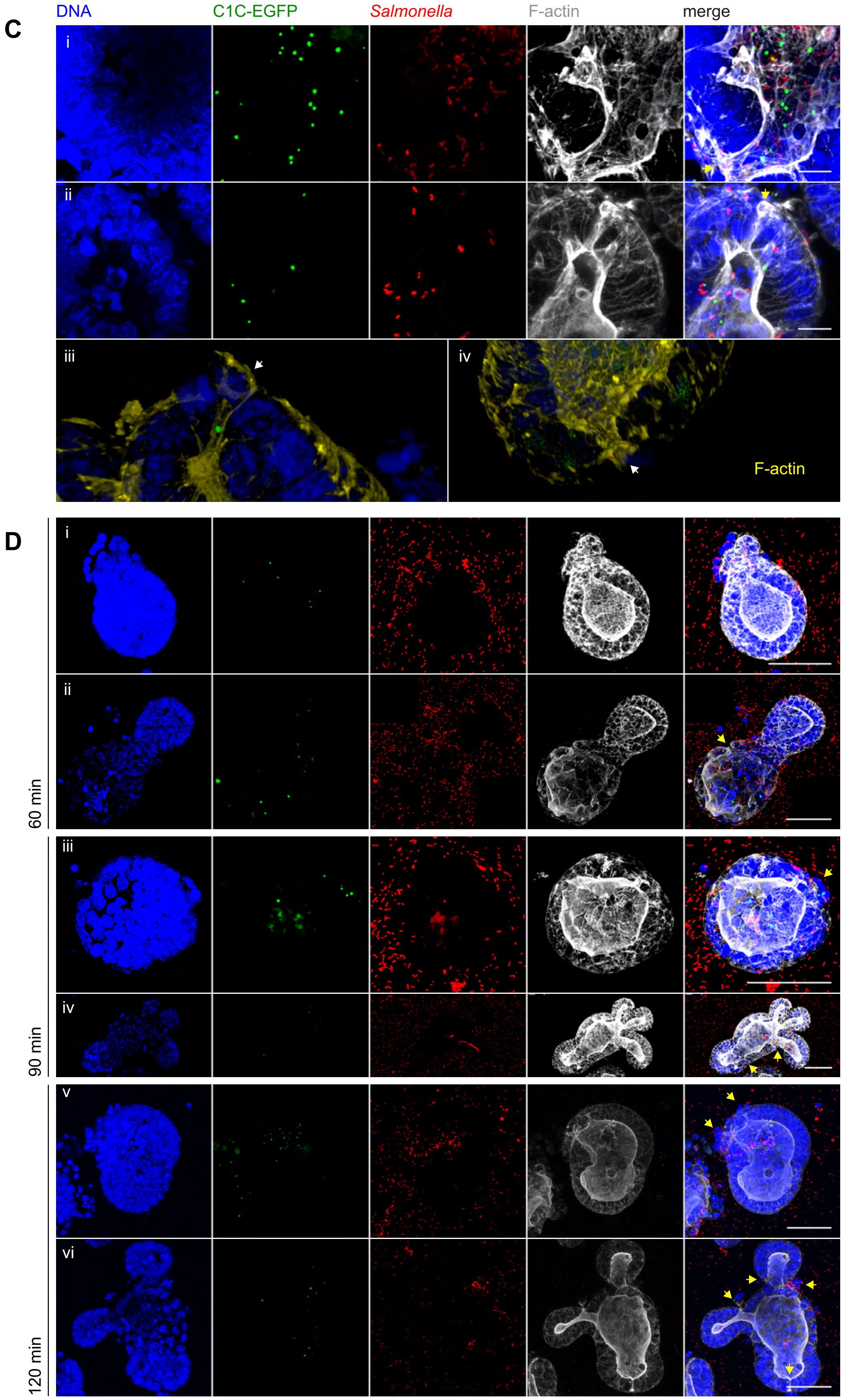
C
DNA
C1C-EGFP
Salmonella
F-actin
merge
i
ii
iii
iv
F-actin
D
i
ii
60 min
iii
iv
90 min
v
vi
120 min

Figure 4.4: Enteric bacteria induce inflammasomes in mouse IECs. (**A**) MIE$^{mC1C\text{-}EGF}$ were infected with *S.* Typhimurium mCherry (ii, iii) or *S. flexneri* RFP (iv) for 2 h. F-actin was stained with ActiStain Phalloidin 670 (TebuBio). For panels ii and iii, a maximum intensity projection of a Z-stack is shown. Scale bars (from top to bottom): 50, 50, 50, 10 µM. (**B**-**C**) MIE$^{mC1C\text{-}EGF}$ were infected with *S.* Typhimurium mCherry and recorded as in A. Maximum intensity projections of Z-stacks are shown. 3-dimenional reconstructions (C iii, iv) were generated with Leica Application suite X. Scale bars: 10 µM. (**D**) MIE$^{mC1C\text{-}EGF}$ were infected with *S.* Typhimurium mCherry for the indicated times. Maximum intensity projections of Z-stacks are shown. Arrows indicate expelled cells or anomalies in the enteroid morphology. Scale bars: 50 µm.

infection revealed that these morphological anomalies were already present as early as 60 min, albeit more prevalent at later time points (Figure 4.4D). It is worth noticing that, in contrast to overstimulation with MxiH, infected enteroids maintained overall integrity over the duration of the experiment, probably because fewer cells assembled inflammasomes.

4.2.2.2 Virus infection

Since the C1C-EGFP reporter was successful in showing antimicrobial inflammasomes, and our observations were in agreement with previous literature, we moved on with the original objective to study antiviral inflammasomes in enteroids. We produced encephalomyocarditis virus (EMCV) in BHK-21 cells and the simian rotavirus (RV) strain SA11 in MA104 cells. Both viruses were purified by sedimentation through a sucrose cushion. Initial infection experiments showed that both viruses are capable of killing MIEs (data not shown). For EMCV, infection could be confirmed by flow cytometry after staining of dsRNA, which occurs as a replication intermediate (Figure 4.5A). RV, on the other hand, could not be stained with this antibody, presumably because the dsRNA is protected by capsid proteins at all stages of replication. Staining of RV-infected cells with this particular antibody had also failed elsewhere (Uzri and Greenberg, 2013). For detection of RV-infected cells, it is therefore preferable to stain a capsid protein instead. Nanobody VHH 2KD1 had been published to bind RV VP6 (Garaicoechea *et al.*, 2008). We ordered DNA encoding the nanobody, generated an expression vector, produced the nanobody in the periplasm of *E. coli,* and purified it by Ni-NTA affinity chromatography using its His-tag. The elution

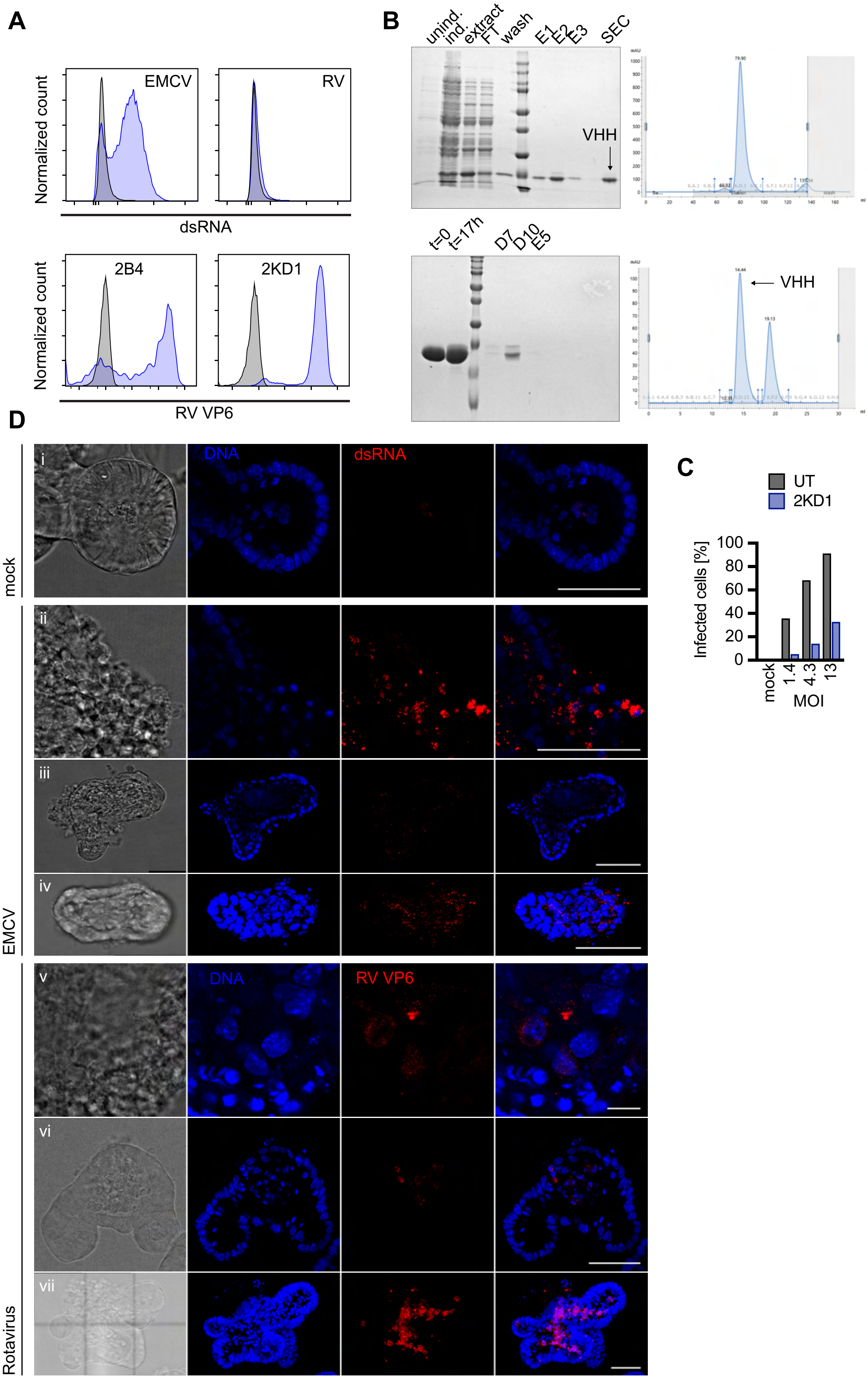
A
Normalized count
EMCV
RV
dsRNA
Normalized count
2B4
2KD1
RV VP6
B
unind.
ind.
extract
FT
wash
E1
E2
E3
SEC
VHH
t=0
t=17h
D7
D10
E5
VHH
C
UT
2KD1
Infected cells [%]
100
80
60
40
20
0
mock
1.4
4.3
13
MOI
D
mock
EMCV
Rotavirus
i
ii
iii
iv
v
vi
vii
DNA
dsRNA
DNA
RV VP6

Figure 4.5: RV and EMCV do not induce inflammasomes in mouse IECs. (**A**) Upper panel: HEK 293T cells were infected with EMCV or RV SA11 for 6 h. dsRNA was stained. Lower panel: MA104 cells were infected with rotavirus overnight. VP6 was stained either with the 2B4 antibody or VHH 2KD1-AF647. The cells were measured by flow cytometry. (**B**) Production of VHH 2KD1-AF647. Upper left panel: SDS-PAGE of different production stages. unind.: uninduced bacteria, ind.: induced bacteria, FT: Ni-NTA flow through, E1-3: Ni-NTA elution fractions, SEC: size exclusion chromatography. Upper right panel: elution profile from SEC. Lower left panel: SDS-PAGE from different stages of sortase labelling. D7, D10, E5: elution fractions from SEC. Lower right panel: elution profile from SEC. (**C**) MA104 cells were infected with RV SA11 overnight with the indicated MOIs. RV was pre-incubated with 1 µM VHH 2KD1 for 1 h at 37 °C as indicated. Infected cells were stained with VHH 2KD1-AF647 and measured by flow cytometry. (**D**) WT MIEs were infected with EMCV (ii-iv) or RV SA11 (v-vii) overnight. EMCV infected cells were stained via dsRNA, and RV was stained via the VP6 protein (2KD1). The cells were recorded by confocal microscopy. Scale bars: panel v: 10µm, all others: 50 µm.

fractions containing the nanobody were further purified by size exclusion chromatography (SEC) (Figure 4.5B, upper panels). The Coomassie gel showed that the protein was already pure after Ni-NTA chromatography. Using the C-terminal LPETG motif, the nanobody was then coupled to Alexa Fluor 647 (AF647) in a sortase-catalysed reaction (Figure 4.5B, lower panels). When the SEC fractions were examined in a Coomassie gel, the VHH-containing fractions resulted in two bands, which probably represent labelled and unlabelled nanobody and cannot be separated via SEC due to the small difference in size. We then infected MA104 cells with RV and stained the cells with either the commercially available VP6 antibody 2B4 combined with an AF647-labelled secondary antibody, or with VHH 2KD1-AF647. 2B4 staining resulted in two separate broad peaks, separating uninfected and infected cells by flowcytometry. VHH 2KD1 produced two sharp and even better separated peaks (Figure 4.5A). Thus, we decided to use the nanobody for future experiments. We then asked if it also has neutralizing activity. We pre-incubated RV with 1 µM VHH 2KD1, and infected HEK 293T cells (Figure 4.5C). The nanobody substantially reduced the fraction of infected cells, indicating that VHH 2KD1 has neutralizing activity against RV. The nanobody has been demonstrated to ameliorate RV-induced disease in neonatal mice (Maffey *et al.*, 2016).

We proceeded to infect 3-dimensional WT MIEs with EMCV and RV overnight and stained dsRNA and RV VP6, respectively. Infected cells were detectable for both viruses (Figure 4.5D). We next tested if inflammasomes are formed upon infection of MIE$^{C1C\text{-}EGFP}$ (data not shown). However, no C1C-EGFP specks were observable after one day. When kept in culture, the EMCV-infected enteroids started dying after one day and the RV-infected enteroids after two to three days. Specks were not observed in any case, suggesting that inflammasomes do not play a role in IECs infected with either virus. Vaccinia virus and vesicular stomatitis virus were also able to infect and kill enteroids but induced no inflammasome formation (data not shown).

4.2.3 Inflammasomes in human enteroids

One key advantage of organoids is that they allow genetic manipulation in human primary cells, which do not benefit from the genetic tools available for mice. We therefore established human intestinal enteroids (HIEs) from the duodenum, jejunum, and ileum of multiple patients. Pieces of intestinal mucosa were freed from fat and blood vessels, and crypts were isolated similarly to mouse intestine. In contrast to MIEs, HIEs require supplementation of Wnt or a surrogate in order to maintain stemness and the ability to be cultured *in vitro*. Therefore, they were cultivated in commercial IntestiCult^{TM} organoid growth medium (OGM), in which they maintained an undifferentiated, spherical state with a high number of stem cells. To differentiate enteroids, the medium was changed to IntestiCult^{TM} organoid differentiation medium (ODM) and supplemented with the γ-secretase inhibitor DAPT.

We generated enteroid lines that express C1C-EGFP constitutively under the control of the UbC promoter (HIE$^{C1C\text{-}EGFP}$). An interesting observation was that HIE$^{C1C\text{-}EGFP}$ exhibit a substantial specking background: cells spontaneously formed C1C-EGFP specks and thereafter were expelled from the epithelium (data not shown). This is in stark contrast to MIE$^{C1C\text{-}EGFP}$, which do not display any specking background under normal culture conditions. Even though HIEs form spontaneous specks, they did not respond to any inflammasome triggers, including the NAIP/NLRC4 triggers MxiH, BsaK, and PrgI, which successfully induced inflammasomes in MIEs (data not shown). Other triggers that we tested were LPS and nigericin for NLRP3, talabostat for NLRP1, and bile acid analogues that have been proposed to activate the pyrin inflammasome (Alimov *et al.*, 2019). None of these additional proposed triggers induced inflammasome formation in HIE$^{C1C\text{-}EGFP}$ (data not shown). For infection, we converted the enteroids into 2-dimensional monolayers, exposing the apical site of the cells to the culture medium. We infected these reporter monolayers with RV (SA11), EMCV, Norovirus, Influenza A virus (SC35M), Vaccinia virus (WR), VSV, Herpes simplex virus (ΔVP22, Δ27.1), Semliki forest virus and SARS-CoV-2. In contrast to the other virus infections, human norovirus infection could not be confirmed. As an example, the infections of duodenal and jejunal HIEs with RV are shown in Figure 4.6. The virus elicited CPE in infected cells, but no inflammasome responses.

As HIE$^{C1C\text{-}EGFP}$ did not form inflammasomes under any of the various treatments or infections performed, we wondered if HIEs can form inflammasomes at all. To detect the potential expression of inflammasome-associated proteins, we extracted the RNA from HIEs from three different intestinal sections (duodenum, jejunum, ileum), either undifferentiated or differentiated with IntestiCult™ ODM and DAPT, and submitted it to bulk 3’ RNA sequencing (Figure 4.7A-K). ASC (gene name: PYCARD) was strongly expressed in all samples, which is not surprising, as we could observe spontaneous speck formation, which is not possible in the absence of ASC. GSDMD and, to a lesser extent, GSDME were expressed as well. With respect to cytokines, there were small amounts of IL-18 and even smaller amounts of IL-1β mRNA, which was slightly upregulated in differentiated enteroids. Caspase-1 was expressed mostly in differentiated enteroids with only minute amounts in undifferentiated enteroids. Caspase-8 tended to be more strongly expressed. Most importantly, however, the transcriptome analysis did not yield reads of any inflammasome sensors, that are

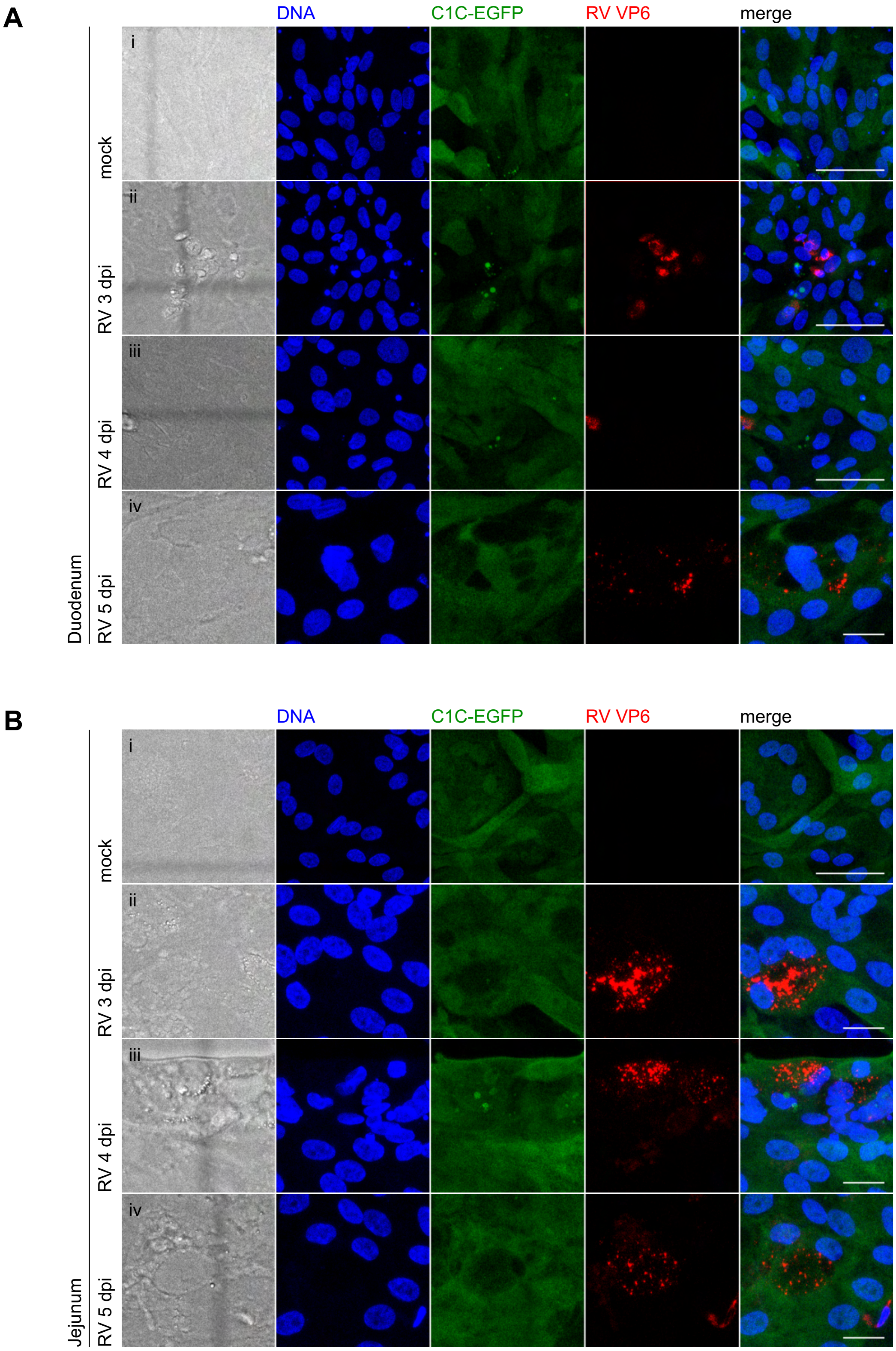

Figure 4.6: Human IECs do not form inflammasomes in response to RV infections. HIE$^{C1C\text{-}EGFP}$ from duodenum (**A**) and jejunum (**B**) were seeded as monolayers, differentiated for 3 days, and infected with an excess of activated RV. After 3, 4, and 5 days, the cells were fixed and RV VP6 was stained with VHH 2KD1-AH647. The cells were recorded by confocal microscopy. Scale bars: A i, ii, iii: 50µm, iv: 20 µm; B i: 50 µm, ii-iv: 20 µm.

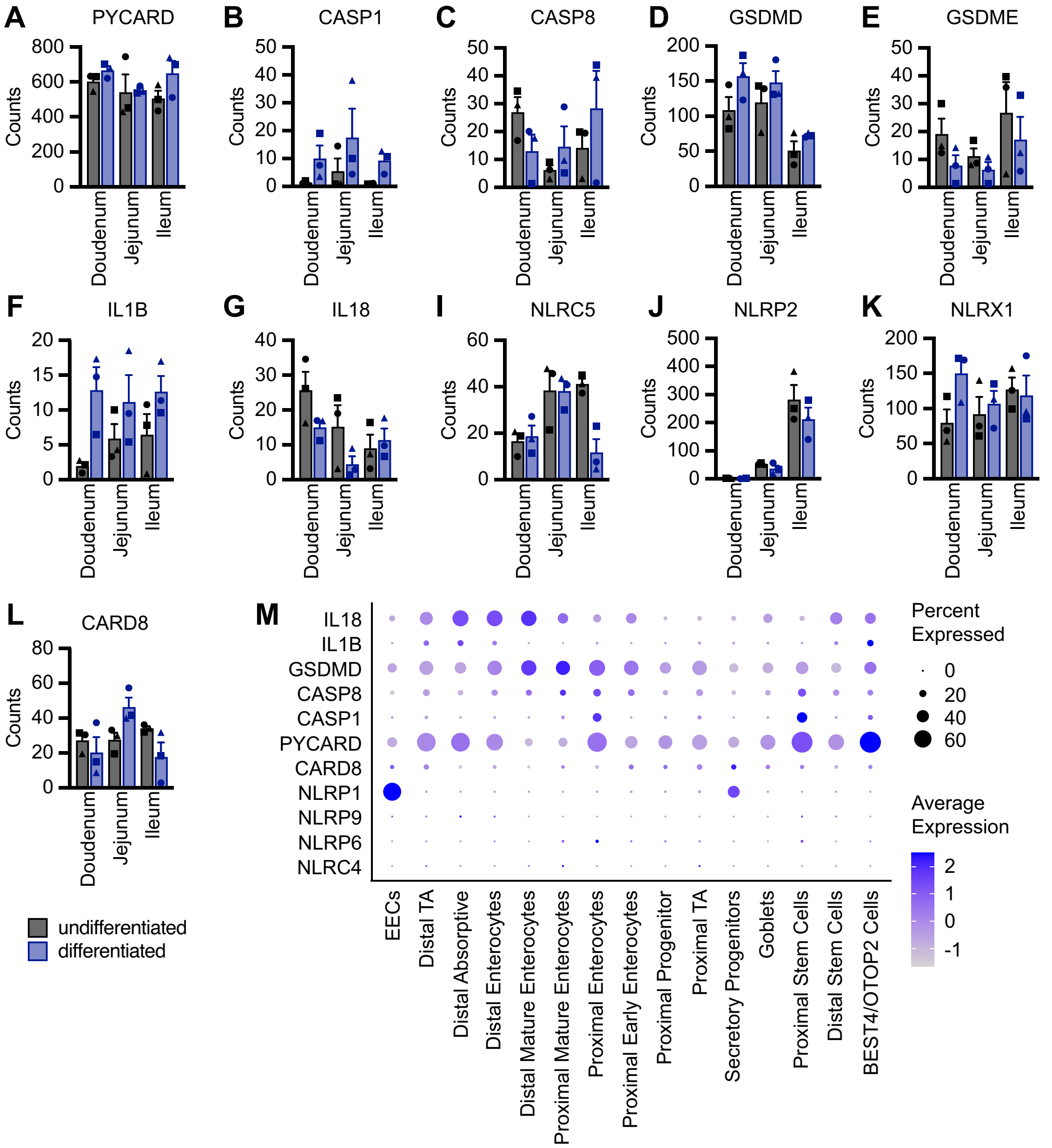

Figure 4.7: Inflammasome expression in human HIEs. (**A-G**) HIEs from duodenum, jejunum, and ileum were differentiated in the presence of 5 µM DAPT for 3 days. The RNA was extracted and submitted to 3’ RNA sequencing. The count matrix was examined using R, and the counts (DESeq2’s median of ratios) for the genes of interest are shown. (**H**) Single cell RNA sequencing data from primary human IECs were downloaded (GEO: GSE158702, Fawkner-Corbett et al., 2021). The expression of genes of interest was visualised using R with the Seurat package.

thought to be expressed in the intestinal epithelium, such as NLRP6, NLRP9, or pyrin (Zhu *et al.*, 2017; Alimov *et al.*, 2019; Ghimire *et al.*, 2020). The only NLR proteins that were detected in the sequencing were NLRC5, NLRX1 and NLRP2

(Figure 4.7I-K). AIM2 was also not found in the data set. CARD8 was expressed in most samples (Figure 4.7L), but the organoids did not respond to talabostat, a known activator of CARD8 (Johnson *et al.*, 2018; Taabazuing *et al.*, 2020).

At this point, it remains unclear if human IECs can express inflammasome sensors and whether the lack of sensors is a limitation of the enteroid model, which is plausible because HIEs are cultured in an unnatural, undifferentiated state. In order to investigate the expression levels of primary human tissue, we analysed a data set from a study in which single cell RNA sequencing was performed on primary human intestinal cells (Fawkner-Corbett *et al.*, 2021). When we queried this data set for inflammasome-related genes, we found that it largely agreed with the results we obtained from bulk RNA sequencing of the enteroids (Figure 4.7M): ASC is robustly expressed across many cell subsets. IL-18 and GSDMD are also broadly expressed, among other cell types in abundant enterocytes. Caspase-1 and -8 are expressed to a lesser extent in enterocytes. NLRC4, NLRP6 and NLRP9 were, if at all, only detected in a very small fraction of cells. These data suggest that the lack of inflammasome sensors might not be a limitation of enteroid culture, but instead the result of tissue-specific regulation in the intestine that we do not yet understand. It has to be noted, however, that single cell sequencing is not very sensitive and weakly expressed genes such as inflammasome sensors might not be detected. Surprisingly, we found that enteroendocrine cells (EECs) express high amounts of NLRP1 according to this data set, opening new avenues for future research in intestinal inflammasomes.

While the absence of most inflammasome sensors explains the lack of inflammasome assembly in HIEs, the expression of other inflammasome components, especially the strong expression of ASC across most cell types, indicates that HIEs can form inflammasomes under certain circumstances in which a relevant sensor is expressed. A strict regulation of inflammasome sensors in epithelial cells seems plausible, because those cells are constantly in contact with PAMPs derived from *e.g.* the gut microbiota. We thus screened for components that could potentially induce the expression of inflammasome sensors. The screen included macrophage supernatant and stool filtrate as crude preparation that mimic the conditions found in the intestine. We also included IFN-α, IFN-β, IFN-γ, and IFN-λ, as well as the bacterial TLR agonists LPS, flagellin, and PAM3CSK4 (Figure 4.8). After incubating HIEs from three different

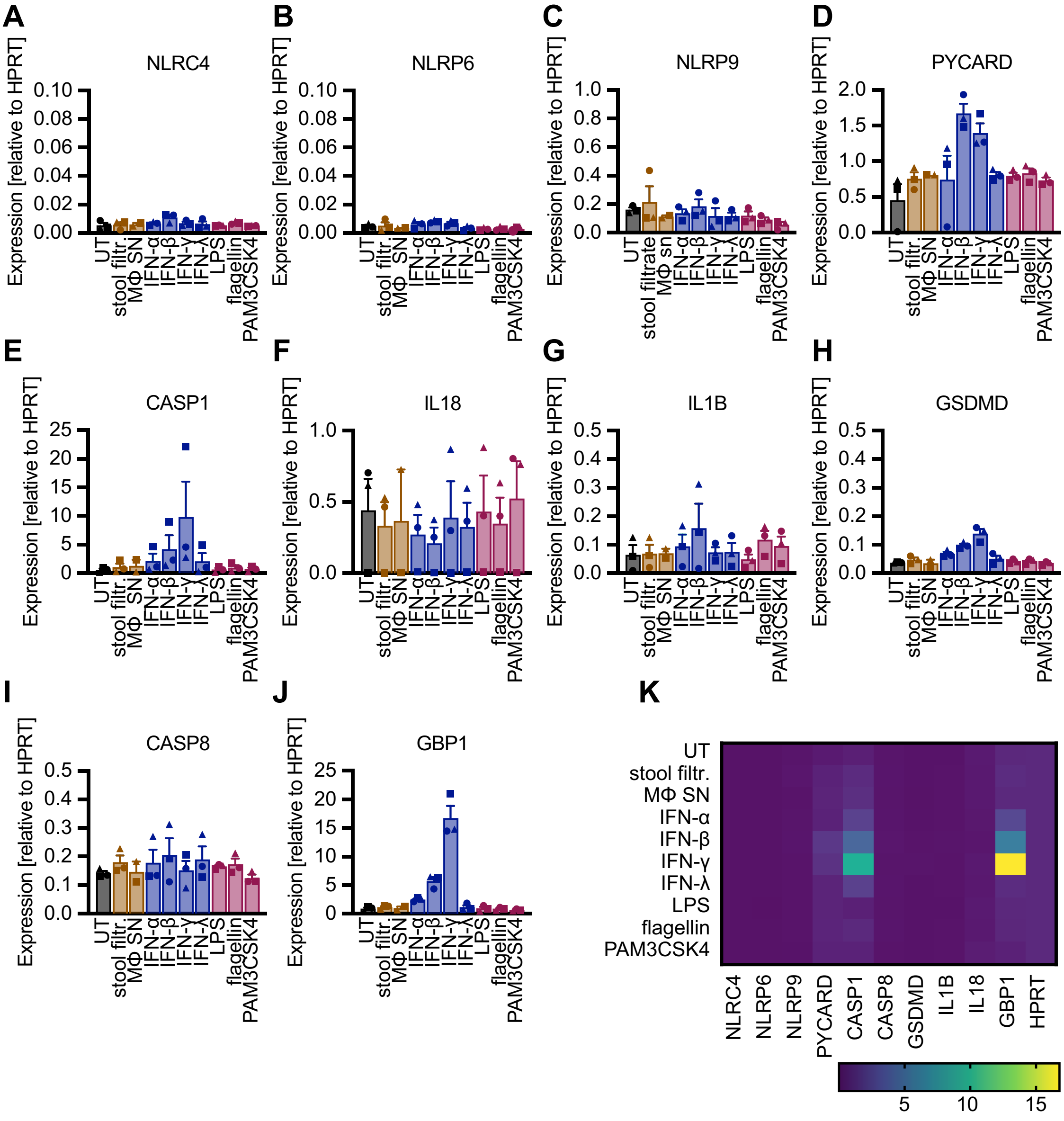

Figure 4.8: Human IECs do not express inflammasome sensors. Jejunal HIEs from 3 different donors were differentiated and treated with 10 % stool filtrate (1:10), macrophage supernatant (1:10), IFN-α (500 U/mL), IFN-β (500 U/mL), IFN-γ (500 U/mL), IFN-λ (500 U/mL), LPS (200 ng/mL), flagellin (1 µg/mL), or PAM3SCK4 (1 µg/mL) overnight. The RNA was then extracted, and the expression of genes of interest was measured by RT-qPCR. The expression was normalized to HPRT using the ΔCT method.

donors with these components, we extracted RNA from all samples and measured the expression of different inflammasome-related genes using RT-qPCR (Figure 4.8). We included GBP1 as a positive control an IFN-γ inducible genes. GBP1 was indeed highly upregulated by IFN-γ and to a lesser extent by other interferons (Figure 4.8J). A similar induction pattern was observed for caspase-1 (Figure 4.8I) and GSDMD (Fig 8H), which were upregulated by IFNs, especially IFN-γ. ASC expression was also increased by IFN-β and IFN-γ (Figure 4.8D). NLRC4 and NLRP6 were not expressed in any of the tested conditions (considering the values on the y-axis) (Figure 4.8A,B). NLRP9 was weakly expressed in all conditions.

In summary, these results highlight the difficulty of studying intestinal inflammasomes even with advanced cell culture techniques. Many claims from literature could not be verified and the functions of NLRP6 and NLRP9 remain elusive. Yet, we could demonstrate that cellular reporters can be established in HIEs, which can also be helpful to investigate other innate immune pathways.

4.2.4 Reporter enteroids can be used to study other immune pathways

Guanylate-binding proteins (GBPs) have been described to link bacterial detection with inflammatory signalling (Santos *et al.*, 2020; Wandel *et al.*, 2020). Santos and colleagues described fluorescent fusions of GBPs as reporters for GBP localization. We constructed lentiviral vectors for the expression of EGFP-GBP1 and used them to transduce HeLa cells (HeLa$^{\text{EGFP-GBP1}}$). The reporter formed some punctae even in untreated cells, but when infected with *Salmonella*, EGFP-GBP1 readily coated the bacteria as described previously (Figure 4.9A). Since *Salmonella* infections are relevant in the intestine, we generated jejunal HIEs harbouring EGFP-GBP1 (HIE$^{\text{EGFP-GBP1}}$) and infected monolayers with *Salmonella* (Figure 4.9B). The infection elicited strong CPE, but GBP1 coating was clearly visible.

Another innate immune pathway that is highly relevant in IECs, especially in the context of virus infections, is IFN signalling. IFN signalling leads to

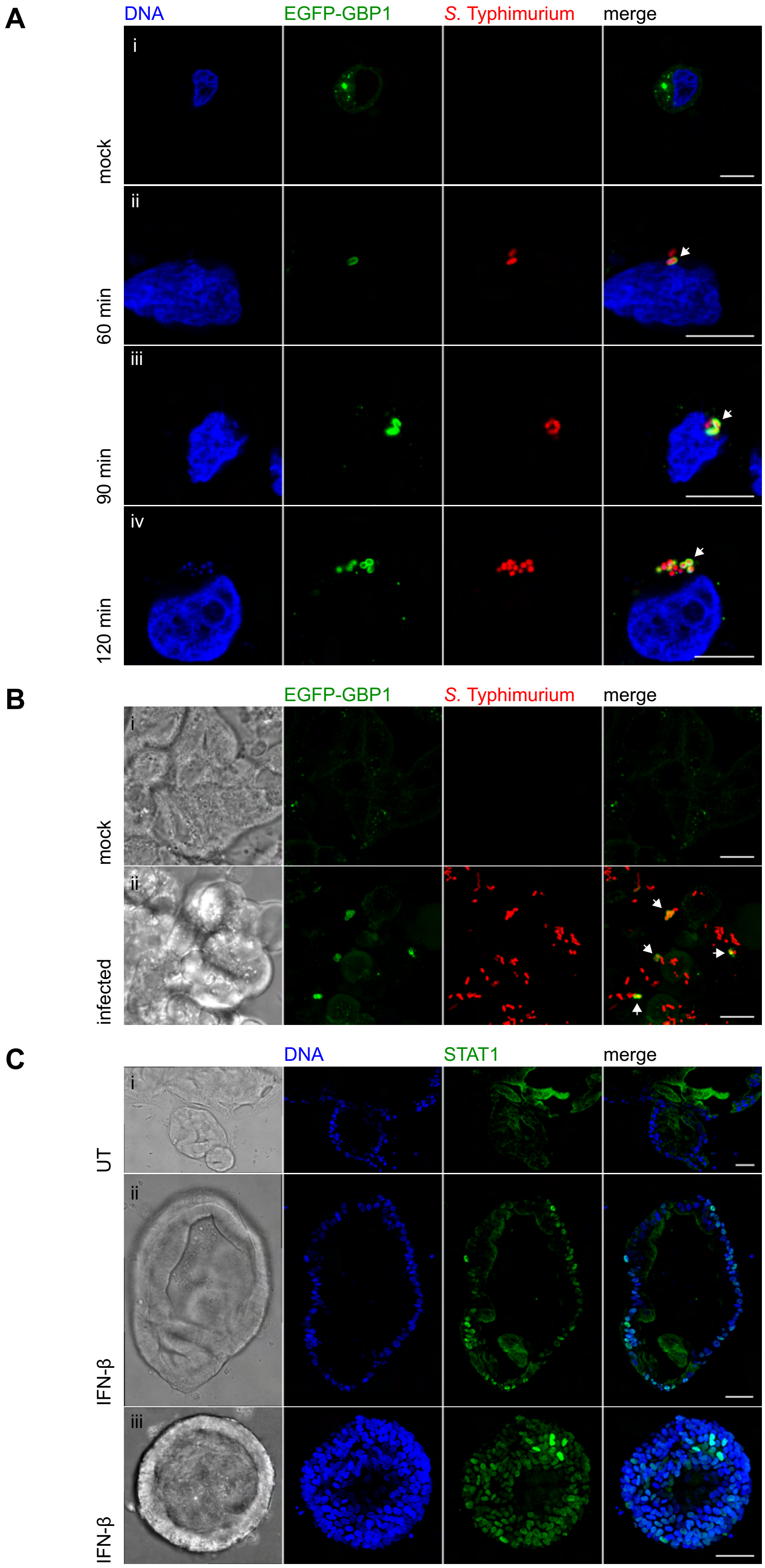
A
DNA
EGFP-GBP1
S. Typhimurium
merge
i
mock
ii
60 min
iii
90 min
iv
120 min
B
EGFP-GBP1
S. Typhimurium
merge
i
mock
ii
infected
C
DNA
STAT1
merge
i
UT
ii
IFN-β
iii
IFN-β

Figure 4.9: Cellular reporters function in human enteroids. (**A**) HeLa$^{\text{EGFP-GFP1}}$ cells were infected with *S.* Typhimurium mCherry for the indicated durations. The cells were then recorded by confocal microscopy. Scale bars: 10 µm. (**B**) Jejunal HIE$^{\text{EGFP-GFP1}}$ were seeded into monolayers, differentiated, and infected with *S.* Typhimurium for 1.5 h. The cells were recorded by confocal microscopy. Scale bars: 10 µm. (**C**) Jejunal HIE$^{\text{STAT1-EGFP}}$ were differentiated, and treated with 500 U/mL IFN-β for 1.5 h. The cells were recorded by confocal microscopy. Arrows indicate GBP-coated bacteria (A,B). Scale bars: 50 µm.

phosphorylation, dimerization, and nuclear translocation of signal transducer and activator of transcription 1 (STAT1). This process can be tracked using STAT1-EGFP as a reporter. We generated jejunal HIEs expressing STAT1-EGFP (HIE$^{\text{STAT1-EGFP}}$) and treated them with IFN-β for 1.5 hours (Figure 4.9C). The translocation of STAT1-EGFP was then assessed by confocal microscopy. We observed that in untreated HIE$^{\text{STAT1-EGFP}}$, STAT1-EGFP appeared confined to the cytoplasm and was localised in a diffuse pattern (Figure 4.9C i). Upon IFN-β treatment we observed that a significant portion of the STAT1-EGFP efficiently translocated to the nucleus (Figure 4.9C ii, iii), thereby confirming the functionality of the reporter in HIEs.

These examples demonstrate that HIEs can be used together with different reporters to study various cellular processes that regulate the immune response.

4.3 Discussion

In this chapter, I studied intestinal inflammasomes. In reconstituted HEK 293T cells, I found that NLRP6 can polymerize ASC, while NLRP9 cannot. However, both sensors did not respond to postulated triggers. As a more physiological model, I established MIEs and HIEs and transduced them to express the newly developed inflammasome reporter C1C-EGFP. I found that MIEs respond to NAIP/NLRC4 triggers, including enteric bacteria, by assembling inflammasomes and expelling affected cells. Other triggers, including virus infections, did not induce inflammasome assembly. The role of inflammasomes in human IECs remains uncertain, as HIEs did not express known inflammasome sensors, which was in agreement with sequencing data from primary human tissue. In general, HIEs can be combined with cellular reporters, as has been demonstrated for GBP1 and STAT1 (IFN signalling).

4.3.1 NLRP6 as an intestinal inflammasome sensor

In HEK 293T cells, overexpression of NLRP6 led to the polymerization of ASC-EGFP (Fig 1A,B). This strongly indicates that NLRP6 forms canonical, ASC-dependent inflammasomes. *In vitro* studies and structural analyses have resulted in two distinct models of NLRP6 oligomerization: one study found that LPS binding induces the formation of rigid dimers, which further oligomerize into linear assemblies when supplemented with ATP (Leng *et al.*, 2020). Another study observed that NLRP6 forms filaments with the PYD at its core, similar to those described for NAIP5/NLRC4 (Diebolder *et al.*, 2015; Shen *et al.*, 2019). $\mathrm{NLRP6}^{\mathrm{PYD}}$ filaments are able to directly nucleate $\mathrm{ASC}^{\mathrm{PYD}}$ assembly. The formation of full-length NLRP6 filaments was concentration-dependent, which explains why NLRP6 nucleated ASC-EGFP specks when overexpressed. We found that the postulated triggers of NLRP6, namely LTA, taurine, and HMW poly(I:C), did not induce inflammasomes in reconstituted HEK 293T cells. This discrepancy could potentially be explained by additional factors that are needed for NLRP6 activation that are missing in HEK 293T cells. However, HMW poly(I:C) and LTA have been shown to directly bind NLRP6 (Hara *et al.*, 2018; Shen *et al.*, 2021), suggesting that additional factors might not be necessary. I observed a weak specking response in NLRP6 reporter cells in response to lipofectamine or the potassium ionophore nigericin (Figure 4.1I), which points towards a potential role of membrane damage or ion flux in NLRP6 activation. However, this would need to be followed up with further experiments.

Recent investigations found that, upon interaction with RNA or LTA, NLRP6 forms condensates through liquid-liquid phase separation (LLPS). Those condensates solidify during ASC polymerization (Shen *et al.*, 2021). It is possible that NLRP6-induced LLPS is somehow restricted in HEK 293T cells, and it is unclear if additional steps are needed for the transition from NLRP6 condensates to the polymerization of ASC. Shen *et al.* (2021) also describe a role for NLRP6 and

LLPS in response to RV infection in the intestine as well as murine hepatitis virus infection in the liver. Furthermore, they found that DHX15 colocalizes with NLRP6 in RNA-induced condensates. Extrapolating from their findings, the authors propose LLPS as a mechanism to unify the different roles described for NLRP6: various upstream signals can induce LLPS and thereby activate NLRP6. Inclusion of different factors into the condensate could then diversify and control the downstream signalling. Even though the study provides compelling approaches to solve the mysteries around NLRP6, further investigation is needed to consolidate the findings and delineate the behaviour of NLRP6 in different contexts. Even though phase separations play roles in many cell biological processes, including RV viroplasm formation, LLPS is a rather new but emerging concept in cell biology (Boeynaems *et al.*, 2018; Alberti *et al.*, 2019; Lyon *et al.*, 2021; Geiger *et al.*, 2021). LLPS might serve as a means to create a milieu that favours the polymerization of inflammasome components, and therefore it should be taken into consideration in future investigations of the activation of NLRP6 and potentially other inflammasomes.

MIEs did not assemble inflammasomes in response to EMCV infection, which was previously described to activate NLRP6-dependent interferon responses in the gastrointestinal tract of mice (Wang *et al.*, 2015). Since the authors found that NLRP6 acted independently of caspase-1, they concluded that NLRP6 does not signal via an inflammasome. Inflammasome assembly is thus perhaps not expected after EMCV infection of enteroids. The authors report that NLRP6 binds viral RNA by employing DXH15 as an adaptor, and interacts with MAVS, leading to its activation and the induction of type I/III IFNs. Interestingly, Shen *et al.* (2021) found that DHX15 associates with NLRP6 in RNA-induced condensates. Since NLRP6 can bind RNA directly, further experiments are needed to delineate whether DHX15 plays an active role in NLRP6 activation or whether it passively binds the RNA within the droplets. A recent study confirmed the role of DHX15 for poly(I:C)- and RV-mediated IFN induction, but also IL-18 production in a human IEC line and in primary mouse IECs (Xing *et al.*, 2021). They also found that IEC-specific DHX15 knockout mice were more susceptible to enteric reovirus infection, concomitant with a decreased intestinal IFN-λ3 and IL-18 responses. Furthermore, the study describes a direct interaction between DHX15 and NLRP6 in mouse IECs, which was enhanced after reovirus infection. After overexpression of all components in HEK 293T cells, the authors found that DHX15 increased the interaction between ASC and NLRP6 as well as IL-18 cleavage. It has to be highlighted that this observation is based on overexpressed proteins and without specific activation of NLRP6. These findings suggest that DHX15 plays a role in both, NLRP6-mediated IFN and inflammasome signalling.

Taken together, it is undisputed that NLRP6 can induce inflammasomes. However, the current knowledge on NLRP6, its activation, and function is convoluted with findings that are challenging to unify. It is for example difficult to understand how compounds as different as RNA, LTA, and taurine could possibly activate the same molecule. There are also different types of NLRP6 assembly states: diffuse protein, phase-separated condensation, linear assemblies as observed after LPS binding, and filaments. Extrapolating from other inflammasome sensors and based on its ability to nucleate ASC, the filament form is likely to induce inflammasomes. The LPS-induced linear oligomers have only been shown *in vitro*, and while LPS induced colocalization of overexpressed NLRP6 and ASC in HeLa cells (Leng *et al.*, 2020), it remains unknown if the linear assemblies also exist within cells. Moreover, it needs to be assessed to what extent LLPS is involved in all of these possible assemblies. Finally, it has to be clarified what role NLRP6 plays in IFN induction. If NLRP6 can activate MAVS, it has to be delineated if inflammasome and IFN induction are mutually exclusive and how the response is modulated. DHX15 is a candidate to drive NLRP6 towards IFN induction, but it has now also been associated with inflammasome signalling. If we can truly understand how NLRP6 behaves on a molecular and cellular level, this will help to comprehend its different biological roles.

4.3.2 NLRP9 – likely not an inflammasome sensor?

We did not find a scenario in which NLRP9 induced inflammasome assembly. Only one study reported that an NLRP9b inflammasome protected mice from RV based on knockout studies (Zhu *et al.*, 2017). Next to NLRP9b, the protection depended on ASC, caspase-1/11, and GSDMD, suggesting that a canonical inflammasome is assembled in response to RV infection. The authors further described DHX9 as an adaptor for NLRP9b to bind dsRNA. They show that DHX9 can be co-precipitated with NLRP9b after RV infection but did not investigate whether it is required for RV restriction. My overexpression experiments suggest that human NLRP9 cannot polymerize ASC and therefore does not assemble inflammasomes (Fig 1A,B). RV infection of MIEs did also not induce inflammasome formation. PYDs of inflammasome sensors tend to form oligomers and filaments when they are purified. We produced NLRP6^{PYD} and NLRP9^{PYD} in bacteria and found that NLRP6^{PYD} formed insoluble oligomers, whereas NLRP9^{PYD} was soluble and did not oligomerize (data not shown). Later, the crystal structure of NLRP9^{PYD} was solved (Marleaux *et al.*, 2020; Ha and Park, 2020). Both studies confirmed that NLRP9^{PYD} does not self-polymerize in solution. This can be explained by several charge inversions within the PYD interaction interfaces in comparison to the filament forming PYDs of NLRP3, NLRP6, AIM2, and ASC. Nevertheless, Marleaux *et al.* (2020) modelled a hypothetical NLRP9^{PYD} filament based on the structure of the NLRP6^{PYD} filament (Shen *et al.*, 2021). The predicted electrostatic surfaces of this model oppose the existence of such filaments and ASC nucleation. Ha and Park (2020) found a unique bent N-terminal loop, which is also likely to restrict filament formation.

Between our own experiments and the study by Zhu *et al.* (2017), which describes the NLRP9b inflammasome in response to RV infection, there are two differences that might be important: 1) The NLRP9b inflammasome was reported in mice, but my overexpression experiments were done with human NLRP9. It is important to note that mice have three isoforms of NLRP9, whereas human have only one. 2) We used a different RV strain for enteroid infection. Most available data suggest that NLRP9 cannot readily form inflammasomes. It is of course possible that NLRP9 is tightly regulated and needs further modifications that enable it to oligomerize. PTMs, for example, could change the surface charges that prevent NLRP9^{PYD} self-assembly. The current evidence and the fact that so far no other study has confirmed the existence of an NLRP9 inflammasome, makes it doubtful that NLRP9 is a genuine inflammasome sensor. Another indication that NLRP9 rather serves an inflammasome-independent function is that it is highly expressed in oocytes, which express neither ASC nor caspase-1 (Karlsson *et al.*, 2021; The Human Protein Atlas, n.d.).

4.3.3 Differences between mouse and human enteroids

To study inflammasome responses in IECs, I established the generation, culture, and modification of mouse and human intestinal enteroids. Regarding the culture of mouse and human enteroids, it is important to understand the differences in their respective culture systems and the resulting implications. MIEs, because they are cultured in a differentiated state, are readily available for experiments that require differentiated cells. The scarcity of stem cells, on the other hand, makes some applications more challenging. These include lentiviral transduction and conversion into 2-dimensional monolayers. Those methods rely on stem cells for survival and proliferation after the procedure, thus requiring the enrichment of stem cells. This can be achieved by the addition of recombinant Wnt3a. Because recombinant Wnt3a is not well soluble in water and poorly suitable as a stable medium supplement (Janda *et al.*, 2012; Janda and Garcia, 2015), undefined Wnt3a-conditioned medium is commonly used as an alternative. More recently, a ‘next generation surrogate’ Wnt has been reported as an alternative (Miao *et al.*, 2020). In the present study, I used the glycogen synthase kinase-3 (GSK3) inhibitor CHIR99021 to boost Wnt signalling. In contrast, HIEs are cultured in an undifferentiated state and therefore do not require further enrichment of stem cells for such applications. However, it can be difficult to fully differentiate HIEs and differentiated enteroids lose their integrity over few days.

I generated mouse and human (m)C1C-EGFP reporter enteroids. MIE$^{mC1C\text{-}EGFP}$ displayed no specking background. That is, I did not observe a single speck in untreated mouse enteroids over the period of my PhD studies. HIE$^{C1C\text{-}EGFP}$, on the other hand, displayed a low but considerable background of C1C-EGFP specks. At this point, it is unclear whether these specks represent *bona fide* inflammasomes or are artifacts caused by the expression of C1C-EGFP. When C1C-EGFP is overexpressed, it typically oligomerizes into filaments instead of specks. However, we observed C1C-EGFP background as specks in THP-1 cells as well (see 3.2.2). As discussed earlier, this might be due to the involvement of endogenous ASC. Interestingly, specking cells were efficiently expelled from the epithelium and underwent pyroptosis, as assessed by propidium iodide uptake and morphology, implying that downstream inflammasome functions are activated. Even though this may be caused by artificial C1C-EGFP-(ASC)-caspase-1 assemblies, this observation exemplifies that human IECs possess the ability to expel cells after inflammasome assembly akin to the findings in mouse IECs (Rauch *et al.*, 2017). When I dedifferentiated MIEs for the purpose of seeding monolayers, I found that they displayed the same specking background as HIEs, including cell expulsion. The difference in specking background is therefore dependent on the differentiation state of the enteroids and not necessarily the species. This phenomenon could be explained by two different hypotheses: 1) Dedifferentiated highly proliferative IECs employ inflammasomes as a means to eliminate aberrant cells. 2) As proposed for THP-1 cells earlier (see 3.3.2), IECs might possess a mechanism to curtail high caspase-1 expression in order to prevent its self-activation. This ability might be lost upon dedifferentiation, rendering the cells susceptible to C1C-EGFP self-oligomerization and subsequent caspase-1 activation. The most important question when investigating this is whether the specks are caused by C1C-EGFP expression. To elucidate this, WT and reporter enteroids would have to be compared after staining of endogenous ASC. If the specks appear in WT enteroids as well, this is likely to be a physiological phenomenon that calls for further investigation.

The main difference between MIEs and HIEs is in which state of differentiation they are cultured. The difference in the specking background of reporter enteroids may be a direct implication of this. While many principles of enteroid culture apply for mouse and human, the models have practical differences, which might pose limitations, and not all methods can be easily transferred between mouse and human enteroids.

4.3.4 Inflammasomes in mouse enteroids

By ASC staining, we showed that mouse IECs, cultivated as enteroids, form ASC specks in response to NAIP/NLRC4 triggers. As an alternative approach, I introduced the inflammasome reporter mC1C-EGFP into the MIEs and confirmed the functionality of MIE$^{\text{mC1C-EGFP}}$ by microscopy and flow cytometry. In contrast to the classical ASC staining, the reporter allows real-time observation of inflammasome assembly via live-cell imaging and thus facilitates the investigation of the response kinetics. This way, we could confirm that mouse IECs assemble a canonical inflammasome and expel affected cells into the lumen. Overstimulation of NAIP1/NLRC4 by MxiH caused rapid disintegration of the enteroids. Cell expulsion could be observed more easily in apical-out enteroids. We also observed inflammasome assembly and cell expulsion after infection with *Salmonella*. *Shigella* also induced inflammasome assembly, but the response was comparably scarce. The most curious observation in *Salmonella*-infected MIEs was the occurrence of apparent channels between the lumen of the enteroid and the surrounding medium. This is important because they constitute a breach of the epithelial barrier. These channels were always associated with bacteria and specking cells. Of note, these specking cells and bacteria were located at the outside of the enteroid, *i.e.* the basolateral site of the epithelium, meaning that bacteria have successfully breached the epithelial barrier. *Salmonella* is known to manipulate the host actin cytoskeleton. This is most prominent during bacteria uptake and in the formation of an actin meshwork around *Salmonella*-containing vacuoles (Patel and Galán, 2005; Lhocine *et al.*, 2015; Heggie *et al.*, 2021). It is thus possible that *Salmonella* prevents actin-mediated closure of gaps in the epithelium. The main route for *Salmonella* to cross the epithelium is by targeting M cells in Peyer’s patches (Jensen *et al.*, 1998; Hallstrom and McCormick, 2011), but it can also traverse the epithelium, likely by manipulating vesicular trafficking and exiting at the basolateral side (Müller *et al.*, 2012). Jensen *et al.* (1998) observed holes in the epithelium after infection with *Listeria monocytogenes* and

Shigella flexneri. My observations might represent a similar phenomenon. The ability of *Salmonella* to manipulate host cells depends on its pathogenicity islands. Infecting enteroids with *Salmonella* that lack SPI-1 or SPI-2, and testing for potential epithelial breaches, would provide insights into how these holes are caused by the bacteria. In addition, it would be valuable to record the dynamics of this process by live-cell microscopy. A live actin dye or reporter would be helpful to monitor epithelial integrity.

Multiple viruses were able to infect and kill MIEs. EMCV could be readily detected by its dsRNA genome intermediate. To detect RV-infected cells, I used a nanobody that I recombinantly produced and labelled myself. All infection experiments indicated that inflammasomes are not formed in enteroids in response to the tested viruses. It would be interesting to test different virus strains, since they can behave differently with regard to inflammasome responses in our experience. It would be of particular interest to investigate the RV strain used by *Zhu at al.* who originally described the NLRP9b inflammasome (Zhu *et al.*, 2017). The experiments with HIEs, as will be discussed below, exemplified the need to verify the expression of relevant proteins, as inflammasome sensors were not expressed. Before undertaking additional infection experiments with MIEs, it is therefore advisable to test them for the expression of *e.g.* NLRP6 and NLRP9b. Bulk 3' RNA sequencing would provide useful information on the whole transcriptome, whereas RT-qPCR could be used to sample a set of genes of interest. The translation of the proteins could be examined by immunoblotting.

4.3.5 Inflammasomes in human enteroids

Genetic manipulation and *in vivo* studies are valuable tools to investigate mouse biology but are not available for humans. Yet, the human biology is more relevant regarding medical applications. Organoids provide new opportunities to investigate human cell biology in more complex and physiological models, while allowing access to many cell biological tools. We took advantage of this by generating human reporter enteroids to study inflammasome activation in human IECs. However, HIEs from three different gut segments and from different donors did not assemble inflammasomes in response to any triggers or infections that we tested, including those that induced inflammasomes in MIEs, *i.e.* the NAIP/NLRC4 triggers MxiH and *Salmonella*. The only C1C-EGFP specks that we observed were the ones that formed in the absence of stimulation as discussed in 4.3.3. Bulk 3' RNA sequencing and RT-qPCR revealed that the HIEs did not express any inflammasome sensors of interest, and their expression could not be induced by a panel of stimuli. These results largely overlapped with single cell sequencing data from primary human intestinal tissue (Fawkner-Corbett *et al.*, 2021), suggesting that inflammasome sensors might not be expressed in the IECs under steady-state conditions. However, the expression of other inflammasome components, such as ASC and GSDMD, imply that human IECs generally have the capability for inflammasome signalling. Indeed, the unspecific C1C-EGFP assemblies induced pyroptosis and cell expulsion in HIEs, demonstrating that human IECs are able to respond appropriately to inflammasome assembly. Staining of endogenous ASC will reveal if these specks represent *bona fide* inflammasome. Since the intestinal epithelium is populated by numerous microbes, which can potentially activate inflammasomes, it is reasonable that inflammasome sensors are tightly regulated to prevent an overt response and an ensuing inflammation. It is also possible that some inflammasome sensors, such as NLRP6, are only expressed in distinct locations within the intestine and were therefore missing in the samples for organoid generation or sequencing.

The single cell data from Fawkner-Corbett *et al.* (2021) shows that human enteroendocrine cells (EECs) express NLRP1, an inflammasome sensor that is mainly associated with the skin. This is especially interesting, because we know that some RV strains can activate NLRP1 (Schmidt lab, unpublished data). If intestinal cells express NLRP1, they could present a physiological case where RV comes into contact with this sensor. Recently, a model for the study of EECs was established (Chang-Graham *et al.*, 2019). The authors generated an HIE line with doxycycline-inducible expression of neurogenin-3, a transcription factor that induces the differentiation towards EECs. They used RNA sequencing to characterise the effects of neurogenin-3 expression and kindly provided us the data set, in which I found that NLRP1 was drastically upregulated upon doxycycline treatment. These insights highly encourage the study of NLRP1 activation in HIEs. We thus cloned neurogenin-3 into an appropriate lentiviral vector and transduced HIEs. In preliminary experiments, we could confirm the upregulation of chromogranin A, a marker for EECs, but not NLRP1 after doxycycline induction. Accordingly, the enteroids did not respond to talabostat or anisomycin, which are known activators of NLRP1 (data not shown). Alternatively, EEC differentiation can be induced by supplementing the medium with small molecules. Various combinations of rimonabant, SP600125 and AS1842856 led to robust EEC differentiation and hormone production (Zeve *et al.*, 2022).

T3SS ligands are known to bind to NAIP proteins and activate an NLRC4 inflammasome. A recent study, however, found that human IECs express, if at all, only marginal amounts of NAIP and NLRC4, which is in agreement with my own findings (Holly *et al.*, 2020; Naseer, Zhang, *et al.*, 2022). It was reported that human IECs instead responded to *Salmonella* infection with a caspase-4-dependent noncanonical inflammasome. This response was dependent on SPI-1, and the authors suggest that caspase-4 binds LPS directly. In mice, caspase-11 responds in a similar way to *Salmonella* infection (Broz *et al.*, 2012; Crowley *et al.*, 2020). When I infected HIEs with *Salmonella* to test the GBP1 reporter, I observed strong cytopathic effects, that could have been pyroptosis. According to the RNA sequencing, caspase-4 is robustly expressed in my enteroids (data not shown). It is thus possible that we observed a non-canonical inflammasome as described by Naseer, Zhang, *et al.*, (2022). Future investigations of inflammasomes in human IECs should thus take non-canonical inflammasomes into consideration.

In previous studies, non-canonical inflammasomes did not lead to direct cytokine maturation but only induced pyroptosis (Rühl and Broz, 2015; Schmid-Burgk *et al.*, 2015). K^+ efflux then activated a secondary NLRP3 inflammasome and thereby also cytokine maturation. In contrast, Naseer, Zhang, *et al.*, (2022) found that IL-18 was cleaved in an ASC-independent manner. This raises the question whether caspase-4 and other non-canonical inflammasome-related caspases are regulated in their range of substrates akin to caspase-1 (see 3.3.6). The exact mode of assembly for non-canonical inflammasomes is not clear. For example, it is unknown whether all inflammatory caspases form filaments as caspase-1 does. Although all inflammatory caspases possess potential cleavage sites in their IDLs as well as their CDLs, their processing is less well investigated compared to caspase-1. It was shown that LPS induces the cleavage of caspase-5 but not caspase-4 (Viganò *et al.*, 2015). In contrast, a recent preprint describes that also caspase-4 self-cleaves its IDL after dimerization or LPS stimulation, and the resulting p34/p9 species was able to directly process GSDMD and IL-1β (Chan *et al.*, 2023). The authors further found that IDL processing is required for cleavage of both substrates.

4.3.6 Future directions

This chapter describes multiple avenues for future investigations. Others and I have demonstrated that MIEs are a powerful tool to study intestinal inflammasomes and the associated cellular events such as cell expulsion. After infection with *Salmonella*, MIEs exhibited apparent channels, which compromise the epithelial integrity. Because this may be relevant for bacterial invasion, this phenomenon should be further investigated. Live-cell microscopy would offer further insights in the formation of these channels, and the inclusion of *Salmonella* strains that lack SPI-1, SPI-2, or individual proteins could help to uncover the underlying mechanism.

HIEs did not assemble specific inflammasomes in this study. However, the potential expression of NLRP1 in EECs offers a new angle to investigate inflammasomes in human IECs. Enteroids expressing doxycycline-inducible neurogenin-3 or other means to enrich EECs should be further evaluated to recapitulate the models developed by Chang-Graham *et al.*, (2019) and Zeve *et al.* (2022). Combined with C1C-EGFP, this can be used to study NLRP1 in EECs.

Next to classical NLRP1 triggers, it should be tested whether RV can activate NLRP1 in EECs.

There is evidence that human IECs form a caspase-4-dependent non-canonical inflammasome in response to *Salmonella* infection. HIE$^{C1C\text{-}EGFP}$ would not be able to detect non-canonical inflammasomes, because caspase-1 is not involved. While classical inflammasome readouts like IL-18 measurements could potentially be used to investigate non-canonical inflammasomes, it would be interesting to also visualise the assembly of caspase-4. To this end, a reporter similar to C1C-EGFP could be generated *i.e.* caspase-4^{CARD}-EGFP (C4C-EGFP). Besides caspase-1, it is currently unknown if other inflammatory caspases can polymerize into filaments or form other assemblies. C4C-EGFP and homologue reporters for other caspases would allow us to answer that question. Knowledge about the assemblies of these caspases might also help us to understand how these caspases are regulated in terms of self-processing and substrate specificity. So far, it has not been investigated if GBPs are involved in the detection of bacteria and the recruitment of caspase-4 in human IECs. Combining C4C-EGFP with fluorescent GBP reporters could visualise large parts of the non-canonical inflammasome assembly and further our understanding of this signalling platform. Such studies would also help to comprehend the differences between mouse and human regarding the defence of enteric bacteria.

The case of non-canonical inflammasomes and GBPs suggests that a combination of cellular reporters can yield valuable insights, because different components can be observed at the same time. While STAT1-EGFP demonstrated that most cells within HIEs are capable of IFN signalling, it is unclear which cells can induce interferons. Combining a STAT1 reporter (IFN signalling) with an IRF3 reporter (IFN induction) would allow an evaluation of the function of each cell within a tissue. Similar considerations can be made across different types of immune responses. For example, IFN reporters can be combined with inflammasome reporters to see how those signalling pathways are distributed across cells, if they are mutually exclusive, and if there are cells that specialise in one or the other type of signalling.

4.3.7 Conclusion

In terms of the less well understood inflammasome sensors, I found that NLRP6 can certainly assemble inflammasomes, while NLRP9 might be limited to different functions. However, many questions remain about NLRP6, its activation, and functions, and further research will be needed to fully understand this protein. MIEs did not form inflammasomes in response to postulated NLRP6 or NLRP9b triggers. On the other hand, I could confirm the published findings regarding NAIP/NLRC4 inflammasomes and include the observation of inflammasome assembly, encouraging the use of MIEs as a model to study intestinal inflammasomes. HIEs did not assemble inflammasomes, but non-canonical inflammasomes as well as NLRP1 in EECs can likely be investigated using this model. Finding modes of inflammasome activation in HIEs will enable us to transfer the knowledge of mouse intestinal inflammasomes to the human intestine to study accompanying cellular processes such as cell expulsion.

Chapter 5: Nanobodies against SARS-CoV-2 demonstrate a novel neutralization mechanism

5.1 Introduction

The recent SARS-CoV-2 pandemic posed unprecedented challenges to society, health care systems, and science. Although effective and safe vaccines offer the best chance to control the pandemic, they may not sufficiently protect immunocompromised patients (Boyarsky *et al.*, 2021b; Boyarsky *et al.*, 2021a). For high-risk patients additional prophylaxis or treatment might also be necessary. Passive immunisation by antibodies or related molecules offers an additional tool to prevent or treat viral infections (Abraham, 2020). In such efforts nanobodies constitute suitable lead molecules, because of their favourable properties in terms of size, stability, ease of engineering, and manufacturing.

The cognate receptor for SARS-CoV-2 entry is ACE2, to which it binds via the RBD of its trimeric spike protein. The RBD can adopt either a ‘down’ or an ‘up’ configuration. The up configuration is associated with ACE2 binding and membrane fusion (Song *et al.*, 2018; Hoffmann, Kleine-Weber, Schroeder, *et al.*, 2020). Most neutralizing antibodies bind to the up conformation and prevent ACE2 binding through competition (Wrapp, Wang, *et al.*, 2020; Walls *et al.*, 2020; Lv *et al.*, 2020). Other antibodies neutralize the virus by locking the RBD in the down configuration and thereby prevent the conformational changes required for cell entry (Tortorici *et al.*, 2020; Schoof *et al.*, 2020).

All work presented in this chapter is published (Koenig *et al.*, 2021). The publication is attached in the appendix. An alpaca and a llama were immunised with the RBD or the RBD and inactivated virus. A nanobody library was then generated and screened for nanobodies specific for the RBD of the SARS-CoV-2 spike protein, leading to the identification of 23 candidates. For 10 of these, binding was confirmed by enzyme-linked immunosorbent assay and four nanobodies proved to potently neutralize SARS-CoV-2 and SARS-CoV-2-

pseudotyped vesicular stomatitis virus (VSV): VHHs E (derived from the llama), U, V, and W (derived from the alpaca). The binding affinity to the RBD was determined by surface plasmon resonance (SPR) spectrometry, by which dissociation constants of 2 nM, 21 nM, 9 nM, and 22 nM for VHHs E, U, V, and W were measured, respectively. SPR and X-ray crystallography revealed that the nanobodies bind to two distinct epitopes on the RBD, which are denoted interfaces *E* and *UVW*, referring to the nanobodies that bind them. VHH E binds to the ACE2 binding site on the RBD and is therefore expected to compete with ACE2 binding. VHHs U and W bind the distinct *UVW* interface. Their mode of binding is the same, as the only amino acids that differ between them are found in the framework region and are not involved in binding. VHH V also binds *UVW* but is oriented differently. Although nanobodies U, V, and W bind to an epitope distinct to the ACE2 binding site, they are also expected to compete with ACE2 binding due to steric clashes with glycans on ACE2. Cryo-electron microscopy (cryo-EM) of trimeric spike in complex with VHH E and VHH V revealed that VHH E stabilises a conformation of the spike with all three RBDs in the up configuration (3-up), a state that is compatible with ACE2 binding (Song *et al.*, 2018). Spike with bound VHH V, on the other hand, yielded structures with two of the RBDs in the up and one in the down conformation (2-up). Interestingly, VHH V displaced all RBDs by 8 or 11 Å in order to accommodate binding of three nanobodies.

Based on the structural information, we designed biparatopic nanobodies, which bind to the different epitopes, *i.e.* VHH E linked to either VHH V or W connected by a $(GGGGS)_3$ linker. The C-terminus of VHH V and the N-terminus of VHH E, when bound to a single RBD, are close enough to allow VHH VE to bind to one RBD with both valences. In the reverse configuration (VHH EV), this would not be possible and, as a result, VHH EV would induce strain when bound to a single RBD, bind to two different RBDs in a spike trimer simultaneously, or employ only one valence at a time. Both biparatopic nanobodies bound more strongly to the RBD – probably due to higher avidity – and showed increased neutralizing activity, which exceeded the best performing single nanobody (VHH E). VHH VE stabilises the RBD 3-up conformation, probably due to the VHH E portion. The structure also suggests that binding of different RBDs in a trimer by the same epitope is feasible, prompting us to produce VHHs EE, EEE, and VV. While VHHs EE and EEE displayed greatly enhanced neutralizing activity with VHH EEE being the most potently neutralizing construct in this study, VHH VV neutralized only slightly better than monoparatopic VHH V, likely due to an inability to bind two different epitopes simultaneously. The kinetic parameters of the nanobodies are summarised in the Table A.2 (appendix).

5.2 Results

5.2.1 Cell fusion assays can visualise SARS-CoV-2 spike-catalysed membrane fusion

ACE2 can only bind to the spike trimer with at least one RBD in the up state, and binding to ACE2 leads to more RBDs adopting the up state (Benton *et al.*, 2020). The 3-up conformation is expected to trigger conformational changes that release the S1 subunit and expose the secondary cleavage site for processing, which then induces membrane fusion. Because the EM structures revealed that some nanobodies stabilised the RBD 3-up conformation, we aimed to examine whether the nanobodies also activate the spike fusion machinery. We established HEK 293-based assays, in which two cell lines that either expressed EGFP or tagRFP-t were mixed at a 1:1 ratio. Cell fusion was then induced either by ACE2-spike interaction after induction of ACE2 expression or by spike alone in the presence of nanobodies. Cell-cell fusion is expected to yield syncytia that contain a mixture of both fluorescent proteins. This event could be microscopically observed via the formation of yellow (green + red) syncytia, which can be quantified by correlating the fluorescence of both proteins.

We established quantification of fusion using a first fusion assay that relies on the ACE2-mediated activation of SARS-CoV-2 spike, which induces spike-catalysed fusion (Figure 5.1A). We generated HEK 293 cell lines that express SARS-CoV-2 spike Δ18 via an inducible promoter and constitutively express EGFP (HEK$^{\text{spike(i)+EGFP}}$) or ACE2-tagRFP-t (HEK$^{\text{ACE2-tagRFP-t}}$). The cell lines were seeded to an equal amount of both cell lines, cultivated for 24 h, and doxycycline was added to induce spike expression. Because HEK 293 cells do not express ACE2, the SARS-CoV-2 spike is not expected to mediate cell fusion without ACE2 induction. Doxycycline induction led to the formation of syncytia and eventually to nearly complete cell-cell fusion within 12 hours, as could be observed by widefield microscopy. Unfortunately, the membrane-bound ACE2-tagRFP-t

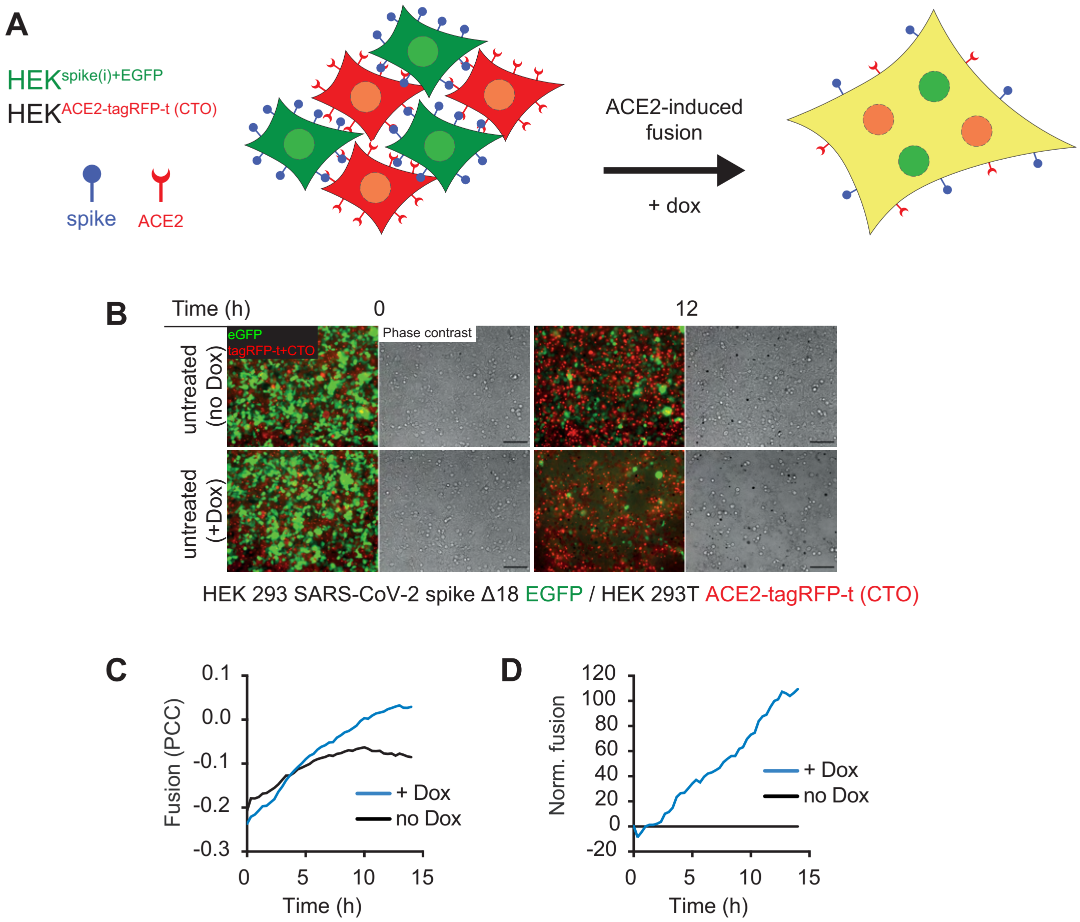

Figure 5.1: Cell fusion assays quantify the spike fusion activity. (**A**) Experimental setup. HEK$^{spike(i)+EGFP}$ cells and CTO-labelled HEK$^{ACE2-tagRFP-t}$ cells were seeded in a 1:1 ratio. Spike expression was induced with doxycycline and microscopy images were recorded every 20 minutes for 14 h at 37°C. (**B**) Representative images of cells at 0 h and 12 h post induction. Scale bars: 100 µm. (**C**) Fusion was quantified by calculating the Pearson correlation coefficient (PCC) between green and red fluorescence. Mean values from 4 fields of view of an experiment representative of 3 independent experiments are shown. Since the punctate ACE2-tagRFP-t signal precluded strong absolute PCCs, PCC values were normalized subtracting the values at t = 1 h as well as the signal in the control without doxycycline, and corrected PCC values at 12 h in doxycycline-treated cells were defined as 100% fusion.

appeared as punctate structures, which precluded proper colocalization with EGFP and thus quantification. Therefore, we additionally stained ACE2-tagRFP-t cells with CellTracker^{TM} Orange CMRA (CTO), a fluorescent dye, which is cell permeable but is converted to be non-permeable within the cell. CTO staining led to efficient colour mixing (Figure 5.1B) and allowed colocalization. We quantified the fusion by calculating the Pearson correlation coefficient (PCC) between the green and the red signal (Figure 5.1C). The punctate tagRFP-t still interfered with the correlation, prompting us to normalize the fusion by subtracting the PCC value from the uninduced control at the first time point and defining the corrected 12 hours endpoint value of the induced sample as 100 % (Figure 5.1D). The normalization resulted in a clear and time-dependent increase in cell fusion, that matched the formation of syncytia.

5.2.2 Nanobodies can cause spike to mediate cell fusion

We next tested whether stabilisation of the RBDs in the up conformation by nanobodies activates the fusion machinery in the absence of ACE2. For this, we used two HEK 293-based cell lines that both express the SARS-CoV-2 spike protein on their cell surface and that additionally and constitutively express either EGFP (HEK$^{\text{spike(i)+EGFP}}$) or tagRFP-t (HEK$^{\text{spike(i)+tagRFP-t}}$). We mixed the green and red fluorescent cell lines at an equal ratio, treated them with the different nanobodies (spike-specific nanobodies: VHH E, U, V, W, Ty1 (Hanke *et al.*, 2020); control nanobody against mCherry: VHH LaM-4 (Fridy *et al.*, 2014) (Figure 5.2A), and recorded the cells by fluorescence microscopy over a period of 14 hours (Figure 5.2B). As expected, untreated cells and cells treated with the control nanobody LaM-4 did not show any signs of fusion or toxicity. However, treating the cells with VHH E, U, or W resulted in clearly visible cell-cell fusion. In this case, because both fluorescent proteins can freely diffuse, the fusion could be quantified using the PCC directly without the need for normalization. VHH-induced fusion was particularly prominent for VHH U and W, resulting in fusion of all cells in the field of view, but was substantially weaker for VHH E, which only induced partial fusion. VHH V barely induced fusion, whereas no fusion was observed upon addition of VHH Ty1. The results are summarised in Figure

5.2D,E. Binding of the RBD by some nanobodies may thus induce conformational changes that mediate fusion. The fact that VHH E but not VHH V induces fusion, indicates that the RBD 2-up conformation is not sufficient to activate the fusion machinery and that stabilisation of the RBD 3-up conformation is necessary. The fusogenicity of the nanobodies did not correlate with their neutralizing potency.

Since binding to ACE2 or to nanobodies can both activate the spike protein to fuse with proximal membranes, we aimed to investigate whether the nanobodies influence ACE2-induced fusion. This would be especially interesting for VHH E, which shares an epitope with ACE2, thus competing with binding. We again mixed $\text{HEK}^{\text{spike(i)+EGFP}}$ cells with $\text{HEK}^{\text{ACE2-tagRFP-t}}$ cells and subsequently added the nanobodies together with the doxycycline. Nearly complete cell fusion was observed in almost all samples (Figure 5.3). The only nanobody that had an effect was VHH E, which reduced spike-ACE2-mediated fusion to half. This is probably due to VHH E masking the ACE2 binding site and thereby preventing ACE2-mediated fusion. However, VHH E itself leads to moderate amounts of cell-cell fusion, which explains this observation.

It is somewhat counterintuitive that the nanobodies, which were shown to neutralize SARS-CoV-2, do not inhibit spike-catalysed membrane fusion, but instead activate it. It has to be considered that in the VHH-mediated fusion assays, the cells were treated with the nanobodies one day after induction of spike expression. At the onset of the experiment, a large number of spike trimers at the cell surface was thus exposed to membranes of neighbouring cells in close proximity. In this context, activation of spike by nanobodies catalysed cell-cell fusion. During neutralization of virions, however, the nanobodies bind to the spike on virions in the absence of target membranes. Thus, premature activation of this metastable state cannot facilitate infection but rather irreversibly converts the spike protein into its post-fusion conformation, precluding *bona fide* fusion events upon host cell contact.

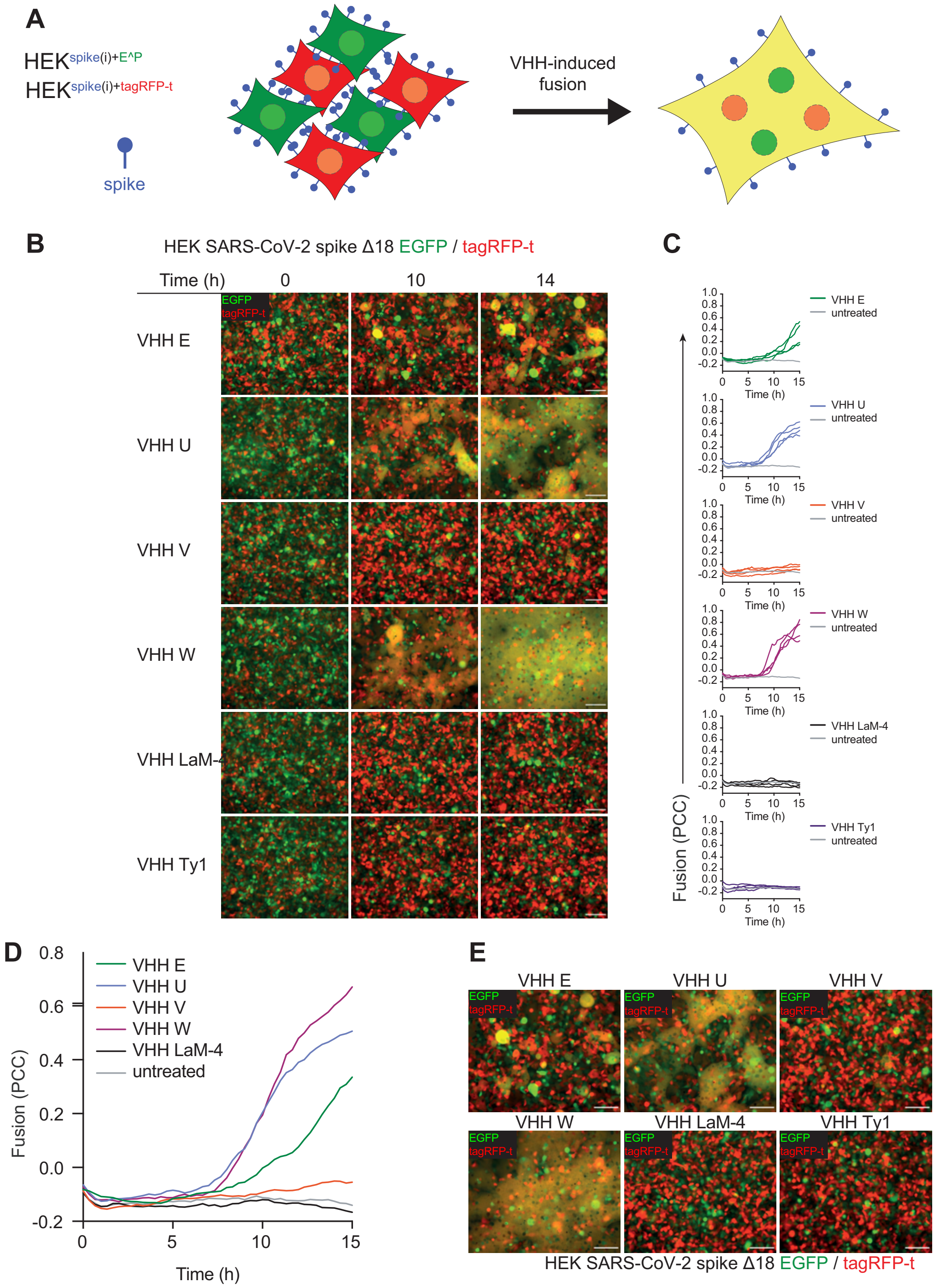

Figure 5.2: Nanobodies induce spike-mediated fusion. (**A**) Experimental setup. HEK$^{spike(i)+EGFP}$ cells and HEK$^{spike(i)+tagRFP\text{-}t}$ cells were seeded in a 1:1 ratio, and spike expression was induced with doxycycline for 20 h. Cells were then treated with 1 µM of the indicated nanobody and microscopy images were recorded every 20 minutes for 14 h at 37°C. (**B**,**E**) Representative images of cells at 0, 10, and 14 hours post treatment are shown. Scale bars: 100 µm. (**C**,**D**) Fusion was quantified by PCC between EGFP and tagRFP-t. Average values from four fields of view of an experiment representative of three independent experiments are shown.

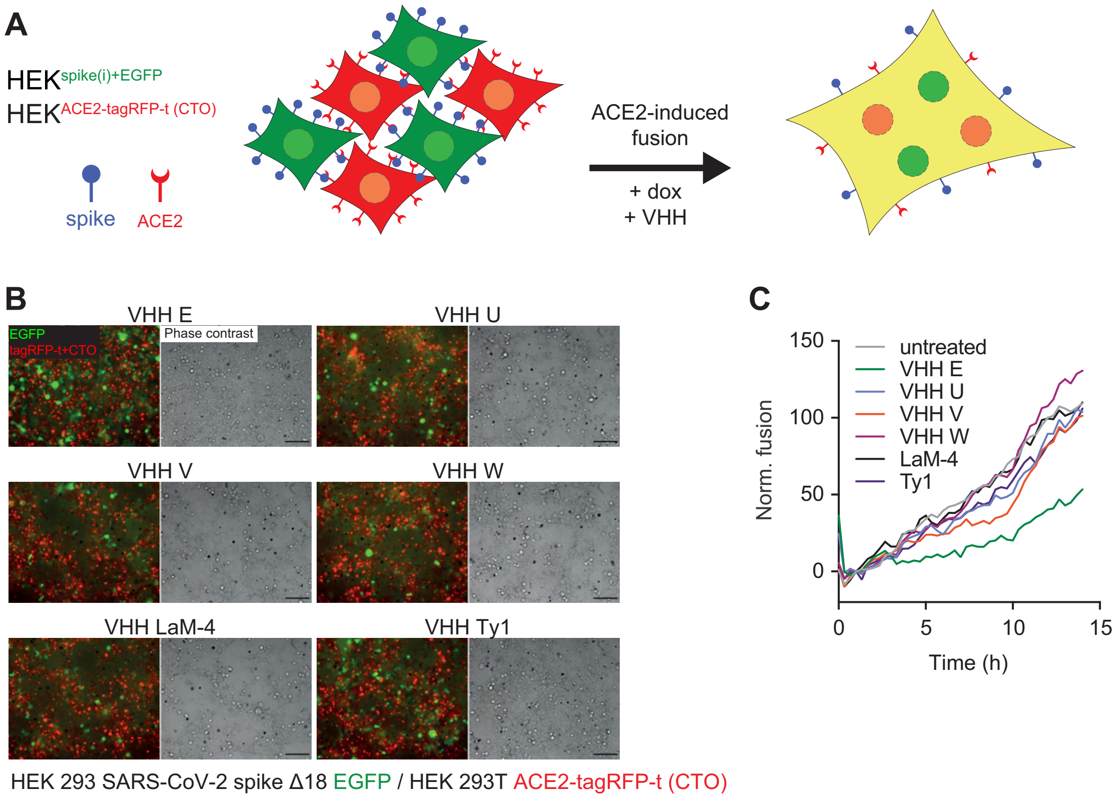

Figure 5.3: VHH E inhibits spike-mediated fusion. (**A**) Experimental setup. HEK$^{spike(i)+EGFP}$ cells and CTO-labelled HEK$^{ACE2\text{-}tagRFP\text{-}t}$ cells were seeded in a 1:1 ratio. Spike expression was induced with doxycycline and cells were treated with 1 µM of the indicated nanobody. Microscopy images were recorded every 20 minutes for 14 h at 37°C. (**B**) Representative images of cells at 12 h post induction. Scale bars: 100 µm. (**C**) Fusion was quantified by calculating the Pearson correlation coefficient (PCC) between green and red fluorescence. Mean values from 4 fields of view of an experiment representative of 3 independent experiments are shown. PCC values were normalized by subtracting the values at t = 1 h as well as the signal in the control without doxycycline, and corrected PCC values at 12 h in doxycycline-treated cells were defined as 100% fusion.

5.2.3 Multivalence promotes or blocks fusogenicity

The neutralization potency of the nanobodies could be drastically enhanced by genetically fusing two or three nanobodies. Thus, we were intrigued to understand what effect the valence has on nanobody-induced spike-catalysed cell fusion. We assessed whether the addition of multivalent nanobodies triggers the fusion machinery in SARS-CoV-2 spike-expressing cells in the absence of ACE2, as observed for VHHs E, U, and W. VHHs EV, VE, EW, and WE caused nearly

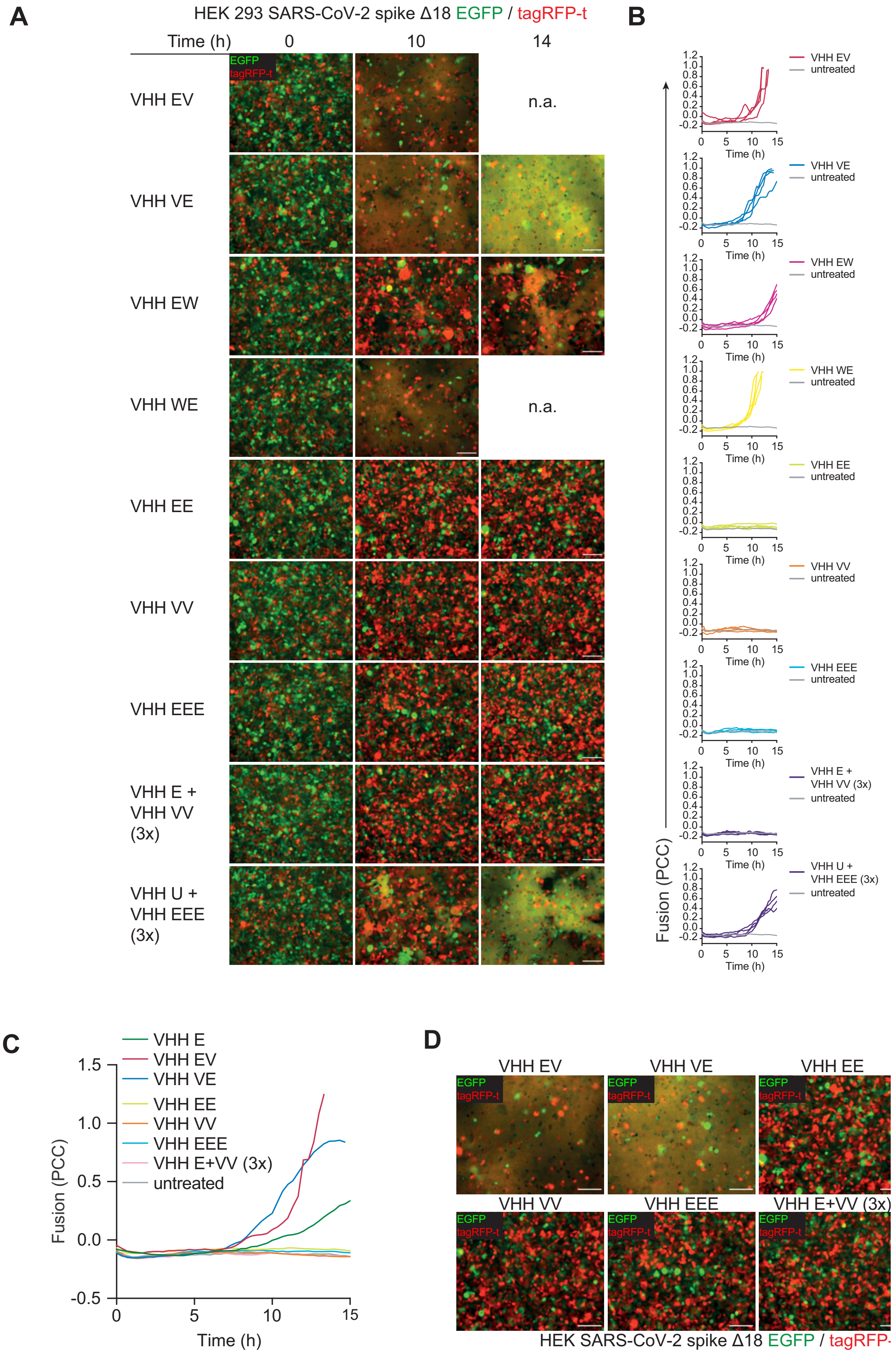
A
HEK 293 SARS-CoV-2 spike Δ18 EGFP / tagRFP-t
Time (h)
0
10
14
EGFP
tagRFP-t
VHH EV
n.a.
VHH VE
VHH EW
VHH WE
n.a.
VHH EE
VHH VV
VHH EEE
VHH E + VHH VV (3x)
VHH U + VHH EEE (3x)
B
Fusion (PCC)
1.2
1.0
0.8
0.6
0.4
0.2
0.0
-0.2
0
5
10
15
Time (h)
VHH EV
untreated
VHH VE
untreated
VHH EW
untreated
VHH WE
untreated
VHH EE
untreated
VHH VV
untreated
VHH EEE
untreated
VHH E + VHH VV (3x)
untreated
VHH U + VHH EEE (3x)
untreated
C
VHH E
VHH EV
VHH VE
VHH EE
VHH VV
VHH EEE
VHH E+VV (3x)
untreated
Fusion (PCC)
1.5
1.0
0.5
0.0
-0.5
0
5
10
15
Time (h)
D
VHH EV
VHH VE
VHH EE
VHH VV
VHH EEE
VHH E+VV (3x)
EGFP
tagRFP-t
HEK SARS-CoV-2 spike Δ18 EGFP / tagRFP-

Figure 5.4: Nanobodies induce spike-mediated fusion. Experimental setup as in Fig 5.2. $HEK^{spike(i)+EGFP}$ cells and $HEK^{spike(i)+tagRFP\text{-}t}$ cells were seeded in a 1:1 ratio, and spike expression was induced with doxycycline for 20 h. Cells were then treated with 1 µM of the indicated nanobody and a 3-fold molar excess of another nanobody was added where specified. Microscopy images were recorded every 20 minutes for 14 h at 37°C. (**A**,**D**) Representative images of cells at 0, 10, and 14 hours post treatment are shown. Scale bars: 100 µm. (**C**,**D**) Fusion was quantified by PCC between EGFP and tagRFP-t. Average values from four fields of view of an experiment representative of three independent experiments are shown.

complete cell fusion (Figure 5.4). In the case of the VHH EV and VE, the fusogenicity of the bivalent nanobodies clearly exceeded that of the individual nanobodies VHHs V and E. This correlates with enhanced neutralizing potency, which cannot be attributed to ACE2 competition. For WE and EW this consideration is less clear because of the strong fusogenic activity of VHH W. We concluded that binding of VHHs EV, VE, EW, and WE to the spike protein induces conformational changes that induce fusion. To what extent the improved neutralizing activity can be attributed to increased fusogenicity or binding strength, respectively, remains unclear.

The homo-bivalent and homo-trivalent VHHs EE, VV, and EEE did not induce fusion despite a substantial boost in neutralizing activity in the case of VHH E, suggesting that binding of multiple covalently coupled nanobodies to the same epitope is not compatible with spike activation (Figure 5.4). To investigate whether cross-linking of individual spike protomers by homo-multivalent nanobodies interferes with fusion, we incubated spike-expressing cells with fusogenic VHH E or U and a threefold molar excess of VHH VV or EEE, respectively (Figure 5.4). Although VHH U-mediated fusion was not restricted by VHH EEE, fusion induced by VHH E was inhibited by VHH VV, demonstrating that nanobody binding can interfere with fusion in other ways, possibly by preventing the RBD 3-up conformation.

5.2.4 Multivalent nanobodies can inhibit spike-ACE2-mediated fusion

Because multivalent nanobodies showed the potential to inhibit cell-cell fusion, we aimed to determine whether they can interfere with the fusion of SARS-CoV-2 spike- and ACE2-expressing cells (Figure 5.5). Thus, we induced spike expression at the onset of the experiment, so that newly synthesized spike that arrived at the plasma membrane would encounter an excess of nanobodies. Depending on the neutralization potency, fusogenicity, and the concentration of nanobodies, this may induce premature activation of spike or interfere with binding of spike to ACE2, recapitulating the setup of the neutralization assays.

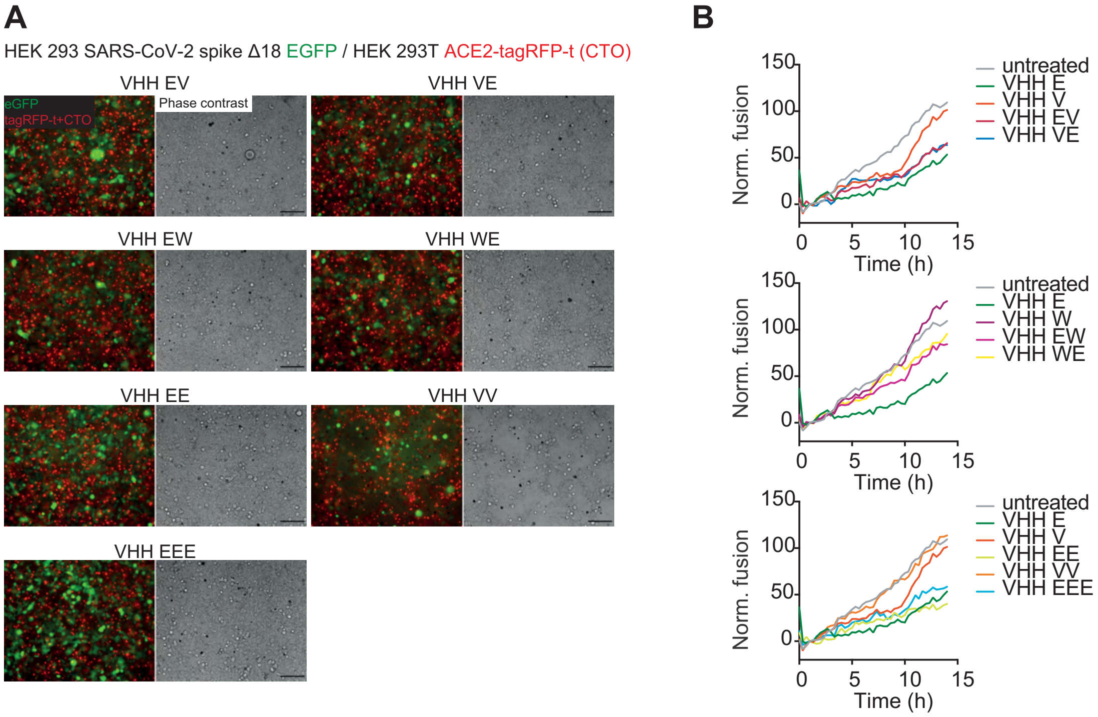

Figure 5.5: VHH E and derivatives inhibits spike-mediated fusion. Experimental setup as in Fig 5.2. HEK$^{spike(i)+EGFP}$ cells and CTO-labelled HEK$^{ACE2-tagRFP-t}$ cells were seeded in a 1:1 ratio. Spike expression was induced with doxycycline and cells were treated with 1 µM of the indicated nanobody. Microscopy images were recorded every 20 minutes for 14 h at 37°C. (**A**) Representative images of cells at 12 h post induction. Scale bars: 100 µm. (**B**) Fusion was quantified by calculating the Pearson correlation coefficient (PCC) between green and red fluorescence. Mean values from 4 fields of view of an experiment representative of 3 independent experiments are shown. PCC values were normalized by subtracting the values at t = 1 h as well as the signal in the control without doxycycline, and corrected PCC values at 12 h in doxycycline-treated cells were defined as 100% fusion.

We observed that fusion was partly inhibited by VHHs E, EE, EEE, EV, and VE (Figure 5.5). VHH VV did not inhibit fusion, whereas VHHs EW and WE caused intermediate phenotypes.

In summary, inhibition depended on the presence of VHH E, which directly binds to the ACE2 binding site, hinting at a relevance for outcompeting ACE2 binding. In line with that, only the most potent binders interfered with ACE2-induced fusion. However, it has to be noted, that only one concentration was measured. An important consideration with this experimental setup is that potential target membranes were always present in the form of neighbouring cells, which is especially relevant for those nanobodies that induce considerable fusion themselves, namely VHH E, EV, VE, EW, and WE, as it is not possible to scrutinise whether cell fusion is caused by the nanobody or by ACE2 binding.

5.2.5 The fusogenicity of some nanobodies is sensitive to protease inhibition

It remains unclear whether nanobody binding to spike is sufficient to induce direct fusion or whether it rather facilitates secondary proteolytic processing of S2, which is necessary for naturally induced fusion. To address this question, we mixed spike-expressing cells of both colours and added nanobodies to induce cell fusion in the presence of a protease inhibitor cocktail to determine if the fusion depends on proteolytic events. VHH E-induced fusion was partly inhibited by the protease inhibitor cocktail (Figure 5.6), suggesting that extracellular or membrane-associated proteases may be involved in the VHH-triggered fusion, as described for ACE2-triggered fusion by SARS-CoV-1 spike (Simmons *et al.*, 2011). It is thus possible that VHH binding mimics binding of ACE2 to the spike protein and exposes otherwise inaccessible protease cleavage sites. Regardless of the exact mechanism, only neutralizing nanobodies were found to trigger spike-mediated cell fusion, suggesting that aberrant activation of the fusion machinery is involved in the mechanism of neutralization.

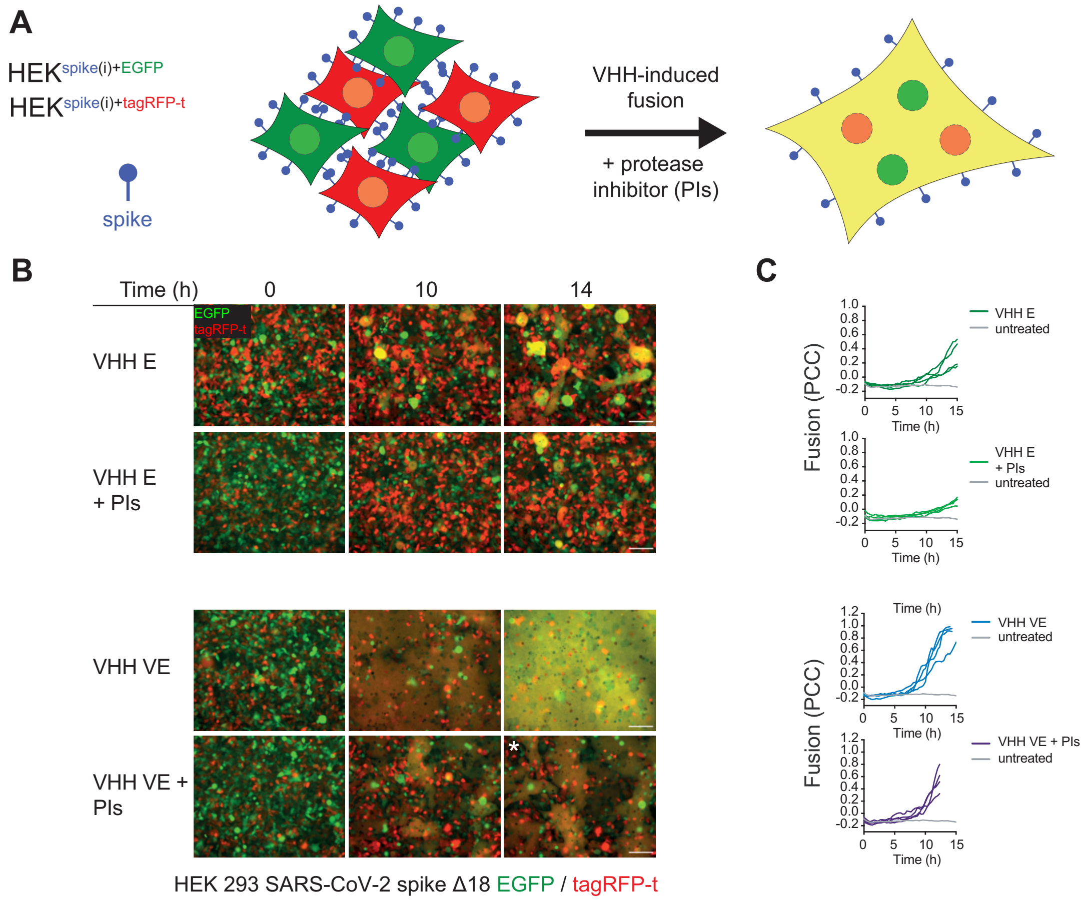

Figure 5.6: VHHE-induced fusogenicity is partly protease-dependent. (**A**) Experimental setup. HEK$^{spike(i)+EGFP}$ cells and HEK$^{spike(i)+tagRFP\text{-}t}$ cells were seeded in a 1:1 ratio, and spike expression was induced with doxycycline for 20 h. Cells were then treated with 1 µM of the indicated nanobody and a protease inhibitor cocktail (PIs) was added where specified. Microscopy images were recorded every 20 minutes for 14 h at 37°C. (**B**) Representative images of cells at 0, 10, and 14 hours post treatment are shown. Scale bars: 100 µm. (**C**) Fusion was quantified by PCC between EGFP and tagRFP-t. Average values from four fields of view of an experiment representative of three independent experiments are shown.

5.3 Discussion

In this study we demonstrated that nanobodies are valuable tools in our arsenal to fight infectious diseases, as they hold a variety of advantages over conventional antibodies, ranging from their physical properties to the possibilities in their engineering and manufacturing. With our four potently neutralizing nanobodies, we contributed to a rapidly emerging list of nanobodies able to neutralize SARS-CoV-2 (Walter *et al.*, 2020; Wrapp, De Vlieger, *et al.*, 2020; Huo, Le Bas, *et al.*, 2020; Hanke *et al.*, 2020; Li *et al.*, 2020; Custódio *et al.*, 2020; Tortorici *et al.*, 2020; Schoof *et al.*, 2020). Some of these nanobodies were generated from immunolibraries against SARS-CoV-1, and others were selected from synthetic libraries and further improved by *in vitro* evolution. Our nanobodies are among those that were generated from animals immunised with SARS-CoV-2 or its RBD and have thus been selected by the adaptive immune system of an animal. We further improved our nanobodies by arranging them into multivalent formats based on the knowledge we gathered from SPR, X-ray crystallography, and cryo-EM studies. Multivalence offers the opportunity to target two different epitopes by biparatopic nanobodies (VHHs VE, EV, WE, EW). While this approach increases binding and neutralization potency, it also prevents or delays the emergence of resistant mutant viruses, because in order to escape, two epitopes would have to be altered simultaneously. The prevention of mutational escape has been demonstrated for VHHs VE and EV in evolution experiments (Koenig *et al.*, 2021). Another approach is to generate multivalent but monoparatopic nanobodies, that target one epitope but potentially different RBDs (VHHs EE, EEE, VV). VHHs EE and EEE are the most potently neutralizing nanobodies we generated in the study. A disadvantage of monoparatopic nanobodies is their susceptibility to escape mutants: despite its potency, a single amino acid change in the spike protein sufficed to render it completely insensitive to inhibition by VHH EEE.

5.3.1 Spike activation as a neutralization mechanism

We have presented a new neutralization mechanism, by which nanobodies inactivate the viral fusion machinery and permanently converts it into its post-fusion conformation. Similar phenomena have been reported for antibodies against SARS-CoV-1 and Middle East respiratory syndrome (MERS)-CoV (Walls *et al.*, 2019; Huo, Zhao, *et al.*, 2020). In the absence of target membranes, activation of the spike protein drives the irreversible transition to the energetically favoured post-fusion state and the loss of S1, including the RBDs, without catalysing actual membrane fusion. Because this permanently inactivates virions, premature spike activation has the potential to be a potent mechanism to neutralize viruses. As we identified nanobody-induced spike activation in three of our four nanobodies, this phenomenon might not be uncommon. Notably, it may also play a role in antibody-dependent enhancement: while Fcγ receptor-expressing cells can take up virus-antibody complexes, it is unclear how subsequent membrane fusion and escape from the endosome is achieved in the absence of cognate receptors (Li, 2016; Wan *et al.*, 2020). Our observations provide a possible explanation: antibodies, which are perhaps Fc-receptor-bound, are taken up together with the virus. Antibody-induced spike activation then drives membrane fusion and thus escape of the virus into the cytosol. More detailed understanding of the parameters that drive or inhibit spike-catalysed fusions is thus highly desirable. I established an assay to determine the fusogenicity of the nanobodies and performed a range of experiments with different nanobodies and combinations thereof.

Using cryo-EM, we discovered that some nanobodies, *e.g.* VHH E and VHH VE stabilised the RBD 3-up conformation of the spike protein, which hinted at the possibility that those nanobodies activate the spike fusion machinery. Indeed, some nanobodies exhibited a strong fusogenic activity, *i.e.* they affected the spike protein in a way that causes it to activate the fusion machinery. On the other hand, some nanobodies were capable of blocking fusion caused by other nanobodies or ACE2 binding, indicating that different neutralization mechanisms are employed. We identified that the nanobodies with high fusogenic activity were VHHs U, W, VE, EV, EW, and WE. VHH E also caused fusion, albeit to a considerably smaller extent. In contrast, VHHs V, VV, EE, and EEE were not fusogenic. Considering possible spike activation mechanisms, the most likely explanation is that nanobodies activate spike by stabilising the RBD 3-up conformation, thus mimicking ACE2 binding. This would imply that all fusogenic nanobodies induce the RBD 3-up conformation and non-fusogenic nanobodies do not. We obtained cryo-EM-structures from trimeric spike bound by VHHs E, V, and VE. Fusogenic VHHs E and VE stabilised the RBD 3-up conformation and VHH V the RBD 2-up conformation, which is in line with the proposed mechanism.

This would predict that VHHs U and W also stabilise the RBD 3-up conformation, but this would have to be confirmed experimentally.

VHH E loses its fusogenicity in its multivalent forms (VHHs EE and EEE) indicating that cross-linking of multiple RBDs prevents fusion, even though it can be assumed that all RBDs are in the up state when bound to these nanobodies. Nevertheless, VHHs EE and EEE are exceptionally potent neutralizers, illustrating that those nanobodies can neutralize the virus without activating spike, presumably via outcompeting ACE2 binding and preventing activation. While cross-linking is sufficient to prevent VHH E-induced fusion, VHH EEE was not capable to inhibit fusion induced by VHH U. This may simply be due to the stronger fusogenicity of VHH U, which might not be overcome by cross-linking. Furthermore, it remains unclear why VHH E is less fusogenic than the other nanobodies, especially when considering that VHH E induced the highest frequency of RBD 3-up particles (61 % compared to 41.5 % for the highly fusogenic VHH VE). It is either possible that VHH E, despite inducing RBD 3-up, suppresses the conformational changes needed for fusion or that the other nanobodies efficiently induce further changes to facilitate S2 processing and S1 dissociation. In any way, the induction of fusion seems to be more nuanced than whether or not the RBD 3-up conformation is stabilised.

An intriguing observation is that VHH E becomes much more fusogenic in combination with VHH V, which is non-fusogenic on its own, implying a cooperative effect. It is also more potent in terms of virus neutralization than a combination of the individual monomeric nanobodies. This suggests that the boost in potency could be attributed to the boost in fusogenicity. It is unclear whether the increased fusogenicity is caused by an allosteric effect that can be achieved by simply engaging both epitopes simultaneously or whether the linker plays a role. In order to delineate this, we would have to test the combination of monomeric VHHs E and V, which was not part of the experiments. However, we combined VHH E with VHH VV, which is expected to not bind two epitopes simultaneously because of structural restrictions and because of the only mildly increased neutralization potency over monomeric VHH V. I predict that VHH VV should thus behave similarly to VHH V. The combination of VHH E with VHH VV did not recapitulate the extensive fusogenicity of VHH VE or EV. Instead VHH VV completely blocked the fusogenic action of VHH E. Cryo-EM revealed that VHH V-bound spike was in a 2-up configuration with all three RBDs displaced. VHH E induced fusion might thus be inhibited by preventing the RBD 3-up state. The inhibiting effect of VHH V does not occur in the highly fusogenic VHHs VE and EV, possibly because the VHH V portion is restrained by being linked to VHH E. This may force the biparatopic nanobody to bind in a different way than the respective monovalent nanobodies and thereby induce conformational changes that lead to spike activation. We did not observe meaningful conformational changes, but this might be because the spike used for cryo-EM experiments was stabilised by proline substitutions and a lack of the furin cleavage site. Some conformational changes induced by the nanobodies might thus not appear in the cryo-EM structures.

VHH EV is an interesting case, because the linker is expected to be too short to accommodate binding of both epitopes on a single RBD. Its high fusogenicity, in combination with the above consideration, would preclude binding of only one valence at a time. Cross-linking multiple RBDs also seems unfavourable for spike activation. Therefore, it is likely that VHH EV forces conformational changes, possibly under strain, that facilitate binding of both epitopes as well as spike activation. This notion is supported by the increased binding strength of VHH EV compared to VHHs E and V, with dissociation constants of 200 pM, 2 nM, and 9 nM, respectively. VHHs WE and EW are also highly fusogenic. However, because monovalent VHH W is highly fusogenic on its own, a strong impact of the bivalence cannot be concluded. Yet, VHHs WE and EW exhibit a marked increase in neutralization potency compared to its monovalent counterparts, suggesting that spike activation is not the sole factor responsible for its neutralization potency. Instead, the enhanced potency is likely driven by an increased avidity.

When spike expression is induced in the presence of ACE2-expressing cells, cell fusion is readily induced. This process could only be partly inhibited by nanobodies. Only nanobody constructs containing VHH E prevented fusion to a meaningful extent, demonstrating the importance of outcompeting ACE2 in this context. A problem of this experimental setup is that target membranes are always present at the border of neighbouring cells, so that some of the nanobodies, for example VHH VE, are expected to induce fusion themselves, even though some of the ACE2-induced fusion is inhibited. One possible explanation for the partial inhibition is that, because only a portion of the cell surface faces neighbouring cell membranes, spike proteins could arrive at a surface without proximal target membranes and be activated by nanobodies without causing fusion. The observations are probably a result of multiple effects.

For ACE2-induced fusion, the secondary proteolytic cleavage of S2 plays an important role. We were, thus, intrigued whether this cleavage is also necessary for nanobody-induced fusion. In my experiments, addition of a protease inhibitor cocktail was able to inhibit fusion caused by VHH E but not by VHH VE. It is thus possible that the nanobodies exhibit different mechanisms of spike activation: VHH E stabilises the RBD 3-up conformation and is sensitive to protease inhibitors. In that regard, it resembles the way spike is activated by ACE2. In contrast, the fusogenic activity by VHH VE seems to be independent of proteolytic processing. It is possible that VHH VE induces a conformation that makes spike an even better substrate for proteases compared to VHH E and perhaps increases the range of suitable proteases. Thus, the concentration of the inhibitor might not have been sufficient or may not inhibit all proteases. Alternatively, VHH VE might employ a different, protease-independent mechanism of spike activation since the cleavage between S1 and S2 of spike already happens in the SARS-CoV-2 producing cell (Hoffmann, Kleine-Weber and Pöhlmann, 2020; Shang, Wan, *et al.*, 2020), protease-independent activation could be achieved by nanobody induced conformational changes that drive direct dissociation of S1 and thereby exposure of the fusion peptide. It has to be noted that for the cryo-EM studies, in which the spike trimer was intact despite VHH VE binding, a spike mutant without the S1/S2 furin cleavage site and with stabilising proline substitutions was used (Wrapp, Wang, *et al.*, 2020). In this context, it would first be interesting to experimentally test whether the other highly fusogenic nanobodies (VHH U, W, EV, WE, EW) are also protease-independent. Next, it would be helpful to formally prove that spike can be activated without secondary cleavage. This could be achieved by mutating the S2' cleavage site or perhaps by employing a cell- and protease-free assay. Alternatively, it could be tested if the nanobody-induced release of S1 depends on S2' cleavage by analysing the spike cleavage patterns by immunoblot.

Taken together, the nanobodies exhibit two different mechanisms of neutralization, namely preventing ACE2 binding through direct competition and premature spike activation. Since all nanobodies showed at least signs of competition with ACE2 binding, the former mechanism is likely to play a role in the neutralization activity of all nanobodies. For VHHs VE and EV, neutralizing potency correlates with fusogenicity but also with binding strength. Nevertheless, ACE2 displacement of VHH VE was not increased compared to VHH E. The increased fusogenicity is therefore likely the main reason for the increased neutralizing activity. In contrast, fusing VHH E into EE and EEE increased neutralization while the fusogenicity was lost. The different nanobodies, thus, employ a different mix of ACE2 competition and premature spike activation. In order to prove that spike activation is a means of neutralization of its own, we would need a nanobody that induces fusion but does not compete with ACE2 binding.

5.3.2 Conclusion

The search of neutralizing antibodies or nanobodies typically focusses on finding molecules with high affinity and neutralization potency. Most of these agents neutralize by preventing receptor binding. However, it can be valuable to identify antibodies or nanobodies with alternative neutralization mechanisms. Alternative epitopes might be more conserved and escape mutants might not be possible without compromising virus fitness. On the other hand, some nanobodies could help us investigate the fusion machinery by inducing or stabilising states that are otherwise difficult to observe. Nanobodies with their wide range of applications serve a fascinating dual role in fighting diseases, as they can be used either directly in treatment and diagnosis or in basic research to open up new avenues for mechanistic studies in the future.

Chapter 6: General discussion and outlook

During my PhD studies, I characterised a new reporter for inflammasome formation and caspase-1 recruitment. Using this reporter, I showed that caspase-1 forms filaments within inflammasome assemblies, which can be targeted for regulation by COPs (Chapter 3). I further used the reporter to study inflammasomes in mouse and human IECs. Mouse intestinal enteroids (MIE) readily responded to NAIP ligands and bacterial infection. Human intestinal enteroids (HIE) proved to be limited in their inflammasome responses, but I identified NLRP1 and non-canonical inflammasomes as possible avenues for future research (Chapter 4). In an additional project, I established a cell fusion assay to investigate the neutralization mechanism of SARS-CoV-2 nanobodies, which were discovered in our lab. The newly discovered mechanism of nanobody-induced spike activation demonstrates that nanobodies are not only a valuable tool to fight infectious diseases but can also be useful to understand biological processes such as the fusion machinery of the spike protein (Chapter 3).

In principle, canonical inflammasome signalling is rather straightforward: a cytosolic sensor self-oligomerizes and recruits ASC, which in turn recruits caspase-1. Caspase-1 then self-activates and cleaves its substrates GSDMD and IL-1β. GSDMD forms pores in the plasma membrane, which ultimately leads to pyroptosis. IL-1β is released through the GSDMD pores or cell rupture, and inflammation is induced by IL-1β signalling and DAMPs provided by the ruptured cell (Martinon *et al.*, 2002; Broz and Dixit, 2016; Hayward *et al.*, 2018). However, while research of the last two decades has greatly advanced our knowledge of inflammasomes, it has also unravelled intricacies that we do not yet fully understand. Inflammasomes do not always employ ASC, and caspase-1 can instead be directly recruited by CARD-containing sensors, likely as simple filaments (Poyet *et al.*, 2001). This also has an impact on the degree of caspase-1 processing and its range of substrates (Broz, von Moltke, *et al.*, 2010; Chen *et al.*, 2014; He *et al.*, 2015; Boucher *et al.*, 2018). Most caspases have more than one cleavage site in their IDL, and it has been proposed that the substrate repertoire could be expanded and modulated by cleavage of distinct sites in the IDL across individual caspase-1 dimers within a cell (Ross *et al.*, 2022). Not all cells carry out the full range of inflammasome-mediated effects. There are multiple accounts of inflammasomes that induce pyroptosis but do not directly process cytokines (Mariathasan *et al.*, 2004; Broz, Newton, *et al.*, 2010; Broz, von Moltke, *et al.*, 2010; Rühl and Broz, 2015; Schmid-Burgk *et al.*, 2015; Dick *et al.*, 2016; Okondo *et al.*, 2017). *Vice versa*, inflammasomes are not always lethal to the cell while releasing cytokines (Chen *et al.*, 2014; Yow *et al.*, 2022). As mentioned before, this can be an effect of differential caspase-1 processing. Other reasons for varied inflammasome outcomes can be differences in the expression of gasdermins or cytokines, cellular regulators such as COPs, or, in the case of infection, modulatory effects of an invading pathogen (Chung *et al.*, 2015; Veyer *et al.*, 2017; Maruzuru *et al.*, 2018; Devi *et al.*, 2020). While this highlights the importance to investigate the consequences of inflammasome signalling, it also implies that this approach is prone to fail in the detection of inflammasomes in certain scenarios. It is therefore beneficial to screen for inflammasome signalling at a more upstream step. The most upstream event that is common among all canonical inflammasomes is the assembly of ASC. C1C-EGFP reliably indicates inflammasome assembly without altering the endogenous pool of ASC and encourages to include the detection of inflammasome assembly into the arsenal of standard readouts. A further advantage over bulk readouts is the single cell resolution that can be obtained with assembly-based readouts. This will be especially valuable in more complex models such as tissues. When combined with complex cell culture models like organoids, the single cell resolution of the reporter will allow us to allocate inflammasome responses to distinct cells. This may help to identify specialized cells or understand the coordination between affected and bystander cells. It will also be possible to resolve multiple signalling pathways simultaneously, *e.g.* inflammasomes and interferons, to elucidate how different responses are divided between the individual cells of a tissue.

C1C-EGFP is the first reporter that can detect the formation of ASC-independent inflammasomes. This will help to further our understanding of sensors like CARD8. Comparing specks versus filaments might also help to differentiate between NLRP1 and CARD8. The only inflammasomes that cannot be detected by C1C-EGFP are caspase-1-independent, non-canonical inflammasomes. This might be overcome by generating reporters specific for other caspases like C4C-EGFP if they form larger, detectable assemblies. An obvious application for this reporter lies in HIEs, since human IECs seem to rely more on non-canonical inflammasomes than NLRC4 to respond to enteric bacteria, even though they widely express ASC (Naseer, Zhang, *et al.*, 2022). Although the consequences of canonical and non-canonical inflammasomes largely overlap, it is commonly believed that non-canonical inflammasomes cannot process cytokines. However, caspase-4 was recently reported to cleave IL-1β and IL-18 (Chan *et al.*, 2023). This makes different types of inflammasomes difficult to differentiate when examining downstream readouts, and they are typically identified by knockouts. Moreover, humans possess two caspases that are activated in non-canonical inflammasomes: caspase-4 and caspase-5 (Shi *et al.*, 2014; Downs *et al.*, 2020; Dorfleutner and Stehlik, 2023). Fluorescent CARD-based reporters, potentially with different colours, will allow us to identify each individual type of inflammasome and further our understanding of their biological functions.

Different kinds of inflammasomes differ in their structure and complexity, e.g. by incorporating or excluding ASC. This likely has a direct effect on caspase processing and substrate cleavage. Caspase-1 filaments are also a target of regulation by CARD17. It is therefore important to understand how inflammasomes are assembled on a structural level. Using C1C-EGFP and interaction-deficient mutants of C1C-EGFP, I could show that caspase-1 filaments are formed within specks in living cells. As discussed in Chapter 3, these filaments have functional consequences for inflammasome signalling and regulation. Although ASC assemblies provide an ample amount of seeds for caspase-1 polymerization, CARD17-mediated capping efficiently curtailed IL-1β maturation, suggesting that filaments may be necessary for efficient caspase-1 activation. It is also possible that ASC-independent inflammasomes, such as CARD8 inflammasomes, which provide a far more limited amount of CARD seeds, are much more sensitive to CARD17. On the other hand, ASC-independent inflammasomes would circumvent any regulations that target ASC, for example PYD only proteins. Further research is needed to understand the roles of CARD16 and CARD18. It should be tested what effects these COPs have on different types of inflammasomes. Their most intriguing ability is to seed a C1C filaments themselves, at least *in vitro* (Karasawa *et al.*, 2015; Lu *et al.*, 2016). It is therefore possible that CARD16 or CARD18 can induce inflammasomes, but this has yet to be shown. It is unclear if similar regulatory mechanism exist for caspase-4, -5, or -11. A first step towards understanding the regulation of these caspases would be to determine if they form comparable assemblies, perhaps with the help of fluorescent caspase reporters.

Inflammasomes are a crucial part of our immune system, as they form a link between pathogen or danger detection and the coordination of an immune response. Inflammasome signalling can be beneficial in the defence against pathogens, but it can also be detrimental when not regulated appropriately. In the context of infectious disease, aberrant inflammasome signalling can cause an immune overreaction and severe symptoms. In the absence of an infection, inflammasomes can cause sterile inflammation and autoimmune diseases (Saavedra *et al.*, 2015; Vasudevan *et al.*, 2023). Inflammasomes are of particular interest in tissues that are an entry point for invading pathogens such as mucosal surfaces of the intestine, or the skin. Those tissues can also be the site of auto-inflammatory diseases, for example in inflammatory bowel disease or psoriasis (Khatri and Kalyanasundaram, 2021; Ciążyńska *et al.*, 2021). Mechanistic understanding of inflammasome activation, assembly, signalling, and outcome, particularly in those tissues, is therefore of high medical relevance. The lack of models for human tissues has hampered the research of tissue-specific immune responses on a cellular level. The advent and advance of organoid technologies and other complex cell culture models has opened new angles to study immune signalling in human tissues. The possibilities for research will further increase with the development of more complex organoid models that incorporate additional cell types such as myeloid cells. In this thesis, I have demonstrated that the combination of complex cell culture models with molecular reporters can yield new insights in the biology of intestinal inflammasomes. This concept can be expanded to additional tissues and other immune signalling pathways. The resulting knowledge has the potential to lead to new treatment strategies for a variety of diseases.

References

Abraham, J. (2020) ‘Passive Antibody Therapy in COVID-19’. *Nature Reviews. Immunology*, 20(7), pp. 401–403. DOI: 10.1038/s41577-020-0365-7.

Alberti, S., Gladfelter, A. and Mittag, T. (2019) ‘Considerations and Challenges in Studying Liquid-Liquid Phase Separation and Biomolecular Condensates’. *Cell*, 176(3), pp. 419–434. DOI: 10.1016/j.cell.2018.12.035.

Alimov, I. *et al.* (2019) ‘Bile Acid Analogues Are Activators of Pyrin Inflammasome’. *The Journal of Biological Chemistry*, 294(10), pp. 3359–3366. DOI: 10.1074/jbc.RA118.005103.

An, D.-J. *et al.* (2009) ‘Encephalomyocarditis in Korea: Serological Survey in Pigs and Phylogenetic Analysis of Two Historical Isolates’. *Veterinary Microbiology*, 137(1–2), pp. 37–44. DOI: 10.1016/j.vetmic.2009.01.005.

Anand, P.K. *et al.* (2012) ‘NLRP6 Negatively Regulates Innate Immunity and Host Defence against Bacterial Pathogens’. *Nature*, 488(7411), pp. 389–393. DOI: 10.1038/nature11250.

Anders, S. and Huber, W. (2010) ‘Differential Expression Analysis for Sequence Count Data’. *Genome Biology*, 11(10), p. R106. DOI: 10.1186/gb-2010-11-10-r106.

Anderson, G.P. *et al.* (2008) ‘Development of Antiricin Single Domain Antibodies toward Detection and Therapeutic Reagents’. *Analytical Chemistry*, 80(24), pp. 9604–9611. DOI: 10.1021/ac8019398.

Arbabi Ghahroudi, M. *et al.* (1997) ‘Selection and Identification of Single Domain Antibody Fragments from Camel Heavy-Chain Antibodies’. *FEBS Letters*, 414(3), pp. 521–526. DOI: 10.1016/s0014-5793(97)01062-4.

Arbabi-Ghahroudi, M., Tanha, J. and MacKenzie, R. (2005) ‘Prokaryotic Expression of Antibodies’. *Cancer Metastasis Reviews*, 24(4), pp. 501–519. DOI: 10.1007/s10555-005-6193-1.

Arnold, M., Patton, J.T. and McDonald, S.M. (2009) ‘Culturing, Storage, and Quantification of Rotaviruses’. *Current Protocols in Microbiology*, 15(1), p. 15C.3.1-15C.3.24. DOI: 10.1002/9780471729259.mc15c03s15.

Ball, D.P. *et al.* (2020) ‘Caspase-1 Interdomain Linker Cleavage Is Required for Pyroptosis’. *Life Science Alliance*, 3(3), p. e202000664. DOI: 10.26508/lsa.202000664.

Bangaru, S. *et al.* (2020) ‘Structural Analysis of Full-Length SARS-CoV-2 Spike Protein from an Advanced Vaccine Candidate’. *Science (New York, N.Y.)*, 370(6520), pp. 1089–1094. DOI: 10.1126/science.abe1502.

Bao, H. *et al.* (2020) ‘Salmonella Secretion Systems: Differential Roles in Pathogen-Host Interactions’. *Microbiological Research*, 241, p. 126591. DOI: 10.1016/j.micres.2020.126591.

Bauernfeind, F. *et al.* (2009) ‘NF-kB Activating Pattern Recognition and Cytokine Receptors License NLRP3 Inflammasome Activation by Regulating NLRP3 Expression’. *Journal of Immunology (Baltimore, Md. : 1950)*, 183(2), pp. 787–791. DOI: 10.4049/jimmunol.0901363.

Bauernfried, S. *et al.* (2021) ‘Human NLRP1 Is a Sensor for Double-Stranded RNA’. *Science (New York, N.Y.)*, 371(6528), p. eabd0811. DOI: 10.1126/science.abd0811.

Bauernfried, S. and Hornung, V. (2022) ‘Human NLRP1: From the Shadows to Center Stage’. *The Journal of Experimental Medicine*, 219(1), p. e20211405. DOI: 10.1084/jem.20211405.

Bayati, A. *et al.* (2021) ‘SARS-CoV-2 Infects Cells after Viral Entry via Clathrin-Mediated Endocytosis’. *The Journal of Biological Chemistry*, 296, p. 100306. DOI: 10.1016/j.jbc.2021.100306.

Bazzone, L.E. *et al.* (2019) ‘A Disintegrin and Metalloproteinase 9 Domain (ADAM9) Is a Major Susceptibility Factor in the Early Stages of Encephalomyocarditis Virus Infection’. *mBio*, 10(1), p. 10.1128/mbio.02734-18. DOI: 10.1128/mbio.02734-18.

Benton, D.J. *et al.* (2020) ‘Receptor Binding and Priming of the Spike Protein of SARS-CoV-2 for Membrane Fusion’. *Nature*, 588(7837), pp. 327–330. DOI: 10.1038/s41586-020-2772-0.

Bierschenk, D. *et al.* (2019) ‘The Salmonella Pathogenicity Island-2 Subverts Human NLRP3 and NLRC4 Inflammasome Responses’. *Journal of Leukocyte Biology*, 105(2), pp. 401–410. DOI: 10.1002/JLB.MA0318-112RR.

Billinis, C. (2009) ‘Encephalomyocarditis Virus Infection in Wildlife Species in Greece’. *Journal of Wildlife Diseases*, 45(2), pp. 522–526. DOI: 10.7589/0090-3558-45.2.522.

Birchenough, G.M.H. *et al.* (2016) ‘A Sentinel Goblet Cell Guards the Colonic Crypt by Triggering Nlrp6-Dependent Muc2 Secretion’. *Science (New York, N.Y.)*, 352(6293), pp. 1535–1542. DOI: 10.1126/science.aaf7419.

Blaess, M. *et al.* (2020) ‘COVID-19/SARS-CoV-2 Infection: Lysosomes and Lysosomotropism Implicate New Treatment Strategies and Personal Risks’. *International Journal of Molecular Sciences*, 21(14), p. 4953. DOI: 10.3390/ijms21144953.

Boeynaems, S. *et al.* (2018) ‘Protein Phase Separation: A New Phase in Cell Biology’. *Trends in Cell Biology*, 28(6), pp. 420–435. DOI: 10.1016/j.tcb.2018.02.004.

Booshehri, L.M. and Hoffman, H.M. (2019) ‘CAPS and NLRP3’. *Journal of Clinical Immunology*, 39(3), pp. 277–286. DOI: 10.1007/s10875-019-00638-z.

Boucher, D. *et al.* (2018) ‘Caspase-1 Self-Cleavage Is an Intrinsic Mechanism to Terminate Inflammasome Activity’. *The Journal of Experimental Medicine*, 215(3), pp. 827–840. DOI: 10.1084/jem.20172222.

Boyarsky, B.J. *et al.* (2021a) ‘Antibody Response to 2-Dose SARS-CoV-2 mRNA Vaccine Series in Solid Organ Transplant Recipients’. *JAMA*, 325(21), pp. 2204–2206. DOI: 10.1001/jama.2021.7489.

Boyarsky, B.J. *et al.* (2021b) ‘Immunogenicity of a Single Dose of SARS-CoV-2 Messenger RNA Vaccine in Solid Organ Transplant Recipients’. *JAMA*, 325(17), pp. 1784–1786. DOI: 10.1001/jama.2021.4385.

Broz, P. *et al.* (2012) ‘Caspase-11 Increases Susceptibility to Salmonella Infection in the Absence of Caspase-1’. *Nature*, 490(7419), pp. 288–291. DOI: 10.1038/nature11419.

Broz, P., von Moltke, J., *et al.* (2010) ‘Differential Requirement for Caspase-1 Autoproteolysis in Pathogen-Induced Cell Death and Cytokine Processing’. *Cell Host & Microbe*, 8(6), pp. 471–483. DOI: 10.1016/j.chom.2010.11.007.

Broz, P., Newton, K., *et al.* (2010) ‘Redundant Roles for Inflammasome Receptors NLRP3 and NLRC4 in Host Defense against Salmonella’. *The Journal of Experimental Medicine*, 207(8), pp. 1745–1755. DOI: 10.1084/jem.20100257.

Broz, P. and Dixit, V.M. (2016) ‘Inflammasomes: Mechanism of Assembly, Regulation and Signalling’. *Nature Reviews. Immunology*, 16(7), pp. 407–420. DOI: 10.1038/nri.2016.58.

Brubaker, S.W. *et al.* (2015) ‘Innate Immune Pattern Recognition: A Cell Biological Perspective’. *Annual Review of Immunology*, 33, pp. 257–290. DOI: 10.1146/annurev-immunol-032414-112240.

Burness, A.T. and Pardoe, I.U. (1983) ‘A Sialoglycopeptide from Human Erythrocytes with Receptor-like Properties for Encephalomyocarditis and Influenza Viruses’. *The Journal of General Virology*, 64(Pt 5), pp. 1137–1148. DOI: 10.1099/0022-1317-64-5-1137.

Burrill, C.P., Strings, V.R. and Andino, R. (2013) ‘Poliovirus: Generation, Quantification, Propagation, Purification, and Storage’. *Current Protocols in Microbiology*, 29(1), p. 15H.1.1-15H.1.27. DOI: 10.1002/9780471729259.mc15h01s29.

Cai, Y. *et al.* (2020) ‘Distinct Conformational States of SARS-CoV-2 Spike Protein’. *Science (New York, N.Y.)*, 369(6511), pp. 1586–1592. DOI: 10.1126/science.abd4251.

Canelli, E. *et al.* (2010) ‘Encephalomyocarditis Virus Infection in an Italian Zoo’. *Virology Journal*, 7, p. 64. DOI: 10.1186/1743-422X-7-64.

Carocci, M. *et al.* (2011) ‘Encephalomyocarditis Virus 2A Protein Is Required for Viral Pathogenesis and Inhibition of Apoptosis’. *Journal of Virology*, 85(20), pp. 10741–10754. DOI: 10.1128/JVI.00394-11.

Carocci, M. and Bakkali-Kassimi, L. (2012) ‘The Encephalomyocarditis Virus’. *Virulence*, 3(4), pp. 351–367. DOI: 10.4161/viru.20573.

Casson, C.N. *et al.* (2015) ‘Human Caspase-4 Mediates Noncanonical Inflammasome Activation against Gram-Negative Bacterial Pathogens’. *Proceedings of the National Academy of Sciences of the United States of America*, 112(21), pp. 6688–6693. DOI: 10.1073/pnas.1421699112.

Caussinus, E., Kanca, O. and Affolter, M. (2011) ‘Fluorescent Fusion Protein Knockout Mediated by Anti-GFP Nanobody’. *Nature Structural & Molecular Biology*, 19(1), pp. 117–121. DOI: 10.1038/nsmb.2180.

Chan, A.H. *et al.* (2023) DOI: 10.1101/2023.01.05.522955.

Chang-Graham, A.L. *et al.* (2019) ‘Human Intestinal Enteroids With Inducible Neurogenin-3 Expression as a Novel Model of Gut Hormone Secretion’. *Cellular and Molecular Gastroenterology and Hepatology*, 8(2), pp. 209–229. DOI: 10.1016/j.jcmgh.2019.04.010.

Chen, K.W. *et al.* (2014) ‘The Neutrophil NLRC4 Inflammasome Selectively Promotes IL-1β Maturation without Pyroptosis during Acute Salmonella Challenge’. *Cell Reports*, 8(2), pp. 570–582. DOI: 10.1016/j.celrep.2014.06.028.

Cheung, W. *et al.* (2010) ‘Rotaviruses Associate with Cellular Lipid Droplet Components to Replicate in Viroplasms, and Compounds Disrupting or Blocking Lipid Droplets Inhibit Viroplasm Formation and Viral Replication’. *Journal of Virology*, 84(13), pp. 6782–6798. DOI: 10.1128/JVI.01757-09.

Chung, W.-C. *et al.* (2015) ‘Influenza A Virus NS1 Protein Inhibits the NLRP3 Inflammasome’. *PloS One*, 10(5), p. e0126456. DOI: 10.1371/journal.pone.0126456.

Ciążyńska, M. *et al.* (2021) ‘The Role of NLRP1, NLRP3, and AIM2 Inflammasomes in Psoriasis: Review’. *International Journal of Molecular Sciences*, 22(11), p. 5898. DOI: 10.3390/ijms22115898.

Co, J.Y. *et al.* (2019) ‘Controlling Epithelial Polarity: A Human Enteroid Model for Host-Pathogen Interactions’. *Cell Reports*, 26(9), pp. 2509-2520.e4. DOI: 10.1016/j.celrep.2019.01.108.

Crawford, S.E. *et al.* (2019) ‘COPII Vesicle Transport Is Required for Rotavirus NSP4 Interaction with the Autophagy Protein LC3 II and Trafficking to Viroplasms’. *Journal of Virology*, 94(1), pp. e01341-19. DOI: 10.1128/JVI.01341-19.

Crawford, S.E. *et al.* (2017) ‘Rotavirus Infection’. *Nature Reviews. Disease Primers*, 3, p. 17083. DOI: 10.1038/nrdp.2017.83.

Crowley, S.M. *et al.* (2020) ‘Intestinal Restriction of Salmonella Typhimurium Requires Caspase-1 and Caspase-11 Epithelial Intrinsic Inflammasomes’. *PLoS Pathogens*, 16(4), p. e1008498. DOI: 10.1371/journal.ppat.1008498.

Crowley, S.M., Knodler, L.A. and Vallance, B.A. (2016) ‘Salmonella and the Inflammasome: Battle for Intracellular Dominance’. *Current Topics in Microbiology and Immunology*, 397, pp. 43–67. DOI: 10.1007/978-3-319-41171-2_3.

Custódio, T.F. *et al.* (2020) ‘Selection, Biophysical and Structural Analysis of Synthetic Nanobodies That Effectively Neutralize SARS-CoV-2’. *Nature Communications*, 11(1), p. 5588. DOI: 10.1038/s41467-020-19204-y.

Czechowicz, J. *et al.* (2011) ‘Prevalence and Risk Factors for Encephalomyocarditis Virus Infection in Peru’. *Vector Borne and Zoonotic Diseases (Larchmont, N.Y.)*, 11(4), pp. 367–374. DOI: 10.1089/vbz.2010.0029.

Dalskov, L., Gad, H.H. and Hartmann, R. (2023) ‘Viral Recognition and the Antiviral Interferon Response’. *The EMBO Journal*, 42(14), p. e112907. DOI: 10.15252/embj.2022112907.

Dea, S. *et al.* (1991) ‘Outbreaks in Quebec Pig Farms of Respiratory and Reproductive Problems Associated with Encephalomyocarditis Virus’. *Journal of Veterinary Diagnostic Investigation: Official Publication of the American Association of Veterinary Laboratory Diagnosticians, Inc*, 3(4), pp. 275–282. DOI: 10.1177/104063879100300401.

Devi, S. *et al.* (2023) ‘CARD-Only Proteins Regulate in Vivo Inflammasome Responses and Ameliorate Gout’. *Cell Reports*, 42(3), p. 112265. DOI: 10.1016/j.celrep.2023.112265.

Devi, S., Stehlik, C. and Dorfleutner, A. (2020) ‘An Update on CARD Only Proteins (COPs) and PYD Only Proteins (POPs) as Inflammasome Regulators’. *International Journal of Molecular Sciences*, 21(18), p. 6901. DOI: 10.3390/ijms21186901.

Dick, M.S. *et al.* (2016) ‘ASC Filament Formation Serves as a Signal Amplification Mechanism for Inflammasomes’. *Nature Communications*, 7, p. 11929. DOI: 10.1038/ncomms11929.

Diebolder, C.A. *et al.* (2015) ‘Cryoelectron Tomography of the NAIP5/NLRC4 Inflammasome: Implications for NLR Activation’. *Structure*, 23(12), pp. 2349–2357. DOI: 10.1016/j.str.2015.10.001.

Dorfleutner, A. and Stehlik, C. (2023) ‘Chapter 9 - Cellular Signaling, Molecular Activation, and Regulation of the Noncanonical Inflammasome’. In Pelegrin, P. (ed.) *Inflammasome Biology*. Academic Press, pp. 127–139. DOI: 10.1016/B978-0-323-91802-2.00028-1.

D’Osualdo, A. *et al.* (2011) ‘CARD8 and NLRP1 Undergo Autoproteolytic Processing through a ZU5-like Domain’. *PloS One*, 6(11), p. e27396. DOI: 10.1371/journal.pone.0027396.

Downs, K.P. *et al.* (2020) ‘An Overview of the Non-Canonical Inflammasome’. *Molecular Aspects of Medicine*, 76, p. 100924. DOI: 10.1016/j.mam.2020.100924.

Druilhe, A. *et al.* (2001) (6) ‘Regulation of IL-1β Generation by Pseudo-ICE and ICEBERG, Two Dominant Negative Caspase Recruitment Domain Proteins’. *Cell Death & Differentiation*, 8(6), pp. 649–657. DOI: 10.1038/sj.cdd.4400881.

Dull, T. *et al.* (1998) ‘A Third-Generation Lentivirus Vector with a Conditional Packaging System’. *Journal of Virology*, 72(11), pp. 8463–8471.

Eichwald, C., Rodriguez, J.F. and Burrone, O.R. (2004) ‘Characterization of Rotavirus NSP2/NSP5 Interactions and the Dynamics of Viroplasm Formation’. *The Journal of General Virology*, 85(Pt 3), pp. 625–634. DOI: 10.1099/vir.0.19611-0.

Elinav, E. *et al.* (2018) ‘NLRP6 and Dysbiosis: Avoiding the Luring Attraction of Over-Simplification’. *Immunity*, 48(4), pp. 603–604. DOI: 10.1016/j.immuni.2018.04.002.

Elinav, E. *et al.* (2011) ‘NLRP6 Inflammasome Regulates Colonic Microbial Ecology and Risk for Colitis’. *Cell*, 145(5), pp. 745–757. DOI: 10.1016/j.cell.2011.04.022.

Elliott, J.M. *et al.* (2009) ‘Crystal Structure of Procaspase-1 Zymogen Domain Reveals Insight into Inflammatory Caspase Autoactivation’. *The Journal of Biological Chemistry*, 284(10), pp. 6546–6553. DOI: 10.1074/jbc.M806121200.

Faenza, I. and Blalock, W.L. (2022) ‘Innate Immunity: A Balance between Disease and Adaption to Stress’. *Biomolecules*, 12(5), p. 737. DOI: 10.3390/biom12050737.

Fan, X. *et al.* (2020) ‘Cryo-EM Analysis of the Post-Fusion Structure of the SARS-CoV Spike Glycoprotein’. *Nature Communications*, 11(1), p. 3618. DOI: 10.1038/s41467-020-17371-6.

Fattinger, S.A. *et al.* (2021) ‘Epithelium-Autonomous NAIP/NLRC4 Prevents TNF-Driven Inflammatory Destruction of the Gut Epithelial Barrier in Salmonella-Infected Mice’. *Mucosal Immunology*, 14(3), pp. 615–629. DOI: 10.1038/s41385-021-00381-y.

Fawkner-Corbett, D. *et al.* (2021) ‘Spatiotemporal Analysis of Human Intestinal Development at Single-Cell Resolution’. *Cell*, 184(3), pp. 810-826.e23. DOI: 10.1016/j.cell.2020.12.016.

Finger, J.N. *et al.* (2012) ‘Autolytic Proteolysis within the Function to Find Domain (FIIND) Is Required for NLRP1 Inflammasome Activity’. *The Journal of Biological Chemistry*, 287(30), pp. 25030–25037. DOI: 10.1074/jbc.M112.378323.

Frenken, L.G. *et al.* (2000) ‘Isolation of Antigen Specific Llama VHH Antibody Fragments and Their High Level Secretion by Saccharomyces Cerevisiae’. *Journal of Biotechnology*, 78(1), pp. 11–21. DOI: 10.1016/s0168-1656(99)00228-x.

Frenken, L.G. *et al.* (1998) ‘Recent Advances in the Large-Scale Production of Antibody Fragments Using Lower Eukaryotic Microorganisms’. *Research in Immunology*, 149(6), pp. 589–599. DOI: 10.1016/s0923-2494(98)80011-4.

Fridy, P.C. *et al.* (2014) ‘A Robust Pipeline for Rapid Production of Versatile Nanobody Repertoires’. *Nature Methods*, 11(12), pp. 1253–1260. DOI: 10.1038/nmeth.3170.

Furman, D. *et al.* (2019) ‘Chronic Inflammation in the Etiology of Disease across the Life Span’. *Nature Medicine*, 25(12), pp. 1822–1832. DOI: 10.1038/s41591-019-0675-0.

Gainer, J.H. (1967) ‘Encephalomyocarditis Virus Infections in Florida, 1960-1966’. *Journal of the American Veterinary Medical Association*, 151(4), pp. 421–425.

Gálvez, E.J.C. *et al.* (2017) ‘Shaping of Intestinal Microbiota in Nlrp6- and Rag2-Deficient Mice Depends on Community Structure’. *Cell Reports*, 21(13), pp. 3914–3926. DOI: 10.1016/j.celrep.2017.12.027.

Gamarnik, A.V. and Andino, R. (1998) ‘Switch from Translation to RNA Replication in a Positive-Stranded RNA Virus’. *Genes & Development*, 12(15), pp. 2293–2304. DOI: 10.1101/gad.12.15.2293.

Garaicoechea, L. *et al.* (2008) ‘Llama-Derived Single-Chain Antibody Fragments Directed to Rotavirus VP6 Protein Possess Broad Neutralizing Activity in Vitro and Confer Protection against Diarrhea in Mice'. *Journal of Virology*, 82(19), pp. 9753–9764. DOI: 10.1128/JVI.00436-08.

Ge, X. *et al.* (2010) 'Seroprevalence of Encephalomyocarditis Virus in Intensive Pig Farms in China'. *The Veterinary Record*, 166(5), pp. 145–146. DOI: 10.1136/vr.b4766.

Geiger, F. *et al.* (2021) 'Liquid–Liquid Phase Separation Underpins the Formation of Replication Factories in Rotaviruses'. *The EMBO Journal*, 40(21), p. e107711. DOI: 10.15252/embj.2021107711.

Ghimire, L. *et al.* (2018) 'NLRP6 Negatively Regulates Pulmonary Host Defense in Gram-Positive Bacterial Infection through Modulating Neutrophil Recruitment and Function'. *PLoS Pathogens*, 14(9), p. e1007308. DOI: 10.1371/journal.ppat.1007308.

Ghimire, L. *et al.* (2020) 'The NLRP6 Inflammasome in Health and Disease'. *Mucosal Immunology*, 13(3), pp. 388–398. DOI: 10.1038/s41385-020-0256-z.

Gobeil, S.M.-C. *et al.* (2021) 'D614G Mutation Alters SARS-CoV-2 Spike Conformation and Enhances Protease Cleavage at the S1/S2 Junction'. *Cell Reports*, 34(2), p. 108630. DOI: 10.1016/j.celrep.2020.108630.

Göblös, A. *et al.* (2016) 'Keratinocytes Express Functional CARD18, a Negative Regulator of Inflammasome Activation, and Its Altered Expression in Psoriasis May Contribute to Disease Pathogenesis'. *Molecular Immunology*, 73, pp. 10–18. DOI: 10.1016/j.molimm.2016.03.009.

Gong, Q. *et al.* (2021) 'Structural Basis for Distinct Inflammasome Complex Assembly by Human NLRP1 and CARD8'. *Nature Communications*, 12, p. 188. DOI: 10.1038/s41467-020-20319-5.

Greenberg, A.S. *et al.* (1995) (6518) 'A New Antigen Receptor Gene Family That Undergoes Rearrangement and Extensive Somatic Diversification in Sharks'. *Nature*, 374(6518), pp. 168–173. DOI: 10.1038/374168a0.

Guimaraes, C.P. *et al.* (2013) 'Site-Specific C-Terminal and Internal Loop Labeling of Proteins Using Sortase-Mediated Reactions'. *Nature Protocols*, 8(9), pp. 1787–1799. DOI: 10.1038/nprot.2013.101.

Günther, S.D. *et al.* (2020) 'Cytosolic Gram-Negative Bacteria Prevent Apoptosis by Inhibition of Effector Caspases through Lipopolysaccharide'. *Nature Microbiology*, 5(2), pp. 354–367. DOI: 10.1038/s41564-019-0620-5.

Gutiérrez, M. *et al.* (2010) 'Different Rotavirus Strains Enter MA104 Cells through Different Endocytic Pathways: The Role of Clathrin-Mediated Endocytosis'. *Journal of Virology*, 84(18), pp. 9161–9169. DOI: 10.1128/JVI.00731-10.

Ha, H.J. and Park, H.H. (2020) ‘Crystal Structure of the Human NLRP9 Pyrin Domain Reveals a Bent N-Terminal Loop That May Regulate Inflammasome Assembly’. *FEBS Letters*, 594(15), pp. 2396–2405. DOI: 10.1002/1873-3468.13866.

Hallstrom, K. and McCormick, B.A. (2011) ‘Salmonella Interaction with and Passage through the Intestinal Mucosa: Through the Lens of the Organism’. *Frontiers in Microbiology*, 2, p. 88. DOI: 10.3389/fmicb.2011.00088.

Hamers-Casterman, C. *et al.* (1993) ‘Naturally Occurring Antibodies Devoid of Light Chains’. *Nature*, 363(6428), pp. 446–448. DOI: 10.1038/363446a0.

Hanke, L. *et al.* (2020) ‘An Alpaca Nanobody Neutralizes SARS-CoV-2 by Blocking Receptor Interaction’. *Nature Communications*, 11(1), p. 4420. DOI: 10.1038/s41467-020-18174-5.

Hara, H. *et al.* (2018) ‘The NLRP6 Inflammasome Recognizes Lipoteichoic Acid and Regulates Gram-Positive Pathogen Infection’. *Cell*, 175(6), pp. 1651-1664.e14. DOI: 10.1016/j.cell.2018.09.047.

Harmsen, M.M. *et al.* (2000) ‘Llama Heavy-Chain V Regions Consist of at Least Four Distinct Subfamilies Revealing Novel Sequence Features’. *Molecular Immunology*, 37(10), pp. 579–590. DOI: 10.1016/s0161-5890(00)00081-x.

Hausmann, A. *et al.* (2020) ‘Intestinal Epithelial NAIP/NLRC4 Restricts Systemic Dissemination of the Adapted Pathogen Salmonella Typhimurium Due to Site-Specific Bacterial PAMP Expression’. *Mucosal Immunology*, 13(3), pp. 530–544. DOI: 10.1038/s41385-019-0247-0.

Hayward, J.A. *et al.* (2018) ‘Cytosolic Recognition of Microbes and Pathogens: Inflammasomes in Action’. *Microbiology and Molecular Biology Reviews: MMBR*, 82(4), pp. e00015-18. DOI: 10.1128/MMBR.00015-18.

He, W. *et al.* (2015) ‘Gasdermin D Is an Executor of Pyroptosis and Required for Interleukin-1β Secretion’. *Cell Research*, 25(12), pp. 1285–1298. DOI: 10.1038/cr.2015.139.

Heggie, A., Cerny, O. and Holden, D.W. (2021) ‘SteC and the Intracellular Salmonella-Induced F-Actin Meshwork’. *Cellular Microbiology*, 23(4), p. e13315. DOI: 10.1111/cmi.13315.

Helwig, F.C. and Schmidt, C.H. (1945) ‘A FILTER-PASSING AGENT PRODUCING INTERSTITIAL MYOCARDITIS IN ANTHROPOID APES AND SMALL ANIMALS’. *Science (New York, N.Y.)*, 102(2637), pp. 31–33. DOI: 10.1126/science.102.2637.31.

Heneka, M.T. *et al.* (2015) ‘Neuroinflammation in Alzheimer’s Disease’. *The Lancet. Neurology*, 14(4), pp. 388–405. DOI: 10.1016/S1474-4422(15)70016-5.

Herrmann, T. *et al.* (2021) ‘Functional Refolding of the Penetration Protein on a Non-Enveloped Virus’. *Nature*, 590(7847), pp. 666–670. DOI: 10.1038/s41586-020-03124-4.

Hochheiser, I.V., Behrmann, H., *et al.* (2022) ‘Directionality of PYD Filament Growth Determined by the Transition of NLRP3 Nucleation Seeds to ASC Elongation’. *Science Advances*, 8(19), p. eabn7583. DOI: 10.1126/sciadv.abn7583.

Hochheiser, I.V., Pilsl, M., *et al.* (2022) ‘Structure of the NLRP3 Decamer Bound to the Cytokine Release Inhibitor CRID3’. *Nature*, 604(7904), pp. 184–189. DOI: 10.1038/s41586-022-04467-w.

Hoffmann, M., Kleine-Weber, H., Schroeder, S., *et al.* (2020) ‘SARS-CoV-2 Cell Entry Depends on ACE2 and TMPRSS2 and Is Blocked by a Clinically Proven Protease Inhibitor’. *Cell*, 181(2), pp. 271-280.e8. DOI: 10.1016/j.cell.2020.02.052.

Hoffmann, M., Kleine-Weber, H. and Pöhlmann, S. (2020) ‘A Multibasic Cleavage Site in the Spike Protein of SARS-CoV-2 Is Essential for Infection of Human Lung Cells’. *Molecular Cell*, 78(4), pp. 779-784.e5. DOI: 10.1016/j.molcel.2020.04.022.

Hogle, J.M. (2002) ‘Poliovirus Cell Entry: Common Structural Themes in Viral Cell Entry Pathways’. *Annual Review of Microbiology*, 56, pp. 677–702. DOI: 10.1146/annurev.micro.56.012302.160757.

Hollingsworth, R., Sharif, H., *et al.* (2021) ‘DPP9 Sequesters the C Terminus of NLRP1 to Repress Inflammasome Activation’. *Nature*, 592(7856), pp. 778–783. DOI: 10.1038/s41586-021-03350-4.

Hollingsworth, R., Liron, D., *et al.* (2021) ‘Mechanism of Filament Formation in UPA-Promoted CARD8 and NLRP1 Inflammasomes’. *Nature Communications*, 12(1), p. 189. DOI: 10.1038/s41467-020-20320-y.

Holly, M.K. *et al.* (2020) ‘Salmonella Enterica Infection of Murine and Human Enteroid-Derived Monolayers Elicits Differential Activation of Epithelium-Intrinsic Inflammasomes’. *Infection and Immunity*, 88(7), pp. e00017-20. DOI: 10.1128/IAI.00017-20.

Hornung, V. *et al.* (2009) ‘AIM2 Recognizes Cytosolic dsDNA and Forms a Caspase-1 Activating Inflammasome with ASC’. *Nature*, 458(7237), pp. 514–518. DOI: 10.1038/nature07725.

Hu, Z. *et al.* (2013) ‘Crystal Structure of NLRC4 Reveals Its Autoinhibition Mechanism’. *Science*, 341(6142), pp. 172–175. DOI: 10.1126/science.1236381.

Huang, M. *et al.* (2021) ‘Structural and Biochemical Mechanisms of NLRP1 Inhibition by DPP9’. *Nature*, 592(7856), pp. 773–777. DOI: 10.1038/s41586-021-03320-w.

Huber, S.A. (1994) 'VCAM-1 Is a Receptor for Encephalomyocarditis Virus on Murine Vascular Endothelial Cells'. *Journal of Virology*, 68(6), pp. 3453–3458. DOI: 10.1128/JVI.68.6.3453-3458.1994.

Humke, E.W. *et al.* (2000) 'ICEBERG: A Novel Inhibitor of Interleukin-1β Generation'. *Cell*, 103(1), pp. 99–111. DOI: 10.1016/S0092-8674(00)00108-2.

Huo, J., Zhao, Y., *et al.* (2020) 'Neutralization of SARS-CoV-2 by Destruction of the Prefusion Spike'. *Cell Host & Microbe*, 28(3), pp. 445-454.e6. DOI: 10.1016/j.chom.2020.06.010.

Huo, J., Le Bas, A., *et al.* (2020) 'Neutralizing Nanobodies Bind SARS-CoV-2 Spike RBD and Block Interaction with ACE2'. *Nature Structural & Molecular Biology*, 27(9), pp. 846–854. DOI: 10.1038/s41594-020-0469-6.

ICTV (2011) *ICTV 9th Report*. Available at: https://ictv.global/report_9th/RNApos/Nidovirales/Coronaviridae (Accessed: 22 August 2023).

Ingram, J.R., Schmidt, F.I. and Ploegh, H.L. (2018) 'Exploiting Nanobodies' Singular Traits'. *Annual Review of Immunology*, 36, pp. 695–715. DOI: 10.1146/annurev-immunol-042617-053327.

Ismaili, A. *et al.* (2007) 'Production and Characterization of Anti-(Mucin MUC1) Single-Domain Antibody in Tobacco (Nicotiana Tabacum Cultivar Xanthi)'. *Biotechnology and Applied Biochemistry*, 47(Pt 1), pp. 11–19. DOI: 10.1042/BA20060071.

Jackson, C.B. *et al.* (2022) 'Mechanisms of SARS-CoV-2 Entry into Cells'. *Nature Reviews. Molecular Cell Biology*, 23(1), pp. 3–20. DOI: 10.1038/s41580-021-00418-x.

Jakobs, C. *et al.* (2013) 'Immunoblotting for Active Caspase-1'. *Methods in Molecular Biology (Clifton, N.J.)*, 1040, pp. 103–115. DOI: 10.1007/978-1-62703-523-1_9.

Janda, C.Y. *et al.* (2012) 'Structural Basis of Wnt Recognition by Frizzled'. *Science (New York, N.Y.)*, 337(6090), pp. 59–64. DOI: 10.1126/science.1222879.

Janda, C.Y. and Garcia, K.C. (2015) 'Wnt Acylation and Its Functional Implication in Wnt Signalling Regulation'. *Biochemical Society Transactions*, 43(2), pp. 211–216. DOI: 10.1042/BST20140249.

Jensen, V.B., Harty, J.T. and Jones, B.D. (1998) 'Interactions of the Invasive Pathogens Salmonella Typhimurium, Listeria Monocytogenes, and Shigella Flexneri with M Cells and Murine Peyer's Patches'. *Infection and Immunity*, 66(8), pp. 3758–3766. DOI: 10.1128/IAI.66.8.3758-3766.1998.

Jenster. (2024) *Return of the First Inflammasome: Elucidation of NLRP1 Inflammasome Activation by P38-Mediated Phosphorylation and Ubiquitination*. [Dissertation Thesis]. Bonn: University of Bonn. Available at: https://bonndoc.ulb.uni-bonn.de/xmlui/handle/20.500.11811/11284.

Jenster, L.-M. *et al.* (2023) ‘P38 Kinases Mediate NLRP1 Inflammasome Activation after Ribotoxic Stress Response and Virus Infection’. *The Journal of Experimental Medicine*, 220(1), p. e20220837. DOI: 10.1084/jem.20220837.

Jin, Y.M. *et al.* (1994) ‘Identification and Characterization of the Cell Surface 70-Kilodalton Sialoglycoprotein(s) as a Candidate Receptor for Encephalomyocarditis Virus on Human Nucleated Cells’. *Journal of Virology*, 68(11), pp. 7308–7319. DOI: 10.1128/JVI.68.11.7308-7319.1994.

Johnson, D.C. *et al.* (2018) ‘DPP8/9 Inhibitor-Induced Pyroptosis for Treatment of Acute Myeloid Leukemia’. *Nature Medicine*, 24(8), pp. 1151–1156. DOI: 10.1038/s41591-018-0082-y.

Juncker-Voss, M. *et al.* (2004) ‘[Screening for antibodies against zoonotic agents among employees of the Zoological Garden of Vienna, Schönbrunn, Austria]’. *Berliner Und Munchener Tierarztliche Wochenschrift*, 117(9–10), pp. 404–409.

Kalocsay, M. (2019) ‘APEX Peroxidase-Catalyzed Proximity Labeling and Multiplexed Quantitative Proteomics’. *Methods in Molecular Biology (Clifton, N.J.)*, 2008, pp. 41–55. DOI: 10.1007/978-1-4939-9537-0_4.

Kanzaki, S. *et al.* (2020) ‘Involvement of Nlrp9a/b/c in Mouse Preimplantation Development’. *Reproduction (Cambridge, England)*, 160(2), pp. 181–191. DOI: 10.1530/REP-19-0516.

Karasawa, T. *et al.* (2015) ‘Oligomerized CARD16 Promotes Caspase-1 Assembly and IL-1β Processing’. *FEBS Open Bio*, 5, pp. 348–356. DOI: 10.1016/j.fob.2015.04.011.

Karlsson, M. *et al.* (2021) ‘A Single-Cell Type Transcriptomics Map of Human Tissues’. *Science Advances*, 7(31), p. eabh2169. DOI: 10.1126/sciadv.abh2169.

Kayagaki, N. *et al.* (2015) ‘Caspase-11 Cleaves Gasdermin D for Non-Canonical Inflammasome Signalling’. *Nature*, 526(7575), pp. 666–671. DOI: 10.1038/nature15541.

Kayagaki, N. *et al.* (2011) ‘Non-Canonical Inflammasome Activation Targets Caspase-11’. *Nature*, 479(7371), pp. 117–121. DOI: 10.1038/nature10558.

Ke, Z. *et al.* (2020) ‘Structures and Distributions of SARS-CoV-2 Spike Proteins on Intact Virions’. *Nature*, 588(7838), pp. 498–502. DOI: 10.1038/s41586-020-2665-2.

Kelley, N. *et al.* (2019) ‘The NLRP3 Inflammasome: An Overview of Mechanisms of Activation and Regulation’. *International Journal of Molecular Sciences*, 20(13), p. 3328. DOI: 10.3390/ijms20133328.

Khatri, V. and Kalyanasundaram, R. (2021) ‘Therapeutic Implications of Inflammasome in Inflammatory Bowel Disease’. *FASEB Journal: Official Publication of the Federation of American Societies for Experimental Biology*, 35(5), p. e21439. DOI: 10.1096/fj.202002622R.

Koenig, P.-A. *et al.* (2021) ‘Structure-Guided Multivalent Nanobodies Block SARS-CoV-2 Infection and Suppress Mutational Escape’. *Science (New York, N.Y.)*, 371(6530), p. eabe6230. DOI: 10.1126/science.abe6230.

Kofoed, E.M. and Vance, R.E. (2013) ‘Blue Native Polyacrylamide Gel Electrophoresis to Monitor Inflammasome Assembly and Composition’. *Methods in Molecular Biology (Clifton, N.J.)*, 1040, pp. 169–183. DOI: 10.1007/978-1-62703-523-1_13.

Koo, B.-K. *et al.* (2011) ‘Controlled Gene Expression in Primary Lgr5 Organoid Cultures’. *Nature Methods*, 9(1), pp. 81–83. DOI: 10.1038/nmeth.1802.

Koo, B.-K., Sasselli, V. and Clevers, H. (2013) ‘Retroviral Gene Expression Control in Primary Organoid Cultures’. *Current Protocols in Stem Cell Biology*, 27(1), p. 5A.6.1-5A.6.8. DOI: 10.1002/9780470151808.sc05a06s27.

Lamkanfi, M. *et al.* (2004) ‘INCA, a Novel Human Caspase Recruitment Domain Protein That Inhibits Interleukin-1β Generation*’. *Journal of Biological Chemistry*, 279(50), pp. 51729–51738. DOI: 10.1074/jbc.M407891200.

Lan, J. *et al.* (2020) ‘Structure of the SARS-CoV-2 Spike Receptor-Binding Domain Bound to the ACE2 Receptor’. *Nature*, 581(7807), pp. 215–220. DOI: 10.1038/s41586-020-2180-5.

Lancieri, M. *et al.* (2023) ‘An Update on Familial Mediterranean Fever’. *International Journal of Molecular Sciences*, 24(11), p. 9584. DOI: 10.3390/ijms24119584.

Lee, S.H., Stehlik, C. and Reed, J.C. (2001) ‘COP, a Caspase Recruitment Domain-Containing Protein and Inhibitor of Caspase-1 Activation Processing*’. *Journal of Biological Chemistry*, 276(37), pp. 34495–34500. DOI: 10.1074/jbc.M101415200.

Lemire, P. *et al.* (2017) ‘The NLR Protein NLRP6 Does Not Impact Gut Microbiota Composition’. *Cell Reports*, 21(13), pp. 3653–3661. DOI: 10.1016/j.celrep.2017.12.026.

Leng, F. *et al.* (2020) ‘NLRP6 Self-Assembles into a Linear Molecular Platform Following LPS Binding and ATP Stimulation’. *Scientific Reports*, 10, p. 198. DOI: 10.1038/s41598-019-57043-0.

Levy, M. *et al.* (2015) ‘Microbiota-Modulated Metabolites Shape the Intestinal Microenvironment by Regulating NLRP6 Inflammasome Signaling’. *Cell*, 163(6), pp. 1428–1443. DOI: 10.1016/j.cell.2015.10.048.

Lhocine, N. *et al.* (2015) ‘Apical Invasion of Intestinal Epithelial Cells by Salmonella Typhimurium Requires Villin to Remodel the Brush Border Actin Cytoskeleton’. *Cell Host & Microbe*, 17(2), pp. 164–177. DOI: 10.1016/j.chom.2014.12.003.

Li, B. *et al.* (2017) ‘Drebrin Restricts Rotavirus Entry by Inhibiting Dynamin-Mediated Endocytosis’. *Proceedings of the National Academy of Sciences of the United States of America*, 114(18), pp. E3642–E3651. DOI: 10.1073/pnas.1619266114.

Li, F. (2016) ‘Structure, Function, and Evolution of Coronavirus Spike Proteins’. *Annual Review of Virology*, 3(1), pp. 237–261. DOI: 10.1146/annurev-virology-110615-042301.

Li, R. *et al.* (2022) ‘The Latest Breakthrough on NLRP6 Inflammasome’. *Precision Clinical Medicine*, 5(3), p. pbac022. DOI: 10.1093/pcmedi/pbac022.

Li, T. *et al.* (2020) DOI: 10.1101/2020.06.09.143438.

Lin, Y. and Luo, Z. (2017) ‘NLRP6 Facilitates the Interaction between TAB2/3 and TRIM38 in Rheumatoid Arthritis Fibroblast-like Synoviocytes’. *FEBS Letters*, 591(8), pp. 1141–1149. DOI: 10.1002/1873-3468.12622.

van der Linden, R. *et al.* (2000) ‘Induction of Immune Responses and Molecular Cloning of the Heavy Chain Antibody Repertoire of Lama Glama’. *Journal of Immunological Methods*, 240(1–2), pp. 185–195. DOI: 10.1016/s0022-1759(00)00188-5.

Linder, A. and Hornung, V. (2022) ‘Inflammasomes in T Cells’. *Journal of Molecular Biology*, 434(4), p. 167275. DOI: 10.1016/j.jmb.2021.167275.

Liu, C. *et al.* (2020) ‘The Architecture of Inactivated SARS-CoV-2 with Postfusion Spikes Revealed by Cryo-EM and Cryo-ET’. *Structure (London, England: 1993)*, 28(11), pp. 1218-1224.e4. DOI: 10.1016/j.str.2020.10.001.

Liu, Z. *et al.* (2020) ‘Caspase-1 Engages Full-Length Gasdermin D through Two Distinct Interfaces That Mediate Caspase Recruitment and Substrate Cleavage’. *Immunity*, 53(1), pp. 106-114.e5. DOI: 10.1016/j.immuni.2020.06.007.

Long, C.P. and McDonald, S.M. (2017) ‘Rotavirus Genome Replication: Some Assembly Required’. *PLoS Pathogens*, 13(4), p. e1006242. DOI: 10.1371/journal.ppat.1006242.

Lopez, S. and Arias, C.F. (2006) ‘Early Steps in Rotavirus Cell Entry’. *Current Topics in Microbiology and Immunology*, 309, pp. 39–66. DOI: 10.1007/3-540-30773-7_2.

Lu, A. *et al.* (2016) ‘Molecular Basis of Caspase-1 Polymerization and Its Inhibition by a New Capping Mechanism’. *Nature Structural & Molecular Biology*, 23(5), pp. 416–425. DOI: 10.1038/nsmb.3199.

Lu, A. *et al.* (2015) ‘Plasticity in PYD Assembly Revealed by Cryo-EM Structure of the PYD Filament of AIM2’. *Cell Discovery*, 1, p. 15013. DOI: 10.1038/celldisc.2015.13.

Lu, A. *et al.* (2014) ‘Unified Polymerization Mechanism for the Assembly of ASC-Dependent Inflammasomes’. *Cell*, 156(6), pp. 1193–1206. DOI: 10.1016/j.cell.2014.02.008.

Lu, A. and Wu, H. (2015) ‘Structural Mechanisms of Inflammasome Assembly’. *The FEBS Journal*, 282(3), pp. 435–444. DOI: 10.1111/febs.13133.

Lu, W.L. *et al.* (2019) ‘NLRP6 Suppresses the Inflammatory Response of Human Periodontal Ligament Cells by Inhibiting NF-κB and ERK Signal Pathways’. *International Endodontic Journal*, 52(7), pp. 999–1009. DOI: 10.1111/iej.13091.

Lv, Z. *et al.* (2020) ‘Structural Basis for Neutralization of SARS-CoV-2 and SARS-CoV by a Potent Therapeutic Antibody’. *Science (New York, N.Y.)*, 369(6510), pp. 1505–1509. DOI: 10.1126/science.abc5881.

Lyon, A.S., Peeples, W.B. and Rosen, M.K. (2021) ‘A Framework for Understanding Functions of Biomolecular Condensates on Molecular to Cellular Scales’. *Nature Reviews. Molecular Cell Biology*, 22(3), pp. 215–235. DOI: 10.1038/s41580-020-00303-z.

Maass, D.R. *et al.* (2007) ‘Alpaca (Lama Pacos) as a Convenient Source of Recombinant Camelid Heavy Chain Antibodies (VHHs)’. *Journal of Immunological Methods*, 324(1–2), pp. 13–25. DOI: 10.1016/j.jim.2007.04.008.

Madshus, I.H., Olsnes, S. and Sandvig, K. (1984) ‘Different pH Requirements for Entry of the Two Picornaviruses, Human Rhinovirus 2 and Murine Encephalomyocarditis Virus’. *Virology*, 139(2), pp. 346–357. DOI: 10.1016/0042-6822(84)90380-5.

Maffey, L. *et al.* (2016) ‘Anti-VP6 VHH: An Experimental Treatment for Rotavirus A-Associated Disease’. *PloS One*, 11(9), p. e0162351. DOI: 10.1371/journal.pone.0162351.

Mamantopoulos, M. *et al.* (2018) ‘Inflammasomes Make the Case for Littermate-Controlled Experimental Design in Studying Host-Microbiota Interactions’. *Gut Microbes*, 9(4), pp. 374–381. DOI: 10.1080/19490976.2017.1421888.

Mamantopoulos, M. *et al.* (2017) ‘Nlrp6- and ASC-Dependent Inflammasomes Do Not Shape the Commensal Gut Microbiota Composition’. *Immunity*, 47(2), pp. 339-348.e4. DOI: 10.1016/j.immuni.2017.07.011.

Mariathasan, S. *et al.* (2006) ‘Cryopyrin Activates the Inflammasome in Response to Toxins and ATP’. *Nature*, 440(7081), pp. 228–232. DOI: 10.1038/nature04515.

Mariathasan, S. *et al.* (2004) (6996) ‘Differential Activation of the Inflammasome by Caspase-1 Adaptors ASC and Ipaf’. *Nature*, 430(6996), pp. 213–218. DOI: 10.1038/nature02664.

Marleaux, M. *et al.* (2020) ‘Crystal Structure of the Human NLRP9 Pyrin Domain Suggests a Distinct Mode of Inflammasome Assembly’. *FEBS Letters*, 594(15), pp. 2383–2395. DOI: 10.1002/1873-3468.13865.

Martinon, F., Burns, K. and Tschopp, J. (2002) ‘The Inflammasome: A Molecular Platform Triggering Activation of Inflammatory Caspases and Processing of proIL-Beta’. *Molecular Cell*, 10(2), pp. 417–426. DOI: 10.1016/s1097-2765(02)00599-3.

Maruzuru, Y. *et al.* (2018) ‘Herpes Simplex Virus 1 VP22 Inhibits AIM2-Dependent Inflammasome Activation to Enable Efficient Viral Replication’. *Cell Host & Microbe*, 23(2), pp. 254-265.e7. DOI: 10.1016/j.chom.2017.12.014.

Maurice, H. *et al.* (2005) ‘The Occurrence of Encephalomyocarditis Virus (EMCV) in European Pigs from 1990 to 2001’. *Epidemiology and Infection*, 133(3), pp. 547–557. DOI: 10.1017/s0950268804003668.

Meerbrey, K.L. *et al.* (2011) ‘The pINDUCER Lentiviral Toolkit for Inducible RNA Interference in Vitro and in Vivo’. *Proceedings of the National Academy of Sciences of the United States of America*, 108(9), pp. 3665–3670. DOI: 10.1073/pnas.1019736108.

Meunier, E. and Broz, P. (2017) ‘Evolutionary Convergence and Divergence in NLR Function and Structure’. *Trends in Immunology*, 38(10), pp. 744–757. DOI: 10.1016/j.it.2017.04.005.

Miao, E.A. *et al.* (2010) ‘Innate Immune Detection of the Type III Secretion Apparatus through the NLRC4 Inflammasome’. *Proceedings of the National Academy of Sciences of the United States of America*, 107(7), pp. 3076–3080. DOI: 10.1073/pnas.0913087107.

Miao, Y. *et al.* (2020) ‘Next-Generation Surrogate Wnts Support Organoid Growth and Deconvolute Frizzled Pleiotropy In Vivo’. *Cell Stem Cell*, 27(5), pp. 840-851.e6. DOI: 10.1016/j.stem.2020.07.020.

Müller, A.J. *et al.* (2012) ‘Salmonella Gut Invasion Involves TTSS-2-Dependent Epithelial Traversal, Basolateral Exit, and Uptake by Epithelium-Sampling

Lamina Propria Phagocytes'. *Cell Host & Microbe*, 11(1), pp. 19–32. DOI: 10.1016/j.chom.2011.11.013.

Mullins, B. and Chen, J. (2021) 'NLRP9 in Innate Immunity and Inflammation'. *Immunology*, 162(3), pp. 262–267. DOI: 10.1111/imm.13290.

Muñoz-Planillo, R. *et al.* (2013) 'K^+ Efflux Is the Common Trigger of NLRP3 Inflammasome Activation by Bacterial Toxins and Particulate Matter'. *Immunity*, 38(6), pp. 1142–1153. DOI: 10.1016/j.immuni.2013.05.016.

Murphy, Kenneth and Weaver, Casey (2017) *Janeway's Immunobiology*. 9th Edition. Garland Science, Taylor & Francis Group, LLC.

Muyldermans, S. (2013) 'Nanobodies: Natural Single-Domain Antibodies'. *Annual Review of Biochemistry*, 82, pp. 775–797. DOI: 10.1146/annurev-biochem-063011-092449.

Naseer, N., Egan, M.S., *et al.* (2022) 'Human NAIP/NLRC4 and NLRP3 Inflammasomes Detect Salmonella Type III Secretion System Activities to Restrict Intracellular Bacterial Replication'. *PLoS Pathogens*, 18(1), p. e1009718. DOI: 10.1371/journal.ppat.1009718.

Naseer, N., Zhang, J., *et al.* (2022) 'Salmonella Enterica Serovar Typhimurium Induces NAIP/NLRC4- and NLRP3/ASC-Independent, Caspase-4-Dependent Inflammasome Activation in Human Intestinal Epithelial Cells'. *Infection and Immunity*, 90(7), p. e0066321. DOI: 10.1128/iai.00663-21.

Oberste, M.S. *et al.* (2009) 'Human Febrile Illness Caused by Encephalomyocarditis Virus Infection, Peru'. *Emerging Infectious Diseases*, 15(4), pp. 640–646. DOI: 10.3201/eid1504.081428.

Okondo, M.C. *et al.* (2017) 'DPP8 and DPP9 Inhibition Induces Pro-Caspase-1-Dependent Monocyte and Macrophage Pyroptosis'. *Nature Chemical Biology*, 13(1), pp. 46–53. DOI: 10.1038/nchembio.2229.

Okondo, M.C. *et al.* (2018) 'Inhibition of Dpp8/9 Activates the Nlrp1b Inflammasome'. *Cell Chemical Biology*, 25(3), pp. 262-267.e5. DOI: 10.1016/j.chembiol.2017.12.013.

Omatola, C.A. and Olaniran, A.O. (2022) 'Rotaviruses: From Pathogenesis to Disease Control—A Critical Review'. *Viruses*, 14(5), p. 875. DOI: 10.3390/v14050875.

Papa, G., Borodavka, A. and Desselberger, U. (2021) 'Viroplasms: Assembly and Functions of Rotavirus Replication Factories'. *Viruses*, 13(7), p. 1349. DOI: 10.3390/v13071349.

Patel, J.C. and Galán, J.E. (2005) ‘Manipulation of the Host Actin Cytoskeleton by Salmonella--All in the Name of Entry’. *Current Opinion in Microbiology*, 8(1), pp. 10–15. DOI: 10.1016/j.mib.2004.09.001.

Patton, J.T. and Spencer, E. (2000) ‘Genome Replication and Packaging of Segmented Double-Stranded RNA Viruses’. *Virology*, 277(2), pp. 217–225. DOI: 10.1006/viro.2000.0645.

Perregaux, D. and Gabel, C.A. (1994) ‘Interleukin-1 Beta Maturation and Release in Response to ATP and Nigericin. Evidence That Potassium Depletion Mediated by These Agents Is a Necessary and Common Feature of Their Activity’. *The Journal of Biological Chemistry*, 269(21), pp. 15195–15203.

Poyet, J.-L. *et al.* (2001) ‘Identification of Ipaf, a Human Caspase-1-Activating Protein Related to Apaf-1*’. *Journal of Biological Chemistry*, 276(30), pp. 28309–28313. DOI: 10.1074/jbc.C100250200.

Rauch, I. *et al.* (2016) ‘NAIP Proteins Are Required for Cytosolic Detection of Specific Bacterial Ligands in Vivo’. *The Journal of Experimental Medicine*, 213(5), pp. 657–665. DOI: 10.1084/jem.20151809.

Rauch, I. *et al.* (2017) ‘NAIP-NLRC4 Inflammasomes Coordinate Intestinal Epithelial Cell Expulsion with Eicosanoid and IL-18 Release via Activation of Caspase-1 and -8’. *Immunity*, 46(4), pp. 649–659. DOI: 10.1016/j.immuni.2017.03.016.

Rayamajhi, M., Zak, D.E., *et al.* (2013) ‘Cutting Edge: Mouse NAIP1 Detects the Type III Secretion System Needle Protein’. *Journal of Immunology (Baltimore, Md.: 1950)*, 191(8), pp. 3986–3989. DOI: 10.4049/jimmunol.1301549.

Rayamajhi, M., Zhang, Y. and Miao, E.A. (2013) ‘Detection of Pyroptosis by Measuring Released Lactate Dehydrogenase Activity’. *Methods in Molecular Biology (Clifton, N.J.)*, 1040, pp. 85–90. DOI: 10.1007/978-1-62703-523-1_7.

Reddacliff, L.A. *et al.* (1997) ‘Encephalomyocarditis Virus Infections in an Australian Zoo’. *Journal of Zoo and Wildlife Medicine: Official Publication of the American Association of Zoo Veterinarians*, 28(2), pp. 153–157.

Robinson, K.S. *et al.* (2020) ‘Enteroviral 3C Protease Activates the Human NLRP1 Inflammasome in Airway Epithelia’. *Science*, 370(6521), p. eaay2002. DOI: 10.1126/science.aay2002.

Robinson, K.S. *et al.* (2022) ‘ZAKα-Driven Ribotoxic Stress Response Activates the Human NLRP1 Inflammasome’. *Science (New York, N.Y.)*, 377(6603), pp. 328–335. DOI: 10.1126/science.abl6324.

Rodriguez Gama, A. *et al.* (2023) ‘Protein Supersaturation Powers Innate Immune Signaling’. *bioRxiv: The Preprint Server for Biology*, p. 2023.03.20.533581. DOI: 10.1101/2023.03.20.533581.

Romanova, L.I. *et al.* (2009) 'Antiapoptotic Activity of the Cardiovirus Leader Protein, a Viral "Security" Protein'. *Journal of Virology*, 83(14), pp. 7273–7284. DOI: 10.1128/JVI.00467-09.

Ross, C. *et al.* (2018) 'Dimerization and Auto-Processing Induce Caspase-11 Protease Activation within the Non-Canonical Inflammasome'. *Life Science Alliance*, 1(6), p. e201800237. DOI: 10.26508/lsa.201800237.

Ross, C. *et al.* (2022) 'Inflammatory Caspases: Toward a Unified Model for Caspase Activation by Inflammasomes'. *Annual Review of Immunology*, 40, pp. 249–269. DOI: 10.1146/annurev-immunol-101220-030653.

Rothbauer, U. *et al.* (2006) 'Targeting and Tracing Antigens in Live Cells with Fluorescent Nanobodies'. *Nature Methods*, 3(11), pp. 887–889. DOI: 10.1038/nmeth953.

Rühl, S. and Broz, P. (2015) 'Caspase-11 Activates a Canonical NLRP3 Inflammasome by Promoting K(+) Efflux'. *European Journal of Immunology*, 45(10), pp. 2927–2936. DOI: 10.1002/eji.201545772.

Saavedra, P.H.V. *et al.* (2015) 'Protective and Detrimental Roles of Inflammasomes in Disease'. *Seminars in Immunopathology*, 37(4), pp. 313–322. DOI: 10.1007/s00281-015-0485-5.

Samperio Ventayol, P. *et al.* (2021) 'Bacterial Detection by NAIP/NLRC4 Elicits Prompt Contractions of Intestinal Epithelial Cell Layers'. *Proceedings of the National Academy of Sciences of the United States of America*, 118(16), p. e2013963118. DOI: 10.1073/pnas.2013963118.

Sandstrom, A. *et al.* (2019) 'Functional Degradation: A Mechanism of NLRP1 Inflammasome Activation by Diverse Pathogen Enzymes'. *Science*, 364(6435), p. eaau1330. DOI: 10.1126/science.aau1330.

Santos, J.C. *et al.* (2020) 'Human GBP1 Binds LPS to Initiate Assembly of a Caspase-4 Activating Platform on Cytosolic Bacteria'. *Nature Communications*, 11(1), p. 3276. DOI: 10.1038/s41467-020-16889-z.

Sato, T. *et al.* (2011) 'Long-Term Expansion of Epithelial Organoids from Human Colon, Adenoma, Adenocarcinoma, and Barrett's Epithelium'. *Gastroenterology*, 141(5), pp. 1762–1772. DOI: 10.1053/j.gastro.2011.07.050.

Schlegel, A. *et al.* (1996) 'Cellular Origin and Ultrastructure of Membranes Induced during Poliovirus Infection'. *Journal of Virology*, 70(10), pp. 6576–6588. DOI: 10.1128/JVI.70.10.6576-6588.1996.

Schmid-Burgk, J.L. *et al.* (2015) 'Caspase-4 Mediates Non-Canonical Activation of the NLRP3 Inflammasome in Human Myeloid Cells'. *European Journal of Immunology*, 45(10), pp. 2911–2917. DOI: 10.1002/eji.201545523.

Schmidt, F.I. *et al.* (2016) ‘A Single Domain Antibody Fragment That Recognizes the Adaptor ASC Defines the Role of ASC Domains in Inflammasome Assembly’. *The Journal of Experimental Medicine*, 213(5), pp. 771–790. DOI: 10.1084/jem.20151790.

Schmidt, F.I. (2023) ‘Chapter 13 - Inflammatory Caspases’. In Pelegrin, P. (ed.) *Inflammasome Biology*. Academic Press, pp. 205–214. DOI: 10.1016/B978-0-323-91802-2.00018-9.

Schneider, K.S., Thomas, C.J. and Groß, O. (2013) ‘Inflammasome Activation and Inhibition in Primary Murine Bone Marrow-Derived Cells, and Assays for IL-1α, IL-1β, and Caspase-1’. *Methods in Molecular Biology (Clifton, N.J.)*, 1040, pp. 117–135. DOI: 10.1007/978-1-62703-523-1_10.

Schoof, M. *et al.* (2020) ‘An Ultrapotent Synthetic Nanobody Neutralizes SARS-CoV-2 by Stabilizing Inactive Spike’. *Science (New York, N.Y.)*, 370(6523), pp. 1473–1479. DOI: 10.1126/science.abe3255.

Schwank, G. and Clevers, H. (2016) ‘CRISPR/Cas9-Mediated Genome Editing of Mouse Small Intestinal Organoids’. *Methods in Molecular Biology (Clifton, N.J.)*, 1422, pp. 3–11. DOI: 10.1007/978-1-4939-3603-8_1.

Sellin, M.E. *et al.* (2014) ‘Epithelium-Intrinsic NAIP/NLRC4 Inflammasome Drives Infected Enterocyte Expulsion to Restrict Salmonella Replication in the Intestinal Mucosa’. *Cell Host & Microbe*, 16(2), pp. 237–248. DOI: 10.1016/j.chom.2014.07.001.

Sester, D.P. *et al.* (2015) ‘A Novel Flow Cytometric Method to Assess Inflammasome Formation’. *Journal of Immunology (Baltimore, Md.: 1950)*, 194(1), pp. 455–462. DOI: 10.4049/jimmunol.1401110.

Shang, J., Wan, Y., *et al.* (2020) ‘Cell Entry Mechanisms of SARS-CoV-2’. *Proceedings of the National Academy of Sciences of the United States of America*, 117(21), pp. 11727–11734. DOI: 10.1073/pnas.2003138117.

Shang, J., Ye, G., *et al.* (2020) ‘Structural Basis of Receptor Recognition by SARS-CoV-2’. *Nature*, 581(7807), pp. 221–224. DOI: 10.1038/s41586-020-2179-y.

Shen, C. *et al.* (2019) ‘Molecular Mechanism for NLRP6 Inflammasome Assembly and Activation’. *Proceedings of the National Academy of Sciences of the United States of America*, 116(6), pp. 2052–2057. DOI: 10.1073/pnas.1817221116.

Shen, C. *et al.* (2021) ‘Phase Separation Drives RNA Virus-Induced Activation of the NLRP6 Inflammasome’. *Cell*, 184(23), pp. 5759-5774.e20. DOI: 10.1016/j.cell.2021.09.032.

Shi, J. *et al.* (2014) ‘Inflammatory Caspases Are Innate Immune Receptors for Intracellular LPS’. *Nature*, 514(7521), pp. 187–192. DOI: 10.1038/nature13683.

Simmons, G. *et al.* (2011) 'Different Host Cell Proteases Activate the SARS-Coronavirus Spike-Protein for Cell–Cell and Virus–Cell Fusion'. *Virology*, 413(2), pp. 265–274. DOI: 10.1016/j.virol.2011.02.020.

So, A.K. and Martinon, F. (2017) 'Inflammation in Gout: Mechanisms and Therapeutic Targets'. *Nature Reviews. Rheumatology*, 13(11), pp. 639–647. DOI: 10.1038/nrrheum.2017.155.

Song, W. *et al.* (2018) 'Cryo-EM Structure of the SARS Coronavirus Spike Glycoprotein in Complex with Its Host Cell Receptor ACE2'. *PLoS Pathogens*, 14(8), p. e1007236. DOI: 10.1371/journal.ppat.1007236.

Spel, L. and Martinon, F. (2020) 'Inflammasomes Contributing to Inflammation in Arthritis'. *Immunological Reviews*, 294(1), pp. 48–62. DOI: 10.1111/imr.12839.

Stanifer, M.L., Pervolaraki, K. and Boulant, S. (2019) 'Differential Regulation of Type I and Type III Interferon Signaling'. *International Journal of Molecular Sciences*, 20(6), p. 1445. DOI: 10.3390/ijms20061445.

Stauffer, W., Sheng, H. and Lim, H.N. (2018) 'EzColocalization: An ImageJ Plugin for Visualizing and Measuring Colocalization in Cells and Organisms'. *Scientific Reports*, 8, p. 15764. DOI: 10.1038/s41598-018-33592-8.

Stehlik, C. and Dorfleutner, A. (2007) 'COPs & POPs: Modulators of Inflammasome Activity'. *Journal of Immunology (Baltimore, Md. : 1950)*, 179(12), pp. 7993–7998.

Stutz, A. *et al.* (2013) 'ASC Speck Formation as a Readout for Inflammasome Activation'. In De Nardo, C.M. and Latz, E. (eds.) *The Inflammasome: Methods and Protocols*. Methods in Molecular Biology. Totowa, NJ: Humana Press, pp. 91–101. DOI: 10.1007/978-1-62703-523-1_8.

Taabazuing, C.Y., Griswold, A.R. and Bachovchin, D.A. (2020) 'The NLRP1 and CARD8 Inflammasomes'. *Immunological Reviews*, 297(1), pp. 13–25. DOI: 10.1111/imr.12884.

Takeuchi, O. and Akira, S. (2010) 'Pattern Recognition Receptors and Inflammation'. *Cell*, 140(6), pp. 805–820. DOI: 10.1016/j.cell.2010.01.022.

Tate, J.E. *et al.* (2016) 'Global, Regional, and National Estimates of Rotavirus Mortality in Children <5 Years of Age, 2000-2013'. *Clinical Infectious Diseases: An Official Publication of the Infectious Diseases Society of America*, 62 Suppl 2, pp. S96–S105. DOI: 10.1093/cid/civ1013.

Tesh, R.B. (1978) 'The Prevalence of Encephalomyocarditis Virus Neutralizing Antibodies among Various Human Populations'. *The American Journal of Tropical Medicine and Hygiene*, 27(1 Pt 1), pp. 144–149. DOI: 10.4269/ajtmh.1978.27.144.

The Human Protein Atlas. *The Human Protein Atlas*. Available at: https://www.proteinatlas.org/ (Accessed: 13 February 2024).

Tian, X.X. *et al.* (2021) ‘NLRP6-Caspase 4 Inflammasome Activation in Response to Cariogenic Bacterial Lipoteichoic Acid in Human Dental Pulp Inflammation’. *International Endodontic Journal*, 54(6), pp. 916–925. DOI: 10.1111/iej.13469.

Tomuschat, C. *et al.* (2019) ‘Reduced Expression of the NLRP6 Inflammasome in the Colon of Patients with Hirschsprung’s Disease’. *Journal of Pediatric Surgery*, 54(8), pp. 1573–1577. DOI: 10.1016/j.jpedsurg.2018.08.059.

Tortorici, M.A. *et al.* (2020) ‘Ultrapotent Human Antibodies Protect against SARS-CoV-2 Challenge via Multiple Mechanisms’. *Science (New York, N.Y.)*, 370(6519), pp. 950–957. DOI: 10.1126/science.abe3354.

Troeger, C. *et al.* (2018) ‘Rotavirus Vaccination and the Global Burden of Rotavirus Diarrhea Among Children Younger Than 5 Years’. *JAMA Pediatrics*, 172(10), pp. 958–965. DOI: 10.1001/jamapediatrics.2018.1960.

Turoňová, B. *et al.* (2020) ‘In Situ Structural Analysis of SARS-CoV-2 Spike Reveals Flexibility Mediated by Three Hinges’. *Science (New York, N.Y.)*, 370(6513), pp. 203–208. DOI: 10.1126/science.abd5223.

Tzeng, T.-C. *et al.* (2016) ‘A Fluorescent Reporter Mouse for Inflammasome Assembly Demonstrates an Important Role for Cell-Bound and Free ASC Specks during In Vivo Infection’. *Cell Reports*, 16(2), pp. 571–582. DOI: 10.1016/j.celrep.2016.06.011.

Uzri, D. and Greenberg, H.B. (2013) ‘Characterization of Rotavirus RNAs That Activate Innate Immune Signaling through the RIG-I-Like Receptors’. *PLoS ONE*, 8(7), p. e69825. DOI: 10.1371/journal.pone.0069825.

Van Opdenbosch, N. and Lamkanfi, M. (2019) ‘Caspases in Cell Death, Inflammation, and Disease’. *Immunity*, 50(6), pp. 1352–1364. DOI: 10.1016/j.immuni.2019.05.020.

Vance, R.E. (2015) ‘The NAIP/NLRC4 Inflammasomes’. *Current Opinion in Immunology*, 32, pp. 84–89. DOI: 10.1016/j.coi.2015.01.010.

Vasudevan, S.O., Behl, B. and Rathinam, V.A. (2023) ‘Pyroptosis-Induced Inflammation and Tissue Damage’. *Seminars in Immunology*, 69, p. 101781. DOI: 10.1016/j.smim.2023.101781.

Venegas, C. and Heneka, M.T. (2019) ‘Inflammasome-Mediated Innate Immunity in Alzheimer’s Disease’. *FASEB Journal: Official Publication of the Federation of American Societies for Experimental Biology*, 33(12), pp. 13075–13084. DOI: 10.1096/fj.201900439.

Veyer, D.L. *et al.* (2017) ‘Vaccinia Virus Evasion of Regulated Cell Death’. *Immunology Letters*, 186, pp. 68–80. DOI: 10.1016/j.imlet.2017.03.015.

Viganò, E. *et al.* (2015) (1) ‘Human Caspase-4 and Caspase-5 Regulate the One-Step Non-Canonical Inflammasome Activation in Monocytes’. *Nature Communications*, 6(1), p. 8761. DOI: 10.1038/ncomms9761.

Vind, A.C. *et al.* (2020) ‘ZAKα Recognizes Stalled Ribosomes through Partially Redundant Sensor Domains’. *Molecular Cell*, 78(4), pp. 700-713.e7. DOI: 10.1016/j.molcel.2020.03.021.

V’kovski, P. *et al.* (2021) (3) ‘Coronavirus Biology and Replication: Implications for SARS-CoV-2’. *Nature Reviews Microbiology*, 19(3), pp. 155–170. DOI: 10.1038/s41579-020-00468-6.

Volk, J.K. *et al.* (2019) ‘The Nlrp6 Inflammasome Is Not Required for Baseline Colonic Inner Mucus Layer Formation or Function’. *The Journal of Experimental Medicine*, 216(11), pp. 2602–2618. DOI: 10.1084/jem.20190679.

Walls, A.C. *et al.* (2020) ‘Structure, Function, and Antigenicity of the SARS-CoV-2 Spike Glycoprotein’. *Cell*, 181(2), pp. 281-292.e6. DOI: 10.1016/j.cell.2020.02.058.

Walls, A.C. *et al.* (2017) ‘Tectonic Conformational Changes of a Coronavirus Spike Glycoprotein Promote Membrane Fusion’. *Proceedings of the National Academy of Sciences of the United States of America*, 114(42), pp. 11157–11162. DOI: 10.1073/pnas.1708727114.

Walls, A.C. *et al.* (2019) ‘Unexpected Receptor Functional Mimicry Elucidates Activation of Coronavirus Fusion’. *Cell*, 176(5), pp. 1026-1039.e15. DOI: 10.1016/j.cell.2018.12.028.

Walter, J.D. *et al.* (2020) DOI: 10.1101/2020.04.16.045419.

Wan, Y. *et al.* (2020) ‘Molecular Mechanism for Antibody-Dependent Enhancement of Coronavirus Entry’. *Journal of Virology*, 94(5), pp. e02015-19. DOI: 10.1128/JVI.02015-19.

Wandel, M.P. *et al.* (2020) ‘Guanylate-Binding Proteins (GBPs) Convert Cytosolic Bacteria into Caspase-4 Signaling Platforms’. *Nature Immunology*, 21(8), pp. 880–891. DOI: 10.1038/s41590-020-0697-2.

Wang, K. *et al.* (2020) ‘Structural Mechanism for GSDMD Targeting by Autoprocessed Caspases in Pyroptosis’. *Cell*, 180(5), pp. 941-955.e20. DOI: 10.1016/j.cell.2020.02.002.

Wang, P. *et al.* (2015) ‘Nlrp6 Regulates Intestinal Antiviral Innate Immunity’. *Science (New York, N.Y.)*, 350(6262), pp. 826–830. DOI: 10.1126/science.aab3145.

Wang, Q., Wang, C. and Chen, J. (2018) ‘NLRP6, Decreased in Gastric Cancer, Suppresses Tumorigenicity of Gastric Cancer Cells’. *Cancer Management and Research*, 10, pp. 6431–6444. DOI: 10.2147/CMAR.S182980.

Wang, Q. *et al.* (2020) ‘Structural and Functional Basis of SARS-CoV-2 Entry by Using Human ACE2’. *Cell*, 181(4), pp. 894-904.e9. DOI: 10.1016/j.cell.2020.03.045.

Wang, X. *et al.* (2020) ‘NLRP6 Suppresses Gastric Cancer Growth via GRP78 Ubiquitination’. *Experimental Cell Research*, 395(1), p. 112177. DOI: 10.1016/j.yexcr.2020.112177.

WHO (2023) *WHO Coronavirus (COVID-19) Dashboard*. Available at: https://covid19.who.int (Accessed: 22 August 2023).

Wlodarska, M. *et al.* (2014) ‘NLRP6 Inflammasome Orchestrates the Colonic Host-Microbial Interface by Regulating Goblet Cell Mucus Secretion’. *Cell*, 156(5), pp. 1045–1059. DOI: 10.1016/j.cell.2014.01.026.

Wrapp, D., Wang, N., *et al.* (2020) ‘Cryo-EM Structure of the 2019-nCoV Spike in the Prefusion Conformation’. *Science (New York, N.Y.)*, 367(6483), pp. 1260–1263. DOI: 10.1126/science.abb2507.

Wrapp, D., De Vlieger, D., *et al.* (2020) ‘Structural Basis for Potent Neutralization of Betacoronaviruses by Single-Domain Camelid Antibodies’. *Cell*, 181(5), pp. 1004-1015.e15. DOI: 10.1016/j.cell.2020.04.031.

Xia, S. *et al.* (2020) ‘Inhibition of SARS-CoV-2 (Previously 2019-nCoV) Infection by a Highly Potent Pan-Coronavirus Fusion Inhibitor Targeting Its Spike Protein That Harbors a High Capacity to Mediate Membrane Fusion’. *Cell Research*, 30(4), pp. 343–355. DOI: 10.1038/s41422-020-0305-x.

Xiao, T. *et al.* (2021) ‘A Trimeric Human Angiotensin-Converting Enzyme 2 as an Anti-SARS-CoV-2 Agent’. *Nature Structural & Molecular Biology*, 28(2), pp. 202–209. DOI: 10.1038/s41594-020-00549-3.

Xing, J. *et al.* (2021) ‘DHX15 Is Required to Control RNA Virus-Induced Intestinal Inflammation’. *Cell Reports*, 35(12), p. 109205. DOI: 10.1016/j.celrep.2021.109205.

Yan, R. *et al.* (2020) ‘Structural Basis for the Recognition of SARS-CoV-2 by Full-Length Human ACE2’. *Science (New York, N.Y.)*, 367(6485), pp. 1444–1448. DOI: 10.1126/science.abb2762.

Yang, J. *et al.* (2013) ‘Human NAIP and Mouse NAIP1 Recognize Bacterial Type III Secretion Needle Protein for Inflammasome Activation’. *Proceedings of the National Academy of Sciences of the United States of America*, 110(35), pp. 14408–14413. DOI: 10.1073/pnas.1306376110.

Yao, H. *et al.* (2020) ‘Molecular Architecture of the SARS-CoV-2 Virus’. *Cell*, 183(3), pp. 730-738.e13. DOI: 10.1016/j.cell.2020.09.018.

Yow, S.J., Yeap, H.W. and Chen, K.W. (2022) ‘Inflammasome and Gasdermin Signaling in Neutrophils’. *Molecular Microbiology*, 117(5), pp. 961–972. DOI: 10.1111/mmi.14891.

Yu, Y. *et al.* (2021) ‘SP1 Transcriptionally Activates NLRP6 Inflammasome and Induces Immune Evasion and Radioresistance in Glioma Cells’. *International Immunopharmacology*, 98, p. 107858. DOI: 10.1016/j.intimp.2021.107858.

Zeve, D. *et al.* (2022) ‘Robust Differentiation of Human Enteroendocrine Cells from Intestinal Stem Cells’. *Nature Communications*, 13(1), p. 261. DOI: 10.1038/s41467-021-27901-5.

Zhang, J. *et al.* (2021) ‘Structural Impact on SARS-CoV-2 Spike Protein by D614G Substitution’. *Science (New York, N.Y.)*, 372(6541), pp. 525–530. DOI: 10.1126/science.abf2303.

Zhao, Y. *et al.* (2011) ‘The NLRC4 Inflammasome Receptors for Bacterial Flagellin and Type III Secretion Apparatus’. *Nature*, 477(7366), pp. 596–600. DOI: 10.1038/nature10510.

Zhou, T. *et al.* (2020) ‘Cryo-EM Structures of SARS-CoV-2 Spike without and with ACE2 Reveal a pH-Dependent Switch to Mediate Endosomal Positioning of Receptor-Binding Domains’. *Cell Host & Microbe*, 28(6), pp. 867-879.e5. DOI: 10.1016/j.chom.2020.11.004.

Zhu, S. *et al.* (2017) ‘Nlrp9b Inflammasome Restricts Rotavirus Infection in Intestinal Epithelial Cells’. *Nature*, 546(7660), pp. 667–670. DOI: 10.1038/nature22967.

Zielonka, S. *et al.* (2015) ‘Structural Insights and Biomedical Potential of IgNAR Scaffolds from Sharks’. *mAbs*, 7(1), pp. 15–25. DOI: 10.4161/19420862.2015.989032.

Zmora, N. *et al.* (2017) ‘Inflammasomes and Intestinal Inflammation’. *Mucosal Immunology*, 10(4), pp. 865–883. DOI: 10.1038/mi.2017.19.

Zou, W.Y. *et al.* (2019) ‘Human Intestinal Enteroids: New Models to Study Gastrointestinal Virus Infections’. *Methods in Molecular Biology (Clifton, N.J.)*, 1576, pp. 229–247. DOI: 10.1007/7651_2017_1.

Table A.1: Cell lines

Name in this thesis	Lab Intern name	Parental cell line	transgene	Plasmid	Information	Selection
HEK$^{\text{ASC-EGFP}}$	H1	HEK 293T WT	ASC-EGFP	pRRL UbCp ASC-EGFP Puro	lentiviral monoclonal	1 µg/mL Puromycin, 50 µg/mL Hygromycin
HEK$^{\text{NLRP1-HA+ASC--EGFP}}$	H8	H1	ASC-GS-EGFP + NLRP1-HA	pRRL UbC NLRP1-HA HygromycinB	lentiviral polyclonal	1 µg/mL Puromycin, 50 µg/mL Hygromycin
HEK$^{\text{ACE2-tagRFP-t}}$	H92	HEK 293T	ACE2-tag-RFP-t	pRRL pEF1alpha ACE2-tag-RFP-t Hyg	lentiviral polyclonal	50 ug/mL Hygromycin
HEK$^{\text{NLRP6-HA(i)}}$	HFT18	HEK 293 Flp-In T-Rex	NLRP6-SH	pEXPR TO FRT NLRP6-SH	Flp recombination	4 µg/mL blasticidin + 50 µg/mL hygromycin
HEK$^{\text{NLRP9-HA(i)}}$	HFT21	HEK 293 Flp-In T-Rex	NLRP9-SH	pEXPR TO FRT NLRP9-SH	Flp recombination	4 µg/mL blasticidin + 50 µg/mL hygromycin

Name in this thesis	Lab Intern name	Parental cell line	transgene	Plasmid	Information	Selection
$\text{HEK}^{\text{NLRP6-HA(i)+ASC-EGFP}}$	HFT28	HFT18	NLRP6-HA + ASC-EGFP	pRRL UbCp ASC-EGFP Puro	lentiviral monoclonal	4 µg/mL blasticidin + 50 µg/mL hygromycin + 1 µg puromycin
$\text{HEK}^{\text{NLRP9-HA(i)+ASC-EGFP}}$	HFT29	HFT21	NLRP9-HA + ASC-EGFP	pRRL UbCp ASC-EGFP Puro	lentiviral monoclonal	4 µg/mL blasticidin + 50 µg/mL hygromycin + 1 µg puromycin
$\text{HEK}^{\text{spike(i)+EGFP}}$	HFT61	HEK 293 Flp-In T-Rex	EGFP	pRRL pCMV EGFP Puro	Flp recombination	4 µg/mL blasticidin + 50 µg/mL hygromycin
$\text{HEK}^{\text{spike(i)+tagRFP-t}}$	HFT63	HEK 293 Flp-In T-Rex	tagRFP-t	pRRL pCMV tagRFP-t Puro	Flp recombination	4 µg/mL blasticidin + 50 µg/mL hygromycin
$\text{HEK}^{\text{NLRP1-SH(i)+C1C-EGFP}}$	HFT85	HFT30	NLRP1-SH + C1C-EGFP	pRRL pUbC C1C-EGFP Puro	lentiviral	4 µg/mL blasticidin + 50 µg/mL hygromycin + 1 µg puromycin

Name in this thesis	Lab Intern name	Parental cell line	transgene	Plasmid	Information	Selection
$\text{HEK}^{\text{CARD8-SH(i)+C1C-EGFP}}$	HFT87	HFT66	CARD8-SH + C1C EGFP	pRRLpUBC C1C-EGFP puro	lentiviral	4 µg/mL blasticidin + 50 µg/mL hygromycin + 1 µg puromycin
$\text{HeLa}^{\text{EGFP-GBP1}}$	HL12	HeLa WT	EGFP-GBP1	pRRL pCMV EGFP -GBP1 stop puro	lentiviral polyclonal	0.75 µg/mL Puromycin
HIE (duodenum)	hOD1	-	none	none	duodenum	none
$\text{HIE}^{\text{C1C-EGFP}}$ (duodenum)	hOD2	hOD1	C1C-EGFP	pRRL UbCp C1C-EGFP puro	duodenum	2 µg/mL Puromycin
HIE (ileum)	hOI1	-	none	none	ileum	none

Name in this thesis	**Lab Intern name**	**Parental cell line**	**transgene**	**Plasmid**	**Information**	**Selection**
HIE (jejunum)	hOJ1	-	none	none	jeunum	none
HIE$^{\text{STAT1-EGFP}}$ (jejunum)	hOJ11	hOJ6	Stat1β-EGFP	pRRL pUbC Stat1β-EGFP puro	jeunum	2 µg/mL Puromycin
HIE$^{\text{C1C-EGFP}}$ (jejunum)	hOJ2	hOJ1	C1C-EGFP	pRRL UbCp C1C-EGFP Puro	jeunum	2 µg/mL Puromycin
HIE (jejunum)	hOJ5	-	none	none	jeunum	none
HIE (jejunum)	hOJ6	-	none	none	jeunum	none

Name in this thesis	Lab Intern name	Parental cell line	transgene	Plasmid	Information	Selection
HIE$^{\text{EGFP-GBP1}}$ (jejunum)	hOJ9	hOJ6	EGFP-GBP1 stop	pRRL pCMV EGFP-GBP1 stop Puro	jeunum	2 ug/mL Puromycin
iMac$^{\text{mC1C-EGFP}}$	iMAC1	iMAC WT	C1C-EGFP	pInducer20-NA mC1C-EGFP neo	-	500 µg/mL G418
NTERT-$^{\text{1C1C-EGFP}}$	K14	N/TERT WT	pRRL UbCp C1C-EGFP	pRRL UbCp C1C-EGFP Puro	lentiviral polyclonal	1 µg/mL Puromycin
MIE	mOS1	-	none	none	small intestine	none
MIE$^{\text{ASC-mCherry}}$	mOS4	-	none	none	small intestine (ASC-mCherry mouse)	none

Name in this thesis	Lab Intern name	Parental cell line	transgene	Plasmid	Information	Selection
MIE$^{\text{mC1C-EGF}}$	mOS6	mOS1	mC1C-EGFP	pRRL UbCp mC1C-EGFP Puro	small intestine	2 µg/mL Puromycin
THP-1$^{\text{C1C-EGFP(i)}}$	T55	THP-1 WT	C1C-EGFP	pInducer20-NA C1C-EGFP	lentiviral polyclonal	500 µg/mL G418
THP-1$^{\text{C1C-EGFP(i)}}$	T590	THP-1 WT	C1C-EGFP	pInducer20 C1C-EGFP	lentiviral polyclonal	500 µg/mL G418
THP-1$^{\text{C1C-EGFP D27R E28R(i)}}$	T591	THP-1 WT	C1C-EGFP D27R E28R	pInducer20 C1C-EGFP D27R E28R	lentiviral polyclonal	500 µg/mL G418
THP-1$^{\text{C1C-EGFP Y82E(i)}}$	T592	THP-1 WT	C1C-EGFP Y82E	pInducer20 C1C-EGFP Y82E	lentiviral polyclonal	500 µg/mL G418

Name in this thesis	**Lab Intern name**	**Parental cell line**	**transgene**	**Plasmid**	**Information**	**Selection**
THP-1$^{\text{C1C-mCherry(i)}}$	T60	THP-1 WT	C1C-mCherry	pInducer20-NA C1C-mCherry	lentiviral polyclonal	500 µg/mL G418
THP-1$^{\text{C1C-EGFP R10E K11E(i)}}$	T635	THP-1 WT	C1C EGFP R10E K11E	pInducer20 C1C EGFP R10E K11E	lentiviral polyclonal	500 µg/mL G418
THP-1$^{\text{C1C-mCherry(i)+ CARD17-EGFP}}$	T683	T60	CARD17-EGFP	pRRL pEF1α CARD17-EGFP Puro	lentiviral polyclonal	500 µg/mL G418 + 0.75 µg/mL puromycin
THP-1$^{\text{C1C-mCherry(i)+ CARD17 R55E-EGFP}}$	T684	T60	CARD17 R55E-EGFP	pRRL pEF1α CARD17 R55E-EGFP Puro	lentiviral polyclonal	500 µg/mL G418 + 0.75 µg/mL puromycin
THP-$^{\text{1C1C-EGFP,}\Delta\text{ASC}}$	T72	THP-1 ΔASC	C1C-EGFP	pInducer20-NA C1C-EGFP	lentiviral polyclonal	500 µg/mL G418

Name in this thesis	**Lab Intern name**	**Parental cell line**	**transgene**	**Plasmid**	**Information**	**Selection**
THP-1$^{\text{C1C-EGFP,}\Delta\text{caspase-1}}$	T74	THP-1 Δcaspase-1	C1C-EGFP	pInducer20-NA C1C-EGFP	lentiviral polyclonal	500 µg/mL G418
THP-1$^{\text{C1C-EGFP}}$	T76S	THP-1 WT	C1C-EGFP	pRRL UbCp C1C-EGFP Hyg	sorted	50 µg/mL Hygromycin
THP-1 WT	THP-1 WT	-	none	none		none

Table A.2: Kinetic binding parameters of VHH. Parameters were obtained using surface plasmon resonance spectrometry. NB: no binding. Data from Koenig *et al.* (2021)

VHH	RBD k_a [1/Ms]	RBD k_d [1/s]	RBD K_D [M]
D	NB	NB	NB
F	NB	NB	NB
J	NB	NB	NB
N	$2.74 \cdot 10^{2}$	$1.04 \cdot 10^{-2}$	$3.78 \cdot 10^{-8}$
O	$3.31 \cdot 10^{4}$	$1.65 \cdot 10^{-3}$	$5.01 \cdot 10^{-8}$
Q	$4.38 \cdot 10^{5}$	$1.53 \cdot 10^{-1}$	$3.49 \cdot 10^{-7}$
U	$3.39 \cdot 10^{5}$	$7.27 \cdot 10^{-3}$	$2.14 \cdot 10^{-8}$
W	$6.77 \cdot 10^{5}$	$1.50 \cdot 10^{-2}$	$2.22 \cdot 10^{-8}$
V	$1.93 \cdot 10^{4}$	$1.72 \cdot 10^{-4}$	$8.92 \cdot 10^{-9}$
E	$4.59 \cdot 10^{5}$	$8.55 \cdot 10^{-4}$	$1.86 \cdot 10^{-9}$
EE	$1.04 \cdot 10^{6}$	$2.20 \cdot 10^{-4}$	$2.12 \cdot 10^{-10}$
VV	$1.02 \cdot 10^{5}$	$2.36 \cdot 10^{-4}$	$2.31 \cdot 10^{-9}$
EV	$3.70 \cdot 10^{5}$	$7.37 \cdot 10^{-5}$	$1.99 \cdot 10^{-10}$
VE	$4.80 \cdot 10^{5}$	$4.05 \cdot 10^{-5}$	$8.44 \cdot 10^{-11}$
Ty1	$3.68 \cdot 10^{5}$	$6.05 \cdot 10^{-3}$	$1.64 \cdot 10^{-8}$
VHH 72	$3.16 \cdot 10^{5}$	$6.64 \cdot 10^{-2}$	$2.10 \cdot 10^{-7}$
Sb 042	$4.44 \cdot 10^{5}$	$5.26 \cdot 10^{-2}$	$1.18 \cdot 10^{-7}$
SN-28	NB	NB	NB

RESEARCH ARTICLE SUMMARY

CORONAVIRUS

Structure-guided multivalent nanobodies block SARS-CoV-2 infection and suppress mutational escape

Paul-Albert Koenig*, Hrishikesh Das†, Hejun Liu†, Beate M. Kümmerer, Florian N. Gohr‡, Lea-Marie Jenster‡, Lisa D. J. Schiffelers‡, Yonas M. Tesfamariam‡, Miki Uchima‡, Jennifer D. Wuerth‡, Karl Gatterdam, Natalia Ruetalo, Maria H. Christensen, Caroline I. Fandrey, Sabine Normann, Jan M. P. Tödtmann, Steffen Pritzl, Leo Hanke, Jannik Boos, Meng Yuan, Xueyong Zhu, Jonathan L. Schmid-Burgk, Hiroki Kato, Michael Schindler, Ian A. Wilson, Matthias Geyer, Kerstin U. Ludwig, B. Martin Hällberg*, Nicholas C. Wu*, Florian I. Schmidt*

INTRODUCTION: The global scale and rapid spread of severe acute respiratory syndrome coronavirus 2 (SARS-CoV-2) pose unprecedented challenges to society, health care systems, and science. In addition to effective and safe vaccines, passive immunization by antibody-related molecules offers an opportunity to harness the vertebrate immune system to fight viral infections in high-risk patients. Variable domains of heavy-chain–only antibodies (VHHs), also known as nanobodies, are suitable lead molecules in such efforts, as they are small, extremely stable, easy to engineer, and economic to produce in simple expression systems.

RATIONALE: We engineered improved multivalent nanobodies neutralizing SARS-CoV-2 on the basis of two principles: (i) detailed structural information of their epitopes and binding modes to the viral spike protein and (ii) mechanistic insights into viral fusion with cellular membranes catalyzed by the spike.

RESULTS: Nanobodies specific for the receptor binding domain (RBD) of SARS-CoV-2 spike were identified by phage display using nanobody libraries from an alpaca and a llama immunized with the RBD and inactivated virus. Four of the resulting nanobodies—VHHs E, U, V, and W—potently neutralize SARS-CoV-2 and SARS-CoV-2–pseudotyped vesicular stomatitis virus. X-ray crystallography revealed that the nanobodies bind to two distinct epitopes on the RBD, interfaces “E” and “UVW,” which can be synergistically targeted by combinations of nanobodies to inhibit infection. Cryo–electron microscopy (cryo-EM) of trimeric spike in complex with VHH E and VHH V revealed that VHH E stabilizes a conformation of the spike with all three RBDs in the “up” conformation (3-up), a state that is typically associated with activation by receptor binding. In line with this observation, we found that VHH E triggers the fusion activity of spike in the absence of the cognate receptor ACE2. VHH V, by contrast, stabilizes spike in a 2-up conformation and does not induce fusion. On the basis of the structural information, we designed bi- and trivalent nanobodies with improved neutralizing properties. VHH EEE most potently inhibited infection, did not activate fusion, and likely inactivated virions by outcompeting interaction of the virus with its receptor. Yet evolution experiments revealed emergence of escape mutants in the spike with single–amino acid changes that were completely insensitive to inhibition by VHH EEE. VHH VE also neutralized more efficiently than VHH E or VHH V alone; stabilized the 3-up conformation of spike, as determined by cryo-EM; and more strongly induced the spike fusogenic activity. We conclude that the premature activation of the fusion machinery on virions was an unexpected mechanism of neutralization, as enhanced neutralization could not be attributed simply to better blocking of virus-receptor interactions. Activation of spike in the absence of target membranes likely induces irreversible conformational changes to assume the energetically favorable postfusion conformation without catalyzing fusion per se. Simultaneous targeting of two independent epitopes by VHH VE largely prevented the emergence of resistant escape mutants in evolution experiments.

CONCLUSION: Our results demonstrate the strength of the modular combination of nanobodies for neutralization. Premature activation of spike by nanobodies reveals an unusual mode of neutralization and yields insights into the mechanism of fusion. ■

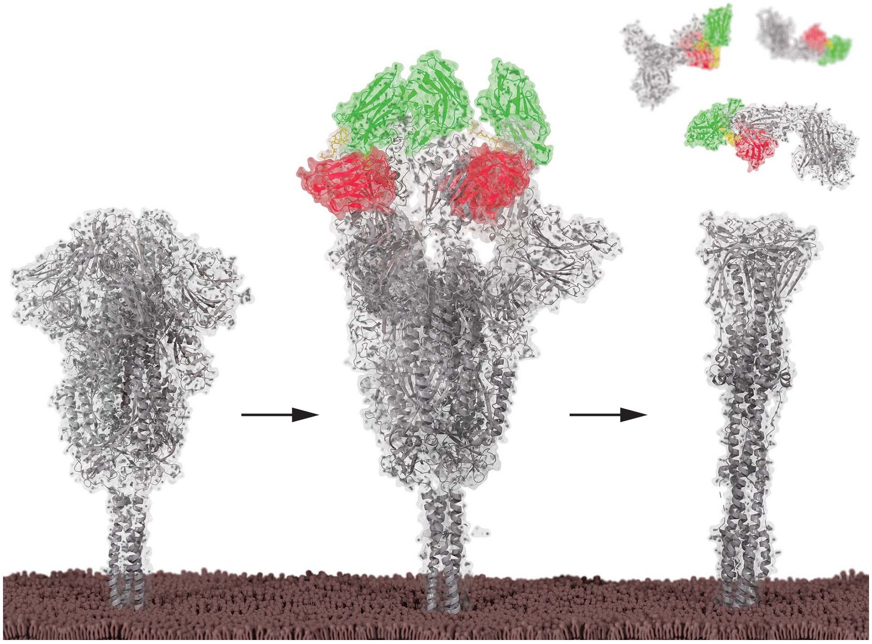

Bivalent nanobodies neutralize by inducing postfusion conformation of the SARS-CoV-2 spike. On virions, SARS-CoV-2 spike trimers are mostly in an inactive configuration with all RBDs in the down conformation (left). Binding of bivalent nanobody VE stabilizes the spike in an active conformation with all RBDs up (middle), triggering premature induction of the postfusion conformation, which irreversibly inactivates the spike protein (right).

The list of author affiliations is available in the full article online.

*Corresponding author. Email: pakoenig@uni-bonn.de (P.-A.K.); martin.hallberg@ki.se (B.M.H.); nicwu@illinois.edu (N.C.W.); fschmidt@uni-bonn.de (F.I.S.)

†These authors contributed equally to this work.

‡These authors contributed equally to this work.

Cite this article as P.-A. Koenig *et al.*, *Science* 371, eabe6230 (2021). DOI: 10.1126/science.abe6230

READ THE FULL ARTICLE AT
https://doi.org/10.1126/science.abe6230

Koenig *et al.*, *Science* **371**, 691 (2021) 12 February 2021 **1 of 1**

RESEARCH ARTICLE

CORONAVIRUS

Structure-guided multivalent nanobodies block SARS-CoV-2 infection and suppress mutational escape

Paul-Albert Koenig[1,2]*, Hrishikesh Das[3]†, Hejun Liu[4]†, Beate M. Kümmerer[5,6], Florian N. Gohr[2]‡, Lea-Marie Jenster[2]‡, Lisa D. J. Schiffelers[2]‡, Yonas M. Tesfamariam[2]‡, Miki Uchima[2]‡, Jennifer D. Wuerth[2]‡, Karl Gatterdam[7], Natalia Ruetalo[8], Maria H. Christensen[2], Caroline I. Fandrey[2], Sabine Normann[2], Jan M. P. Tödtmann[1], Steffen Pritzl[1], Leo Hanke[9], Jannik Boos[10], Meng Yuan[4], Xueyong Zhu[4], Jonathan L. Schmid-Burgk[11], Hiroki Kato[12], Michael Schindler[8], Ian A. Wilson[4,13], Matthias Geyer[7], Kerstin U. Ludwig[10], B. Martin Hällberg[3,14]*, Nicholas C. Wu[15,16,17]*, Florian I. Schmidt[1,2]*

The pandemic caused by severe acute respiratory syndrome coronavirus 2 (SARS-CoV-2) continues to spread, with devastating consequences. For passive immunization efforts, nanobodies have size and cost advantages over conventional antibodies. In this study, we generated four neutralizing nanobodies that target the receptor binding domain of the SARS-CoV-2 spike protein. We used x-ray crystallography and cryo–electron microscopy to define two distinct binding epitopes. On the basis of these structures, we engineered multivalent nanobodies with more than 100 times the neutralizing activity of monovalent nanobodies. Biparatopic nanobody fusions suppressed the emergence of escape mutants. Several nanobody constructs neutralized through receptor binding competition, whereas other monovalent and biparatopic nanobodies triggered aberrant activation of the spike fusion machinery. These premature conformational changes in the spike protein forestalled productive fusion and rendered the virions noninfectious.

The current pandemic caused by severe acute respiratory syndrome coronavirus 2 (SARS-CoV-2) poses serious challenges to patients, health care systems, and economic and social activity. Although efforts to develop vaccines are advancing rapidly, vaccines will likely not be suitable for immunocompromised patients. Additional therapeutic modalities for prophylaxis or treatment of high-risk patients are needed, as is testing of vaccines in children. Neutralizing antibodies or related molecules therefore offer great potential as immediate and direct-acting antiviral agents (*1*). Yet they cannot be easily and economically produced in sufficient amounts for mass application and cannot be readily modified to include multiple specificities without major costs in yield and quality. Conventional antibodies will also have to be assessed for any possibility of antibody-dependent enhancement (ADE) of infection (*2*). By contrast, variable domains of camelid heavy-chain–only antibodies (VHHs), also known as nanobodies, offer an opportunity to rapidly produce antiviral agents for passive immunization. Production in prokaryotic expression systems is cheap, is easily scaled up, and allows straightforward protein engineering, including multivalent nanobodies with enhanced functionalities (*3*). Nanobodies have favorable biochemical properties, including high thermostability and deep tissue penetration. ALX-0171, a trivalent nanobody that neutralizes respiratory syncytial virus, was developed for application using inhalators and accelerated viral clearance in patients, although treatment several days after symptom onset did not improve the clinical outcome (*4*).

The SARS-CoV-2 spike protein binds the cellular receptor ACE2 and catalyzes membrane fusion (*5*). Conformational flexibility of the trimeric spike protein allows each of its receptor binding domains (RBDs) to exist in two major configurations: a "down" conformation that is thought to be less accessible to binding of most neutralizing antibodies (NAbs) and an "up" conformation that binds ACE2 and most NAbs to the RBD (*6*–*8*). Many NAbs bind to the RBD of the spike protein and compete with ACE2 binding when the RBD is in the up conformation, thereby hindering infection (*9*, *10*). A few NAbs can bind to and stabilize the down conformation and thus prevent the conformational changes required for viral entry (*11*, *12*). Other mechanisms of neutralization or prevention of infection, such as antibody-dependent cellular toxicity (*13*), are possible, but none have been characterized in molecular detail.

Camelid nanobodies that bind two different epitopes on the SARS-CoV-2 spike RBD neutralize infection

We immunized one alpaca and one llama with the RBD of SARS-CoV-2 spike as well as formalin-inactivated SARS-CoV-2 to elicit neutralizing heavy-chain–only antibodies (fig. S1A). We identified 23 candidate nanobodies (Fig. 1A and fig. S1B) by phage display and confirmed binding of 10 hits by enzyme-linked immunosorbent assay (ELISA) (Fig. 1B and fig. S1, C and D). Their neutralizing activity was assessed in single-round infections with replication-deficient vesicular stomatitis virus (VSV) ΔG eGFP pseudotyped with SARS-CoV-2 spike Δ18. Four nanobodies—VHH E derived from the llama and VHHs U, V, and W from the alpaca—potently neutralized infection in a dose-dependent manner, with a half-maximal inhibitory concentration (IC_{50}) value of 60 nM for the most potent nanobody, VHH E (Fig. 1C and fig. S1, E and F). The neutralizing activity of VHH E is thus similar to bivalent recombinant ACE2-Fc. Three nanobodies from a synthetic library did not neutralize (*14*), whereas neutralizing activity of nanobody Ty1 (*15*) was confirmed. As a monomer, SARS-CoV-1–specific nanobody VHH 72 (*16*) neutralized SARS-CoV-2–pseudotyped virus at concentrations above 1 μM (Fig. 1C) but potently inhibited SARS-CoV-1–pseudotyped virus at nanomolar concentrations (fig. S1G). None of the four nanobody hits neutralized SARS-CoV-1–pseudotyped virus (fig. S1H). Plaque reduction neutralization tests (PRNTs) with SARS-CoV-2 on Vero E6

---

[1]Core Facility Nanobodies, Medical Faculty, University of Bonn, 53127 Bonn, Germany. [2]Institute of Innate Immunity, Medical Faculty, University of Bonn, 53127 Bonn, Germany. [3]Department of Cell and Molecular Biology, Karolinska Institutet, 17177 Stockholm, Sweden. [4]Department of Integrative Structural and Computational Biology, The Scripps Research Institute, La Jolla, CA 92037, USA. [5]Institute of Virology, Medical Faculty, University of Bonn, 53127 Bonn, Germany. [6]German Centre for Infection Research (DZIF), partner site Bonn-Cologne, 53127 Bonn, Germany. [7]Institute of Structural Biology, Medical Faculty, University of Bonn, 53127 Bonn, Germany. [8]Institute for Medical Virology and Epidemiology, Section Molecular Virology, University Hospital Tübingen, 72076 Tübingen, Germany. [9]Department of Microbiology, Tumor and Cell Biology, Karolinska Institutet, 17177 Stockholm, Sweden. [10]Institute of Human Genetics, Medical Faculty, University of Bonn, 53127 Bonn, Germany. [11]Institute for Clinical Chemistry and Clinical Pharmacology, Medical Faculty, University of Bonn, 53127 Bonn, Germany. [12]Institute of Cardiovascular Immunology, Medical Faculty, University of Bonn, 53127 Bonn, Germany. [13]The Skaggs Institute for Chemical Biology, The Scripps Research Institute, La Jolla, CA 92037, USA. [14]Centre for Structural Systems Biology (CSSB) and Karolinska Institutet VR-RÅC, Notkestrasse 85, 22607 Hamburg, Germany. [15]Department of Biochemistry, University of Illinois at Urbana-Champaign, Urbana, IL 61801, USA. [16]Carl R. Woese Institute for Genomic Biology, University of Illinois at Urbana-Champaign, Urbana, IL 61801, USA. [17]Center for Biophysics and Quantitative Biology, University of Illinois at Urbana-Champaign, Urbana, IL 61801, USA.

***Corresponding author. Email: pakoenig@uni-bonn.de (P.-A.K.); martin.hallberg@ki.se (B.M.H.); nicwu@illinois.edu (N.C.W.); fschmidt@uni-bonn.de (F.I.S.)** †These authors contributed equally to this work. ‡These authors contributed equally to this work.

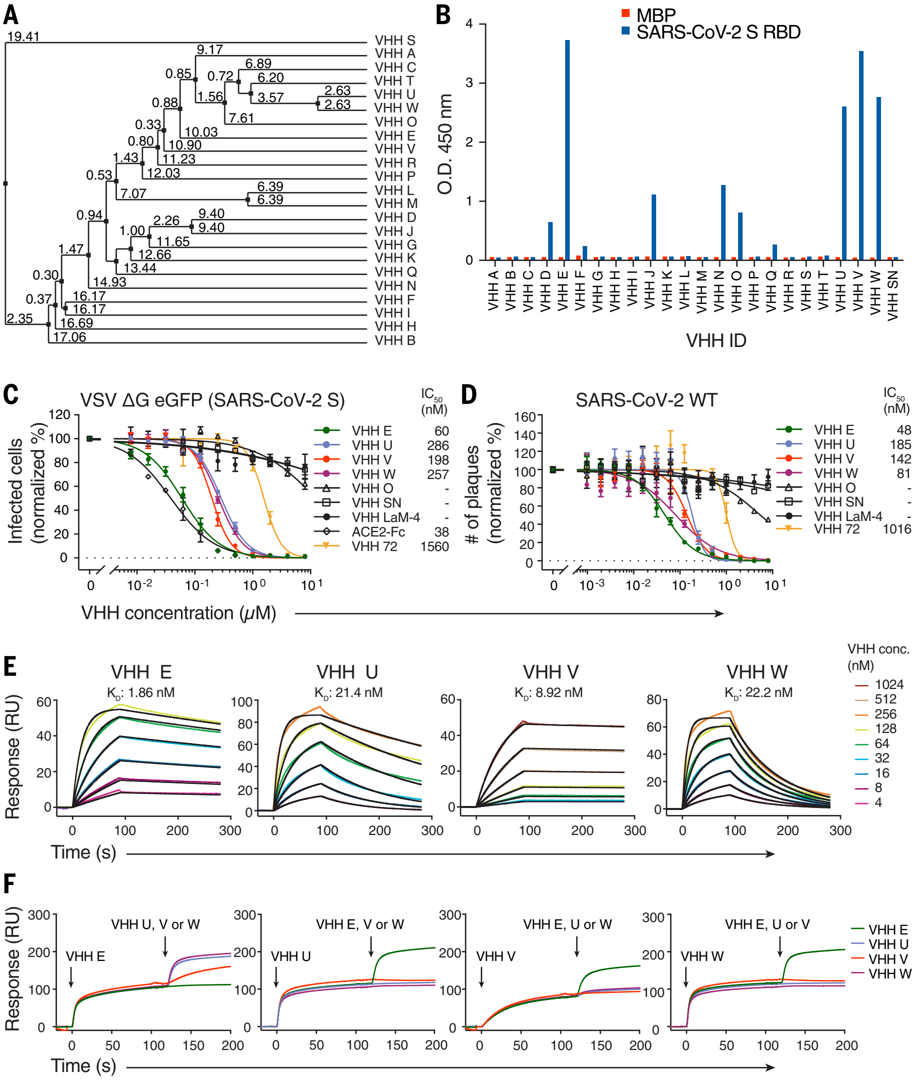

Fig. 1. Camelid nanobodies against two epitopes on the SARS-CoV-2 spike RBD neutralize infection. (**A**) Average distance tree of nanobody candidates identified by phage display, calculated by percentage identity (66). (**B**) Binding of 100 nM HA-tagged VHHs to immobilized SARS-CoV-2 spike RBD or a control protein (MBP) was quantified by ELISA with horseradish peroxidase (HRP)–coupled anti-HA antibody. Unrelated VHH SN was used as a negative control. O.D., optical density. (**C**) SARS-CoV-2 spike–pseudotyped VSV ΔG eGFP was incubated with the indicated concentrations of HA- or LPETG-tagged (VHH LaM-4, VHH 72) VHHs or ACE2-Fc at 37°C for 1 hour, followed by infection of Vero E6 cells for 8 hours. eGFP-positive cells were measured by flow cytometry to quantify infection. Normalized values from three independent experiments ± SEM and IC_{50} values are plotted. (**D**) SARS-CoV-2 was incubated with the indicated concentrations of HA- or LPETG-tagged VHHs as in (C), followed by plaque assay on Vero E6 cells. Plaques were enumerated 3 days after infection; normalized values of three independent experiments ± SEM and IC_{50} values are plotted. (**E** and **F**) Biotinylated SARS-CoV-2 spike RBD was immobilized on SPR spectroscopy chips. (E) Indicated HA-tagged VHHs were injected for 90 s, followed by dissociation for 180 s. Dissociation constants (K_D) were determined on the basis of fits, applying a 1:1 interaction model. (F) Epitope binning was performed by first injecting a single VHH for 120 s, followed by injection of a 1:1 mixture of the first nanobody in combination with VHH E, U, V, or W for 80 s.

cells confirmed the neutralizing activity, yielding IC_{50} values ranging from 48 to 185 nM (Fig. 1D). We further validated virus neutralization microscopically by quantifying the replication of an mNeonGreen-expressing clone of SARS-CoV-2 on human Caco2 cells in the presence of nanobodies over time (fig. S1I and movies S1 to S7). We measured binding affinities of the VHHs to the RBD by surface plasmon resonance (SPR) (Fig. 1E and fig. S1J) and obtained dissociation constants of 2 nM (VHH E), 21 nM (VHH U), 9 nM (VHH V), and 22 nM (VHH W) in the kinetic mode (table S1). An SPR-based binding competition assay revealed that the nanobodies bind to two distinct regions: U, V, and W competed for the same binding interface on RBD (interface *UVW*), whereas VHH E binds to a different RBD interface (interface *E*) and could bind to the RBD at the same time as U, V, or W (Fig. 1F).

Binding epitopes of neutralizing VHHs on the spike RBD

We next determined x-ray crystal structures of complexes of VHH E and VHH U with SARS-CoV-2 RBD at 1.87 Å (Fig. 2, A to C), VHH V with RBD and Fab CC12.3 (9) at 2.55 Å (Fig. 2, D and E), and VHH W with RBD and Fab CC12.3 at 2.73 Å (fig. S2, A and B) (table S2). VHH E and U bind to distinct epitopes on the RBD (Fig. 2A). VHH E employs its complementarity determining region (CDR) 1 and its unusually long CDR3 (22 amino acids) to bind the ACE2 binding site on the RBD (Fig. 2B). The VHH E epitope is similar to that of the potent SARS-CoV-2–neutralizing antibody CC12.3 (17) and nanobodies H11-D4 (18), MR17, and SR4 (19) (fig. S2C). Nevertheless, VHH E binds in an orientation that markedly differs from that of other neutralizing nanobodies (fig. S2C). Its CDR3 adopts an extended β-hairpin conformation that inserts into the receptor binding site (RBS) using both polar and hydrophobic interactions as well as bridging water molecules (Fig. 2B). The flexibility of CDR3 is confined at one end by a disulfide bond between C50 in CDR2 and C100h (Kabat numbering) in CDR3 that is involved in a hydrophobic and aromatic patch that interacts with the RBS (fig. S2H). Of the 27 epitope residues that bind VHH E, 16 are also involved in ACE2 binding (Fig. 2B) (20).

Although VHH U binds to a distinct epitope on the RBD, it should also compete with ACE2 for binding to the RBD, owing to clashes with the ACE2 protein and with the glycans at N322 and N546 of ACE2 (Fig. 2F and fig. S2D). VHH U uses all three CDRs to bind the RBD. CDR3 is tethered to CDR2 by a disulfide bond between C100b and C50 that creates two distinct loops in a flat, bilobed CDR3 that interact with the RBD (fig. S2H). The epitope of VHH U overlaps with the binding site of SARS-CoV-1–neutralizing antibody CR3022 (17) and VHH 72 (16) (fig. S2C). Although most of the residues involved in the interaction of the SARS-CoV-2 RBD with VHH U are identical in the SARS-CoV-1 RBD, VHH U does not neutralize SARS-CoV-1 (fig. S1H). In agreement with the neutralization data, fluorescently labeled VHH U binds to SARS-CoV-2 spike transiently expressed on human embryonic kidney (HEK) 293T cells, but not to SARS-CoV-1 spike (fig. S2G). SARS-CoV-1 spike N357 is part of an NxT sequon for N-glycosylation, whereas the corresponding SARS-CoV-2 N370 is not glycosylated. Binding of VHH U to SARS-CoV-1 spike is partly restored when T359 is

Fig. 2. X-ray crystallography defines the binding sites of neutralizing VHHs on the SARS-CoV-2 RBD. (**A** to **C**) Crystal structure of SARS-CoV-2 spike RBD in complex with VHH E and VHH U at 1.87 Å (A) and detailed interaction interface of RBD (in white) with VHH E (B) and RBD with VHH U (C), respectively. (**D** and **E**) Crystal structure of SARS-CoV-2 spike RBD in complex with VHH V at 2.55 Å (D) and detailed interaction interface of RBD with VHH V (E). Escape mutants (see Fig. 5 and tables S5 to S8) in the RBD are highlighted in teal and labeled with asterisks. (**F**) Overview of binding sites of three neutralizing nanobodies on the RBD and their overlap with ACE2, based on PDB ID 6M0J (*67*). Steric clashes with VHH E are indicated within the dashed circles. N-glycans at N322 and N546 of ACE2 are depicted as yellow spheres. All structural analyses of VHH U and VHH E in complex with RBD were based on one of the two copies in the asymmetric unit with closer alignment to the localized reconstructions of VHH E with RBD and VHH VE with RBD using cryo-EM. Single-letter abbreviations for the amino acid residues are as follows: A, Ala; C, Cys; D, Asp; E, Glu; F, Phe; G, Gly; H, His; I, Ile; K, Lys; L, Leu; M, Met; N, Asn; P, Pro; Q, Gln; R, Arg; S, Ser; T, Thr; V, Val; W, Trp; and Y, Tyr.

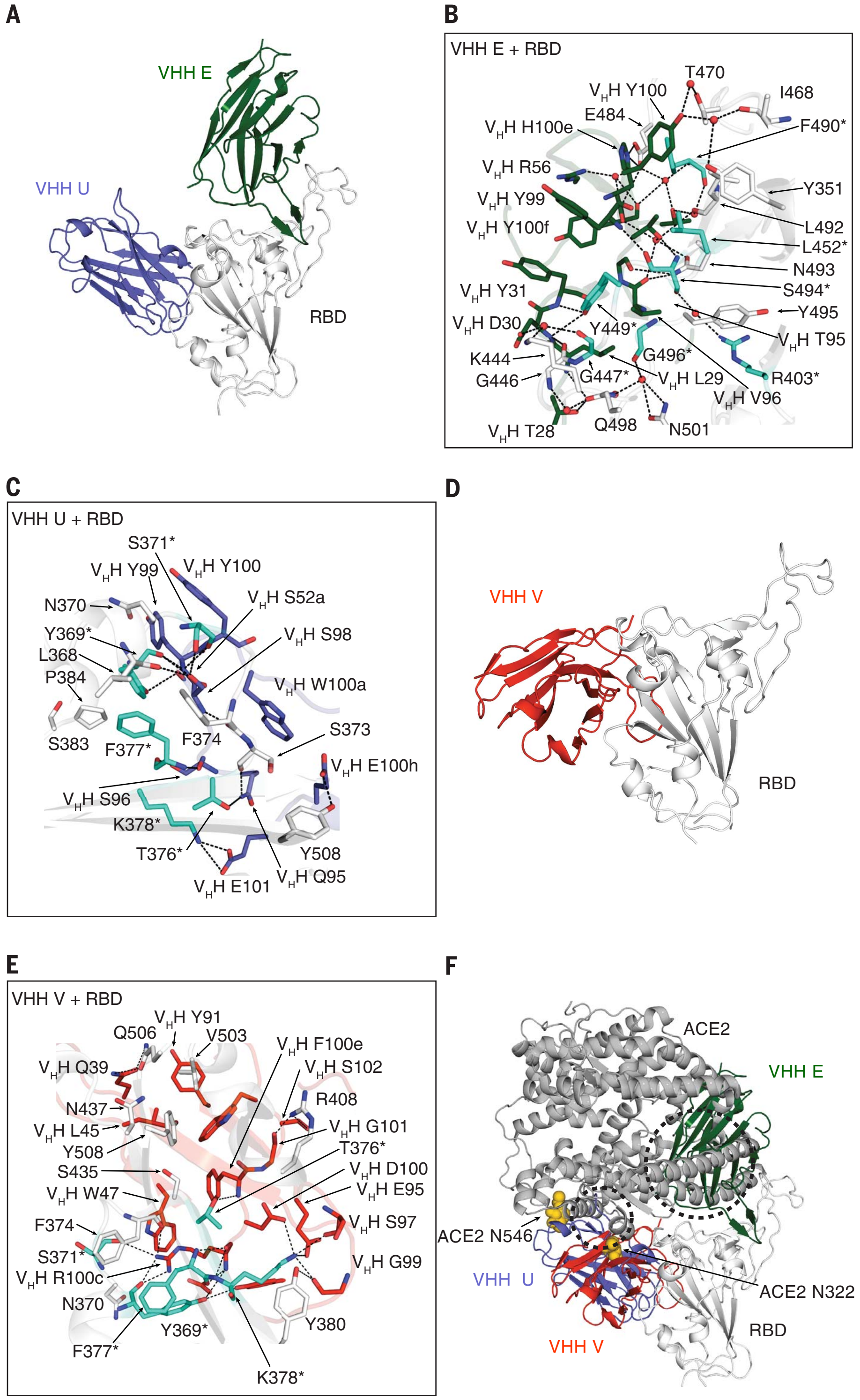

mutated to alanine and the sequon is eliminated, suggesting that differential glycosylation contributes to different binding properties (fig. S2G). Binding of VHH E and U does not substantially alter the overall RBD fold [Cα root mean square deviation (RMSD) = 0.37 Å between RBDs bound by E and U, and ACE2].

VHH W adopts a structure similar to that of VHH U (Cα RMSD = 0.48 Å) and engages the RBD in the same way (Fig. 2A and fig. S2, A and F), consistent with the finding that six of the seven amino acid differences between the two nanobodies occur in the framework and are not involved in binding. Although VHH V binds to a similar epitope as that bound by VHH U and W, it is oriented differently on the RBD. In this case, CDR3 is mainly involved in the binding, and no major changes in the overall RBD structure were observed upon VHH V binding. Binding of VHH V is also expected to compete with ACE2 binding, owing to a steric clash with the glycan at N322 and potentially at N546 of ACE2 (Fig. 2F and fig. S2D). To confirm that nanobody binding to the RBD competes with ACE2 binding on the plasma membrane, we performed a flow cytometry–based competition assay and quantified binding of fluorescently labeled RBD to ACE2-expressing HEK 293T cells (fig. S2E). ACE2 binding was indeed outcompeted by all neutralizing VHHs in a dose-dependent manner, with VHH V being slightly less potent than the others.

Neutralizing nanobodies stabilize the SARS-CoV-2 spike in the RBD-up conformation

The RBDs exist in an equilibrium of up and down conformations in the context of the trimeric spike on virions. Most unperturbed spike trimers exist in the configuration with no or one RBD up, whereas the form with all three RBDs in the up conformation (3-up) is barely populated (*6*, *7*, *21*). Only the up conformation of the RBD is compatible with ACE2 (*22*) binding, which likely induces further conformational changes that favor secondary proteolytic cleavage, dissociation of the S1 subdomain, and eventually conversion to the postfusion conformation (*23*). However, it is unknown how many RBDs must be in the up conformation to permit each of these transitions. To further investigate the mechanism of action of the identified neutralizing nanobodies, we used cryo–electron microscopy (cryo-EM) to determine structures of the soluble, trimeric spike complex bound to individual nanobodies (*6*, *24*). To stabilize the prefusion conformation, mutants of spike lacking the furin cleavage site and containing stabilizing proline substitutions were used throughout this study (*6*). Our initial analysis focused on one representative nanobody for each of the two identified epitopes. Ab initio reconstruction of VHH E bound to the trimeric spike revealed that the predominant complex (61%) contained all RBDs in the up conformation (3-up) with all three VHH E binding sites populated (Fig. 3, A and B, and figs. S3 to S5). The remaining particles resulted in very-low-resolution structures without any density for VHH E. Spike structures containing one or more RBDs in the down conformation were not compatible with binding of three molecules of VHH E, as substantial clashes with the spike glycans or between VHHs were observed when the VHH E structures were modeled into different spike quaternary structures (fig. S6). This finding suggests that binding of VHH E stabilizes (or induces) the 3-up conformation by trapping the RBD in the up-state. Once bound to VHH E, the RBD is unable to access the down conformation.

The cryo-EM structure of trimeric spike in complex with VHH V revealed that the predominant complex (42% of particles) had all three RBDs bound by VHH V (Fig. 3, C and D, and figs. S7 to S9), with two RBDs in the up conformation and one in the down conformation. To accommodate three molecules of VHH V, one of the RBDs in the up conformation was displaced by 8 Å, and the RBD in the down conformation was displaced by 11 Å, relative to the 2-up, 1-down conformation without nanobodies (*25*) (figs. S10 and S11). The remaining complexes did not contain VHH V. Apart from the RBD state, the overall structure of the trimeric spike was not substantially changed by any of the nanobodies. However, VHH E and VHH V altered the abundance of spike-trimer conformational states, and the cryo-EM structures confirmed the binding modes as identified by macromolecular crystallography. Molecular modeling of the VHH V–RBD interface revealed no differences to the crystallographic structure. A small backbone difference in RBD residues 446 to 451 in the interface with VHH E was noted, albeit in different resolution structures and in different complexes (fig. S12A).

Neutralizing nanobodies trigger activation of the fusion machinery

ACE2 can only bind to RBDs in the up conformation and is expected to trigger conformational changes required for secondary proteolytic processing and fusion. Premature activation of these steps will inactivate the fusion machinery, as the energetically favored postfusion conformation is irreversible. To test whether stabilization of the RBDs in the up conformation by nanobodies activates the fusion machinery, we generated a HEK 293–based cell line that can be induced to express the SARS-CoV-2 spike protein on the cell surface. We further generated derivative cell lines that additionally and constitutively express either eGFP or tagRFP-t. Because HEK 293 cells do not express the cognate receptor ACE2, the SARS-CoV-2 spike is not expected to mediate cell-cell fusion. We mixed the green and red fluorescent cell lines at an equal ratio, treated them with nanobodies, and recorded cells by fluorescence microscopy during a period of 14 hours (Fig. 3, E and F, and fig. S13, A and B). Cell-cell fusion, as a macroscopic readout for activation of the viral spike protein, would result in cells containing both eGFP and tagRFP-t. Untreated cells, or cells treated with control nanobodies, did not fuse or exhibit any signs of toxicity. However, incubating spike-expressing cells with VHH E, U, or W resulted in cell-cell fusion, as quantified by mixed eGFP and tagRFP-t fluorescence (Fig. 3F). VHH-induced fusion was particularly prominent for VHH U and W, resulting in fusion of all cells in the field of view, and was somewhat weaker for VHH E. VHH V barely induced fusion, whereas no fusion was observed in the presence of VHH Ty1. Stabilization of the RBD up conformation by neutralizing nanobodies may thus favor conformational changes that mediate fusion. Furthermore, we analyzed fusion between ACE2- and SARS-CoV-2 spike–expressing cell lines (fig. S14). Upon induction of spike expression, near complete cell-cell fusion was observed within 12 hours. When expression was induced in the presence of VHH E, spike-ACE2–mediated fusion was reduced to 50%, consistent with VHH E binding to the ACE2 binding site. No inhibition was observed in the presence of control nanobodies or in the presence of VHHs U, V, W, or Ty1. This fusion assay therefore recapitulated the results of the infection-based neutralization assays.

It remains unclear whether nanobody binding is sufficient to induce fusion directly or whether it rather facilitates secondary proteolytic processing of spike as necessary for fusion. VHH E–induced fusion was partly inhibited by a protease inhibitor cocktail (fig. S13), suggesting that extracellular or membrane-associated proteases may be involved in the VHH-triggered fusion, as described for ACE2-triggered fusion by SARS-CoV-1 spike (*26*). It is thus possible that VHH binding mimics binding of ACE2 to the spike protein and exposes otherwise inaccessible protease cleavage sites. Regardless of the exact mechanism, only neutralizing nanobodies were found to trigger spike-mediated cell-cell fusion, suggesting that aberrant activation of the fusion machinery is involved in the mechanism of neutralization.

Multivalent VHH fusions potentiate neutralization of SARS-CoV-2

In the course of the natural adaptive immune response, viruses face a polyclonal antibody response, which may enhance neutralizing activity by additive or synergistic effects (*27*). To test whether the four neutralizing nanobodies act synergistically, we compared the neutralizing activity of combinations of individual nanobodies. For direct comparison, we established starting concentrations of the individual nanobodies that led to similar dose-response curves in a twofold dilution series (Fig. 4A and fig. S15A). We then compared neutralizing activities of the individual nanobodies with mixtures of nanobodies containing 50% of the concentration of each nanobody combined. Combinations of nanobodies competing for the same epitope (VHHs U and V, U and W, or V and W) exhibited additive inhibition—i.e., mixtures containing half of the concentrations of two nanobodies neutralized to the same extent as did the individual nanobodies alone at full concentration (Fig. 4A and fig. S15A). However, when nanobodies binding to different epitopes were combined (VHHs E and U, E and V, or E and W), mixtures containing 50% of the two VHHs neutralized more efficiently than 100% of each of the individual nanobodies. Combinations of nanobodies that bound to independent epitopes were also more potent in preventing

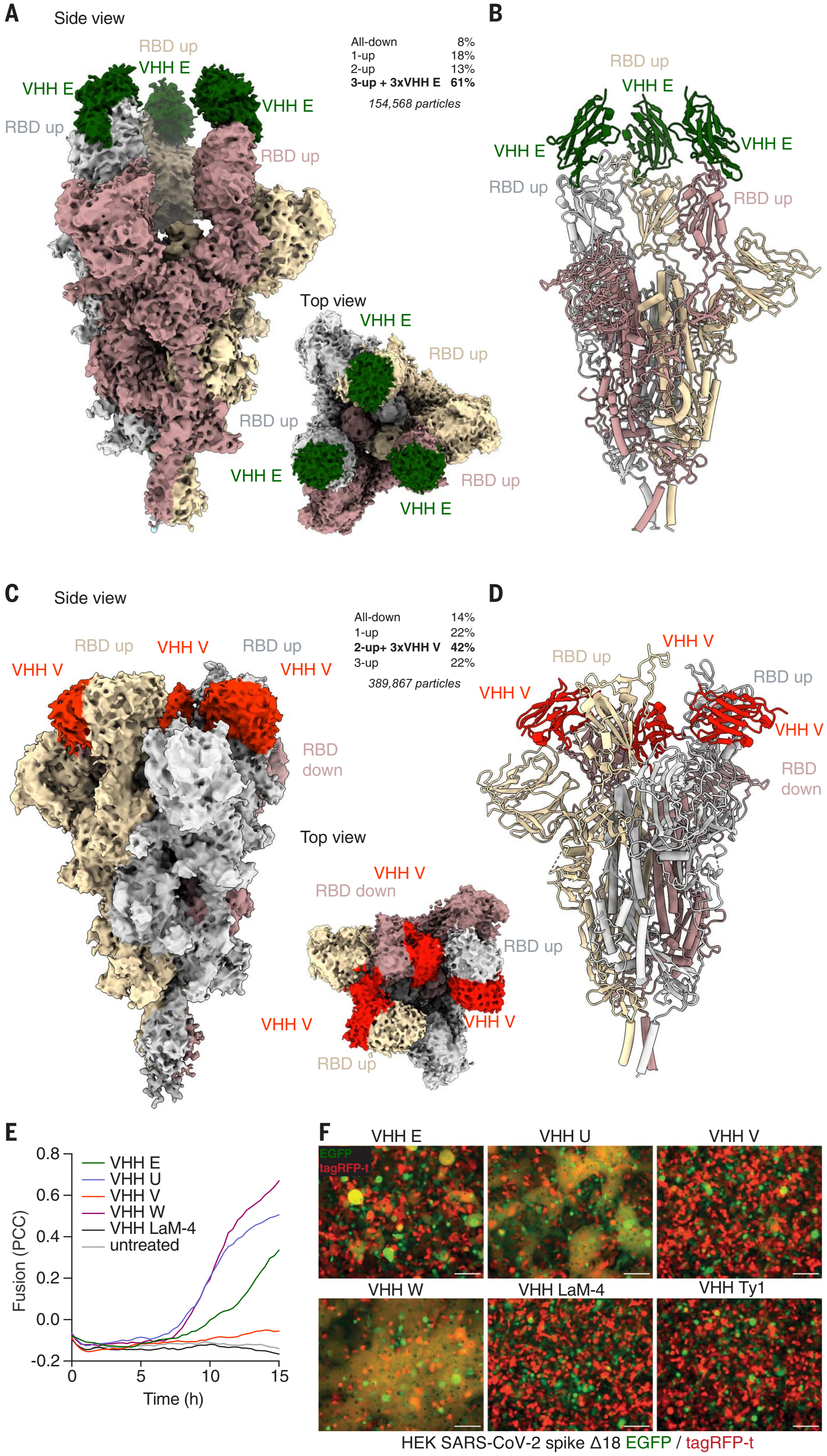

Fig. 3. Cryo-EM structures reveal that VHHs stabilize SARS-CoV-2 spike trimers with RBDs in the up conformation. (**A** to **D**) Cryo-EM reconstructions [(A) and (C)] and atomic models [(B) and (D)] of VHH E [(A) and (B)] and VHH V [(C) and (D)] in complex with trimeric SARS-CoV-2 spike. Frequencies of the identified complexes as well as total numbers of considered particles are noted. (A and B) VHH E (in green) binds to SARS-CoV-2 in a 3-up conformation in the most abundant complex; the resolution is 3.3 Å [0.143 Fourier shell correlation (FSC)]. (C and D) VHH V (in red) binds to SARS-CoV-2 in a 2-up conformation with all VHH binding sites occupied at a resolution of 3.0 Å (0.143 FSC). In the most abundant complex, VHH V binds to the RBD in the up or the down conformation. (**E** and **F**) HEK 293 cells inducibly expressing SARS-CoV-2 S Δ18 and either eGFP or tagRFP-t were seeded into microscopy-grade 96-well plates in a 1:1 ratio and induced with 1 μg/ml doxycycline for 20 hours. Cells were treated with 1 μM of the indicated VHHs, and microscopy images were recorded every 20 min for 14 hours at 37°C. (E) Fusion was quantified by calculating Pearson correlation coefficients (PCC) between eGFP and tagRFP-t. Average values from four fields of view of an experiment representative of three independent experiments are displayed. (F) Representative images of cells 12 hours after treatment are displayed (also see fig. S13 and movies S8 to S13). Scale bars, 100 μm.

SARS-CoV-2 mNeonGreen replication in human cells (Fig. 4B and fig. S15B).

These results suggest that targeting multiple epitopes may be beneficial to interfere with infection. Thus, we produced multivalent nanobody fusions linked by flexible linkers, capitalizing on the relatively unrestrained N and C termini of VHHs. On the basis of a superimposition of complex structures VHH E and VHH V binding to the same RBD, we determined that the C terminus of VHH V and the N terminus of VHH E were close enough (33 Å) to allow fusion with a 15–amino acid–long $(GGGGS)_3$ linker (VHH VE) (28). The distance between the C terminus of VHH E and the

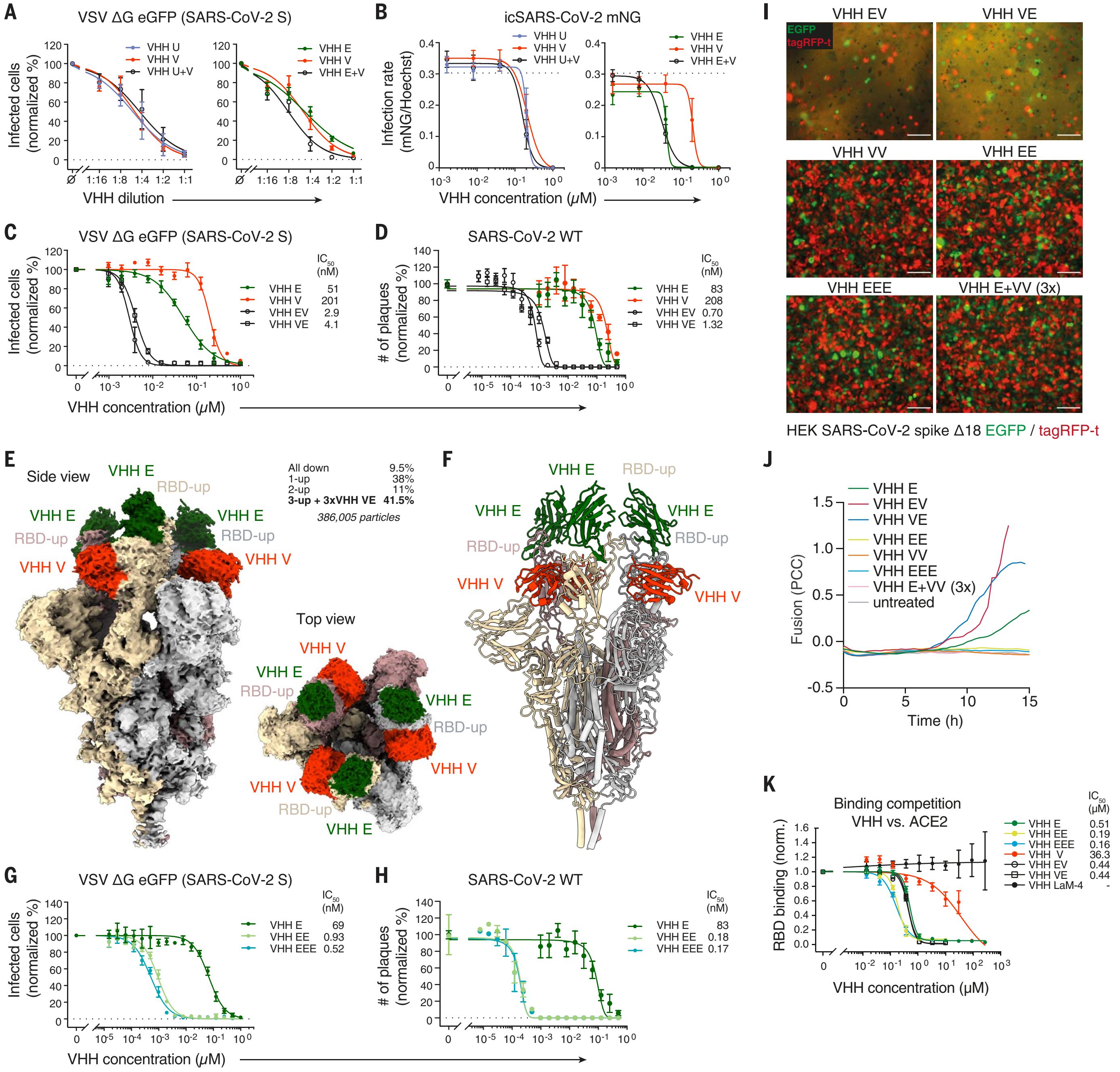

Fig. 4. Multivalent VHH fusions potentiate neutralization of SARS-CoV-2. (**A**) SARS-CoV-2 spike–pseudotyped VSV ΔG eGFP was incubated with twofold serial dilutions of 0.25 μM VHH E, 1 μM VHH U, 1 μM VHH V, or the indicated combinations containing 50% of each VHH at 37°C for 1 hour. Vero E6 cells were subsequently incubated with the mixtures, and infection was quantified as in Fig. 1B. Normalized values from three independent experiments ± SEM are plotted. (**B**) Caco-2 cells were infected with mNeonGreen-expressing infectious-clone-derived SARS-CoV-2 (icSARS-CoV-2-mNG) in the presence of the indicated nanobody concentrations. Cells were fixed 48 hours postinfection and stained for DNA, and infection was quantified by microscopy. Normalized values from three independent experiments ± SEM are plotted. (**C** and **G**) SARS-CoV-2 spike–pseudotyped VSV ΔG eGFP was incubated with the indicated concentrations of HA-tagged single, bivalent, or trivalent VHHs at 37°C for 1 hour, followed by infection of Vero E6 cells as in Fig. 1C. Normalized values from three independent experiments ± SEM and IC_{50} values are plotted. (**D** and **H**) SARS-CoV-2 was incubated with the indicated concentrations of HA-tagged VHHs, followed by plaque assay on Vero E6 cells as in Fig. 1D. Normalized values of three independent experiments ± SEM and IC_{50} values are plotted. (**E** and **F**) Cryo-EM reconstruction (E) and atomic models (F) of VHH VE in complex with trimeric SARS-CoV-2 spike. Frequencies of the identified complexes as well as total number of considered particles are noted. The biparatopic VHH binds to SARS-CoV-2 in the 3-up conformation; the resolution is 2.62 Å (0.143 FSC). (**I** and **J**) HEK 293 cell lines inducibly expressing SARS-CoV-2 S Δ18 and either eGFP or tagRFP-t were treated with the indicated VHHs and analyzed as in Fig. 3, E and F, displaying representative images after 12 hours (I), as well as quantified fusion (J) (also see fig. S22 and movies S14 to S22). Scale bars, 100 μm. (**K**) HEK 293T cells expressing ACE2-tagRFP-t were incubated with DyLight 488–labeled SARS-CoV-2 spike RBD in the presence of the indicated concentrations of nanobodies. RBD bound to ACE2-positive cells was quantified by flow cytometry. Normalized data from three independent experiments ± SEM are plotted. Data presented in fig. S2E and Fig. 4K are from the same experiments, and values for VHHs E, V, and LaM-4 in fig. S2E are plotted for reference.

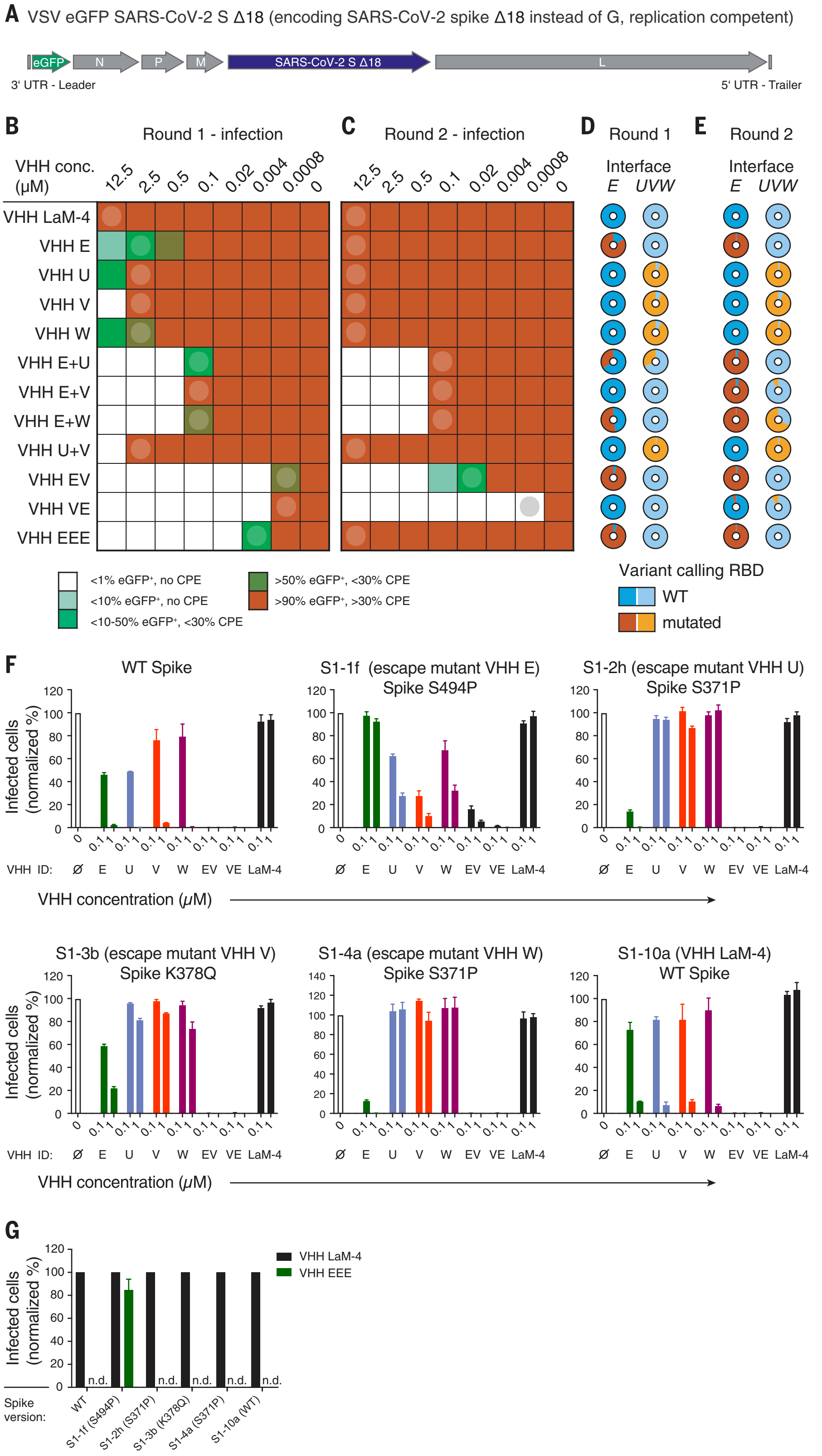

Fig. 5. Simultaneous targeting of two independent epitopes with neutralizing VHHs prevents viral escape. (**A**) Genome structure of VSV SARS-CoV-2 S Δ18 eGFP. UTR, untranslated region. (**B** to **E**) Evolution experiment. (B) Replication-competent VSV SARS-CoV-2 S Δ18 eGFP at a multiplicity of infection (MOI) of 0.5 was incubated with different concentrations of the indicated VHHs and allowed to replicate on Vero E6 cells in 12 wells for 4 days. The fraction of infected (eGFP-positive) cells and the cytopathic effect (CPE) were estimated microscopically and are plotted according to the indicated color code. (C) Cleared supernatants from the wells indicated with a circle in (B) were diluted with four volumes of fresh infection medium (1:5 dilution) and used for a second round of replication on Vero E6 cells in the presence of the indicated VHH concentrations. Cleared supernatants were harvested as in (B). (D and E) Cell lysates from the wells indicated by circles in (B) and (C) [corresponding to (D) and (E), respectively] were subjected to targeted resequencing of the RBD to identify variants that had emerged at the interfaces to VHH E (interface *E*) or to VHH U, V, or W (interface *UVW*) and to quantify their allelic distribution (see tables S5 and S6 for details on detected variants). (**F** and **G**) Wild-type VSV SARS-CoV-2 spike eGFP or plaque-purified escape mutants of VHH E (S1-1f, Spike S494P), VHH U (S1-2h, Spike S371P), VHH V (S1-3b, Spike K378Q), VHH W (S1-4a, Spike S371P), and VHH LaM-4 (S1-10a, WT spike) at an MOI of 0.5 were incubated with the indicated VHH concentrations (F) or 1 μM of the indicated VHH (G) and used for Vero E6 infection experiments as in Fig. 1B. Infection was quantified by flow cytometry; normalized data from three independent experiments ± SEM are plotted. n.d., not detected.

N terminus of VHH V, by contrast, was estimated to be greater than the length of a 15–amino acid linker. The reverse construct (VHH EV) with a (GGGGS)$_3$ linker was thus expected to bind to two different RBDs within a trimeric complex, to employ only one of its binding sites, or to induce some strain or distortion on the targeted RBD. The biparatopic nanobodies VHH VE and EV were produced in bacteria, purified, and subsequently subjected to SPR analysis (fig. S15C). With apparent dissociation constants of 84 pM (VE) and 200 pM (EV), the binding strength of the biparatopic nanobodies to the RBD was, respectively, 22 and 9 times that of the best monoparatopic

VHH (VHH E). Although we also confirmed binding to trimeric spike (fig. S15D), the complex binding behavior precluded the application of standard affinity-calculation models. In neutralization assays with SARS-CoV-2 S–pseudotyped VSV, we found that VE or EV neutralized with IC_{50} values of 4.1 or 2.9 nM—i.e., 12 or 18 times more effective than the neutralizing activity of VHH E alone—respectively (Fig. 4C). We observed similar values for the biparatopic fusions VHH EW and WE (fig. S15E). Neutralizing activity of VHH fusions, as measured by PRNTs with wild-type (WT) SARS-CoV-2, was improved even more, attaining IC_{50} values of 0.7 nM for EV and 1.32 nM for VE (Fig. 4D).

Through examination of the cryo-EM reconstructions of VE in complex with trimeric spike (Fig. 4, E and F, and figs. S16 and S17), we observed that the biparatopic VHH VE stabilized all RBDs in the up conformation, and all six VHH binding sites were occupied on the spike. This configuration was found in 41.5% of all complexes; the remaining spike complexes did not contain any VHH (fig. S18). Although the linker itself was not visible, the 15–amino acid linker length between VHHs V and E is compatible with the observed distance between the C terminus of VHH V and the N terminus of VHH E on the same RBD (35 Å) (28), but not with the distance between VHHs V and E on different RBDs (>80 Å) (fig. S19). Through localized reconstruction techniques, we were able to obtain a map of the VHH VE–RBD region of the full spike that enabled molecular modeling. Notably, the small difference in the backbone around Y449 observed in the localized reconstruction of the VHH E–RBD structure now corresponded in VHH VE–RBD to the conformation seen in the high-resolution x-ray structure of RBD VHH E and VHH U (fig. S12B). These differences hint at possible allostery between the two epitopes, but it is not feasible to determine this with certainty, given the resolution of the present EM reconstructions in the two areas. Complexes of the spike trimer with VHH V alone (Fig. 3, C and D) contained two RBDs in the up conformation and one in the down conformation. Hence, the formation of a 3-up spike trimer is dependent on the inclusion of VHH E in the biparatopic VHH VE complex (fig. S20).

The cryo-EM structures of VHH E in complex with the trimeric spike suggested that three RBDs in the up conformation could also be bound by multivalent fusions of VHH E. We thus produced VHH EE and VHH EEE connected by GS-rich linkers of 15–amino acid length and similarly tested their neutralizing activity. VHH EE and VHH EEE neutralized VSV ΔG eGFP (SARS-CoV-2 S) with IC_{50} values in the pM range (930 and 520 pM, respectively) (Fig. 4G). IC_{50} values in PRNTs with WT virus were even lower, reaching 180 and 170 pM for VHH EE and EEE, respectively (Fig. 4H). We also tested VHH VV and found that it binds RBD with higher apparent affinity than does VHH V alone (fig. S15C). Yet VHH VV improved neutralizing activity only modestly (fig. S15F), possibly because VHH VV is not expected to simultaneously bind different RBDs within the trimeric spike.

Monovalent, multivalent, and biparatopic nanobodies boost SARS-CoV-2 neutralization by distinct mechanisms

Next, we explored the mechanism by which multivalent nanobodies enhance the neutralizing activity of individual nanobodies. We first tested whether multivalent nanobodies outcompeted binding of fluorescently labeled RBD to ACE2-expressing HEK 293T cells (Fig. 4K). VHHs EE and EEE reduced binding to RBD better than VHH E alone, suggesting that the increased (apparent) affinity of these nanobodies may better prevent virus binding to receptor than VHH E. Although VHHs EE and EEE exhibit a threefold lower IC_{50} than VHH E in the RBD competition assays, it is possible that other factors contribute to the 100-fold enhanced neutralizing activity. VHHs VE and EV did not compete with RBD-ACE2 interactions substantially better than VHH E alone. Hence, we conclude that their improved neutralizing activity must be explained by other mechanisms.

We next tested whether incubation of SARS-CoV-2 spike–expressing cells with multivalent nanobodies triggers spike-mediated cell-cell fusion in the absence of ACE2, as observed for VHHs E, U, and W (Fig. 4, I and J). VHHs EV and VE caused extensive cell-cell fusion, clearly exceeding the fusogenic activity of the individual nanobodies alone. VHHs EW and WE caused a similar degree of cell-cell fusion. We conclude that binding of VHHs EV, VE, EW, and WE to the spike potently induces conformational changes required for fusion. Moreover, the enhanced fusogenic activity of EV and VE correlates with the improved neutralizing activity over VHH E, which could not be explained by ACE2 competition. In VHH-mediated cell-cell fusion assays, cells were treated with nanobodies one day after induction of spike expression, exposing a large number of spike trimers at the cell surface at the onset of the experiment, including sites in close proximity to membranes of neighboring cells. Activation of spikes likely catalyzed cell-cell fusion. During neutralization of virions, however, nanobodies bind to spike on virions in the absence of target membranes. Thus, premature activation of this metastable state cannot facilitate infection but rather irreversibly converts the spike into the postfusion conformation precluding bona fide fusion events upon host cell contact.

The homobivalent and homotrivalent VHHs EE and EEE did not induce fusion despite a substantial boost in neutralizing activity, suggesting that binding of multiple covalently coupled nanobodies to the same epitope is not compatible with induction of fusion. To test whether cross-linking of individual spike promoters itself interferes with fusion, we incubated spike-expressing cells with fusogenic VHH U and a threefold molar excess of VHH EEE (fig. S22). Yet VHH U–mediated fusion was not restricted by VHH EEE. Fusion induced by VHH E, however, was inhibited by bivalent VHH VV, demonstrating that VHH binding can interfere with fusion in other ways, perhaps by preventing 3-up conformations.

In addition, we tested whether multivalent nanobodies interfered with fusion of SARS-CoV-2 spike– and ACE2-expressing cells. We induced spike expression at the onset of the experiment; therefore, newly synthesized spike that arrived at the plasma membrane faced an excess of nanobodies. Depending on the neutralization potential and the concentration of nanobodies, this may induce premature activation of spike by nanobodies or may interfere with binding of spike to ACE2, recapitulating the setup of neutralization assays. In line with the previously determined IC_{50} values, we found that fusion was partly inhibited by VHHs EE, EEE, EV, and VE (fig. S21). VHH VV did not inhibit fusion, whereas VHHs EW and WE had intermediate phenotypes. ACE2-mediated fusion assays therefore demonstrated that only the most potent neutralizing nanobodies interfered with spike-ACE2–triggered fusion at the studied concentration.

Targeting two independent vulnerable epitopes on the RBD prevents viral escape

In the course of prolonged infections or therapeutic settings, viruses with escape mutants emerge that evade recognition, and thus neutralization, by specific antibodies. We experimentally tested whether combinations of nanobodies targeting distinct epitopes, or our biparatopic nanobodies, increased resistance to escape mutants (see extended results in the supplementary materials). Briefly, we generated a chimeric, replication-competent VSV strain that expresses eGFP and encodes SARS-CoV-2 spike Δ18 instead of its own glycoprotein (VSV eGFP SARS-CoV-2 S; see Fig. 5A) (29–31). Vero E6 cells were infected with the chimeric virus in the presence of increasing concentrations of nanobodies or nanobody combinations and cultivated for 4 days (Fig. 5B). Virus from the wells with the highest nanobody concentration that still allowed replication (>10% infected cells) was collected and used for a second round of selection (Fig. 5C). Viral RNAs were extracted from infected cells after both rounds of selection and analyzed by next-generation sequencing (NGS) to identify emerging variants (Fig. 5, D and E). No mutations occurred in the presence of control nanobody VHH LaM-4. In the presence of VHH E or VHHs U, V, and W, replication at neutralizing concentrations was observed in the first round, and more than 85% of all viral sequences exhibited mutations in the structurally defined interfaces *E* or *UVW*, respectively. Replication in the second round was seen at all nanobody concentrations, and nearly all sequences contained nonsynonymous mutations in the nanobody epitope, indicating rapid selection for escape mutants. Particularly prominent were escape mutations F490S or S494P in the VHH E interface, as well as S371P and K378Q in the *UVW* interface, which are expected to compromise the structurally defined VHH–RBD interface (see extended results in the supplementary materials). We identified further mutations in interfaces *E* (G447S, Y449H/D/N, L452R, F490S, S494P/S, G496S, and Y508H) and *UVW* (Y369H, S371P, F374I/V, T376I, F377L, and K378Q/N) in this and a separate evolution experiment (tables S5 to S8).

Individual escape mutants encoding spike mutants S494P (VHH E), S371P (VHH U/W), and K378Q (VHH V) were plaque purified and thoroughly characterized (fig. S23, A and B). As expected, spike S494 mutants were resistant to VHH E and VHH EEE, whereas spike mutants S371P and K378Q were resistant to VHHs U, V, and W (Fig. 5, F and G). Escape mutants resistant to one VHH were systematically more sensitive to VHHs EV and VE than to a single nanobody that could still bind to their RBD. This finding suggests that residual binding to the mutated interface may still contribute to neutralization. Ectopically expressed mutants of SARS-CoV-2 spike were no longer stained by fluorescently labeled VHHs targeting the affected epitope, indicating that the detected mutations alone explained the loss of sensitivity (fig. S23C).

Combinations of VHHs E and U, E and V, and E and W did not allow the emergence of escape mutants that were resistant to both nanobodies in the second round of selection (Fig. 5C). Nevertheless, virus with mutations in at least one interface was enriched, and sequences containing mutations in both interfaces were detected after two rounds of replication in the presence of VHHs E and W (Fig. 5E). Replication in the presence of VHH EEE or combinations of VHHs U and V allowed the rapid emergence of escape mutations with nearly completely mutated interfaces in the first round of selection (Fig. 5D). Emerging virus was consequently able to replicate at all nanobody concentrations in the second round (Fig. 5C).

No virus resistant to biparatopic VHHs EV and VE emerged during two rounds of selection (Fig. 5C). Although VHH VE did not lead to the accumulation of any mutations, VHH EV selected for virus mutated in the *E* interface (Fig. 5E). The evolution experiments clearly demonstrate that simultaneous targeting of two neutralizing epitopes severely hampers or prevents the emergence of escape mutants. A single-point mutant was sufficient to escape the most potent homotrivalent nanobody, VHH EEE.

Discussion

Nanobodies represent a versatile alternative to conventional antibodies for passive immunization against SARS-CoV-2. They are efficiently produced in prokaryotic expression systems at low cost; exhibit favorable biophysical properties, including high thermostability; and are amenable to engineering of multimeric nanobody constructs with additional benefits (*3*, *32*).

This study identifies four neutralizing nanobodies that target the RBD of SARS-CoV-2 spike from immunized camelids and demonstrates their inhibitory activity in different in vitro infection models. The described set of nanobodies joins a growing list of neutralizing nanobodies (*11*, *12*, *14*–*16*, *18*, *19*, *25*) that have been mostly selected from synthetic libraries or derived from immunizations with related coronaviruses. Without further in vitro evolution, nanobodies isolated from synthetic libraries often exhibit lower affinities than nanobodies selected by the adaptive immune system of immunized animals. Neutralizing nanobodies raised against other coronaviruses are typically not potent toward SARS-CoV-2 in a monovalent form. In this study, we have rationally designed multivalent nanobody constructs on the basis of epitope mapping data by SPR and x-ray crystallography, as well as extensive information on the conformation of spike-nanobody complexes determined by cryo-EM. By using additional functional data on the synergistic behavior of individual nanobody combinations, we developed two classes of nanobody fusions. First, multivalent nanobodies targeting the ACE2 binding site on the RBD (VHH EE and VHH EEE) likely interfere with virus attachment but can be overcome by single point mutations. Second, biparatopic fusions of two nanobodies targeting the nonoverlapping binding interfaces *E* and *UVW* potentiate neutralization by activating SARS-CoV-2 spike. On virions, premature activation likely induces the conversion to the thermodynamically favorable postfusion conformation without catalyzing a fusion event, a process that is irreversible and naturally observed for a fraction of spike trimers on intact SARS-CoV-2 virions (*21*, *33*, *34*). Similar phenomena, albeit mostly observed in biochemical experiments, were proposed for the SARS-CoV-1–NAbs S230 (*35*) and CR3022 (*36*), and MERS-CoV–NAb Mersmab-1 (MERS, Middle East respiratory syndrome) (*37*). Simultaneous binding of VHH VE to the *E* and *UVW* interfaces may involve additional conformational changes not revealed on the unprocessed spike used for EM, possibly facilitating proteolytic processing of S2 to S2′, or bona fide dissociation of S1 from the SARS-CoV-2 spike. Differential sensitivities to protease inhibitors of cell-cell fusion triggered by VHH E and VE warrant more in-depth analysis of the required proteases.

The identification of three nanobodies (VHH E, U, and W)—with two different binding modes targeting independent epitopes that activate the SARS-CoV-2 fusion machinery—suggests that this mode of action may be more common than previously thought. Different coronaviruses employ either the N or the C terminus of the S1 subunit for receptor engagement and activation of fusion by proteinaceous or carbohydrate receptors, suggesting that the spikes of coronaviruses have evolved a pronounced flexibility with regard to activation of the fusion machinery (*38*). It is conceivable that such versatility is achieved by a mode of receptor activation that primarily warrants enhanced susceptibility to secondary proteolytic cleavage to form the S2′ subunit with an exposed fusion peptide, rather than initiating all of the necessary conformational changes required for fusion per se.

The mechanism of fusion activation may have clinical implications, as current models of ADE explain how virus-antibody complexes are taken up by cells expressing Fcγ receptors (*37*, *39*) but fail to explain how the second function of spike-receptor interactions (i.e., the induction of fusion) is achieved. If engagement of the RBD (or S1) by antibodies or nanobodies is sufficient to activate the spike protein, fusion in the absence of cognate receptors, and thus ADE, is more likely to occur. Nanobodies lack the Fc portion and therefore would represent a safe alternative to antibodies, as they cannot be engaged by scavenging receptors to mediate recruitment and uptake of virions into phagocytic cells. The serum half-life of nanobodies can be extended by chemical modification with polyethylene glycol, fusion to human serum albumin (HSA), or fusion to peptides or proteins that bind to HSA with high affinity (*40*).

We predict that bivalent or trivalent nanobody fusions described in this study will also increase the neutralizing potential in vivo. The substantial delay or prevention of escape mutations to biparatopic nanobodies in vitro may translate to better performance in vivo as well. The application of nanobodies by inhalation directly to the site of infection may further reduce the required dose and is also substantially easier to achieve outside of medical facilities (*41*–*43*). Owing to their similarity to the variable domains of the heavy chain of human antibodies, VHHs are generally expected to be less immunogenic than synthetic antibody–like molecules (*44*) and can be further humanized (*45*). In clinical studies of the U.S. Food and Drug Administration–approved nanobody caplacizumab, immunogenicity of nanobodies occurred in 3% of all patients with no effects on clinical efficacy (*46*).

The structure-based multivalent nanobodies presented here have strong potential clinical applications, owing to increased neutralization activity and in-built protection from rapid emergence of escape mutants. We show that premature activation of the spike can be a mechanism for neutralization, and thus the generated nanobodies may also shed more light on the mechanism of fusion itself.

Materials and methods

Cell lines

Syrian baby hamster kidney (BHK)-21 cell clone BSR-T7/5 (*Mesocricetus auratus,* RRID:CVCL_RW96, a kind gift of Sean Whelan, Harvard Medical School), human embryonic kidney (HEK) 293T cells (ATCC Cat# CRL-3216, RRID: CVCL_0025), and African green monkey Vero E6 cells (*Chlorocebus sabaeus*, RRID:CVCL_0574, a kind gift of Ralf Bartenschlager, University of Heidelberg) were cultivated in DMEM containing 10% FBS and GlutaMax; human colorectal adenocarcinoma Caco-2 cells (RRID: CVCL_0025) were cultured in DMEM complemented with 10% FBS, 2 mM L-glutamine, 100 µg/ml penicillin/ streptomycin (PS), and 1% nonessential amino acids (NEAA). Flp-In 293 T-REx cells (Thermo Fisher Scientific Cat# R78007, RRID:CVCL_U427) inducibly expressing SARS-CoV-2 spike Δ18 with a C-terminal Strep$_2$-HA tag (HEK 293 SARS-CoV-2 spike Δ18) were generated using the Flp-In system (Thermo Fisher Scientific) according to the manufacturer's recommendations, and cultivated in DMEM supplemented with 10% FBS, Glutamax, 4 µg/ml blasticidin S, and 50 µg/ml hygromycin B. Derivatives of HEK 293 SARS-CoV-2 spike Δ18 cells expressing eGFP or tagRFP-t under the control of CMV promoters were generated using customized gateway-compatible lentiviral vectors based on pRRL (*47*), and cultivated in DMEM supplemented with 10% FBS, Glutamax, 4 µg/ml blasticidin S, 50 µg/ml hygromycin B, and 1 µg/ml puromycin. HEK 293T cells expressing ACE2-tagRFP-t under the control of the EF1α promoter were also generated using a pRRL-based lentiviral vector, and cultivated in DMEM supplemented with 10% FBS, Glutamax, and 50 µg/ml hygromycin B.

Viruses

All experiments involving the authentic virus were conducted in Biosafety Level 3 laboratories. SARS-CoV-2 clinical isolate SARS-CoV-2/human/Germany/Heinsberg-01/2020 was isolated from a throat swap of an infected patient at the University of Bonn, Germany, and was used for plaque reduction assays (*48*). To prepare larger stocks of virus, Vero E6 cells were infected with SARS-CoV-2 at a multiplicity of infection (MOI) of 0.01. Supernatants were harvested 2 days postinfection (p.i.), cleared by centrifugation, and quantified by plaque assay. To prepare inactivated virus for camelid immunizations, virus was produced in cells covered with Opti-MEM: Clarified supernatants containing virus were mixed with 37% formaldehyde to obtain a final concentration of 4% formaldehyde and incubated at 4°C for 4 hours. The virus suspension was overlaid on 7 ml of a 30% sucrose cushion in 20 mM HEPES pH 7.4, 150 mM NaCl and virions were sedimented by ultracentrifugation in a SW 32 TI rotor at 4°C, 30.000 rpm for 2.5 hours. Inactivated virus pellets from 28 ml of virus-containing supernatants were resuspended in 100 µl of 20 mM HEPES pH 7.4, 150 mM NaCl and the virus suspensions from five ultracentrifuge tubes were pooled. Inactivation of the virus was verified by the lack of replication in a Vero E6 infection experiment. Recombinant SARS-CoV-2 clone icSARS-CoV-2-mNG expressing mNeonGreen (*49*), derived from isolate SARS-CoV-2/human/USA/WA-CDC-WA1/2020, was obtained from the World Reference Center for Emerging Viruses and Arboviruses (WRCEVA) at the UTMB (University of Texas Medical Branch) and was used for microscopy-based replication assays. To generate icSARS-CoV-2-mNG stocks, 200,000 Caco-2 cells were infected with 50 µl of virus stock in a 6-well plate, the supernatant was harvested 48 hours p.i., centrifuged, and stored at −80°C. Viral titers were determined based on mNeonGreen expression after serial dilutions.

To generate replication-deficient pseudotyped VSV strains for single-round infections, we first recovered VSV ΔG eGFP pseudotyped with VSV G, VSV ΔG eGFP (VSV G), from BSR-T7/5 cells using T7-expressing vaccinia virus (VACV) strain vTF7.3, pVSV eGFP dG (a kind gift from Connie Cepko, Harvard Medical School, Addgene plasmid # 31842), and T7-based expression vectors for VSV polymerase (pL), phosphoprotein (pP), nucleoprotein (pN), and glycoprotein (pG) (all kind gifts from Sean Whelan, Harvard Medical School) using published procedures (*50*). VSV ΔG eGFP (VSV G) was amplified in BSR-T7/5 cells transiently transfected with VSV G expression vector pMD2.G (a kind gift from Didier Trono, EPFL, Addgene plasmid # 12259) at 34°C. VSV ΔG eGFP (SARS-CoV-1 SΔ18) and VSV ΔG eGFP (SARS-CoV-2 SΔ18) were produced in HEK 293T cells transiently transfected with pCAGGS SARS-CoV-1 SΔ18 or pCAGGS SARS-CoV-2 S Δ18, respectively, followed by infection with VSV ΔG eGFP (VSV G) and cultivation at 34°C. pCAGGS SARS-CoV-1 S Δ18 encodes amino acids 1 to 1237 of SARS-CoV-1 strain Frankfurt 1 (cloned from a template kindly provided by Stephan Poehlmann, German Primate Center), while pCAGGS SARS-CoV-2 SΔ18 encodes amino acids 1 to 1255 of SARS-CoV-2/human/China/Wuhan-Hu-1/2019 (cloned from a codon-optimized template kindly provided by Stephan Poehlmann). C-terminal truncations were introduced to avoid retention of spike proteins in the ER/Golgi and maximize exposure at the plasma membrane. Virus-containing supernatants were clarified by centrifugation and stored at −80°C. Viral titers were determined by infection of Vero E6 with dilution series of the virus for 8 hours, followed by quantification of green fluorescent cells by flow cytometry. Supernatants were shown to be free of VSV G pseudotyped virus, as no infection of BSR-T7/5 cells was observed.

To generate replication-competent chimeric VSV strains encoding eGFP and SARS-CoV-2 SΔ18 in place of the VSV glycoprotein, we inserted the coding sequence of SARS-CoV-2 SΔ18 (amino acids 1 to 1255 of SARS-CoV-2/human/China/Wuhan-Hu-1/2019) into pVSV eGFP dG. Replication-competent virus was recovered from BSR-T7/5 cells infected with VACV vTF7.3, transfected with pVSV eGFP SARS-CoV-2 SΔ18, pL, pP, pN, and pG, and cultivated at 34°C. Virus was amplified in Vero E6 cells at 34°C and virus-containing supernatants were clarified and stored at −80°C. Viral titers were determined by infection of Vero E6 with dilution series of the virus for 8 hours, followed by quantification of green fluorescent cells by flow cytometry. Chimeric virus strain VSV eGFP SARS-CoV-2 SΔ18 was confirmed to infect primate ACE2 expressing VeroE6 cells, but not BSR-T7/5 cells.

Proteins

Expression and purification of SARS-CoV-2 S RBD

Cloning and expression of the receptor binding domain (RBD) (residues 319 to 541) of spike protein from SARS-CoV-2/human/China/Wuhan-Hu-1/2019 (GenBank: QHD43416.1) was described earlier (*17*). In brief, the coding sequence was cloned into a customized pFastBac vector and fused with an N-terminal gp67 signal peptide and C-terminal His$_6$ tag. A recombinant bacmid DNA was generated using the Bac-to-Bac system (Thermo Fisher Scientific). Baculovirus was generated by transfecting Sf9 cells with purified bacmid DNA using FuGENE HD (Promega), and subsequently used to infect suspension cultures of High Five cells (Thermo Fisher Scientific) at an MOI of 5 to 10. Infected High Five cells were cultivated at 28°C for 72 hours, shaking at 110 rpm for protein expression. The supernatant was then concentrated using a 10 kDa MW cutoff Centramate cassette (Pall Corporation). The RBD protein was purified by Ni-NTA, followed by size-exclusion chromatography, and buffer exchanged into 20 mM Tris-HCl pH 7.4 and 150 mM NaCl. Fluorescent RBD was produced by reaction with DyLight 488 NHS ester (Thermo Fisher Scientific) in 100 mM sodium phosphate pH 8.0, 150 mM NaCl, pH 8.0, followed by desalting with 7K MWCO Zeba spin desalting columns (Thermo Fisher Scientific).

Expression and purification of nanobodies

Nanobody coding sequences were cloned into pHEN6-based bacterial, periplasmic expression vectors with C-terminal HA-His_6 or LPETG-His_6 tags using Gibson cloning (New England Biolabs). Multivalent nanobodies were either directly cloned into pHEN6, or first assembled in pBluescript II (KS) + cloning vectors lacking promoters by Gibson cloning, followed by subcloning into pHEN6 using conventional ligation with T4 ligase. Nanobodies were produced in *E. coli* WK6 transformed with the respective expression vectors. Expression cultures were grown in Terrific Broth (TB), and expression induced with 1 mM IPTG at an OD_{600} of 0.6, followed by cultivation at 30°C for 16 hours. Bacterial pellets were resuspended in TES buffer (200 mM Tris-HCl pH 8.0, 0.65 mM EDTA, 0.5 M sucrose), and periplasmic extracts generated by osmotic shock in 0.25x TES, followed by Ni-NTA purification and either desalting by PD MiniTrap G-25 columns (GE Healthcare Life Sciences) (small scale purifications), or gel filtration with Superdex 75 Increase 10/300 GL or HiLoad 16/600 Superdex 75 pg columns (medium or large scale purifications) in 20 mM HEPES pH 7.4, 150 mM NaCl. Protein was concentrated using Amicon spin-concentrators with 3 or 10 kDa cutoff (Millipore). To produce fluorescently labeled VHHs by sortase A labeling (*51*), 45 μM VHH-LPETG-His_6 was incubated with 475 μM GGGC-Alexa Fluor 488 and 20 μM His_6-tagged sortase A 7m for 2 hours. Sortase A 7m and unreacted VHHs were removed by depletion with Ni-NTA, followed by gel filtration on a Superdex 75 Increase 10/300 GL column.

Expression and purification of CC12.3 Fab

CC12.3 Fab was produced as described previously (*17*). In brief, the coding sequences of heavy and light chain of CC12.3 Fab were cloned into phCMV3. ExpiCHO cells were transiently co-transfected at a ratio of 2:1 (HC:LC) using ExpiFectamine CHO Reagent (Thermo Fisher Scientific) according to the manufacturer's instructions. The supernatant was collected at 10 days posttransfection. The Fabs were purified with a CaptureSelect CH1-XL Affinity Matrix (Thermo Fisher Scientific) followed by size-exclusion chromatography.

Expression and purification of SARS-CoV-2 spike

Soluble, trimeric SARS-CoV-2 spike was expressed as a fusion of amino acids 1 to 1208 of SARS-CoV-2/human/China/Wuhan-Hu-1/2019 containing mutations R682G, R683S, R685S, K986P, V987P (S2-P), a C-terminal T4 fibritin trimerization motif, an HRV3C protease cleavage site, a TwinStrepTag and a His_8 tag from a mammalian expression vector based on pαH, as previously described (*6*). For some cryo-EM experiments, the SARS-CoV-2 spike HexaPro mutant with additional proline mutations was used (*52*). In brief, protein was produced in FreeStyle 293F cells transfected with FreeStyle MAX reagent (Thermo Fisher Scientific) or Expi293F cells transfected with ExpiFectamine 293 (Thermo Fisher Scientific). The ectodomain was purified from filtered supernatant on Streptactin XT resin (IBA Lifesciences), followed by gel filtration on a HiLoad 16/600 Superdex 200 column in 50 mM Tris pH 8, 200 mM NaCl. Soluble spike protein was biotinylated using UV-traceable ChromaLink Biotin (SoluLink).

Antibodies

The following commercially available antibodies were used: mouse anti-HA antibody HA.11 (clone 16B12, Biolegend, Cat# 901503, RRID:AB_2565005), rabbit anti-DYKDDDDK (FLAG) tag antibody (clone D6W5B, Cell Signaling Technology Cat# 14793, RRID:AB_2572291), HRP-coupled rabbit anti-E tag antibody (Bethyl Laboratories Cat# A190-133P, RRID:AB_345222), HRP-coupled MonoRab rabbit anti-camelid VHH antibody (clone 96A3F5, GenScript Cat# A01860-200, RRID:AB_2734123), HRP-coupled mouse anti-HA-Tag (clone 6E2, Cell Signaling Technology Cat# 2999, RRID:AB_1264166), goat anti-mouse IgG Alexa Fluor Plus 647 (Thermo Fisher Scientific Cat# A32728, RRID:AB_2633277), goat anti-rabbit IgG Alexa Fluor Plus 647 (Thermo Fisher Scientific Cat# A32733, RRID:AB_2633282).

Nanobody library generation

To elicit heavy-chain–only antibodies against SARS-CoV-2 spike, one 7-year-old male llama (*Lama glama*), and one 6-year-old male alpaca (*Vicugna pacos*) were immunized. All immunizations were authorized by the Landesuntersuchungsamt Rheinland-Pfalz (23 177-07/A 17-20-005 HP). The llama was immunized six times every week with 200 μg SARS-CoV-2 S RBD, complemented with 300 μl formaldehyde-inactivated virus (corresponding to ~10^9 pfu) in the last two injections. The alpaca was immunized four times every 2 weeks with 200 μg SARS-CoV-2 S RBD. GERBU Adjuvant Fama (GERBU Biotechnik GmbH) was used as an adjuvant in all immunizations. In two (llama) or one (alpaca) injection, respectively, antigen and adjuvant were injected separately. VHH plasmid libraries in the M13 phagemid vector pD (pJSC) were generated as described before (*53*). In brief, RNA from peripheral blood lymphocytes was extracted and used as a template to generate cDNA using three sets of primers (random hexamers, oligo (dT), and primers specific for the constant region of the alpaca heavy chain gene). VHH coding sequences were amplified by PCR using VHH-specific primers, cut with AscI and NotI, and ligated into pJSC linearized with the same restriction enzymes. *E. coli* TG1 cells (Agilent) were electroporated with the ligation reactions and the obtained ampicillin-resistant colonies were harvested, pooled, and stored as glycerol stocks.

Nanobody identification

SARS-CoV-2 spike RBD-specific VHHs were obtained by phage display and panning with a protocol modified from Schmidt *et al.* (*53*). *E. coli* TG1 cells containing the VHH library were infected with helper phage VCSM13 to produce phages displaying the encoded VHHs as pIII fusion proteins. Phages in the supernatant were purified and concentrated by precipitation. Phages presenting RBD-specific VHHs were enriched using enzymatically or chemically biotinylated RBDs immobilized to MyOne Streptavidin T1 Dynabeads (Thermo Fisher Scientific). The retained phages were used to infect *E. coli* ER2738 and subjected to a second round of panning. 6× 95 *E. coli* ER2837 colonies yielded in the second panning were grown in 96-well plates and VHH expression induced with IPTG. VHHs leaked into the supernatant were tested for specificity using ELISA plates coated with control protein maltose binding protein (MBP) or SARS-CoV-2 spike RBD. Bound VHHs were detected with HRP-coupled rabbit anti-E-Tag antibodies (Bethyl), HRP-coupled MonoRab Rabbit Anti-Camelid VHH Antibody (GenScript), and the chromogenic substrate TMB. Reactions were stopped with 1 M HCl and absorption at 450 nm was recorded. Positive candidates were sequenced, and representative nanobodies cloned into bacterial expression vectors for further analysis.

ELISA

To test nanobody candidates, SARS-CoV-2 spike RBD or the control protein MBP in PBS were immobilized on ELISA plates at a concentration of 1 μg/mL overnight. Serial 10-fold dilutions of HA-tagged nanobodies in 10% FBS/PBS were incubated with the immobilized antigen, followed by incubation with HRP-coupled anti-HA (clone 6E2, 1:5000, Cell Signaling), and the chromogenic substrate TMB. Reactions were stopped with 1 M HCl and absorption measured at 450 nm.

Surface plasmon resonance

Surface plasmon resonance experiments were performed using a Biacore 8K instrument (GE Healthcare). The flow system was cleaned using the maintenance "Desorb" function (Desorb Kit, GE Healthcare). The system was flushed with running buffer (20 mM HEPES pH 7.4, 150 mM NaCl, 0.05% Tween 20) and all steps were performed at 25°C chip temperature. Before immobilization, a streptavidin-functionalized sensor chip (Series S Sensor Chip SA, GE Healthcare) was conditioned with three consecutive 1-min injections of 1 M NaCl in 50 mM NaOH (10 μl/min). After immobilization of biotinylated SARS-CoV-2 spike RBD (50 nM, 5 μl/min, 300 s) on the sensor chip flow cell 2, the flow system was washed using 50% isopropanol in 1 M NaCl and 50 mM NaOH. For kinetic binding measurements, various VHHs were injected (30 μl/min, association: 90 s, dissociation: 180 s) over both flows. For epitope binning, the VHHs were pairwise tested for competitive binding using the ABA-injection feature. After each cycle, the surfaces were regenerated with a 120 s injection step of 10 mM glycine pH 2.1. Data were collected at a rate of 10 Hz. The binding data were double referenced by blank cycle and reference flow cell subtraction. Processed data were fitted by the 1:1 interaction model using Biacore Insight Evaluation Software (version 2.0. 15.12933).

Crystallization and structural determination

VHH E/VHH U/RBD, VHH V/CC12.3/RBD, and VHH W/CC12.3/RBD complexes were formed by mixing each of the protein components at an equimolar ratio and incubating overnight at 4°C. The final concentration for the complexes for crystallization screening ranged from 13.5 to 17.8 mg/ml. Crystallization screening was performed using the vapor-diffusion method in sitting drops containing 0.1 μl of protein and 0.1 μl of reservoir solution with the 384 conditions of the JCSG Core Suite (Qiagen) using the robotic CrystalMation system (Rigaku) at The Scripps Research Institute. Diffraction-quality crystals were obtained in the following conditions

VHH E/VHH U/RBD complex (13.5 mg/ml): 20% PEG 3000, 0.1 M citrate pH 5.5 at 20°C,

VHH V/CC12.3/RBD complex (17.8 mg/ml): 20% PEG 3350, 0.2 M Na2HPO4, pH 9.1 at 20°C,

VHH W/CC12.3/RBD complex (17.6 mg/ml): 1.0 M Li-chloride, 10% PEG 6000, 0.1 M Bicine pH 9.0 at 20°C.

All crystals appeared within 7 days after tray set-up. Before flash cooling in liquid nitrogen for x-ray diffraction studies, crystals were equilibrated in reservoir solution supplemented with 10% ethylene glycol at day 7. Diffraction data were collected at cryogenic temperature (100 K) at either Stanford Synchrotron Radiation Lightsource (SSRL) on beamline 12-1 with a beam wavelength of 0.97946 Å, or at the Advanced Photon Source (APS) at Argonne National Labs on beamline 23ID-B at a wavelength of 1.03317 Å, and processed with HKL2000 (*54*). Structures were solved by molecular replacement (MR) using PHASER (*55*) with MR templates derived from PDB: 6XC7 (*17*), 7JMW (*56*) and 6WAQ (*16*). Iterative model building and refinement were carried out in COOT (*57*) and PHENIX (*58*), respectively. Epitope and paratope residues, as well as their interactions, were identified by accessing PISA at the European Bioinformatics Institute (www.ebi.ac.uk/pdbe/prot_int/pistart.html) (*59*).

Cryo-EM sample preparation and imaging

Spike trimer (2.4 mg/ml S2-P (*6*) for VHH E and VHH V; HexaPro (*52*) for VHH VE) and nanobody were mixed in a 1:6 molar ratio for VHH E and VHH V, and 1:4 for VHH VE, followed by incubation on ice for 10 min. Prior to cryo-EM grid preparation, grids were glow-discharged with 25 mA for 2 min using an EMS 100X (Electron Microscopy Sciences) glow-discharge unit. Grids used were UltrAuFoil Gold 200 mesh (R 2/2 geometry; Quantifoil Micro Tools GmbH; VHH VE) or CryoMatrix holey grids with amorphous alloy film (R 2/1 geometry; Zhenjiang Lehua Technology Co., Ltd; VHH E, VHH V). 3-μl aliquots of sample solutions were applied to the grids and the grids with sample were then vitrified in a Vitrobot Mk IV (Thermo Fisher Scientific) at 4°C and 100% humidity [blot 10 s, blot force 3, 595 filter paper (Ted Pella Inc.)]. Cryo-EM data collection was performed with EPU (Thermo Fisher Scientific) using a Krios G3i transmission-electron microscope (Thermo Fisher Scientific) operated at 300 kV in the Karolinska Institutet's 3D-EM facility. Movies were acquired in nanoprobe EFTEM SA mode with a slit width of 10 eV using a K3 Bioquantum for 1.5 s during which 60 movie frames were collected with a fluency of 0.81 $e^-/Å^2$ per frame (see table S3). Motion correction, CTF-estimation, Fourier cropping (to 1.02 Å per pixel), picking and extraction in 600 pixel boxes (size threshold 200 Å, distance threshold 100 Å, using the pretrained BoxNet2-Mask_20180918 model) were performed on the fly using Warp (*60*).

A total of 6,468 (VHH E), 9,861 (VHH V), and 12,606 (VHH VE) micrographs were selected based on an estimated resolution cutoff of 4 Å and defocus below 2 microns. and 245,000 (VHH E), 509,302 (VHH V), and 982,221 (VHH VE), particles were picked by Warp (*60*). Extracted particles were imported into cryoSPARC v2.15.0 (*61*) for 2D classification, 3D classification and nonuniform 3D refinement. The particles were processed with C1 symmetry. After 2D classification, clean classes with high-resolution features (and with characteristic trimeric spike views) were retained and used to build ab initio 3D reconstructions. These were further processed for heterogeneous refinement (4.78 Å per pixel) that resulted in reconstructions showing high-resolution structural features in the core of the spike. One round of homogeneous refinement was followed by nonuniform refinement. For the VHH VE dataset, the particles from refinement job containing angular information was migrated from cryoSPARC to RELION 3.1 (*62*) for 3D classification without alignment (1.02 Å per pixel, 35 iterations, $T = 8$) and classified into four classes using reconstruction in cryoSPARC as reference map (low-pass filtered to 25Å). One class containing 92,938 particles, where densities for all six nanobodies were visible, was transferred to cryoSPARC for final refinement in C1 (1.02 Å per pixel). All final reconstructions were analyzed using 3D-FSC (*63*) (figs. S4, S8, and S17) and there was no significant anisotropy in the full map reconstructions (sphericity 0.91 to 0.96). All CTF refinements were local CTF refinements interspersed with global aberration correction (beamtilt, trefoil, tetrafoil and spherical aberration). Please see table S3 for data collection and processing statistics and the respective cryo-EM data processing schemes in figs. S3, S7, and S16. VHH VE and VHH E were pseudo-C3 symmetric especially in the RBD-VHH parts. For VHH E, we symmetry-expanded a particle set with partial-signal subtraction of all parts except for one VHH E-RBD. From this symmetry expanded particle set, we performed local reconstruction of the single VHH E-RBD component. This process significantly enhanced the resolvability of the map and thereby enabled molecular fitting of the density. The locally reconstructed density for RBD-VHH E was then combined with the main map using the combined focused map procedure for refinement as implemented in PHENIX (*58*). A similar procedure was used for local reconstruction of the RBD + VHH VE part from the Spike VHH VE particles and ensuing development of a combined focused map for refinement.

Cryo-EM model building and structure refinement

The structure of the spike protein trimer PDB: 6ZXN (*15*) was used as a starting model for model building. The structure of the VHHs bound to the RBDs were modeled from the basis of their respective crystallographic models. Structure refinement and manual model building were performed using COOT (*57*) and PHENIX (*58*) in interspersed cycles with secondary structure, Ramachandran, rotamers and bond geometry restrains. Structure figures and EM density-map figures were generated with UCSF ChimeraX (*64*) and COOT (*57*), respectively. Please see table S4 for refinement and validation.

ACE2-RBD binding assay

HEK 293T cells stably expressing ACE2-tagRFP-t were detached with 1 mM EDTA in PBS. 0.8 μM DyLight 488-labeled SARS-CoV-2 RBD was incubated with different concentrations of VHHs at room temperature (RT) for 60 min. ACE2-expressing cells were subsequently incubated with RBD-VHH mixtures on ice for 30 min. The DyLight 488 signal was measured in all ACE2-tagRFP-t positive cells using a MACS Quant VYB flow cytometer.

VHH-mediated SARS-CoV-2 spike fusion assay (live-cell imaging)

HEK 293 SARS-CoV-2 spike Δ18 eGFP and HEK 293 SARS-CoV-2 spike Δ18 tag-RFP-t cells were seeded in tissue culture-treated CellCarrier-96 Ultra Microplates (Perkin Elmer) at a density of 100,000 cells of each cell line per well in phenol red-free full medium containing 1 μg/ml doxycycline. 24 hours postseeding, cells were treated with the indicated concentrations of nanobodies and cultivated at 37°C, 5% CO_2. Every 20 min, images were recorded in four fields of view per well for 14 hours using a Zeiss Observer Z1 wide-field microscope with 20X PlanApochromat objective (NA = 0.8). eGFP and tagRFP-t colocalization was quantified using ImageJ plugin EzColocalization (65). Pearson correlation coefficients (PCC) between both channels were determined for each time point, including all pixels (no thresholding).

SARS-CoV-2 spike-ACE2 fusion assay (live-cell imaging)

HEK 293 SARS-CoV-2 spike Δ18 eGFP and HEK 293T ACE2-tagRFP-t labeled with CellTracker Orange CMRA (1:5000) were seeded in tissue culture-treated CellCarrier-96 Ultra Microplates (Perkin Elmer) at a density of 100,000 cells of each cell line per well in phenol red-free full medium. 24 hours postseeding, cells were treated with 1 μg/ml doxycycline and 1 μM of the indicated nanobodies, and cultivated at 37°C, 5% CO_2. Every 20 min, images were recorded in four fields of view per well for 14 hours using a Zeiss Observer Z1 wide-field microscope with 20X PlanApochromat objective (NA = 0.8). eGFP and tagRFP-t colocalization was quantified using the ImageJ plugin EzColocalization (65). Pearson correlation coefficients (PCC) between both channels were determined for each time point, including all pixels (no thresholding). To normalize fusion, PCC values at 1 hour were subtracted from PCC values of each time point. Average values of four fields of view were corrected by average values of uninduced cells from the same time point. Fusion at t = 12 hours was defined as 100% fusion.

Neutralization assay with VSV ΔG eGFP (SARS-CoV-1/2) (infection assay)

Single-round infection experiments with replication-deficient VSV ΔG eGFP (SARS-CoV-1) and VSV ΔG eGFP (SARS-CoV-2) were performed in Vero E6 cells. 48-well plates were seeded with $3.5{\cdot}10^4$ Vero E6 cells per well. On the next day, 10^4 infectious units (IU) of VSV ΔG eGFP (SARS-CoV-1/2) in 50 μl DMEM (without FBS) (titered to achieve ~30% infection) were mixed with 50 μl VHH dilution in DMEM (without FBS), yielding the indicated final VHH concentrations. Virus mixtures were incubated at 37°C for 1 hour, and subsequently used to infect Vero E6 cells. The inoculum was removed after 1 hour and cells were covered with 0.5 ml full DMEM (FBS). After 7 hours at 37°C (8 hours p.i.), cells were trypsinized, fixed, and eGFP-positive cells quantified using a MACS Quant VYB flow cytometer. IC_{50} values were calculated using the "log(inhibitor) vs. normalized response" equation in GraphPad Prism.

Neutralization assays with SARS-CoV-2 WT (plaque reduction neutralization test)

Plaque reduction neutralization tests (PRNTs) with SARS-CoV-2/human/Germany/Heinsberg-01/2020 were performed in Vero E6 cells. 24-well plates were seeded with $1.5{\cdot}10^5$ Vero E6 cells per well. The following day, nanobodies were subjected to a two-fold dilution series. 120 μl of each nanobody dilution was mixed with 120 μl of OptiPRO SFM cell culture media (Thermo Fisher Scientific) containing 80 pfu of SARS-CoV-2. After 1 hour at 37°C, 200 μl of each mixture was added to 24-well plates. After 1 hour at 37°C, the inoculum was removed, and cells were overlaid with a 1:1 mixture of 1.5% carboxymethylcellulose (Sigma Aldrich) in 2x MEM (Biochrom) with 4% FBS (Thermo Fisher Scientific). After a 3-day incubation at 37°C, cells were fixed with 6% formaldehyde and stained with 1% crystal violet in 20% ethanol. Plaques were counted manually. IC_{50} values were calculated using the "log (inhibitor) vs. normalized response" equation in GraphPad Prism.

Neutralization assays with SARS-CoV-2 mNeonGreen (replication assay)

Microscopy-based neutralization experiments with SARS-CoV-2 clone icSARS-CoV-2-mNG were performed with Caco-2 cells. 10^4 cells/well were seeded in 96-well plates. The next day, cells were infected with icSARS-CoV-2-mNG at an MOI of 1.1 in media containing 5% FBS and serial dilutions of the indicated nanobodies. Cells were subsequently cultivated for 48 hours in the presence of the nanobodies, fixed with 2% PFA, and stained with 1 μg/ml Hoechst 33342 at 37°C for 10 min. The staining solution was removed and exchanged to PBS. To quantify infection rates, images were recorded with a Cytation3 instrument (Biotek). Total (Hoechst positive) and infected (mNeonGreen positive) cells were quantified using the Gen5 Software (Biotek). IC_{50} values were calculated as the half-maximal inhibitory dose using four-parameter nonlinear regression (GraphPad Prism).

Identification and isolation of escape mutants

To test the emergence or presence of escape mutants of replication-competent VSV SARS-CoV-2 SΔ18 eGFP in the presence of nanobodies, virus was replicated in the presence of serial dilutions of nanobodies in Vero E6 cells (31). $1.4{\cdot}10^5$ cells per well were seeded into 12-well plates. On the next day, 0.5 ml virus dilution (equivalent to an MOI of 0.5) in DMEM (3% FBS, PS) was incubated with 0.5 ml VHH dilution in DMEM (3% FBS, PS) at room temperature for 30 min. The mixture was subsequently transferred to 12-wells with Vero E6 cells and cultivated at 37°C for 4 days. The fraction of eGFP-positive cells as well as cytopathic effect (CPE) were evaluated and selected wells harvested for further cultivation: Cells were lysed in RLT PLUS buffer containing 1% β-mercaptoethanol, followed by purification of RNA with the RNeasy Mini Kit (Qiagen). Supernatants were cleared and stored at 4°C. 1:5 dilutions in DMEM (3% FBS, PS) were used to infect cells for a second round of selection under otherwise identical conditions. eGFP-positive cells and CPE were evaluated 5 days postinfection and selected supernatants and cell lysates harvested.

To quantify escape variants of virus replicated in the presence of neutralizing nanobodies, viral RNA was reversely transcribed to cDNA using a SARS-CoV-2 spike specific primer (FS1957 – 5′-ACTGCTGGAATGGCAGGAAC-3′). The RBD coding sequence flanked by additional 70 bp was amplified by PCR using Phusion DNA polymerase (New England Biolabs) and primer FS1956 (5′-TCTGAGCGAGACAAAGTGCACC-3′) and FS1957, and subjected to Tn5-mediated tagmentation and incorporation of barcoded adapters. Amplicons were sequenced on an Illumina MiSeq machine (v2 nano, 2x150 bp paired-end). After sequencing, FASTQ files were examined using FastQC (Version 0.11.9) and multiqc (Version 1.9). For the alignment, the SARS-CoV-2 spike RBD reference was indexed using bowtie2-build (Version 2.4.1) and samtools (Version 1.10). The reads where aligned using bowtie2 (Version 2.4.1). Conversion into BAM file, sorting and indexing was performed using samtools. BAM files were examined with QualiMap (Version 2.2.2-dev) and multiqc. Variant calling was performed using default GATK HaplotypeCaller (Version 4.1.8.1), and variants were inspected in bam. files using IGV. To quantify the frequencies of mutated interfaces, we determined which mutations within one sample represented individual haplotypes, i.e., in which cases none of the individual reads contained multiple of the mutations (marked with asterisks in tables S5 and S6). Where a global statement was not possible due to the distance of the mutations (marked with hash symbols in tables S5 and S6), the fraction of sequences with at least one mutation was estimated based on visual inspection of individual reads.

To isolate defined escape mutants, resistant virus was amplified from individual virus plaques grown on Vero E6 cells. $1.4{\cdot}10^5$ Vero E6 cells per well were seeded into 12-wells. The next day, 10-fold serial dilutions of supernatants from virus replicated in the presence of VHH E, U, V, W, E and U, E and V, E and W, or LaM-4 (round 1) were prepared and incubated in the presence or absence of 1 μM of VHHs at RT for 30 min. Vero E6 cells were infected for 30 min at 37°C, followed by overlay of cells with 0.75% agarose, MEM, 2% FBS, PS, 25 mM HEPES with or without the respective VHHs. Two days postinfection, fluorescent plaques grown in the presence of individual nanobodies were identified and marked. No VHH-resistant fluorescent plaques emerged from supernatants of the combinations VHH E and U, E and V, or E and W. A plug of the agarose on top of marked plaques was removed with a Pasteur pipette and incubated in 500 µl DMEM for 4 hours at 4°C. 48-wells were infected with 250 µl of this virus dilution and cultivated in DMEM (2% FBS, PS, 25 mM HEPES) at 37°C until all cells were eGFP-positive. Supernatants were stored at 4°C and cells lysed in RLT PLUS buffer containing 1% β-mercaptoethanol, followed by purification of RNA with the RNeasy Mini Kit (Qiagen). Viral RNA was reversely transcribed to cDNA using a SARS-CoV-2 spike specific primer. The RBD coding sequence flanked by additional 70 bp was amplified by PCR and sequenced by Sanger sequencing. 6/6 plaques resistant to VHH E exhibited the point mutation S494P, 5/5 plaques resistant to VHH U and 5/5 plaques resistant to VHH W encoded the point mutant S371P, and 8/8 plaques resistant to VHH V contained the point mutation K378Q. 4/4 plaques from virus cultivated in the presence of control VHH LaM-4 did not contain any mutations. Selected clones were amplified in Vero E6 cells and cleared supernatants stored at −80°C.

Growth curves of VSV eGFP SARS-CoV-2 S∆18 (replication assay)

Vero E6 cells were seeded in 24-well plates ($7{\cdot}10^4$ cells per well). The next day, cells were infected with plaque-purified VSV eGFP SARS-CoV-2 ∆18 isolates at an MOI of 0.02 for 1 hour. The inoculum was removed, cells were washed with PBS twice, and subsequently cultivated in DMEM (2% FBS, 30 mM HEPES, PS). At the indicated time points, supernatants were cleared by centrifugation at 1000 ×g, 4°C, for 10 min and frozen at −80°C until titration. For titration, Vero E6 cells were seeded into 96-well plates at a density of 10^4 cells per well. Cells were infected with twofold serial dilutions of virus-containing supernatants for 1 hour, followed by cultivation in full medium for 7 hours. Cells were trypsinized, fixed in formaldehyde, and green fluorescence was quantified using a MACS Quant VYB flow cytometer.

REFERENCES AND NOTES

1. J. Abraham, Passive antibody therapy in COVID-19. *Nat. Rev. Immunol.* **20**, 401–403 (2020). doi: 10.1038/s41577-020-0365-7; pmid: 32533109
2. A. Iwasaki, Y. Yang, The potential danger of suboptimal antibody responses in COVID-19. *Nat. Rev. Immunol.* **20**, 339–341 (2020). doi: 10.1038/s41577-020-0321-6; pmid: 32317716
3. J. R. Ingram, F. I. Schmidt, H. L. Ploegh, Exploiting nanobodies' singular traits. *Annu. Rev. Immunol.* **36**, 695–715 (2018). doi: 10.1146/annurev-immunol-042617-053327; pmid: 29490163
4. S. Cunningham *et al*., Nebulised ALX-0171 for respiratory syncytial virus lower respiratory tract infection in hospitalised children: A double-blind, randomised, placebo-controlled, phase 2b trial. *Lancet Respir. Med.* **9**, 21–32 (2021). doi: 10.1016/S2213-2600(20)30320-9; pmid: 33002427
5. M. Hoffmann *et al*., SARS-CoV-2 cell entry depends on ACE2 and TMPRSS2 and is blocked by a clinically proven protease inhibitor. *Cell* **181**, 271–280.e8 (2020). doi: 10.1016/j.cell.2020.02.052; pmid: 32142651
6. D. Wrapp *et al*., Cryo-EM structure of the 2019-nCoV spike in the prefusion conformation. *Science* **367**, 1260–1263 (2020). doi: 10.1126/science.abb2507; pmid: 32075877
7. A. C. Walls *et al*., Structure, function, and antigenicity of the SARS-CoV-2 spike glycoprotein. *Cell* **181**, 281–292.e6 (2020). doi: 10.1016/j.cell.2020.02.058; pmid: 32155444
8. Z. Lv *et al*., Structural basis for neutralization of SARS-CoV-2 and SARS-CoV by a potent therapeutic antibody. *Science* **369**, 1505–1509 (2020). doi: 10.1126/science.abc5881; pmid: 32703908
9. T. F. Rogers *et al*., Isolation of potent SARS-CoV-2 neutralizing antibodies and protection from disease in a small animal model. *Science* **369**, 956–963 (2020). doi: 10.1126/science.abc7520; pmid: 32540903
10. C. O. Barnes *et al*., Structures of human antibodies bound to SARS-CoV-2 spike reveal common epitopes and recurrent features of antibodies. *Cell* **182**, 828–842.e16 (2020). doi: 10.1016/j.cell.2020.06.025; pmid: 32645326
11. M. Schoof *et al*., An ultrapotent synthetic nanobody neutralizes SARS-CoV-2 by stabilizing inactive Spike. *Science* **370**, 1473–1479 (2020). doi: 10.1126/science.abe3255; pmid: 33154106
12. M. A. Tortorici *et al*., Ultrapotent human antibodies protect against SARS-CoV-2 challenge via multiple mechanisms. *Science* **370**, 950–957 (2020). doi: 10.1126/science.abe3354; pmid: 32972994
13. D. Pinto *et al*., Cross-neutralization of SARS-CoV-2 by a human monoclonal SARS-CoV antibody. *Nature* **583**, 290–295 (2020). doi: 10.1038/s41586-020-2349-y; pmid: 32422645
14. J. D. Walter, C. A. J. Hutter, I. Zimmermann, J. Earp, P. Egloff, M. Sorgenfrei, L. M. Hürlimann, I. Gonda, G. Meier, S. Remm, S. Thavarasah, P. Plattet, M. A. Seeger, Sybodies targeting the SARS-CoV-2 receptor-binding domain. bioRxiv, 10.1101/2020.04.16.045419 [Preprint]. 16 May 2020. doi: 10.1101/2020.04.16.045419
15. L. Hanke *et al*., An alpaca nanobody neutralizes SARS-CoV-2 by blocking receptor interaction. *Nat. Commun.* **11**, 4420 (2020). doi: 10.1038/s41467-020-18174-5; pmid: 32887876
16. D. Wrapp *et al*., Structural basis for potent neutralization of betacoronaviruses by single-domain camelid antibodies. *Cell* **181**, 1004–1015.e15 (2020). doi: 10.1016/j.cell.2020.04.031; pmid: 32375025
17. M. Yuan *et al*., Structural basis of a shared antibody response to SARS-CoV-2. *Science* **369**, 1119–1123 (2020). doi: 10.1126/science.abd2321; pmid: 32661058
18. J. Huo *et al*., Neutralizing nanobodies bind SARS-CoV-2 spike RBD and block interaction with ACE2. *Nat. Struct. Mol. Biol.* **27**, 846–854 (2020). doi: 10.1038/s41594-020-0469-6; pmid: 32661423
19. T. Li, H. Cai, H. Yao, B. Zhou, Y. Zhao, W. Qin, C. Hutter, Y. Lai, J. Bao, J. Lan, G. Wong, M. Seeger, D. Lavillette, D. Li, A potent synthetic nanobody targets RBD and protects mice from SARS-CoV-2 infection. bioRxiv 10.1101/2020.06.09.143438 [Preprint]. 24 September 2020. doi: 10.1101/2020.06.09.143438
20. Q. Wang *et al*., Structural and functional basis of SARS-CoV-2 entry by using human ACE2. *Cell* **181**, 894–904.e9 (2020). doi: 10.1016/j.cell.2020.03.045; pmid: 32275855
21. B. Turoňová *et al*., In situ structural analysis of SARS-CoV-2 spike reveals flexibility mediated by three hinges. *Science* **370**, 203–208 (2020). doi: 10.1126/science.abd5223; pmid: 32817270
22. W. Song, M. Gui, X. Wang, Y. Xiang, Cryo-EM structure of the SARS coronavirus spike glycoprotein in complex with its host cell receptor ACE2. *PLOS Pathog.* **14**, e1007236 (2018). doi: 10.1371/journal.ppat.1007236; pmid: 30102747
23. D. J. Benton *et al*., Receptor binding and priming of the spike protein of SARS-CoV-2 for membrane fusion. *Nature* **588**, 327–330 (2020). doi: 10.1038/s41586-020-2772-0; pmid: 32942285
24. J. Pallesen *et al*., Immunogenicity and structures of a rationally designed prefusion MERS-CoV spike antigen. *Proc. Natl. Acad. Sci. U.S.A.* **114**, E7348–E7357 (2017). doi: 10.1073/pnas.1707304114; pmid: 28807998
25. T. F. Custódio *et al*., Selection, biophysical and structural analysis of synthetic nanobodies that effectively neutralize SARS-CoV-2. *Nat. Commun.* **11**, 5588 (2020). doi: 10.1038/s41467-020-19204-y; pmid: 33149112
26. G. Simmons *et al*., Different host cell proteases activate the SARS-coronavirus spike-protein for cell-cell and virus-cell fusion. *Virology* **413**, 265–274 (2011). doi: 10.1016/j.virol.2011.02.020; pmid: 21435673
27. J. ter Meulen *et al*., Human monoclonal antibody combination against SARS coronavirus: Synergy and coverage of escape mutants. *PLOS Med.* **3**, e237 (2006). doi: 10.1371/journal.pmed.0030237; pmid: 16796401
28. J. S. Huston *et al*., Protein engineering of antibody binding sites: Recovery of specific activity in an anti-digoxin single-chain Fv analogue produced in *Escherichia coli*. *Proc. Natl. Acad. Sci. U.S.A.* **85**, 5879–5883 (1988). doi: 10.1073/pnas.85.16.5879; pmid: 3045807
29. J. B. Case *et al*., Neutralizing antibody and soluble ACE2 inhibition of a replication-competent VSV-SARS-CoV-2 and a clinical isolate of SARS-CoV-2. *Cell Host Microbe* **28**, 475–485.e5 (2020). doi: 10.1016/j.chom.2020.06.021; pmid: 32735849
30. F. Schmidt *et al*., Measuring SARS-CoV-2 neutralizing antibody activity using pseudotyped and chimeric viruses. *J. Exp. Med.* **217**, e20201181 (2020). doi: 10.1084/jem.20201181; pmid: 32692348
31. A. Baum *et al*., Antibody cocktail to SARS-CoV-2 spike protein prevents rapid mutational escape seen with individual antibodies. *Science* **369**, 1014–1018 (2020). doi: 10.1126/science.abd0831; pmid: 32540904
32. E. Beirnaert *et al*., Bivalent llama single-domain antibody fragments against tumor necrosis factor have picomolar potencies due to intramolecular interactions. *Front. Immunol.* **8**, 867 (2017). doi: 10.3389/fimmu.2017.00867; pmid: 28824615
33. C. Liu *et al*., The architecture of inactivated SARS-CoV-2 with postfusion spikes revealed by cryo-EM and cryo-ET. *Structure* **28**, 1218–1224.e4 (2020). doi: 10.1016/j.str.2020.10.001; pmid: 33058760
34. Z. Ke *et al*., Structures and distributions of SARS-CoV-2 spike proteins on intact virions. *Nature* **588**, 498–502 (2020). doi: 10.1038/s41586-020-2665-2; pmid: 32805734
35. A. C. Walls *et al*., Unexpected receptor functional mimicry elucidates activation of coronavirus fusion. *Cell* **176**, 1026–1039.e15 (2019). doi: 10.1016/j.cell.2018.12.028; pmid: 30712865
36. J. Huo *et al*., Neutralization of SARS-CoV-2 by destruction of the prefusion spike. *Cell Host Microbe* **28**, 445–454.e6 (2020). doi: 10.1016/j.chom.2020.06.010; pmid: 32585135
37. Y. Wan *et al*., Molecular mechanism for antibody-dependent enhancement of coronavirus entry. *J. Virol.* **94**, e02015-19 (2020). doi: 10.1128/JVI.02015-19; pmid: 31826992
38. F. Li, Structure, function, and evolution of coronavirus spike proteins. *Annu. Rev. Virol.* **3**, 237–261 (2016). doi: 10.1146/annurev-virology-110615-042301; pmid: 27578435
39. F. Wu, R. Yan, M. Liu, Z. Liu, Y. Wang, D. Luan, K. Wu, Z. Song, T. Sun, Y. Ma, Y. Zhang, X. Li, P. Ji, Y. Li, C. Li, Y. Wu, T. Ying, S. Jiang, T. Zhu, L. Lu, Y. Zhang, Q. Zhou, Antibody-dependent enhancement (ADE) of SARS-CoV-2 infection in recovered COVID-19 patients: studies based on cellular and structural biology analysis. medRxiv 10.1101/2020.10.08.20209114 [Preprint]. 13 October 2020. .doi: 10.1101/2020.10.08.20209114
40. R. E. Kontermann, Strategies for extended serum half-life of protein therapeutics. *Curr. Opin. Biotechnol.* **22**, 868–876 (2011). doi: 10.1016/j.copbio.2011.06.012; pmid: 21862310
41. L. Detalle *et al*., Generation and characterization of ALX-0171, a potent novel therapeutic nanobody for the treatment of respiratory syncytial virus infection. *Antimicrob. Agents Chemother.* **60**, 6–13 (2015). doi: 10.1128/AAC.01802-15; pmid: 26438495
42. E. A. F. Simões *et al*., Past, present and future approaches to the prevention and treatment of respiratory syncytial virus infection in children. *Infect. Dis. Ther.* **7**, 87–120 (2018). doi: 10.1007/s40121-018-0188-z; pmid: 29470837
43. N. S. Laursen *et al*., Universal protection against influenza infection by a multidomain antibody to influenza hemagglutinin. *Science* **362**, 598–602 (2018). doi: 10.1126/science.aaq0620; pmid: 30385580
44. A. Klarenbeek *et al*., Camelid Ig V genes reveal significant human homology not seen in therapeutic target genes, providing for a powerful therapeutic antibody platform. *mAbs* **7**, 693–706 (2015). doi: 10.1080/19420862.2015.1046648; pmid: 26018625

45. C. Vincke *et al*., General strategy to humanize a camelid single-domain antibody and identification of a universal humanized nanobody scaffold. *J. Biol. Chem.* **284**, 3273–3284 (2009). doi: 10.1074/jbc.M806889200; pmid: 19010777
46. M. Scully *et al*., Caplacizumab treatment for acquired thrombotic thrombocytopenic purpura. *N. Engl. J. Med.* **380**, 335–346 (2019). doi: 10.1056/NEJMoa1806311; pmid: 30625070
47. T. Dull *et al*., A third-generation lentivirus vector with a conditional packaging system. *J. Virol.* **72**, 8463–8471 (1998). doi: 10.1128/JVI.72.11.8463-8471.1998; pmid: 9765382
48. H. Streeck *et al*., Infection fatality rate of SARS-CoV2 in a super-spreading event in Germany. *Nat. Commun.* **11**, 5829 (2020). doi: 10.1038/s41467-020-19509-y; pmid: 33203887
49. X. Xie *et al*., An infectious cDNA clone of SARS-CoV-2. *Cell Host Microbe* **27**, 841–848.e3 (2020). doi: 10.1016/j.chom.2020.04.004; pmid: 32289263
50. S. P. J. Whelan, L. A. Ball, J. N. Barr, G. T. W. Wertz, Efficient recovery of infectious vesicular stomatitis virus entirely from cDNA clones. *Proc. Natl. Acad. Sci. U.S.A.* **92**, 8388–8392 (1995). doi: 10.1073/pnas.92.18.8388; pmid: 7667300
51. C. P. Guimaraes *et al*., Site-specific C-terminal and internal loop labeling of proteins using sortase-mediated reactions. *Nat. Protoc.* **8**, 1787–1799 (2013). doi: 10.1038/nprot.2013.101; pmid: 23989673
52. C.-L. Hsieh *et al*., Structure-based design of prefusion-stabilized SARS-CoV-2 spikes. *Science* **369**, 1501–1505 (2020). doi: 10.1126/science.abd0826; pmid: 32703906
53. F. I. Schmidt *et al*., A single domain antibody fragment that recognizes the adaptor ASC defines the role of ASC domains in inflammasome assembly. *J. Exp. Med.* **213**, 771–790 (2016). doi: 10.1084/jem.20151790; pmid: 27069117
54. Z. Otwinowski, W. Minor, Processing of X-ray diffraction data collected in oscillation mode. *Methods Enzymol.* **276**, 307–326 (1997). doi: 10.1016/S0076-6879(97)76066-X
55. A. J. McCoy *et al*., Phaser crystallographic software. *J. Appl. Crystallogr.* **40**, 658–674 (2007). doi: 10.1107/S0021889807021206; pmid: 19461840
56. H. Liu *et al*., Cross-neutralization of a SARS-CoV-2 antibody to a functionally conserved site is mediated by avidity. *Immunity* **53**, 1272–1280.e5 (2020). doi: 10.1016/j.immuni.2020.10.023; pmid: 33242394
57. P. Emsley, B. Lohkamp, W. G. Scott, K. Cowtan, Features and development of Coot. *Acta Crystallogr. D* **66**, 486–501 (2010). doi: 10.1107/S0907444910007493; pmid: 20383002
58. P. D. Adams *et al*., PHENIX: A comprehensive Python-based system for macromolecular structure solution. *Acta Crystallogr. D* **66**, 213–221 (2010). doi: 10.1107/S0907444909052925; pmid: 20124702
59. E. Krissinel, K. Henrick, Inference of macromolecular assemblies from crystalline state. *J. Mol. Biol.* **372**, 774–797 (2007). doi: 10.1016/j.jmb.2007.05.022; pmid: 17681537
60. D. Tegunov, P. Cramer, Real-time cryo-electron microscopy data preprocessing with Warp. *Nat. Methods* **16**, 1146–1152 (2019). doi: 10.1038/s41592-019-0580-y; pmid: 31591575
61. A. Punjani, J. L. Rubinstein, D. J. Fleet, M. A. Brubaker, cryoSPARC: Algorithms for rapid unsupervised cryo-EM structure determination. *Nat. Methods* **14**, 290–296 (2017). doi: 10.1038/nmeth.4169; pmid: 28165473
62. J. Zivanov *et al*., New tools for automated high-resolution cryo-EM structure determination in RELION-3. *eLife* **7**, e42166 (2018). doi: 10.7554/eLife.42166; pmid: 30412051
63. Y. Z. Tan *et al*., Addressing preferred specimen orientation in single-particle cryo-EM through tilting. *Nat. Methods* **14**, 793–796 (2017). doi: 10.1038/nmeth.4347; pmid: 28671674
64. T. D. Goddard *et al*., UCSF ChimeraX: Meeting modern challenges in visualization and analysis. *Protein Sci.* **27**, 14–25 (2018). doi: 10.1002/pro.3235; pmid: 28710774
65. W. Stauffer, H. Sheng, H. N. Lim, EzColocalization: An ImageJ plugin for visualizing and measuring colocalization in cells and organisms. *Sci. Rep.* **8**, 15764 (2018). doi: 10.1038/s41598-018-33592-8; pmid: 30361629
66. A. M. Waterhouse, J. B. Procter, D. M. A. Martin, M. Clamp, G. J. Barton, Jalview Version 2—A multiple sequence alignment editor and analysis workbench. *Bioinformatics* **25**, 1189–1191 (2009). doi: 10.1093/bioinformatics/btp033; pmid: 19151095
67. J. Lan *et al*., Structure of the SARS-CoV-2 spike receptor-binding domain bound to the ACE2 receptor. *Nature* **581**, 215–220 (2020). doi: 10.1038/s41586-020-2180-5; pmid: 32225176

ACKNOWLEDGMENTS

We thank J. Ciftcioglu, G. Saavedra Perez Salas, J. Wieseler, and G. V. Gese for technical support; R. Businger for help with data analysis; G. Horvath and the Microscopy Core Facility of the Medical Faculty at the University of Bonn for providing help and services; the Karolinska Institutet for access to their 3D-EM facility, which was used for collection of all cryo-EM data; H. Tien for technical support with the crystallization robot; R. Stanfield for assistance with x-ray data collection; and the staff of Stanford Synchrotron Radiation Lightsource (SSRL) beamline 12-1 and Advanced Photon Source (APS) beamline 23ID-B for assistance. **Funding:** This study was partly supported by the Deutsche Forschungsgemeinschaft (DFG; German Research Foundation): GRK2168-272482170 (F.I.S.), SFB1403-414786233 (F.I.S.), TRR237-369799452 (F.I.S. and B.M.K.), SPP1923-429513120 (F.I.S. and M.S.), the Emmy Noether Programme 322568668 (F.I.S.) and LU 1933-3/1 (K.U.L.), GE 976/9-2 (M.G.), SCHI1073 (M.S.), and Germany's Excellence Strategy–EXC2151–390873048 (F.I.S., J.L.S.-B., H.K., and M.G.); by funds from the Medical Faculty of the University of Bonn (P.-A.K. and F.I.S.); by the Klaus Tschira Boost Fund (KT07) (F.I.S.), the Bundesministerium für Bildung und Forschung (BMBF), project TTU 01.806 (B.M.K.); by the Baden-Württemberg foundation (BW-Stiftung, BWST_WSF-022) (M.S.), the MWK Baden-Württemberg (33-7533-6-21/9/1) (M.S.), the University Hospital Tübingen (M.S.); the European Union's Horizon 2020 research and innovation program (CoroNAb consortium, L.H.); the Swedish Research Council (2017-6702 and 2018-3808) (B.M.H.); the Knut and Alice Wallenberg Foundation (B.M.H.); startup funds from the University of Illinois at Urbana-Champaign (N.C.W.); and the Bill and Melinda Gates Foundation OPP1170236 and INV-004923 (I.A.W.). Use of the SSRL, SLAC National Accelerator Laboratory, is supported by the U.S. Department of Energy (DOE), Office of Science, Office of Basic Energy Sciences, under contract DE-AC02–76SF00515. The SSRL Structural Molecular Biology Program is supported by the DOE Office of Biological and Environmental Research and by the National Institutes of Health, National Institute of General Medical Sciences (NIGMS) (including P41GM103393). General Medical Sciences and Cancer Institutes Structural Biology Facility at the Advanced Photon Source (APS) has been funded by federal funds from the National Cancer Institute (ACB-12002) and the NIGMS (AGM-12006). This research used resources of the APS, a DOE Office of Science User Facility operated for the DOE Office of Science by Argonne National Laboratory under contract DE-AC02-06CH11357. Extraordinary facility operations were supported in part by the DOE Office of Science through the National Virtual Biotechnology Laboratory, a consortium of DOE national laboratories focused on the response to COVID-19, with funding provided by the Coronavirus CARES Act. **Author contributions:** P.-A.K.: Conceptualization, Methodology, Formal analysis, Investigation, Data curation, Writing – original draft, Writing – review & editing, Visualization, and Supervision. H.D.: Formal analysis, Investigation, Writing – review & editing, and Visualization. H.L.: Formal analysis, Investigation, Writing – review & editing, and Visualization. B.M.K.: Methodology, Formal analysis, Investigation, Writing – review & editing, and Funding acquisition. F.N.G.: Investigation, Data curation, and Writing – review & editing. L.-M.J.: Investigation, Data curation, and Writing – review & editing. L.D.J.S.: Investigation, Data curation, and Writing – review & editing. Y.M.T.: Investigation and Data curation. M.U.: Investigation and Data curation. J.D.W.: Investigation, Data curation, and Writing – review & editing. K.G.: Methodology, Investigation, and Data curation. N.R.: Investigation and Data curation. M.H.C.: Resources and Investigation. C.I.F.: Resources and Investigation. S.N.: Methodology and Investigation. S.P.: Investigation. J.M.P.T.: Methodology and Investigation. L.H.: Resources. J.B.: Formal Analysis and Data curation. M.Y.: Investigation. X.Z.: Investigation. J.L.S.-B.: Methodology and Resources. H.K.: Methodology and Validation. M.S.: Methodology, Writing – review & editing, Supervision, and Funding acquisition. I.A.W.: Methodology, Writing – original draft; Writing – review & editing, Supervision, and Funding acquisition. M.G.: Methodology, Writing – review & editing, Supervision, and Funding acquisition. K.U.L.: Methodology, Data curation, Writing – review & editing, Supervision, and Funding acquisition. B.M.H.: Conceptualization, Methodology, Formal analysis, Investigation, Data curation, Writing – original draft; Writing – review & editing, Supervision, and Funding acquisition. N.C.W.: Conceptualization, Methodology, Formal analysis, Investigation, Data curation, Writing – original draft; Writing – review & editing, Supervision, and Funding acquisition. F.I.S.: Conceptualization, Methodology, Formal analysis, Investigation, Data curation, Writing – original draft; Writing – review & editing, Supervision, and Funding acquisition. **Competing interests:** B.M.H., P.-A.K., H.L., S.N., F.I.S., J.M.P.T., I.A.W., N.C.W., and M.Y., are listed as inventors of a pending patent application. P.-A.K. and F.I.S. are cofounders and shareholders of Dioscure Therapeutics SE; B.M.H. is a cofounder and shareholder of Macrostruct Holding and Consulting AB.; M.G. is a cofounder and shareholder of IFM Therapeutics; and F.I.S. is a consultant and shareholder of IFM Therapeutics. The other authors declare no competing interests. **Data and materials availability:** All data generated or analyzed during this study are included in this published article and its supplementary materials. Materials generated in this study will be made available for academic research on the basis of a material transfer agreement. Crystallographic coordinates and data have been deposited in Protein Data Bank under IDs 7KN5 (RBD + VHH E + VHH U), 7KN6 (RBD + VHH V + CC12.3), and 7KN7 (RBD + VHH W + CC12.3). The cryo-EM density maps have been deposited in the Electron Microscopy Data Bank under accession codes EMD-23018 (spike + VHH E), EMD-11978 (RBD + VHH E), EMD-11977 (spike + VHH V), EMD-11981 (spike + VHH VE), and EMD-11980 (RBD + VHH VE). The atomic coordinates have been deposited in the Protein Data Bank under IDs 7KSG (spike + VHH E), 7B14 (RBD + VHH E), 7B11 (spike + VHH V), 7B18 (spike + VHH VE), and 7B17 (RBD + VHH VE). NGS data of the RBD sequences of VSV eGFP SARS-CoV-2 S Δ18 derivatives described in Fig. 5 and tables S5 and S6 have been deposited in the Sequence Read Archive (SRA) under BioProject ID PRJNA679438. This work is licensed under a Creative Commons Attribution 4.0 International (CC BY 4.0) license, which permits unrestricted use, distribution, and reproduction in any medium, provided the original work is properly cited. To view a copy of this license, visit https://creativecommons.org/licenses/by/4.0/. This license does not apply to figures/photos/artwork or other content included in the article that is credited to a third party; obtain authorization from the rights holder before using such material.

SUPPLEMENTARY MATERIALS

science.sciencemag.org/content/371/6530/eabe6230/suppl/DC1
Supplementary Text
Figs. S1 to S23
Tables S1 to S8
References (*68*–*74*)
MDAR Reproducibility Checklist
Movies S1 to S22

View/request a protocol for this paper from *Bio-protocol*.

4 September 2020; accepted 6 January 2021
Published online 12 January 2021
10.1126/science.abe6230

Science

Structure-guided multivalent nanobodies block SARS-CoV-2 infection and suppress mutational escape

Paul-Albert Koenig, Hrishikesh Das, Hejun Liu, Beate M. Kümmerer, Florian N. Gohr, Lea-Marie Jenster, Lisa D. J. Schiffelers, Yonas M. Tesfamariam, Miki Uchima, Jennifer D. Wuerth, Karl Gatterdam, Natalia Ruetalo, Maria H. Christensen, Caroline I. Fandrey, Sabine Normann, Jan M. P. Tödtmann, Steffen Pritzl, Leo Hanke, Jannik Boos, Meng Yuan, Xueyong Zhu, Jonathan L. Schmid-Burgk, Hiroki Kato, Michael Schindler, Ian A. Wilson, Matthias Geyer, Kerstin U. Ludwig, B. Martin Hällberg, Nicholas C. Wu and Florian I. Schmidt

Science **371** (6530), eabe6230.
DOI: 10.1126/science.abe6230originally published online January 12, 2021

A double punch against SARS-CoV-2

Monoclonal antibodies are an important weapon in the battle against COVID-19. However, these large proteins are difficult to produce in the needed quantities and at low cost. Attention has turned to nanobodies, which are aptly named, single-domain antibodies that are easier to produce and have the potential to be administered by inhalation. Koenig *et al.* describe four nanobodies that bind to the severe acute respiratory syndrome coronavirus 2 (SARS-CoV-2) spike protein and prevent infection of cells (see the Perspective by Saelens and Schepens). Structures show that the nanobodies target two distinct epitopes on the SARS-CoV-2 spike protein. Multivalent nanobodies neutralize virus much more potently than single nanobodies, and multivalent nanobodies that bind two epitopes prevent the emergence of viral escape mutants.

Science, this issue p. eabe6230; see also p. 681

Science (print ISSN 0036-8075; online ISSN 1095-9203) is published by the American Association for the Advancement of Science, 1200 New York Avenue NW, Washington, DC 20005. The title *Science* is a registered trademark of AAAS.